

Tidal parks in the Rhine-Meuse estuary

Case study Groene Poort

L.W. Nijhuis



Tidal parks in the Rhine-Meuse estuary

Case study Groene Poort

by

Loes Nijhuis

to obtain the degree of Master of Science
at the Delft University of Technology,
to be defended publicly on 07-07-2021.

Student number:	4399188
Project duration:	March 16, 2020 – July 7, 2021
Thesis committee:	Dr.ir. B.C. van Prooijen TU Delft
	Dr.ir. E. Mosselman TU Delft
	Dr.ir. P.L.M. de Vet TU Delft
	R. den Breejen Rijkswaterstaat

An electronic version of this thesis is available at <http://repository.tudelft.nl/>.

Preface

Dear reader,

This thesis concludes the Master of Science programme in Hydraulic Engineering at Delft University of Technology. The research has been executed at Rijkswaterstaat and I am very grateful that I got the opportunity to work on my thesis at the section PPO.

I would like to thank all of my supervisors for their guidance and their support during this project. First of all, Erik Mosselman, thank you for inspiring me with the subject tidal parks in the Rhine-Meuse estuary and for guiding me through the project. Secondly, I would like to thank Lodewijk de Vet, for all the meetings mostly regarding Delft3D, but also the guidance on making this thesis readable. Thirdly I would like to thank Bram van Prooijen, although we did not meet very often, during the progress meetings your remarks really made me dive deeper in the material and by this improved my thesis. And last but not least, I would like to thank Rob van Breejen, my supervisor from Rijkswaterstaat. Thank you for giving me the opportunity to execute this research for Rijkswaterstaat. Unfortunately due to Corona I was not able to see the office, but I am very grateful for your supervision and attention through the year. You gave valuable insights into the subjects that needed more attention, and in addition I would like to express my gratitude for providing me all the data on which this research has been based.

By this thesis I am finalizing my master in Hydraulic Engineering. I had a difficult time choosing my education, but I am glad that I chose civil engineering, as my enthusiasm for hydraulic engineering quickly arose. I am also very enthusiastic and curious about all the work experiences that lie in front of me in the Hydraulic Engineering sector. I would like to thank all my friends, roommates, family and boyfriend for making this time as good as it has been.

*Loes Nijhuis
Delft, June, 2021*

Summary

The Rhine-Meuse estuary is part of the Southwestern Delta area in the Netherlands. The nature present in the estuary suffered a great impact due to urbanization, as a natural delta transformed into an industrialized river, mainly due to port activities. Various parties decided to collaborate in order to return the tidal nature in the Rhine Meuse estuary through constructing tidal parks. Although the idea of reintroducing tidal nature into an industrialized estuary seems promising, problems arise when the projects are being executed. Human interventions necessary to complete the design of the tidal parks often lead to undesired morphological changes. These either consisted of an excessive amount of cohesive sediment import, or hardly any import. Consequently, maintenance in form of dredging or nourishing activities is required. When introducing tidal nature, little maintenance is desired, both from a financial perspective and from an ecological perspective. The undesired morphological changes result from limited knowledge on the impact of human interventions on the hydro- and morphodynamics in tidal parks. This research therefore primarily focuses on gaining new knowledge on the hydrodynamics and morphodynamics inside tidal parks and assessing the effect of different elements such as groynes and longitudinal walls on the latter. This is done through a case study, the Groene Poort, a collective name for the tidal parks located in the Nieuwe Waterweg.

Few tidal parks are already present, and multiple parks are constructed in near future in the Nieuwe Waterweg. The tidal parks at the Groene Poort are developed between previously existing groynes in combination with newly constructed longitudinal walls parallel to the river bank. The presence of these structures creates a lee area in which sediment is expected to deposit. This accretion of sediment is expected to enhance the growth of tidal nature. However, monitoring shows that the time scale of the morphological changes is longer than expected. As a result, sand nourishments are executed at the river bank area which negatively affects the quality of tidal nature. The hydrodynamics present in the Rhine-Meuse estuary originate from the tide, river discharges, density differences, wind effects, and the sluicing programme of the Haringvliet sluices.

At the location of interest, the mean tidal range varies from -0.52 to +1.09 m relative to NAP. The location of the tidal park in the river is an important factor for the morphological development of the river bank. At the outer bends the intertidal area is smaller than average for river banks in the Nieuwe Waterweg. This is ascribed to spiraling flow in river bends. In addition, the river banks located closer to sea contain a lower average bed level, a smaller surface area and lower height of intertidal area compared to average values for the Nieuwe Waterweg.

A depth-averaged (2DH) Delft3D model is used to research the hydro- and morpho-dynamics of the tidal park. A constant tidal forcing and a constant fresh water discharge are used as boundary conditions. The effects of wind, waves and density driven currents are neglected. The effects of changes in hydrodynamic forcing, including a morphological tide, a spring tide and a spring tide in combination with a surge on the morphodynamics are determined. In addition, the effects of changes in geometry, including the bathymetry of the river bank area, the length of the longitudinal wall, the height and length of groynes and the surface area of the entrances on both the hydrodynamics and morphodynamics are researched.

This research showed that the tidal flow results in relatively small velocities inside the studied tidal park with mean velocities around 5 cm/s. The critical velocities for transport of non-cohesive sediment transport are only reached at the west entrance of the studied tidal park. At this location the sediment deposits, further transport towards the river bank is not possible resulting from the magnitude of velocities. A spring tide is responsible for an increased import of non-cohesive sediment at the river bank area. Cohesive sediment is able to deposit during low tide, when the water level is constant for a period of time. The presence of a spring tide is responsible for enhanced sedimentation in the intertidal area above ≈ -0.56 m NAP. The presence of an additional surge of one meter is responsible for additional sediment deposition in the intertidal area present at the corners of the river bank, above -0.48 m NAP.

The bed levels present at the river bank largely affect the flow magnitudes observed in the tidal park. Higher bed levels result in lower flow magnitudes due to larger frictional effects and possibly a smaller tidal prism. Consequently, the import of both cohesive and non-cohesive sediment decreases. The presence of a longitudinal wall decreases the dynamics at the river bank. A decrease in the length of the longitudinal wall in front of the river bank results in an increase in the magnitude of velocities. As a result of the increased dynamics, more erosion and sedimentation of cohesive sediment are present. The height and length of the groynes surrounding the river bank largely impact the velocities inside the considered tidal park. A decrease in blockage by the latter results in larger velocities and the velocity more resembling the profile in the navigation channel. Consequently, a large amount of cohesive sediment present at the river bank is eroded. The eroded sediment is mainly transported into the navigation channel. A small part of the eroded sediment is responsible for an increase in bed level at higher elevations. The presence of a sill decreases the magnitude of velocities present at the river bank. Consequently, this prevents erosion of cohesive sediment at the river bank. Enhanced sedimentation is observed in the area close to the sill. Fully blocking either entrance of the river bank results in a significant decrease in the magnitude of the velocity ($\bar{u}=0.015$ m/s). Erosion is hardly observed although sediment is imported at the river bank. This leads to the river bank accumulating sediment.

This research provides a guide on the effect of relatively small adaptations in geometry which will enhance or decrease the natural processes of sedimentation and erosion in the tidal parks. Tables are included providing the important parameters both with respect to the hydro- and morpho-dynamics of various adaptations in geometry. These tables can be used in future design and adaptations of already constructed tidal parks. However, the effect of the surrounding area including the location in the river greatly impact the hydrodynamics and morphological development of the tidal parks.

Contents

Preface	i
Summary	ii
1 Introduction	1
1.1 Context	1
1.2 Problem definition	2
1.3 Research objective	3
1.4 Research question	3
1.5 Research approach and outline	4
2 Understanding the system	6
2.1 Hydrodynamics of the Rhine-Meuse estuary	6
2.2 Morphodynamics of the Rhine-Meuse estuary	8
2.3 Tidal parks in the Rhine-Meuse estuary	9
3 The study area	13
3.1 Design concept and ecology	13
3.2 Sediment composition	15
3.3 Bed topography	16
3.4 Hydrodynamic forcing	17
3.4.1 Tidal regime	18
3.4.2 Wave climate	19
3.4.3 Wind forcing	22
3.4.4 Spiral flow in river	22
3.5 Affect of several structures on hydrodynamics	22
3.5.1 Groynes	22
3.5.2 Longitudinal walls	24
3.5.3 Sills	24
4 Field observations	26
4.1 Methodology	26
4.1.1 Sediment samples	26
4.1.2 Visual observations	27
4.2 Results	27
4.2.1 Sediment samples	27
4.2.2 Visual observations	29
5 Morphology of the river banks	32
5.1 Methodology	32
5.2 Results	34
5.2.1 Evolution over years	34
5.2.2 Location dependency	37
6 Simulation approach and model set-up	39
6.1 Hypotheses and modelling approach	39
6.1.1 Hydrodynamic forcing related	39
6.1.2 Human intervention-related	39
6.2 Model set-up	44
6.2.1 Process based model	44
6.2.2 Grid and bed schematization	45
6.2.3 Boundary conditions	45
6.2.4 Calibration and validation	47

7	Model results of base case and varying hydrodynamic forcing	50
7.1	Base case.	50
7.1.1	Hydrodynamics results	50
7.1.2	Morphodynamics results	54
7.2	Effect hydrodynamic forcing	60
7.2.1	Hydrodynamic results	60
7.2.2	Morphodynamics results	62
8	Model results of effects of human interventions	70
8.1	Varying bed topography	70
8.2	Varying longitudinal wall	77
8.3	Varying groyne heights/lengths	84
8.3.1	Submergence of groynes	84
8.3.2	Varying length of groynes	88
8.4	Varying inlet.	95
9	Discussion	104
9.1	Literature review on tidal parks	104
9.2	Insights from measurements.	104
9.3	Insights from numerical model simulations	104
9.4	Integration of the results	106
10	Conclusions	109
11	Recommendations	111
11.1	Further research on tidal park the Groene Poort	111
11.2	General recommendations	112
11.3	Recommendation for tidal parks in the Nieuwe Waterweg	112
	References	114
A	Tidal parks in the Rhine-Meuse estuary	120
A.1	Short description of tidal parks.	120
A.1.1	Tidal parks in the Haringvliet.	120
A.1.2	Tidal parks in the 'Noord'.	121
A.1.3	Tidal parks in the Nieuwe Waterweg	122
A.1.4	Tidal parks in the Scheur.	123
A.1.5	Tidal parks in the Nieuwe Maas	123
A.1.6	Tidal Parks in the Oude Maas	125
A.2	Determination of tidal ranges at tidal park.	126
A	Sediment transport in tidal regions	128
A.1	Sediment transport	128
A.2	Sediment transport mechanisms	130
A.2.1	Lag effects	130
A.2.2	Tidal asymmetry	132
A.2.3	Wave driven transport	132
B	Morphology of the river banks - additional data analysis	133
C	Calibration of the model and sensitivity analysis	139
C.1	Bed topography.	139
C.2	Sensitivity analysis non-cohesive sediment.	139
C.3	Sensitivity analysis cohesive sediment	142
C.3.1	Critical shear stress erosion silt	142
C.3.2	Horizontal eddy diffusivity	143
C.3.3	Different concentrations of cohesive sediment	144

D	Supporting simulations	146
D.1	Flow patterns hydrodynamic forcing scenarios	146
D.2	Adaptations in bathymetry	150
D.2.1	Simulation D.1	150
D.2.2	Simulation D.2	151
D.2.3	Simulation D.3	152
D.3	Adaptation longitudinal wall	153
D.3.1	Simulation E.1	153
D.3.2	Simulation E.2	154
D.3.3	Simulation E.3	155
D.3.4	Simulation E.4	156
D.4	Adaptation groynes	157
D.4.1	Simulation F.1	157
D.4.2	Simulation F.2	158
D.4.3	Simulation F.3	159
D.4.4	Simulation F.4	160
D.4.5	Simulation F.5	161
D.4.6	Simulation F.6	162
D.4.7	Simulation F.7	163
D.5	Adaptation inlet	164
D.5.1	Simulation G.1	164
D.5.2	Simulation G.2	165
D.5.3	Simulation G.3	166
D.5.4	Simulation G.4	167
D.5.5	Simulation G.5	168
E	Morphodynamic results from variations in geometry	169
E.1	Bathymetry	169
E.1.1	Non-cohesive sediment	169
E.1.2	Cohesive sediment	170
E.1.2.1	Non-erodible bed layer	170
E.1.2.2	Erodible bed layer	171
E.2	Longitudinal wall	172
E.2.1	Non-cohesive sediment	172
E.2.2	Cohesive sediment	173
E.2.2.1	Non-erodible bed layer	173
E.2.2.2	Erodible bed layer	174
E.3	Groynes - submergence	175
E.3.1	Non-cohesive sediment	175
E.3.2	Cohesive sediment	176
E.3.2.1	Non-erodible bed layer	176
E.3.2.2	Erodible bed layer	177
E.4	Groynes - length	178
E.4.1	Non-cohesive sediment	178
E.4.2	Cohesive sediment	179
E.4.2.1	Non-erodible bed layer	179
E.4.2.2	Erodible bed layer	180
E.5	Inlet	181
E.5.1	Non-cohesive sediment	181
E.5.2	Cohesive sediment	182
E.5.2.1	Non-erodible bed layer	182
E.5.2.2	Erodible bed layer	183

Introduction

1.1. Context

The Rhine-Meuse estuary is part of the Southwest Delta area in the Netherlands. Due to urbanization a lot of nature got affected in the process and a natural delta transformed into an industrialized river for mainly port activities. As a result of this industrialization, the delta character with the rhythm of ebb and flood on a daily basis can hardly be found in the estuary anymore (Gemeente Rotterdam, 2018). Many parties decided to collaborate to return the tidal nature in the Rhine-Meuse estuary by constructing tidal parks. This collaboration resulted in a regional programme which is called 'River as a tidal park' and is operating since 2015 (Gemeente Rotterdam, 2018). A tidal park is defined as a park which is under the effect of tidal forcing and reconnects the city and the river. Multiple causes have led to the wish of restoring nature in the industrialized delta. Examples are the construction of Maasvlakte 2 which lead to a lot of harbour basins losing their function (Dinteren, 2005). Next to that townships are involved because tidal parks are a way of improving the living environment in the city (Gemeente Rotterdam, 2018). Governmental parties are involved as constructing environmentally-friendly river banks is a way of improving the ecological water quality. This is in agreement with the goals of Rijkswaterstaat resulting from the requirements set for water bodies by the EU (Rijkswaterstaat, 2020a). The tidal parks constructed in such an industrialized area have multiple functions, improving ecology, ensuring recreation, creating spaces for social interaction, improving the local economy, and in addition tidal parks are a laboratory for knowledge development (Gemeente Rotterdam, 2018). However, an important function of the river is that it is an important shipping route and this should not be prejudiced.

The idea of restoring tidal nature which was destroyed by industrialization is not only happening in the Netherlands but over the entire world. Multiple projects are executed to restore tidal nature. For example, the 'Lifeline Kirchwerder' and the 'Tidal lowlands Luhe' in the river Elbe located in Hamburg, Germany. In these projects, tidal creeks and tidal flats developed instead of the straightened, trained, and partly fortified river bank (Stiftung Lebensraum elbe, 2020). Besides that in 1996 large-scale marsh restoration (149 ha) was executed in Delaware Bay, United States. In this project tidal inlets were constructed and tidal creek systems were dug (Kimball and Able, 2007). Another technique of restoring tidal nature is executed in Lippenbroek, Scheldt river, Belgium (Van Holland et al., 2010). In this project, a polder of 10 ha is transformed into a flood control area with a controlled reduced tide system, which consists of an overflow dike, by which high water enters through an inlet sluice. The water is stagnant for two hours in the polder for the sediment to settle and when the tide falls the water flows out through an outlet sluice (Van Holland et al., 2010).

Hydrodynamic and morphodynamic processes in the Rhine-Meuse estuary are a topic of ongoing research. Multiple studies are focused upon large-scale processes, for example, the underlying physics behind the large-scale siltation of harbour basins in the Port of Rotterdam (De Nijs et al., 2011), (De Nijs, 2012). Secondly, many studies examine the effect of the closure of the Haringvliet sluices in 1970, including the effect on the morphodynamic changes in river branches in the Rhine-Meuse estuary (Sloff et al., 2013). The tidal parks considered in this research are all constructed inside the Rhine-Meuse estuary. The hydrodynamic and morphodynamic processes inside the tidal park are dependent on the large-scale processes which are extensively treated in researches such as mentioned above. This includes the availability of sediment and the underlying sediment transport mechanisms. Besides these large-scale processes, the geometry of the tidal park affects the morphodynamic changes. As the construction of tidal parks in the Netherlands started a few years ago, previous studies have been carried out to understand and predict sediment transport in tidal parks. For example, the study of Van Delden

(2019) treated the effect of the marsh design and system adjustments on sedimentation and erosion in tidal park 'the Stormpoldervloedbos' by use of a hydrodynamic 1D model SOBEK. The second study is conducted into the existence of a sandy beach and possible siltation problems in tidal park the Rijnhaven and is still in research phase (Freijns, 2020).

1.2. Problem definition

Although the idea of reintroducing tidal nature into an industrialized estuary seems promising, some problems arise when the projects are being executed. When introducing tidal nature, little maintenance is desired both concerning the costs but also for the quality of tidal nature, specifically the benthos communities. Interventions constructed for the design of the tidal park often lead to undesired morphological changes. This introduces maintenance in form of dredging or nourishment activities.

An example of this is a tidal park in the Rhine-Meuse estuary, the Sophiapolder, located near Dordrecht, the Netherlands in which a polder was transformed into a tidal park by constructing a system of tidal creeks and flats in 2011 (Van den Broek and de Wit, 2006). There is a large input of sediment in this area, especially at the shallow channels, but not much sediment transport is transported towards the tidal flats at which reed and brushes were expected to grow, which is not happening according to the desired time scale. Besides that large amounts of erosion is taking place at the entrances and the quay walls of the tidal park (De Haan, 2020). To solve these problems, maintenance is required in form of sand nourishment at the quay wall and possibly dredging of the channels (De Haan, 2020).

Dredging activities harm the benthos communities, as is already obtained from the effect of dredging the shipping channel of the Nieuwe Waterweg, access channel to the port of Rotterdam (Hal et al., 2011). A sand nourishment temporarily destroys benthic life when the sediment layer is larger than 0.5 meters (Baptist et al., 2008). The recovery of the benthos life after a nourishment takes several years. For example, the sand nourishment at the Galgenplaat (Eastern Scheldt) in 2008 showed that the macro benthos community was almost restored after three years (Van Der Werf et al., 2015). This shows that the effect of regular maintenance at the tidal parks has a large impact on the quality of tidal nature, and should be limited to the minimum necessary.

The construction of tidal parks improves the quality of local ecosystems. Besides that, it ensures that the goal of Rijkswaterstaat to improve the ecological quality of water bodies in the Netherlands is reached. Consequently, in near future multiple tidal parks will be constructed in the Nieuwe Waterweg, with already a few being constructed (Gemeente Rotterdam, 2018), see Figure 1.1. Tidal park the Groene Poort has already been partially constructed. All the other tidal parks displayed are in the design phase. The tidal parks at the Groene Poort are developed between previously existing groynes in combination with newly constructed longitudinal walls parallel to the river bank. The presence of these structures creates a lee area in which sediment is expected to deposit. By this natural processes will result in tidal nature. However, monitoring shows that the time scale of the morphological changes is longer than expected. As a result, at certain locations, additional sediment nourishments are executed in the calm area behind the dam. It is expected that this accelerates the process of the river bank becoming a sloping inter-tidal riverbank, and in this way sooner reaching the goal as a good quality water body according to WFD (Water Framework Directive). However, this negatively affects the quality of the tidal nature.

As multiple kilometres of tidal parks are still to be constructed in the same manner as the ones that have already been constructed, there is a need for a comprehensive understanding of the sediment transport in these tidal parks. By this, it will become easier to design a tidal park in which little maintenance is required. In the present day, it is not yet known how sediment is transported into these tidal parks and also, the effect of small adaptations in geometry on sediment transport is still unknown.

Summarizing, the problem statement is defined as follows:

Sediment transport in tidal parks in the Rhine-Meuse estuary is relatively under-examined which leads to unexpected results in terms of morphological behaviour of the tidal parks. A comprehensive understanding of the sediment transport in tidal parks is required to design a tidal park requiring minimal

maintenance and stimulating the development of tidal nature through natural processes. Besides, the application of numerical models on the scale of tidal parks is not thoroughly examined. Neither is the monitoring of abiotic processes in tidal parks.

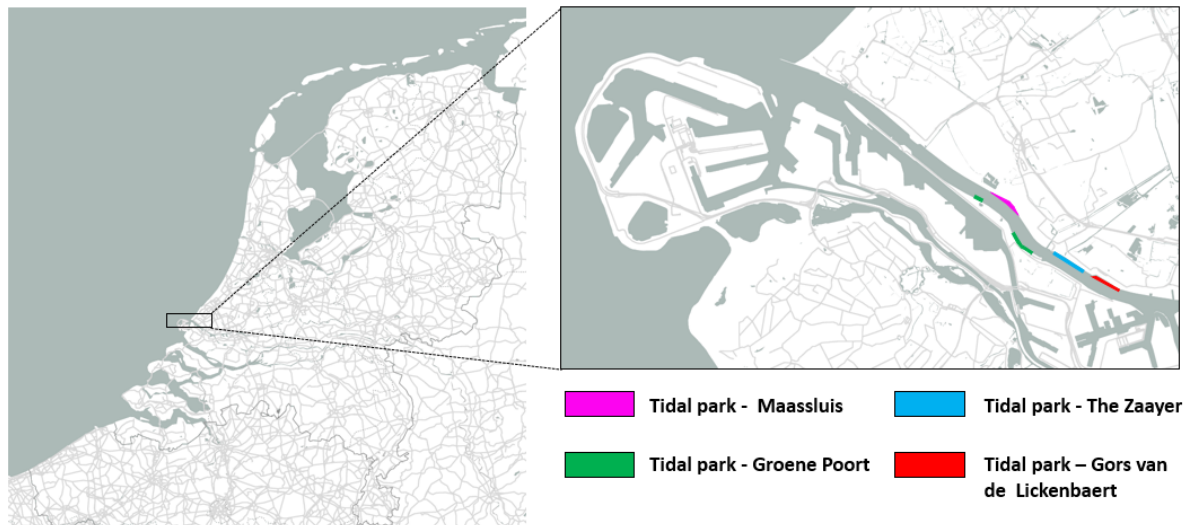


Figure 1.1: Location of constructed and yet to be constructed tidal parks in the Nieuwe Waterweg / the Scheur

1.3. Research objective

The objective of this research is to construct a comprehensive understanding of the physical processes that are of importance in constructed tidal parks in the Rhine-Meuse estuary. This will result in more knowledge on the different processes depending on their location relative to the sea, construction manner but also on the different sources of sediment. The second objective of this research is to investigate the present-day hydrodynamics and morphodynamics in tidal park the Groene Poort (case study location). To this end, a two-dimensional numerical model of the Nieuwe Waterweg is developed. By incorporating different hydrodynamic forcing scenarios in the numerical model the understanding of the morphodynamic response of the tidal park increases. Thereafter the objective includes gathering insights into the effect of changes in geometry of the tidal park on sediment transport towards the tidal park.

1.4. Research question

The above described objectives lead to the following research questions:

What are the physical processes that cause sedimentation and erosion problems in constructed tidal parks in the Rhine-Meuse estuary and how can the design of these tidal parks be adapted such that little maintenance is needed and mainly natural processes lead to the desired tidal nature?

To answer the above research question, several sub-questions are defined:

Sub-questions

- What are the important physical processes in the Rhine-Meuse estuary?
- Which tidal parks are present at the Rhine-Meuse estuary and how are they functioning?
- What are the important physical processes specifically for tidal parks considered in the case study, and how can these processes be affected by adapting the geometry of the tidal parks?
- What is the historical development of the river banks along which the tidal parks from the case study are located?

- How do changes in the hydrodynamics affect the morphodynamics in the tidal parks according to the developed model?
- What is the effect of various changes in geometry on the flow structure and sediment transport in tidal parks according to the developed model?

1.5. Research approach and outline

Literature review

The literature study conducted in this thesis consists of three parts. In part one the necessary background knowledge on the physical processes affecting the hydrodynamics in the Rhine-Meuse estuary is researched. In addition, the characteristics and the transport of the sediment present in the Rhine-Meuse estuary are researched. This part of the literature review is discussed in Chapter 2, 'Understanding the system'. Part two consists of a study into the tidal parks present in the Rhine-Meuse estuary. This provides a comprehensive understanding of the location and types of tidal parks present in combination with problems and correlations between the latter of tidal parks in the Rhine-Meuse estuary. The result of this review is a large overview table consisting of a description of every tidal park, the main purpose, the design, problems occurring, type of sediment, maintenance, physical processes and the tidal range. This part of the literature review is discussed in Chapter 2 and in Appendix A, 'Tidal parks in the Rhine-Meuse estuary'. Part three consist of the necessary background knowledge on the study area of the case study. This knowledge concerns information on the hydrodynamic forcing and the effect of changes in geometry on hydro- and morphodynamics. This is presented in Chapter 3, 'The study area'.

Data analysis

Data is analyzed to determine the morphological evolution of the river banks at the Nieuwe Waterweg. The available data consists of bed level data measured with a multi-beam echo sounder. From this data erosion/sedimentation patterns can be visualised, discussed in Chapter 3. From this bed level data hypsometric curves can be constructed, these are found in Chapter 5, 'Morphology of the river banks'. In addition data obtained from field observations at the tidal park is analysed. This data consists out sediment samples and drone images of the tidal park. This is presented in Chapter 4, 'Field observations'. Data provided by Aquitec, which consists of velocity measurements by two buoys in the tidal park is analysed in Chapter 3 in order to determine the order of magnitude of velocities inside the tidal park.

Modelling study

To get a better understanding of the hydro- and morphodynamics of the tidal parks in the Nieuwe Waterweg, a numerical model is set up in Delft3D. The constructed model is a 2DH model, which indicates that the effect of stratified flows is not taken into account. This effect is assumed to have a minor effect on the sediment transport at the river banks. Although the effect of waves on sediment transport is treated in Chapter 3, waves are not incorporated into the model in view of time and simplicity. The application of the model in terms of morphodynamic modelling is separated into two parts, one regarding the transport of silt and one regarding the transport of sand. Only the sediment characteristics differ in these models. All other model settings are kept the same and are further described in Chapter 6. The numerical model will serve multiple goals. One goal is to gain more insight into the effect of hydrodynamic forcing on the flow velocities and corresponding sediment transport in the tidal park, these variations consist out of the morphological tide, spring tide and a storm surge. Secondly, a sensitivity analysis of the effect of sediment characteristics on the sediment transport into the tidal parks is performed. Lastly, hypotheses written on the effect of changes in geometry on the hydro- and morpho-dynamics of the tidal park are tested by use of this model. The results of the model study are presented in Chapter 7 and 8.

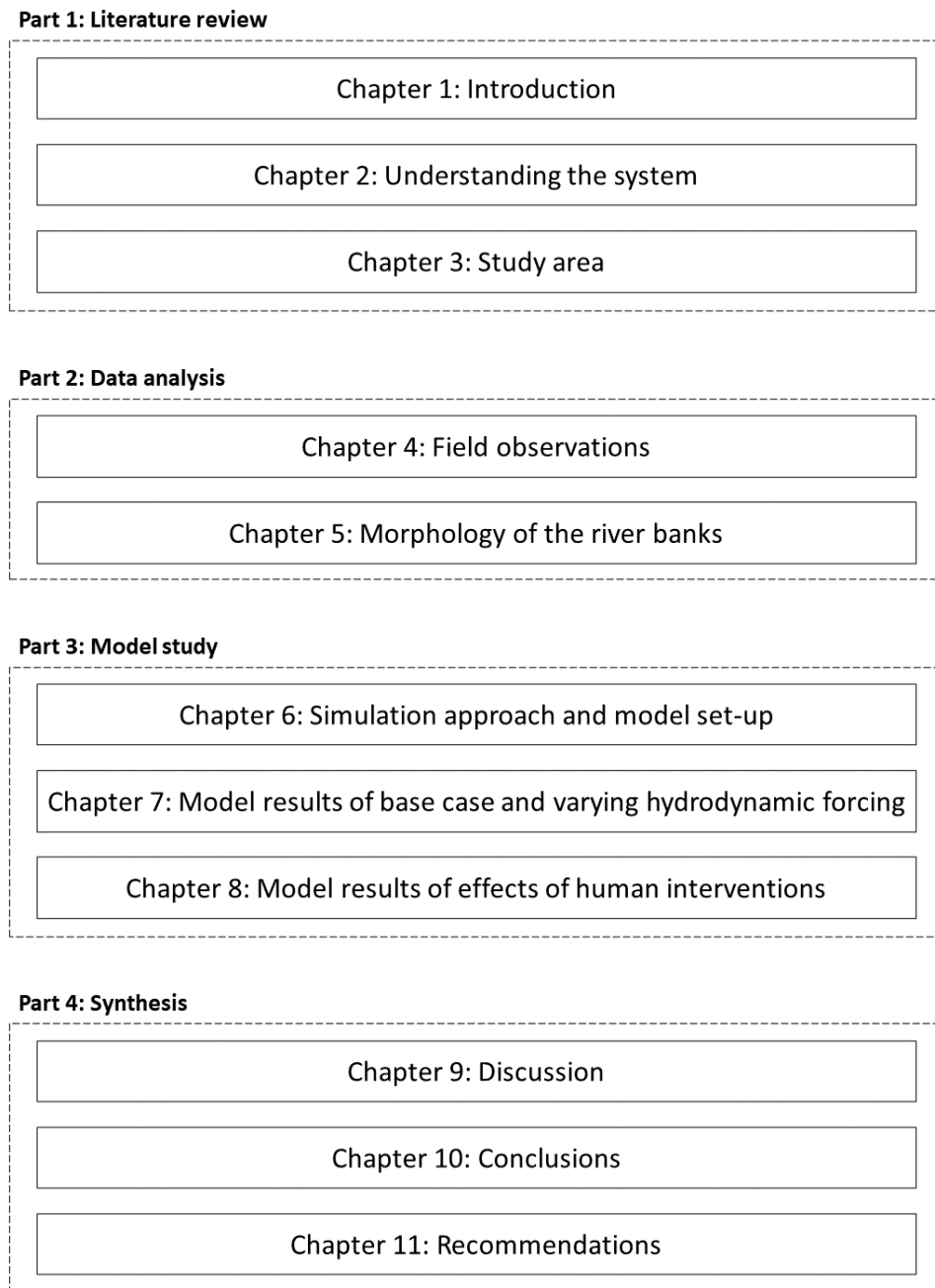


Figure 1.2: Research outline

Understanding the system

In this chapter background knowledge on the Rhine-Meuse estuary is elaborated. This consists of the underlying physical processes governing the estuarine circulation and the sediment present at the Rhine-Meuse estuary. Thereafter the tidal parks present in the Rhine-Meuse estuary, which can be in the design, construction, or user phase are described. The full description of the tidal parks can be found in Appendix A. In this chapter, a large overview table is displayed, consisting of a description of each tidal park, the main purpose, the design, type of sediment, tidal range, and the important physical processes.

2.1. Hydrodynamics of the Rhine-Meuse estuary

In this section, the physical processes governing the water motion inside the Rhine-Meuse estuary are explained. An estuary is defined as a body of water where the freshwater inflow from the rivers meets the saltwater from the coastal zone. The water motion inside the Rhine-Meuse estuary is determined by the tide, river discharges, density differences, wind effects, and the sluicing program of the Haringvliet sluices (De Nijs, 2012). Initially, more information is presented governing the origin of the tide and the discharges present at the Rhine-Meuse estuary. Thereafter the resulting estuarine circulation is discussed. An important aspect of the estuarine circulation is dependent on the presence of the salt wedge, further explained in this section. Inside the tidal parks, more specific processes like waves originating from wind and vessels also affect sediment transport. This is elaborated in Chapter 3, 'The study area'.

The tide originates from the gravitational pull of the moon and the sun on the water in the oceans. The sun and the earth revolve around their common center of gravity and the moon and earth revolve around their common center of gravity. Simplified it can be said that the earth circles around the sun and the moon circles around the earth based upon the gravity center of the earth-sun and the earth-moon. Besides that the earth also rotates about its own axis, the sum of all these forces leads to the generation of the tide (Bosboom and Stive, 2015). At the coast and in estuaries the tide is observed as daily water variations. The value of the water elevations during high and low tide are varying depending on the location of the moon and the sun relative to the earth. When the sun, earth, and moon are in line, the solar and lunar tides reinforce each other and the tidal amplitude gets higher which is called a spring tide. When the sun and the moon are in 90 degrees with another, so-called neap tide occurs and the amplitude of the tide is smaller as the effects of the moon and the sun cancel each other out (Bosboom and Stive, 2015). The tide imposed at the Maasmond, the mouth of the Rhine-Meuse estuary, is semi-diurnal which indicates that it experiences two high and two low tides a day. The mean spring tidal range at the Maasmond is about 2 meters and the mean neap tidal range is 1.2 meters (De Nijs, 2012).

The freshwater inflow reaching the North sea originates from the rivers Rhine and Meuse after bifurcating into several branches. Before the construction of the Haringvliet, the outflow of freshwater occurred along the Northern branch which consists of the Nieuwe Waterweg and the Nieuwe Maas and along the Southern branch which consists of the Haringvliet only (Sloff et al., 2013). The Haringvliet outlet was closed in 1970 by the construction of a barrier, present-day the sluices of the Haringvliet barrier are partly opened. The discharge through the Haringvliet, and thus the management of the sluices is dependent on the discharge from the Rhine and the Meuse. Up until 2018, the Haringvliet sluices were partly opened if freshwater discharges at Lobith exceeded $1100 \text{ m}^3/\text{s}$, thereafter the surface area of the opening of the sluices increases until they are fully opened at a discharge of $9000 \text{ m}^3/\text{s}$ at Lobith (Rijk-

swaterstaat, 2011a). However, due to ecological reasons, since 2019 the sluices of the Haringvliet dam are partly opened during high tide when the water levels in the Haringvliet are smaller than at sea (Rijkswaterstaat, 2018b). The freshwater discharge flowing through the Nieuwe Waterweg is dependent on the incoming discharges from the Oude and the Nieuwe Maas. The discharge through the Nieuwe Waterweg is regulated being equal to 1500 m³/s for a discharge between 1700 and 3900 m³/s in the Rhine at Lobith (Van Spijk, 2009). Thereafter the discharge through the Nieuwe Waterweg increases with the same rate as the incoming discharges from the Oude and the Nieuwe Maas. The average annual discharge at Lobith is 2200 m³/s and the maximum discharge is equal to 12 600 m³/s (Linde and Aerts, 2008). Concluding, it can be obtained that the combination of the variable tidal forcing and freshwater discharges leads to a dynamic system. As a result, the flow directions and magnitudes are constantly changing.

The interaction of the saltwater from the marine environment and the freshwater inflow from the river results in a salinity distribution which is often referred to as a salt wedge. This results from the balance between the export of salinity by the freshwater discharge and import by the gravitational flow (De Nijs, 2012). During high tide, the inflow of saline water can result in a flow pattern in which the saline water flows under the freshwater inflow resulting from the density difference. The resulting system can either be a stratified estuary, which is characterized by a sharp transition between saline and freshwater, or a well-mixed estuary in which a gradual transition between the fresh and saline water is present (Sloff et al., 2012). The type of mixing present depends on the density of both the fresh and saline water, the water depth, tidal velocity, freshwater discharge, tidal period, and the flood volume. The Rhine-Meuse estuary is partially mixed during low river discharges and stratified during high discharges. The presence of the salt wedge affects the velocity profile inside the estuary. The location of the tip of the salt wedge is governed by advection as turbulent mixing is suppressed (De Nijs, 2012). During the measurement campaign in the research of De Nijs (2012), the saltwater intrusion length was maximum near-surface at 2 km and minimum near-bottom at 11 km relative to Hoek van Holland during low water slack. The saltwater intrusion length was maximum near-surface at 13 km and minimum near-bottom at 20 km relative to Hoek van Holland during high water slack. The Rhine-discharge during the period of survey was equal to 4000 m³/s.

The tidal wave inside an estuary often deviates from a perfect sinusoidal tide. This is referred to as tidal asymmetry, which can both concern the horizontal and the vertical tide (current and water level). The distortion between a perfect sinusoidal tide and the observed tide can be described by the inclusion of higher harmonics (Bosboom and Stive, 2015). These are integer fractions of the period of the basic astronomical constituents generated by attraction forces of earth, moon, and sun and are called overtides or shallow-water tides. The source of the non-linearity in tidal propagation, the distortion of a sinusoidal wave, are bottom friction and continuity (Bosboom and Stive, 2015). The deformation of the tide is related to the celerity of the tidal wave. The latter is depended on the gravitational acceleration (g) the water level (h_0) and the wave height (η), in formula $c = \sqrt{g * (h_0 + \eta)}$. From this, it can be obtained that the wave celerity is higher during high water than during low water. This leads to the tidal wave signal becoming skewed. This skewness is further enhanced by the friction affecting the low water wave more than the high water wave (Bosboom and Stive, 2015).

The tidal wave present at the Maasmond is asymmetric when it enters the Rhine-Meuse estuary (De Nijs et al., 2011). The presence of the asymmetry of the tide originates from the interaction of the tidal wave with the shallow coastal zone and interaction with topography and geometry. As mentioned before, tidal asymmetry can be described by the inclusion of higher harmonics. The M2 tide is the principal lunar semi-diurnal constituent and M4 is the overtide of this constituent. The ratio between these constituents indicates the deformation of the sinusoidal tide. The ratio between the amplitudes of M2 and M4 does not increase further upstream the estuary. From this, it can be obtained that the effect of nonlinear shallow-water interactions is small, and thus the generation of M4 overtides within the estuary is small (De Nijs, 2012). This can be related to the relatively deep navigation channel.

The tide imposed at the Maasmond, the mouth of the Rhine-Meuse estuary has phase differences between the M2 and M4 water levels between 0 and 180 degrees, which indicates that the tide rises faster than it falls. This asymmetry in combination with the incoming freshwater discharge from rivers

results in larger ebb than flood periods. Close to the Maasmond, at the surface, an ebb dominant velocity profile is obtained and in the lower part of the water column, a flood dominant velocity profile is obtained. This is related to the presence of the salt wedge, in which the flow is directed in up-estuary direction. The presence of the salt wedge is the governing factor for the large input of sediment at the Rhine-Meuse estuary. At an observation point, a bit upstream from tidal park Gors van de Lickenbaert, indicated with a black rectangle in Figure 2.1b, during a discharge of $4000 \text{ m}^3/\text{s}$ the velocity profile is obtained in the water column. This is displayed in Figure 2.1a. From this figure, it can be observed that the duration of the ebb period is longer than the flood period. Besides, it also displays that close to the surface the velocities are ebb dominant, and close to the bed the maximum flood and ebb velocities are equal. Further upstream in the estuary, the velocity profile changes as the fresh water inflow becomes more dominant. The ebb period and corresponding maximum velocities are larger than the flood periods and velocities (De Nijs, 2012). The incoming tidal wave at the Maasmond generally decreases land inwards, while the phase difference with the incoming wave at Hoek van Holland increases land inwards (Vellinga et al., 2014). The decrease of the tidal amplitude is displayed in Figure 2.1b. This displays that up to Rotterdam the tidal range remains quite high and thereafter there is a quick decrease in tidal amplitude.

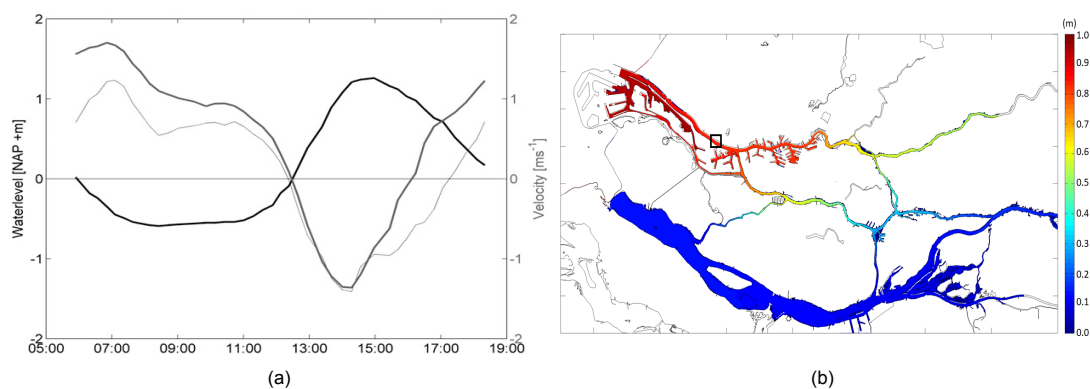


Figure 2.1: In Figure 2.1a the time series of water level (black line), velocity 2.5 m above bed (dashed gray line), and velocity 12.5 m above bed (thick gray line) at station 2, close to tidal park Gors van de Lickebaert are displayed (location displayed in Figure 2.1b with a black rectangle). The reference frame used in the Netherlands is the Normaal Amsterdams Peil (NAP), obtained from De Nijs et al. (2011). In Figure 2.1b an overview of the tidal range (m) in the Rhine-Meuse estuary is displayed, determined by determined by Vellinga et al. (2014). The red color indicates a tidal range of one meter and dark blue zero meter.

2.2. Morphodynamics of the Rhine-Meuse estuary

The Rhine-Meuse estuary can be split up in three sections for clarity, the northern part (Nieuwe Waterweg and Nieuwe Maas), the western part (Lek, Boven Merwede and Beneden Merwede), the connecting branches (Oude Maas, Dordtsce Kil, Spui and Noord) and the southern branches (Haringvliet, Hollandsch Diep, Amer, Bergsche Maas) (Huisman and Hoitink, 2017). These sections are all experiencing different types of sedimentation/erosion processes. These processes can be related to natural processes but also dredging activities play a major role in the total bed level trends (Huisman and Hoitink, 2017). This can be observed from Figure 2.2, in which the left figure represents the total bed level trends including dredging activities and the bottom figure displays the bed level trends if no dredging took place for the period 2000-2012 (Huisman and Hoitink, 2017).

The northern and western part of the Rhine Meuse estuary are naturally experiencing accretion but mainly due to dredging activities the result is an overall bed degradation. The connecting branches are experiencing erosion which can also be seen from Figure 2.2, with the largest erosion rates in the Oude Maas. The southern branches are experiencing an accumulation of sediment, in combination with erosion present in the connecting branches, likely results from the closure of the Haringvliet basin that changed the tidal regime in the Rhine-Meuse estuary (Sloff et al., 2013).

The source of sediment that is responsible for sedimentation in the Rhine-Meuse estuary originates from two sources, the North Sea and from upstream rivers. According to Huisman and Hoitink (2017), the total import of marine sediment at the Mouth of the New Waterway is estimated 1.6 - 2 Mton sand

and 1.4-2.8 Mton silt and clay, per year. The total amount of fluvial sediment import via the rivers Meuse, Waal and Lek is equal to 1.1-1.6 Mton sand, 1.7-3.4 Mton silt and clay, per year.

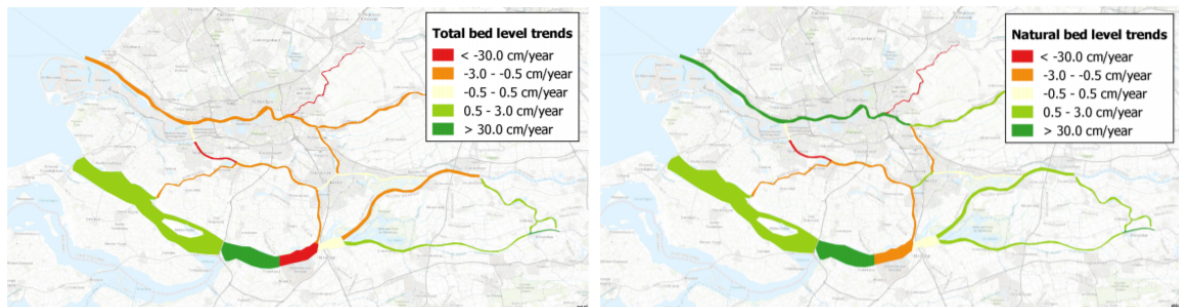


Figure 2.2: The total bed level trends compared to natural bed level trends in the Rhine Meuse estuary between 2000 and 2012 (Huismans and Hoitink, 2017)

The supply of silt is transported through suspended sediment transport, and the supply of sand is governed by bed transport (Snippen et al., 2005). The median grain diameter at the bottom in the middle of the river is determined at several locations. The result is displayed in Figure 2.3. This figure shows that the grain diameter is finer moving from east to west. In the Haringvliet really fine sediment is located. From the sediment balance, it is obtained that in the Nieuwe Waterweg and the Scheur a lot of marine and fluvial silt is deposited. This originates from the feature of an estuary having an estuarine turbidity maximum (ETM). This often results from the accumulation of sediment at the tip of the salt wedge (De Nijs, 2012). At these locations in the Rhine-Meuse estuary, port basins are located which serve as large sediment traps.

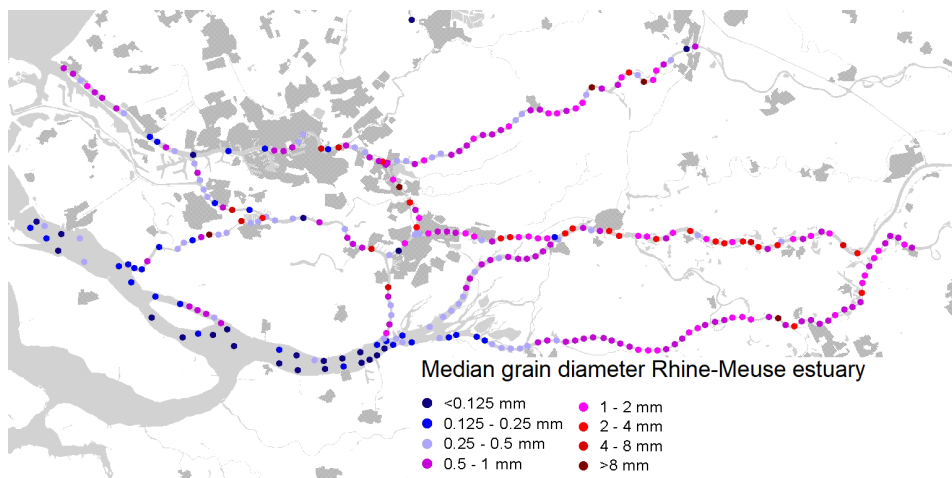


Figure 2.3: The median grain diameter present at several locations inside the Rhine-Meuse estuary

2.3. Tidal parks in the Rhine-Meuse estuary

There are several tidal parks present in the Rhine-Meuse estuary, some are already constructed and some are still in the construction or design phase. The tidal parks considered in this research are displayed in Figure 2.4, in which the green shapes indicate the already constructed tidal parks and the orange shapes represent the not yet constructed tidal parks. The tidal parks in the Dordtse Biesbosch (Noordendijk, Nieuwe Dordtse Biesbosch, Noord bovenpolder) are also located in the Rhine-Meuse estuary, these are however not treated in this research due to time constraints.

The desire to restore tidal nature inside the Rhine-Meuse estuary has been a topic of interest for a long time. Therefore the time scale in which tidal parks are constructed is long. For instance, tidal park the Stormpoldervloedbos has been constructed in 1993 (Natuurvereniging IJsselmonde, n.d.) and

tidal park Tiengemeten in the year 2005 (De Boo, 2008). At some locations, the tidal nature was still present but by human interventions, for instance the closure of the Haringvliet, the circumstances for tidal nature development was not suitable anymore. By changing the geometry at these locations, the circumstances were improved and the tidal nature could be restored. An example of this is tidal park Korendijkse slikken (Wesseling, 2019). The full description of all the tidal parks displayed in Figure 2.4 can be found in Appendix A.

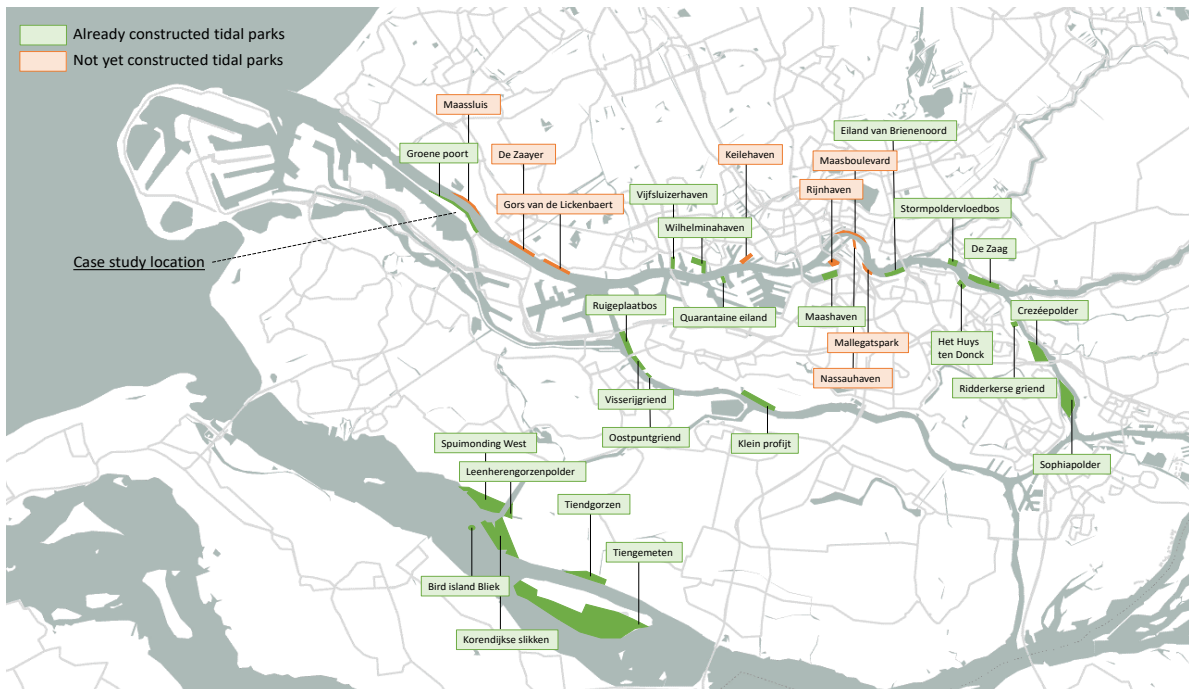


Figure 2.4: Tidal parks in the Rhine-Meuse estuary which are treated in this research. The locations of the tidal parks are indicated. In addition, the case study treated in this research, the Groene Poort, is indicated. The colors indicate if the tidal parks in construction / design phase = orange and already constructed = green.

Table 2.3 contains a summary of the tidal parks including the location, the main purpose, the design, the tidal range, the type of sediment present and the important physical processes of the tidal park. The presence of '(-)' inside the table indicates that the information could not be obtained from literature. Secondly, n/a indicates if that the information could not be obtained as it is not applicable to the tidal park.

The tidal range at the tidal parks is presented in seventh column of Table 2.3. This range is based upon the astronomical tide data-base of Rijkswaterstaat, which is calculated being the difference between the MLW and MHW, based upon two tidal cycles. One should keep in mind that the locations at which the tide is predicted is not located at the same locations as the tidal parks. The locations of the observation points are visualised in Figure A.2, Appendix A. The determination of the tidal range is only executed in order to give an estimation of the tidal range. The sediment present at the tidal parks, if not described in literature is determined based upon information obtained from the dinoloket (data-base in which information of the subsoil for the Netherlands is stored) and the sediment balance of the Rhine Meuse estuary from 1995 to 2000 (Snippen et al., 2005). In addition, a lot of information regarding the sediment present inside the tidal parks is obtained from personal communication with Menno de Jong, an ecologist from Zuid-Hollands landschap.

Lastly, the physical processes indicated in the table are determined on being the processes of most importance. For instance, river discharge always have an impact on the water level elevations inside an estuary, it is however only mentioned in the table if the latter one also clearly affects the situation in the tidal park. For example, in the inner bend of a river, sedimentation is expected resulting from

spiralling flow, if a tidal park is located in the inner bend than 'river' is mentioned as an important physical process. Same accounts for waves, this can both indicate ship waves or wind waves. In the whole estuary vessels are passing by, this however does not mean that this affects the situation inside the tidal park. For instance, in the Nieuwe Waterweg the ship waves are of great importance, but in an tidal park enclosed with longitudinal walls and one entrance, such as Stormpoldervloedbos, the effect of ship waves are negligible. An example in which wind waves are important is the Sophiapolder, as this process is the cause for erosion of the outer quay walls due to the relatively large fetch (De Haan, 2020).

This research provides more information regarding the tidal parks present at the Rhine-Meuse estuary. Besides gaining information on the design of the tidal parks, the objective is to obtain a possible correlation between the sedimentation processes in tidal parks. Information could not be obtained for all tidal parks regarding the problems related to sediment transport and necessary maintenance or monitoring of the tidal parks. In case this could be obtained, it is elaborated in Appendix A. A table is included, considering the tidal parks in which problems are present and if available the required maintenance. The sediment transport into tidal parks is dependent on the sources of sediment and the transport mechanisms. Close to the river mouth, the tide and the river discharge are important forcing mechanisms and the sources of sediment are both marine and fluvial. Further upstream, for instance at the Brabantse Biesbosch, the sediment imported inside the wetland consists of fluvial sediment only (Van der Deijl and Middelkoop, 2018).

From this literature review it can be obtained that the sediment imported inside the tidal parks particularly consists of silt. This indicates that the sediment import in tidal parks mainly originates from suspended sediment transport and not bed load transport as this is the main sediment transport mechanism of sand (Snippen et al., 2005). As sand is mainly transported as bed load transport, for which a critical velocity much be reached, it could be possible that the velocities inside the tidal parks are relatively low so that no sediment import originates as bed load transport. The sediment transport is however still depended on the horizontal tide, the relative ebb and flood velocities, if import or export of sediment would take place resulting from bed load transport.

Table 2.1: Overview table on tidal parks in the Rhine-Meuse estuary, including the location, the main purpose, the design, the tidal range, the type of sediment present and the important physical processes of the tidal park. The presence of '(-)' inside the table indicates that the information could not be obtained from literature. Secondly, n/a indicates if that the information could not be obtained as it is not applicable to the tidal park.

River	Tidal park	Cons- tructed	Location	Main purpose	Design	Tidal range (m)	Sediment	Physical processes
Nieuwe waterweg	Maassluis	No	Outer bend	Nature + recreation	Longitudinal wall	1.57	(n/a)	River, Tide, waves
	Groene Poort	Yes	Inner bend	Nature	Groynes + longitudinal wall	1.57	Sand / silt	River, Tide, waves
	De Zaayer	No	Inner bend	Nature + recreation	Groynes + longitudinal wall	1.57	Sand / silt	River, Tide, waves
De Scheur	Gors van de Lickebaert	No	Inner bend	Nature	Longitudinal wall	1.57	(n/a)	River, Tide, waves
	Vijfsluizerhaven	Yes	Old port basin	Nature + recreation	Shallowing basin area	1.66	Silt	Tide
Nieuwe Maas	Wilhelminahaven	Partly	Old port basin	Nature + recreation	Nature friendly shore	1.66	(n/a)	Tide
	Keilehaven	No	Old port basin	Recreation	Stairs on shore	1.66	(n/a)	Tide, waves
	Quarantaine eiland	Yes	Inner bend	Nature	Sandy beach	1.66	Sand	River, Tide, waves
	Maasboulevard	No	Outer bend	Recreation	Nature friendly shore	1.63	(n/a)	River, tide, waves
	Maashaven	Partly	Old port basin	Nature + Recreation	Nature friendly shore	1.63	(n/a)	Tide, waves
	Rijnhaven	No	Old port basin	Recreation	Sandy beach	1.63	Silt / sand	Tide, waves
	Nassauhaven	No	Old port basin	Living	Nature friendly shore	1.63	(n/a)	Tide
	Mallegatpark	No	Outer bend	Nature + Recreation + Living	Longitudinal wall	1.63	(n/a)	River, Tide
	Eiland van Brieneoord	Partly	Outer bend	Nature + Recreation	Longitudinal wall, nature friendly shore, tidal creek	1.63	Silt	River, Tide, waves
	Stormpolderdvoedbos	Yes	Inner bend	Nature + Recreation	Tidal creek	1.2	Inlet : sand inside :silt	River, Tide
De Zaag	Yes	Inner bend	Nature + Recreation	Creeks+ nature friendly shore	1.2	Inlet : sand inside :silt	River, Tide	
Het huys ten Donk	Yes	Outer bend	Nature	Longitudinal wall + creek	1.2	Sand / silt	River, Tide	
De Noord	Crezeepolder	Yes	Existing wetland	Creating nature	Tidal creek	0.8	Silt	Tide
	Sophiapolder	Yes	Island in river	Creating nature	Tidal creek	0.8	Inlet : sand inside :silt	Tide, waves
	Ridderkerkse griend	Yes	Willow area	Nature	Small tidal creek system	1.2	Silt	Tide
Oude Maas	Ruigeplaatbos	Yes	Willow area	Nature	Inflowing tide through culvert	1.5	Sand / silt	River, Tide
	Visserijgriend	Yes	Willow area	Nature	Creek-system	1.5	Silt little sand	River, Tide
	Oostpuntgriend	Yes	Willow area	Nature	Inflowing tide through culvert	1.5	Silt	River, Tide
	Klein Profijt	Yes	Willow area	Nature	Creek-system	1.5	Silt little sand	River, Tide
Haringvliet	Tiengemetten	Yes	Island in river	Nature + recreation	Tidal creek	0.3	Silt little sand	River, Tide
	Tiendgorzen	Yes	Island in river	Nature + recreation	Tidal creek	0.3	Silt little sand	River, Tide
	Korendijkse slikken	Yes	Existing wetland	Nature + recreation	Tidal creek	0.3	Silt little sand	River, Tide
	Spuimonding west	Yes	Existing wetland	Nature + recreation	Tidal creek	0.3	Silt little sand	River, Tide
	Vogeleiland Blik	Yes	Island in river	Nature + recreation	Sandy beach	0.3	Sand	River, Tide
	Leenherengorzenpolder	Yes	Outer bend	Nature + recreation	Tidal creek	0.3	Silt little sand	River, Tide

The study area

In this chapter several aspects of the case-study are elaborated. In the first section more information is elaborated on the design concept of the tidal park in combination with the desired ecological values. Thereafter more information is presented on the bed composition at the location of the tidal parks. In the third section more information on the bed levels of the groyne areas in the Nieuwe Waterweg are provided and the history of sedimentation or erosion in these areas are determined. Besides that, the effect of the constructed dams/groynes are explored based on these measurements. Thereafter the hydrodynamic forcing at the location of the tidal parks is described, including tidal forcing, results of velocity measurements and more information is presented on the wave conditions. Lastly, the effect of several hydraulic structures on both hydrodynamics and morphodynamics are elaborated. The information on the present-day situation and the different options affecting the hydro and morpho-dynamics result in different solutions affecting the sediment transport suitable for tidal parks in the Nieuwe Waterweg. The resulting hypotheses and model approach is presented in Chapter 6.

3.1. Design concept and ecology

The case study is focused upon tidal parks the Groene Poort. For a distance of five kilometres, tidal parks are being constructed at the river bank. At the river bank groynes are already present, by introducing longitudinal walls in front of the area between the groynes tidal parks are created (Hiddema et al., 2013). Behind the longitudinal walls a calm area is created in which sediment is ought to deposit (Gemeente Rotterdam, 2018). Three longitudinal walls are already constructed in front of the river banks, these longitudinal walls consist out of rock or old sewer pipes. In section 3.3 more information is elaborated on the bed level present at the groyne areas at the Nieuwe Waterweg and the morphological evolution of these river banks. Currently, the sediment imported into the tidal parks, resulting from the construction of a longitudinal wall is occurring on a longer time-scale as desired. The aim of the construction of these tidal parks is to improve the ecological values in the Nieuwe Waterweg. This goal can be obtained if a large part of the surface area of the river banks becomes intertidal. Besides, during all water level elevations present at the Nieuwe Waterweg, fishes should be able to pass through the entrance at all time (Hiddema et al., 2013).

The water body present in the Nieuwe Waterweg is defined as being an O2b type according to the goals set by the government. An O2b type of water body is defined as an estuary with a moderate tidal range with wave impact induced by ships. There are four categories upon which the water quality is tested in terms of biology, these are macrofauna, other water flora, fishes and phytoplankton. In addition there is category hydro-morphological conditions, however, for this type of water the only fulfillment in the section hydrodynamics is the amount of nature-friendly shore in percentage to the total amount of shores. The definition of a nature-friendly shore according to the government is: A shore that serves as a natural transition between land and water and is no constraint to the surface area of the water body (relative to the original situation) (Stichting Toegepast Onderzoek Waterbeheer, 2018). The requirements for the hydrodynamics are coupled to the flora and fishes desired to be present at the location of the tidal parks. The current situation at the locations of the Groene Poort is not yet sufficing the KRW goals. The GET values, the 'Good Ecological Circumstances' are set at 0.6 for both waterflora and fishes, the values in 2016 were equal to 0.35 and 0.6 respectively. The quality of the waterflora at the Groene Poort is lacking (Ministerie van Infrastructuur en Milieu, 2015).

The reference area for tidal parks the Groene Poort is the 'Gors Rozenburg' (Stolk et al., 2015). This area is displayed in Figure 3.1, river bank N in Figure 3.4. In 2006 the groynes present at the Gors

of Rozenburg were increased to stimulate sedimentation and to ensure no further erosion of the river bank as this trend was present in the previous years (Stolk et al., 2015). There are multiple types of vegetation present in this area, but not all of them can be expected at tidal parks the Groene Poort. At these tidal parks there is a limitation of the bed level to not exceed the level of high water concerning water storage (Hiddema et al., 2013). In 2011 vegetation mapping is executed at the Gors of Rozenburg, the most common vegetation present at the intertidal area of the Gors is purua grass. It is therefore likely that this is the type of vegetation that will grow in the tidal parks the Groene Poort. The typical hydrodynamic conditions for this type of vegetation is not specifically known. However, it can be concluded that the velocities should be relatively small regarding the location of the vegetation and the intertidal flat present in front of this vegetation.



Figure 3.1: Vegetation present at the reference area 'Gors of Rozenburg' (Stolk et al., 2015)

In addition hydrodynamics can be coupled to the types of fishes present in the Groene Poort. There are many migratory fishes expected in this area as it is a transitional area between the sea and the river, examples of expected fishes are sturgeon, eel, houting, allis shad and twaite shad. From these fishes mostly the juvenile fishes are concentrated in shallow water and adolescent fishes are seeking deeper water (Hiddema et al., 2013). Tidal park the Groene Poort is therefore a suitable location for juvenile fishes. A species of great interest in this area is the sturgeon, this is a threatened species but a collaboration between WNF nature fund, AKR (foundation for nature development) and multiple more companies resulted in the release of 50 sturgeons in the upper Rhine close to Germany in 2012 and 2015 (Van Dort and Houben, 2015). As a consequence of the closure of the Haringvliet, the only possible route for the sturgeons to reach the North Sea is through the Nieuwe Waterweg. The Groene Poort can provide the juvenile sturgeons with food and a resting place to get accustomed to the fresh water (Van Dort and Houben, 2015). The juvenile sturgeons require a lee area with low flow velocities, low wave impact and an inlet into the area which is available during low and high water (Van Dort and Houben, 2015). By the KRW the achievement of the goal related to fishes is depended on seven types of fishes present at the Nieuwe Waterweg (Stichting Toegepast Onderzoek Waterbeheer, 2018). These are smelt, twaite shad, herring, flounder, pope and common sea snail. Twaite shads are anadromous fishes, the adolescent fishes live at sea and when they are ready for breeding they migrate to the freshwater zone to procreate (Stevens et al., 2011). The juvenile twaite shads are staying at locations with brackish water to get used to the saltwater, the optimal velocity for larvae is between 0.3 and 0.7 m/s and for adolescents up to 1.5 m/s is optimal (Stevens et al., 2011). However, nothing is mentioned about ideal velocities for juvenile twaite shads, it is assumed that the optimal velocity is between the above-mentioned values.

Concluding, the requirement in terms of hydrodynamics related to ecology is that the velocity inside the tidal park should not exceed 0.7 m/s. Besides, it is of great importance that intertidal area is present in order for the waterflora to become present. In addition, it is desired that the conditions in the tidal park are calm, this can be obtained by constructing longitudinal walls and possible increase of the elevation of the groynes.

3.2. Sediment composition

Bed sediment

The concentration of different types of sediment in the Nieuwe Waterweg has been researched by the Port of Rotterdam in 2004, the results are displayed in Figure 3.2a. The locations in which tidal parks the Groene Poort are constructed are from Rhine kilometre 1019 up to 1025. From Figure 3.2a it can be observed that the largest percentage of sediment present at the location of interest is sand, thereafter silt, gravel and last lutum. The percentage of sand at this area is about equal to 50 %, and the average D50, which is the grain diameter where 50 % of the grain mass has a smaller diameter (Schiereck and Verhagen, 2016), is equal to 100-140 μm . Besides that, as part of research into the massive sedimentation events at the mouth of the Rotterdam Waterway, the sediment concentration of fractions below 63 μm is measured. The results of this research are displayed in Figure 3.2b, it can be obtained that the amount of mud present at the Nieuwe Waterweg (Rotterdam Waterway) is relatively low compared to the Maasmond-Calandkanaal. This is in agreement with the measurement campaign executed by the port of Rotterdam in 2004. The sediment samples from both researched were obtained from the main channel and can deviate from the sediment present at the river banks.

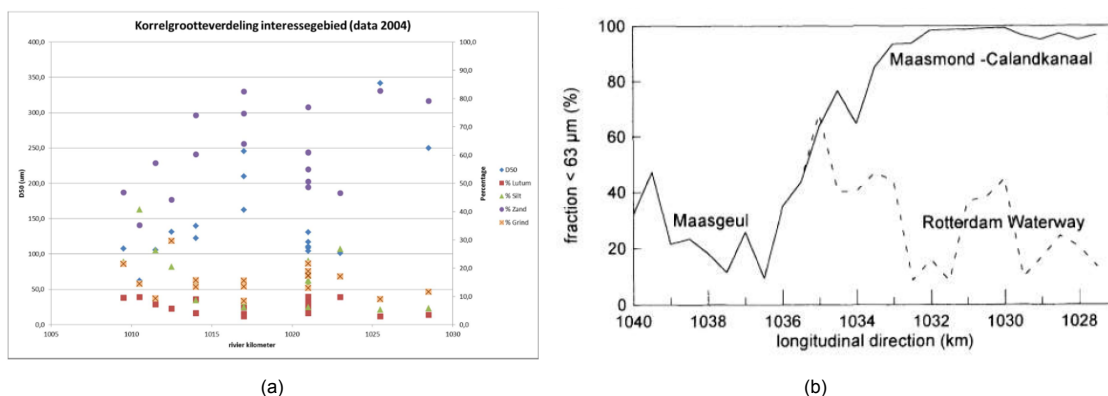


Figure 3.2: In Figure 3.2a the types of sediment and corresponding grain sizes are visualised for the Nieuwe Waterweg (Wensveen, 2014). In Figure 3.2b the measured fraction < 63 μm in bottom sediment (Verlaan and Spanhoff, 2000) is displayed.

Before the construction of the Groene Poort, the subsoil at certain river banks were researched as part of an environmental effect study by the township of Rotterdam in 2013 (Schutjes and Van Leeuwen, 2013). In this research four different river banks were researched, river bank E,H,K and L in Figure 3.4. The sediment types found at these river banks were mainly sand and silt, with almost at every location a sandy top layer present (Schutjes and Van Leeuwen, 2013). At river bank L, the top layer consists of sand with a silt layer present at the east corner. At river bank K, the top layer consists out of sand and locally a silt layer is present. At river bank H the top layer consists out of sand with a small clay layer present. At river bank E only sand layers are present (Schutjes and Van Leeuwen, 2013). More information on the spatial variation of sediment present at river bank L is presented in Chapter 4, obtained by field observations.

Suspended sediment

The suspended sediment matter at the location of tidal park the Groene Poort is very much dependent on the river discharge. In 2006 measurements are executed by Rijkswaterstaat in order to gain more insight into the latter, the suspended sediment matter was measured during three different river discharges. From this research it was obtained that high discharges occur simultaneously with high suspended sediment concentrations. The suspended sediments that are measured are during discharges at Lobith of ca. 3000-4000 m^3/s , 5000-5500 m^3/s and 5500-500 m^3/s , the measured suspended sediment concentrations at Maasluis are 8-14 mg/l , 36-42 mg/l and 36-42 mg/l respectively (Meijers and Icke, 2006). From 1996 up to 1999 Rijkswaterstaat measured the suspended sediment concentrations at Maasluis, the results are displayed in Figure 3.3. Measurement results show that a quarter of the values is below 20 mg/L , half of the values are between 20-50 mg/L and a quarter of the values are above 50 mg/L (Eertman, 2000). The discharges at the moments of measurements are not known,

however, from the average seasonal change in discharge with high discharge during winter and relatively lower discharges during summer at Lobith (Klijn et al., 2012), it can be seen from this graph that high suspended sediment concentrations coincide with high discharges at Lobith. Concluding, the bed sediment present at the Nieuwe waterweg mainly consist out of sand with a diameter of diameter of 100-140 μm . Relatively little silt is present in the bed. The amount of suspended sediment present at the Nieuwe Waterweg is increasing with increasing discharges. The suspended sediment concentrations are on average below 20 mg/l.

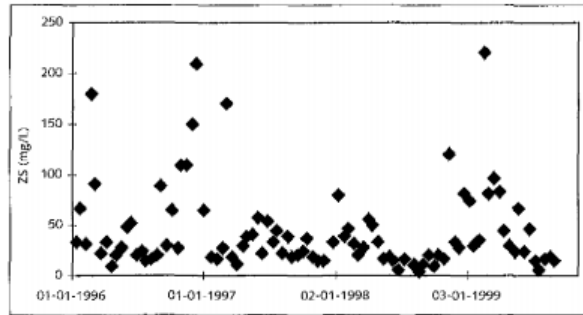


Figure 3.3: Suspended sediment concentrations at Maassluis (km 1019) from 1996 up to 1999

3.3. Bed topography

Bed level data on the river banks of the Nieuwe Waterweg are available for over four years, from 2015 up to 2019. These bed level measurements are executed by multibeam echosounders. From these measurements, it can be studied which areas are by nature importing, or exporting sediment and how much the river bank is increasing in elevation. In Figure 3.4a the change in bed topography from 2015 to 2017 is displayed, the displayed values are averaged yearly bed level changes, the same is executed for the years 2017 to 2019 displayed in Figure 3.4b. From 2015 to 2017 the bed levels were increasing almost everywhere, contrary to the year 2017 to 2019 in which large parts of the bed levels were decreasing. The exact values are displayed in Appendix B. From 2017 up to 2019 the shipping channel of the Nieuwe Waterweg is deepened around 1.5 m, to this extent one can account for possible bed degradation as the sediment would slide down. Besides that, dredging activities result in more suspended sediment in the water column, which can be transported to the river banks. The effect of hydraulic structures in area G is visible in this image, in area G two longitudinal walls were constructed in combination with sand nourishment, the result is a large amount of sedimentation in this area.

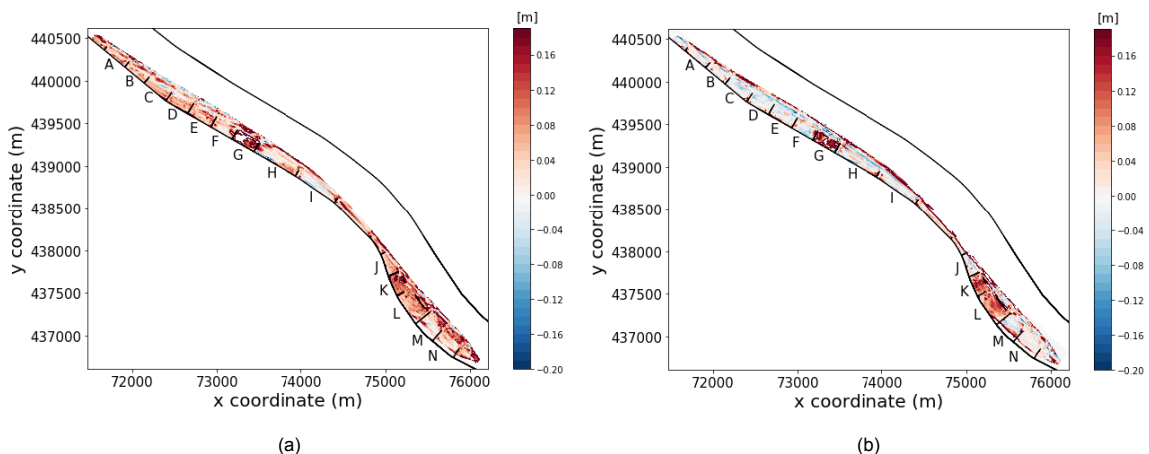


Figure 3.4: Changes in bed level of the river banks located in the Nieuwe Waterweg. In Figure 3.4a the changes in bed level are displayed from 2015 to 2017. Figure 3.4b displays the changes in bed level from 2017 to 2019. The red-colored areas indicate an increase in bed level and the blue colored areas indicate a decrease in bed level

If we zoom further into the groyne area L, in which a longitudinal wall is constructed in front of the river bank in 2018, the effect of the longitudinal wall can already be checked by the relative differences in sedimentation. The bed degradation / aggregation at river bank L is displayed in Figure 3.6, from which it obviously can be concluded that there is an import of sediment in this area. The amount of sediment deposited at the river bank increased after the construction of the longitudinal wall. Also, the change in bed patterns can be recognized as a result of the construction of the longitudinal wall. At first, the waves were not obstructed and the resulting ripples are displayed in Figure 3.6a, from the change in bed topography since 2017 it can be seen that these ripples are disappearing and there is a change in angle at which the sediment transport occurs. Besides that, erosion is visible at the locations where the water enters and leaves the river banks through the openings of the longitudinal wall and groynes. In Figure 3.5a and 3.5b the bed levels in 2015 and 2019 are displayed, from this again the change in bed level ripples are clearly visible. Besides that, on the left side of the right groyne the presence of small channels can be distinguished and these remain over the years.

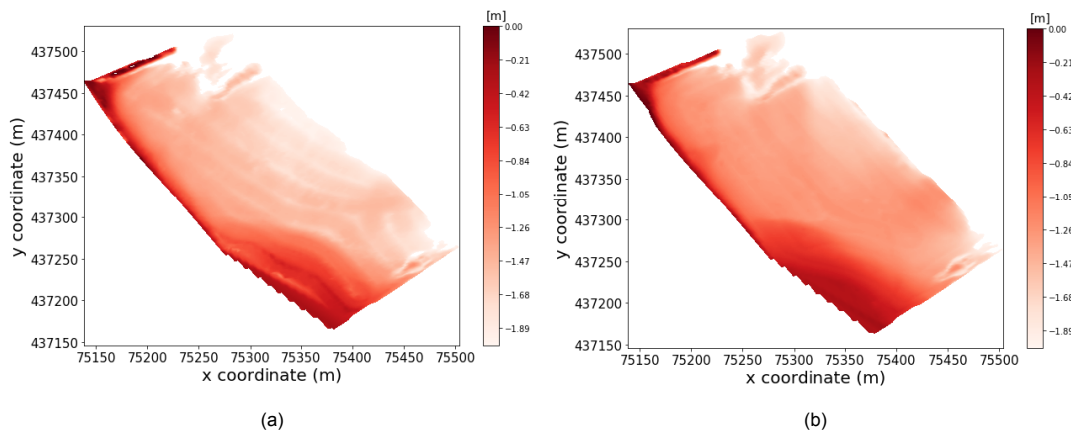


Figure 3.5: In Figure 3.5a the bed topography at river bank L in the year 2015 before the construction of the longitudinal wall is displayed. In Figure 3.5b the latter is displayed in 2019, after the construction of the longitudinal wall. The bed levels are displayed relative to NAP.

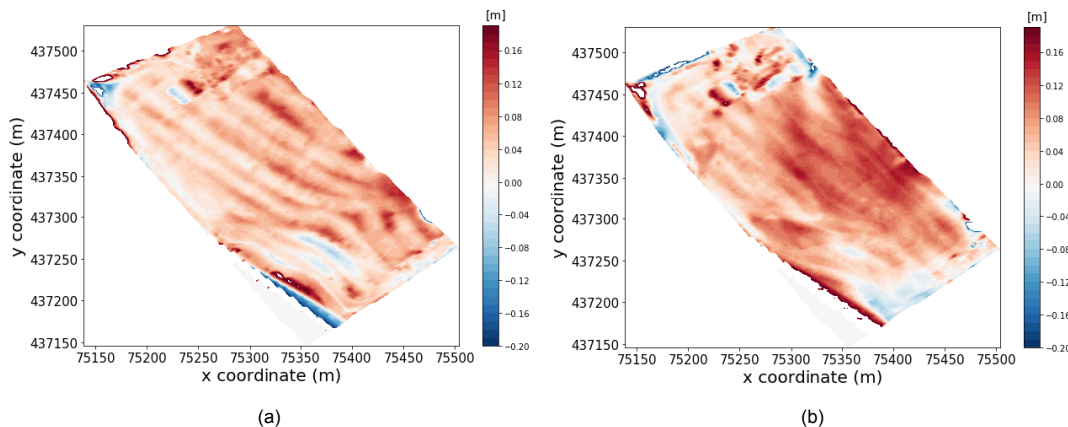


Figure 3.6: Bed level changes over four years at river bank L. The figures are obtained by comparing the measurements obtained by multibeam echosounders in 2015, 2017 and 2019

3.4. Hydrodynamic forcing

The morphological development of the tidal parks is dependent on the hydrodynamic forcing and the available sediment. Important components of the hydrodynamic forcing are the tide, river discharge, wind and waves. In this section these processes are elaborated and possible corresponding shear stresses are calculated. In addition, velocity measurements executed inside river bank L are discussed.

3.4.1. Tidal regime

As is mentioned before, and as the name also suggests, the constructed tidal parks are under the influence of tidal forcing, which means that the flow reverses on a regular basis but in a semi-constant way (spring - neap tidal cycle). As the tide is an important forcing factor on the flow pattern and the sediment transport, a tidal analysis is performed. Data on the water level elevations measured every 10 minutes is available at location Maassluis, data is retrieved from the database of Rijkswaterstaat. Data is analyzed of two spring neap tides in October, from this the average water level, MLW (mean low water), MHW (mean high water), HAT (highest astronomical tide), and the LAT (lowest astronomical tide) are calculated. The water level analysis is displayed in Figure 3.7, the resulting values of elevations are displayed in Table 3.4.1.

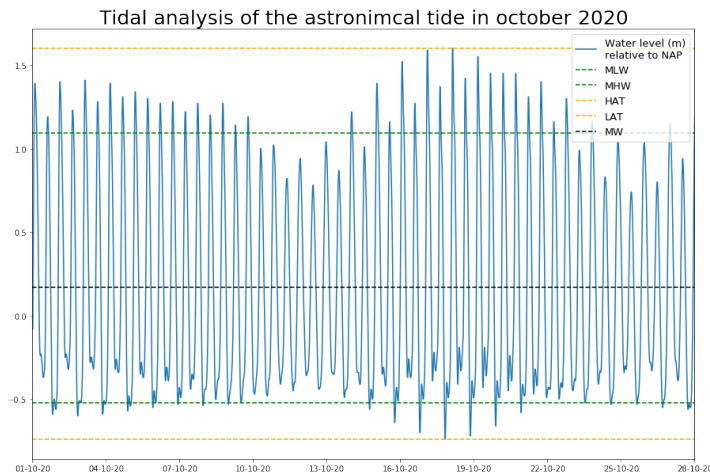


Figure 3.7: Tidal analysis of the astronomical tide at Maassluis in October 2020. The colored lines indicate MLW (mean low water), MHW (mean high water), HAT (highest astronomical tide) and LAT (lowest astronomical tide).

Besides the tidal analysis of one astronomical month, the duration is extended up to three months in order to determine the important tidal constituents in the Rhine-Meuse estuary. This data is obtained from the same location and analyzed using the python package `pytides` from which the tidal constituents are calculated, and the resulting Form factor is determined. The form factor expresses the tidal character (Bosboom and Stive, 2015) and is determined as the ratio between the amplitudes of the sum of the two main diurnal components K1 and O1 and the sum of the two main semi-diurnal components M2 and S2. The major contributions to the tidal amplitudes are displayed in Table 3.4.1. From this analysis, it is obtained that the tide present at the Rhine Meuse estuary is semi-diurnal with a form factor of 0.078. For more information regarding the tidal elevations and corresponding velocity profiles present in the Rhine-Meuse estuary it is referred to Chapter 2. The tidal forcing in combination with the incoming river discharge are the major processes determining the velocities inside the Rhine-Meuse estuary. A higher river discharge results in larger ebb periods and higher peak velocities during ebb. In the previous chapter it is explained how this effects the velocity profile over the vertical in the region relatively close to the river mouth. The river discharge flowing through into the North Sea is affected by seasonal variability's and thus the morphodynamic changes will maintain a fluctuating short-term component even in the long term (Chavarrias et al., 2020).

Tidal level	Water level (m)
MSL	0.17
MLW	-0.52
MHW	1.09
HAT	1.60
LAT	-0.74

Table 3.1: Table containing values on characteristic water levels present at Maassluis

Constituent	Amplitude (m)	Phase (deg)
M2	0.712	95
S2	0.260	140
M4	0.155	189
O1	0.066	204
M6	0.032	166
K1	0.011	345

Table 3.2: Table containing major tidal constituents water levels Maassluis

The change in water levels induced by tidal forcing, result in different velocities during the rise and the fall of the tide. Field measurements of velocities have been executed by aquitec, which is a company specialized in prototypes for data acquisition (Dinkla, 2018). Two measurement buoys were installed at river bank L, located 100 metres below and around 50 metres left and right of the center of the longitudinal wall. As this project was the pilot project of a new measurement device, the data is quite scattered but it gives an indication of the expected range of velocities in the tidal park (Dinkla, 2018). The measurements device extracts data every ten minutes, however, the data-set contains a large amount of missing values. At buoy 1 the data obtained, not being equal to zero, represents 50 percent of the total data set. At buoy two this percentage is equal to twenty. The data excluding the zero measurements together with the water levels are displayed in Figure 3.8. From this data it can be concluded that the velocities inside the tidal park, close to the longitudinal wall are relatively small. The mean velocity are equal to 0.15 and 0.18 m/s for buoy 1 and 2 respectively. Secondly it can be obtained that the largest flow velocities coincides with the rise of the tide. This results from the faster rise than fall of the tide.

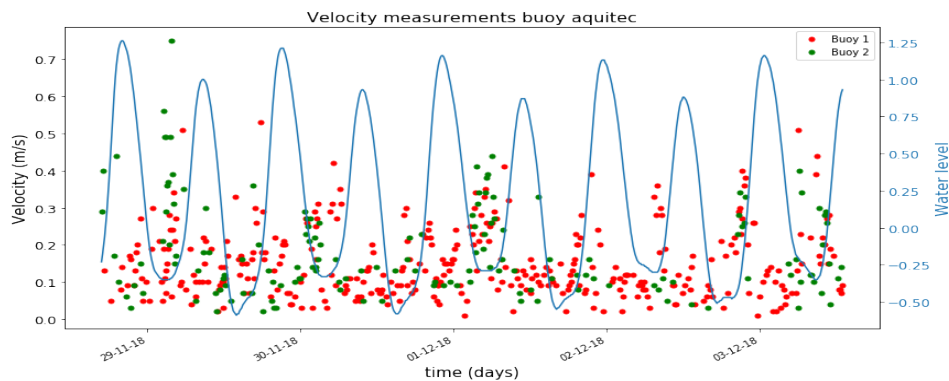


Figure 3.8: Figure displaying the velocity measurements obtained from two measurement buoys (Aquitec (Dinkla, 2018)) at river bank L. The buoys are located close to the longitudinal wall. In addition, the corresponding water levels measured at observation point Maassluis are displayed.

3.4.2. Wave climate

Ship induced waves

As mentioned before, the waves present at the study location consist of the following: tidal waves, wind waves, and ship waves. Due to the presence of obstructions, both groynes and a longitudinal wall), wave diffraction will take place. Besides that, refraction will occur at the river banks resulting from changes in bed topography. At first the ship waves are treated, these vessel induced waves consist of primary waves and secondary waves and can be approximated depending on the width and depth of the channel, and the length and velocity of the vessels (Schiereck and Verhagen, 2016). The primary wave consists of a water level rise at the front of the ship, a water level drop at the side of the vessel, and a stern wave at the back of the ship (Ten Brinke, 2003). Secondary waves are the short waves that are present closely behind the ship. The primary wave has the most impact on the shore, as this results in the largest elevation difference.

In Figure 3.9 river bank L is displayed in combination with the cross-sectional area of the river section of interest is displayed on the left side. This river section is orientated as being in the eastward direction (upstream of the river). From this overview, it is clearly visible that on the right side the slopes are much more gentle than the left side and the location of the longitudinal is indicated with the black rectangle. When the vessels are moving inwards, the travel location is almost at the center of the width of the total channel, and thus the eccentric position of the ship is not taken into account. Common dimensions are taken into account to represent both large and small vessels present in the Nieuwe Waterweg in order to determine the water level depression (primary waves) and the secondary waves of these vessels.

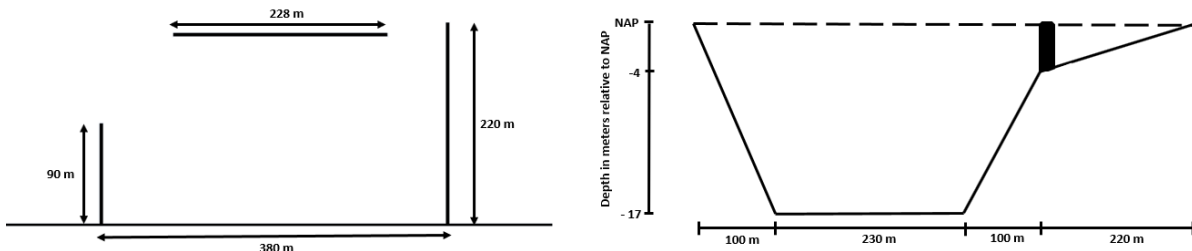


Figure 3.9: In the left figure the geometry of river bank L is visualized, including the lengths of the groynes and longitudinal wall. In the right figure the cross-sectional area at the location of interest is displayed.

For a large vessel the following dimensions are taken into account: length of 150 metres, width of 30 metres and a draught of 8 metres and a velocity of 11 knots. From this information on the vessel and the geometry of the channel, according to the design rules of (Schiereck and Verhagen, 2016), the resulting primary wave is 0.25 metres and the secondary wave height is equal to 0.35 metres with a period of 3.5 seconds. For a relatively small vessel with a length of 80 metres, width of 11 metres, a draught of 4 metres and a vessel speed of 8 knots the resulting primary wave is 0.17 metres and the secondary wave height is equal to 0.1 metre with a period of 2.8 seconds. This is in agreement with the average wave height measured at the river bank at the Maeslantkering (located just upstream of riverbank A) , see Figure 3.10.

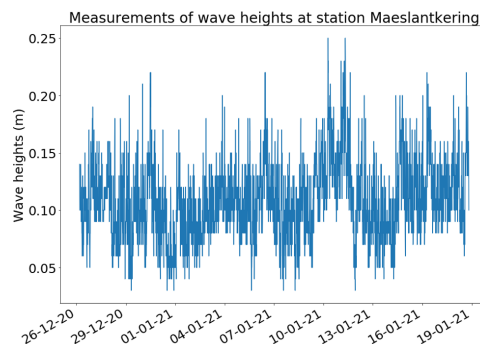


Figure 3.10: The measured wave heights (m) for one month at measurement station Maeslantkering, located in the Nieuwe Waterweg just upstream of river bank A.

The height of the secondary waves hitting the river banks is primarily dependent on the speed of the vessel relative to the limit speed \sqrt{gh} and the distance towards the river bank. The secondary waves attack the river bank at an angle of 55° , when a straight river bank is present. This angle however differs when there are local changes in bed topography which ensure refraction and the presence of obstructions of the flow ensures diffraction. Refraction is the result of wave energy convergence or divergence as a result of convex or concave depth contours (Bosboom and Stive, 2015). Diffraction is the result of a large variation in wave energy along a wave crest, which leads to the transfer of energy along the wave crest (Bosboom and Stive, 2015). The resulting wave rays of the situation at Groene Poort area L are visualized in Figure 3.11. These schematizations are resulting from visual observations in combination with theory as explained in (Bosboom and Stive, 2015). The wave rays in

the shadow zone behind the breakwater have lower wave heights as a result of the lateral transfer of wave energy.

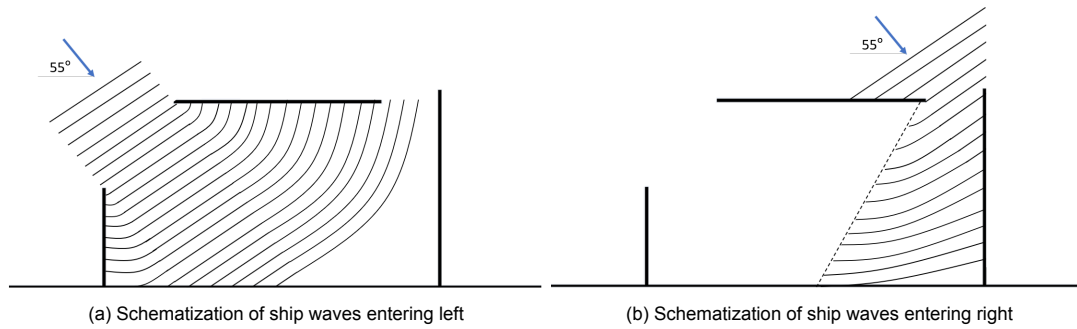


Figure 3.11: Wave diffraction at the groyne area

Wind waves

In Figure 3.12 both the wind rose and the resulting wave heights and periods from this wind rose are displayed. The legend at Figure 3.12a displays the measured wind velocities 10 metres above NAP in m/s, at Figure 3.12b the wave heights in m are displayed, and Figure 3.12c shows the wave period in seconds. These figures are based upon nine and a half years of data on wind speed obtained from the KNMI at location 'Rotterdam Geulhaven' which is the nearest measurement station. One should keep in mind that the wind velocities at 10 metres above NAP are often larger than the wind velocities at the water level. This results from obstruction of the wind by the presence of dikes and buildings. However, the wind speeds of 10 metres above NAP are further used in this calculation. Based on this data, the fetch and the corresponding average depth at location of interest, obtained from (Ratchakom, 2019), the wave height as a result of the wind can be determined by use of the Sverdrup-Munk-Brettschneider method. It can be obtained that the occurring wave heights related to wind are relatively low, and most of the time in the order of zero to thirty centimetres.

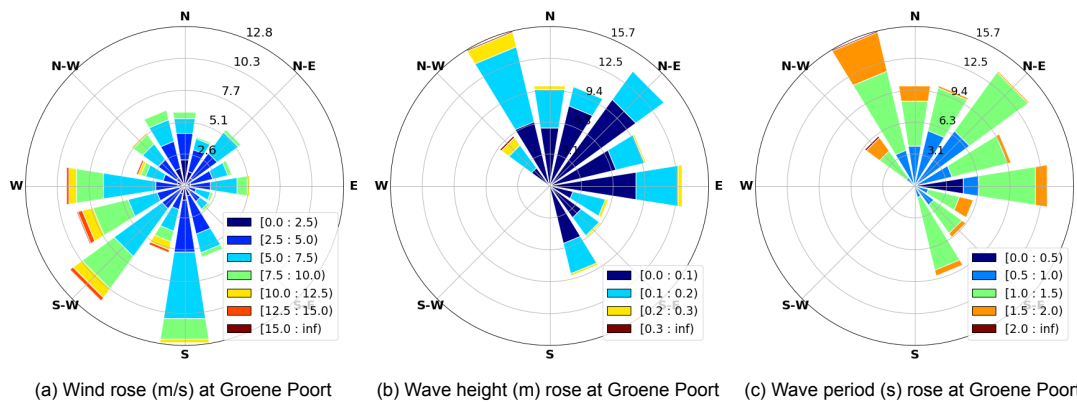


Figure 3.12: In Figure 3.12a the wind rose present at the Groene Poort is displayed in m/s. In Figure 3.12b the wave height (m) rose is presented, and in Figure 3.12c the corresponding wave period (s) is presented for the Groene Poort.

The bed shear stress induced by waves, is depending on the wave height, wave period, water depth, and the roughness of the bed. The roughness of the bed is the most complicated part and mostly based on experiments, it can however be approximated by the Swarts formula (CIRI, 2007). Swarts formula uses the amplitude of the wave and the nikuradse roughness as input, by which in this calculation the nikuradse roughness is assumed to being 2 times a nominal diameter of 200 μm. The composition of the bed is not known by detail, however, it is known that small grains are dominant and that vegetation is not yet present so a smooth bed is assumed. In Table 3.4.2 below the wave forces and the corresponding shear stresses are listed. It should be noted that the aim of calculating the bed shear stresses resulting from waves was to give an estimation on the effect of waves on sediment transport.

	Small vessel H = 0.1 m T = 2.8 s		Large vessel H = 0.35 m T = 3.5 s		Small wind wave H = 0.1 m T = 1.0 s		Large wind wave H = 0.3 m T = 2.0 s	
h (m)	L (m)	τ_w (N/m ²)	L (m)	τ_w (N/m ²)	L (m)	τ_w (N/m ²)	L (m)	τ_w (N/m ²)
1.8	9.93	0.02	13.29	0.16	1.56	1.65E-05	5.98	0.06
1.4	9.14	0.03	11.95	0.21	1.56	1.92E-04	5.70	0.11
1.2	8.63	0.04	11.23	0.24	1.56	6.32E-04	5.49	0.15

3.4.3. Wind forcing

In the above section, the wind forcing and the corresponding waves and resulting shear stresses are determined. It should however be taken into account, that the wind forcing can also result in set-up and set-down inducing large-scale circulation patterns especially in large estuaries (Colosimo et al., 2020). Research showed that even moderate wind can reverse the tidal flow, it is however dependent on the geometry and the surface area of the estuary (Colosimo et al., 2020). Research of Colosimo et al. (2020) showed that at sites in which a weak tide induced flow was present (around 0.2 m/s) the wind forcing was able to reverse the direction of tidal flow even at moderate wind speeds around 10 m/s. The wind forcing can result in circulation flow in closed water bodies, as the wind exerts stresses on the water surface which is also transferred through the water column. Wind forcing can thus affect the flow direction, in a closed area, this can result in water at the surface being directed in one direction, but resulting from continuity at the end of the basin the flow reverses in direction in the lower part of the water column (Bosboom and Stive, 2015). From the wind rose presented in Figure 3.12a, it can be obtained that the largest wind speed originates from the direction in which the wind is largely obstructed by the presence of dikes, buildings and trees. Therefore it is assumed that the effect of wind set up at the location of interest is relatively small.

3.4.4. Spiral flow in river

Besides the flow being affected by the groynes, the effect of the geometry of the river also impacts the flow. Based on the location in a river, flow patterns are affected as a result of spiraling flow, which originates from the following mechanism. In rivers, the flow velocity near the surface is larger than at the bottom, which leads to a non-uniform vertical velocity profile. Besides that, centrifugal forces interact with lateral pressure gradients by which a secondary flow is formed. As a result of this flow, the water in the upper part moves towards the outer bend, and the lower part moves towards the inner bend. Interaction of the non-uniform vertical velocity profile in combination with the secondary flow results in a spiral flow. This leads to erosion of the outer bend and sedimentation at the inner bend of a river (Beygipoor et al., 2013). In addition, the flow velocities at the outer bend are higher than at the inner bend. In terms of this project, this means that some areas are more prone to sedimentation or erosion by nature, uncorrelated with flow obstructions by groynes. In Figure 3.4 the groyne areas are indicated with letters, in which A,B,C are located in the straight part of the channel, D,E,F, are located in the outer bend, G,H,I are located in the inner bend and J,K,L,M,N are located in the outer bend.

3.5. Affect of several structures on hydrodynamics

3.5.1. Groynes

A groyne is a hydraulic structure that is built with an angle towards the main flow from the river bank extending to some length into the channel. A groyne usually consists of stones, wood or concrete, in the Nieuwe Waterweg the groynes consist of stones. This type of hydraulic structure has multiple purposes, it is used to maintain a suitable channel for navigation, for bank protection, and for flood control (Yossef, 2005). The groynes constructed are considered to be impermeable groynes, also called solid groynes, as they are constructed out of stones and rocks. Groynes may be classified either as attracting, deflecting, or repelling groynes (Yossef, 2002). The groynes are constructed perpendicular to the flow and thus are repelling groynes. The flow of the main channel is not directed towards the groyne area, which according to (Copeland, 1983) can result in two types of circulation patterns, see Figure 3.13a. In the above figure, a circulation pattern is displayed of one well developed eddy which prevents the main flow from penetrating the groyne field. In the below figure two eddies are appearing,

this results from the difference in spacing between two groynes.

Based on the length of the groyne and the distance in between the groynes it can be determined what the flow circulation is in between two groynes (Bouwmeester, 1987). In general when a ratio between the distance between groynes (S) and the length of the groynes (L) of $0.5 \cdot L < S < 2 \cdot L$ is present, one eddy is present. For values higher than this ratio, a minimum of two eddies are present in the area in between the groynes, this is displayed in Figure 3.13a. The location of the groynes area with respect to the location in the river section, inner or outer bend, also affects the type of eddy present in the groyne area. When the groynes are present in the outer bend, the effective length between the groynes becomes smaller, resulting in a smaller value for S in the above ratio.

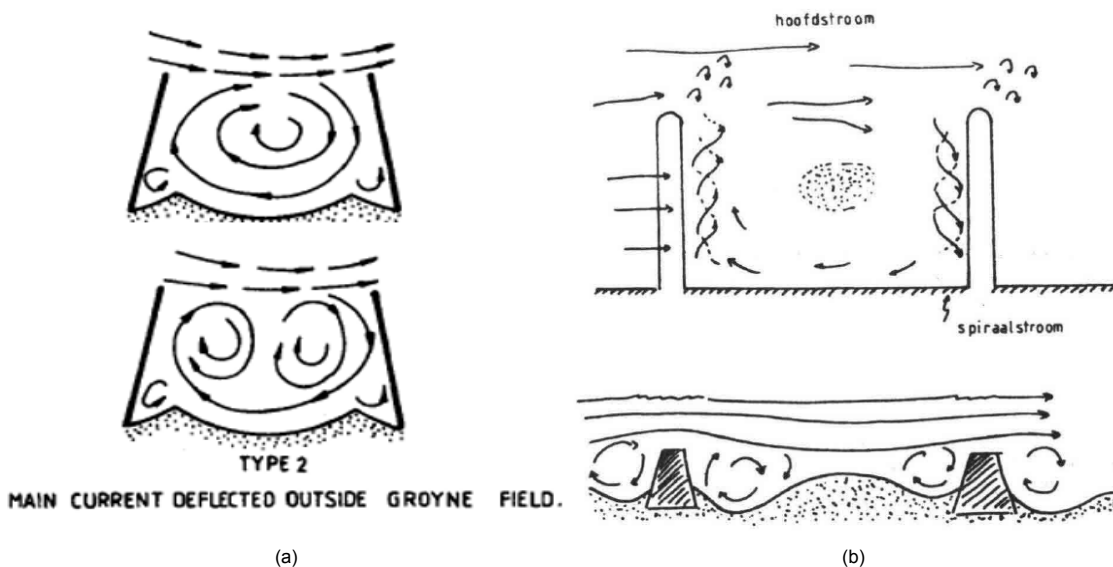


Figure 3.13: In Figure 3.13a two types of circulation patterns are displayed when the flow is not directed towards the groyne as is the case at river bank L (Yossef, 2002). In Figure 3.13b the flow pattern in a river bank is displayed incorporating submerged groynes (Bouwmeester, 1987)

There is a difference in the flow structure between emerged and submerged groynes. When groynes are emerged, the region between the groynes is a calm area in which the flow velocities are really small. When groynes are submerged the flow velocities in the groyne area will increase. As a result, the mass momentum exchange between the main flow and the flow in the groynes is different depended on the groyne type (Yossef, 2004). At emerged groynes the concept of flow circulation is a result of flow separation at the tip of the groyne by which a mixing layer is formed and consequently an eddy is formed inside the groyne area (Uijtewaal et al., 2001), type of eddies are displayed in Figure 3.13a. When groynes are submerged, not the same horizontal eddy is present as with emerged groynes (Yossef and Uijtewaal, 2003). In this case, the momentum transfer by water flowing over the groynes is balancing the momentum transfer through the mixing layer, which causes the recirculating flow in emerged groynes. When the groynes become more submerged, the recirculating pattern which is the case at emerged groynes is disappearing by decreasing groyne height (Yossef and Uijtewaal, 2003).

Research from Yossef and De Vriend (2010) gave insight into the different sediment transport patterns at emerged and submerged groynes. At emerged groynes sediment enters the groyne area close to the groyne at the downstream part of the flow where the circulation pattern 'starts'. As the velocity is decreasing, the sediment tends to settle down along the circulation pattern. This is visualized in Figure 3.14a, with the orange arrows being the flow patterns and the large grey arrows indicating the sediment supply. Often ripples are present at these locations (Yossef and De Vriend, 2010). As in an estuary, the flow is reversing multiple times a day, the flow patterns and associated sediment transport also reverses. In the case of submerged groynes, the mean flow is not directed towards the groyne field and there is no pure advective transport. This results in a different sediment supply, as is visualized in Figure 3.14b. The figures are the result of a conducted experiment with an S/L ratio of 3.1. One should

keep in mind that the relative submergence of the groyne with respect to the water level affects the flow structure in a groyne field.

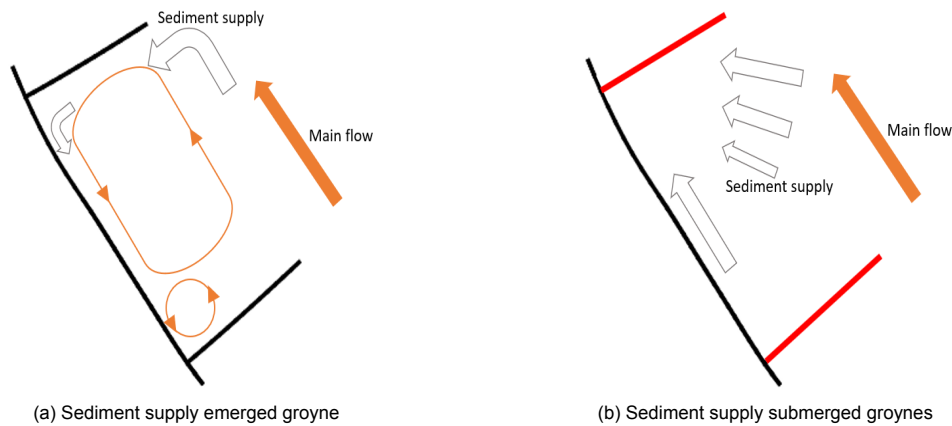


Figure 3.14: Sediment supply into groyne fields, from Yossef and De Vriend (2010)

In Figure 3.5a and 3.5b the bed topography of the years 2015 and 2019 are displayed, one pattern in the bed level can be explained related to the obstruction of groynes on the flow. From Bouwmeester (1987) it is obtained that these resembles flow over submerged groynes, displayed in Figure 3.13b. As the groynes at the area of interest are around +1 m NAP, it is correct that the groynes act as submerged during high tide, as well as during high river discharges. The submergence of groynes leads to a spiraling flow on both sides of the groynes and as a result of this, small channels are present.

3.5.2. Longitudinal walls

The effect of longitudinal walls on the wave rays entering the river bank is explained in section 3.4.2. Besides the effect on the wave rays, the presence of a longitudinal wall affects the flow pattern inside a groyne area as the dam obstructs the eddy which is formed by consecutive groynes. The effect of longitudinal walls in combination with groynes is a topic which is not yet extensively researched. Longitudinal walls are often used for shore protection, by which the longitudinal walls ensure sediment deposition behind the walls as a result of converging wave energy (Bosboom and Stive, 2015). Besides longitudinal training dams are used in the river training project 'Room for the River'. In this project groynes are replaced with long longitudinal training dams, with intentions to reduce the negative affect of ongoing bed erosion inside the navigation channel and to improve the flood protection level, navigability and ecological values (Van Linge, 2017).

3.5.3. Sills

A sill is a structure that resembles a submerged groyne, the crest of the structure is below mean water level. The sills considered in this research are placed in direction of the main flow in the channel. An example of a sill combined with longitudinal walls and groynes is displayed in Figure 3.15a. Behind the sill the flow decelerates, which results in the formation of an eddy just behind the sill and the bifurcation point (Jammers, 2017) The orange arrows indicate the stream patterns, the water that flows over the sill flows into the area with an angle. This angle varies depending on location and discharges. In the Waal river in the Netherlands, longitudinal walls are constructed and researched. It was obtained that the flow angle at these locations was around 0 to 15 ° based on data from Rijkswaterstaat (Jammers, 2017). It is expected that the angle of the flow over the sill will be of the same magnitude.

The presence of a sill affects the sediment entering and leaving the groyne area, in both directions resulting from the reversing flow on the rhythm of the tide. The presence of a sill induces a slope in the flow direction and a slope perpendicular to the flow (Schierneck and Verhagen, 2016). This affects the critical velocities for which sediments start to move, this is displayed in Figure 3.15b, obtained from Jammers (2017). This graph results from a constant side slope of the sill of 20 ° and varying flow angles, the positive values indicate a flow uphill and negative values indicate downhill. From which it

directly can be obtained that downward flows have a smaller critical velocity, which results from gravity forces and uphill flows have higher critical velocities for sediment transport.

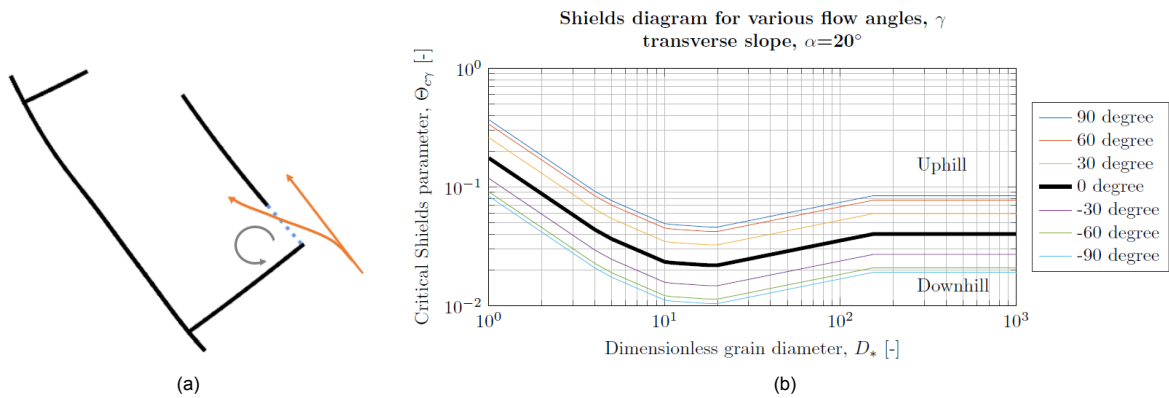


Figure 3.15: In Figure 3.15a the flow pattern over sill. The orange line indicate the direction of the main flow and the flow towards the river bank over the sill. In grey eddy present in the groyne area is visualized. In Figure 3.15b the dimensionless grain size including the effect of the slope of the sill on the critical shields parameter is displayed. This graph results from a constant side slope of the sill of 20° and varying flow angles, the positive values indicate a flow uphill and negative values indicate downhill (Jammers, 2017).

Field observations

In this chapter, the field observations executed in this research are described. These field observations are executed in order to get a better understanding of the case study area. This serves as the foundation of the numerical Delft3D model constructed in this research. The field observations consist out of sediment samples obtained at several locations in river bank L and drone images of the river bank. The sediment samples are used to get a better understanding of sediment transport into the river bank. Besides, information on the sediment characteristics serves as input for the numerical model and as main requirement for determining the critical velocities. The drone images are used to get a better view of the geometry of the river bank and the location of the intertidal areas. Also, top view drone images provide information on the wave fields entering the river bank by which the effect of the longitudinal wall in terms of wave action is visualized.

4.1. Methodology

4.1.1. Sediment samples

The sediment samples are obtained at different locations at the river bank in order to determine the differences in characteristics of the sediment based on location. The locations of the sediment samples are visualized in Figure 4.2, indicated by black octagons. From this information, a better understanding is gained how sediment is transported into the river bank. In addition, the nominal diameters of the samples are estimated in order to determine the critical shear stress for bedload transport.

The calculation of the critical shear stress or velocity is executed using the formulations of Shields (Schierceck and Verhagen, 2016). An important input value for this calculation is the nominal diameter, which is the diameter for which 50 percent of the grains are larger than this value and 50 percent is smaller. This value is estimated from the sediment samples, hereafter the dimensionless diameter is calculated, by 4.1. From this value, the critical shields value is determined by use of Figure 4.1, thereafter the critical velocity is determined by equations 4.2 and 4.3.

$$d_* = d_{50} * \left(\frac{g * \Delta}{v^2} \right)^{1/3} \quad (4.1)$$

$$u_* = \sqrt{\Delta * \Psi * d_{50}} * C \quad (4.2)$$

$$C \approx 18 \log \frac{12R}{k_r} \approx 18 \log \frac{12h}{k_r} \quad (4.3)$$

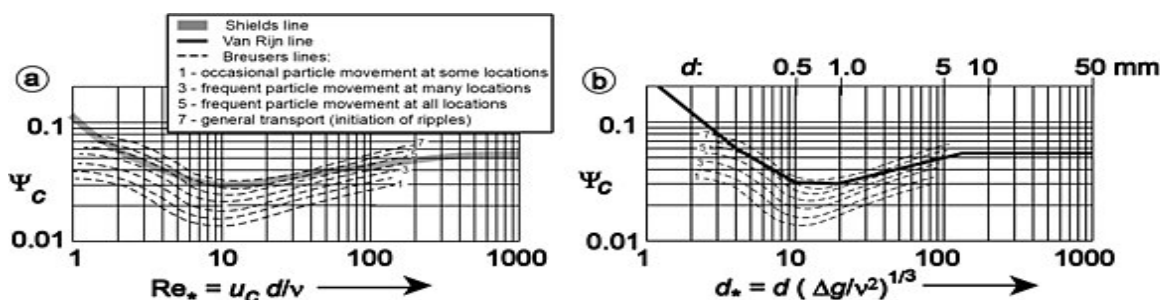


Figure 4.1: The shields curve

Besides sediment samples, two water samples are obtained at the river bank. One sample is obtained at the intertidal flat just after secondary waves entered the river bank. The second sample is obtained at the middle of the east groyne. The locations of the water samples are displayed in Figure 4.2, indicated with blue triangles. From these two samples information is obtained on the suspended sediment present in the water column at the river bank.



Figure 4.2: Location of the obtained sediment samples in black, location of water samples in blue triangles

4.1.2. Visual observations

As more detailed information on the case study location is desired, both on geometry and the location of intertidal areas, drone images are a useful tool to clarify this subject. Besides the above-mentioned subjects, the effect of the longitudinal walls on the wave rays can be clarified by top-view images obtained with a drone. For comprehensibility, the pictures in combination with the location of the picture and the conclusions that can be drawn from the pictures are displayed in the result section.

4.2. Results

4.2.1. Sediment samples

The sediment samples obtained from river bank L are displayed in Figure 4.3, the locations of the sediment samples are presented in Figure 4.4. From these samples, it can be obtained that there is a clear difference between the sediment samples found at the groyne area. There is a variation between relatively coarse sand, fine sand, very fine sand, and silt. The qualification of the sediment samples is presented in table 4.1.



Figure 4.3: Sediment samples at the river bank at the Nieuwe Waterweg

Sediment sample	Qualification
1	Very fine sand / silt
2	Fine sand
3	Fine sand
4	Silt
5	Very fine sand / silt
6	Coarse sand
7	Coarse sand

Table 4.1: Qualification of sediment samples



Figure 4.4: Location of the sediment samples

This information shows that at the south-west corner, coarse sand is present and at the south-east corner fine sand and silt are present. As the river bank is located in an estuary, the regular flow reversal results in two stages of sediment transport, transport during ebb and transport during flood flow. Coarse sediment is mainly transported as bed load transport and is highly affected by the magnitude of the flow velocities during both ebb and flood flow. The transport of fine sediments is different, as sedimentation only occurs if the velocities are below a certain critical velocity. Therefore the time frames in which the velocities are below a certain critical velocity are important, the slack periods.

The presence of coarse sand at the south-west corner can be related to velocities being relatively larger at the west entrance than at the east entrance. This is expected to result from the difference in cross-sectional areas of the entrances and is in accordance with results obtained from the hydrodynamic model, Chapter 7. High flow velocities at the west entrance are mainly expected during the rise of the tide. In this time-span, the transport of coarse sand can be initiated. The flow velocities are supposed to decrease quickly after the flow constriction by the groyne. Therefore it can be expected that coarse sediment settles close to the entrance and is therefore found at the south-west corner.

During the fall of the tide, ebb flow, the transport of coarse sediment is dependent on the circulation of the flow inside the groyne area. The presence of the longitudinal wall disturbs the circulation resulting from the groynes only. However, as the longitudinal wall is constructed in 2018, the sediment present at the river bank likely originates by the sediment transport mechanisms before this adaptation. The sediment transport in between two groynes is described in Chapter 3. When considering a situation with only groynes present, the sediment supply enters the groyne area at the northwest-side of the river bank. The circulation is anti-clockwise, and so the coarse sediment is expected to deposit in the south-west corner resulting from a relatively high settling velocity and small flow velocities. Finer sand particles travel for a longer time-period along with the flow due to the smaller settling velocity, this can be argued to be the reason why fine sand is present at the south-east corner.

Fine sediment settles when the flow velocities are below a small critical velocity. This can declare the presence of fine sediment such as silt at the east-corner of the river bank. During flood flow, the velocities are likely to be large at the west entrance, but not directed towards the river bank and so the velocities at the right corner are expected to remain small. This is in agreement with the results of the hydrodynamics model and further discussed in Chapter 7. If fine sediment particles are present in the water column, and the velocities are small enough, the sediment will deposit in the east corner of the river bank. The circulation pattern inside the river bank is anti-clockwise during ebb flow. Again, if the flow velocities are very small at the east corner, this can lead to the settlement of very fine sediment such as silt.

As mentioned before, slack periods are an important factor for the transport of fine sediment in an area that is under the effect of tidal forcing. A slack period is defined as a period of time during the reversal of the flow in which the velocity is between zero and some critical velocity. During this period, inside the whole river bank velocities are expected to be close to zero and thus can not directly be related to the spatial difference in sediment present at the river bank. Re-suspension of the settled fine sediment can happen if the flow velocities are high enough. Due to the above-mentioned expected velocity profile, this can result in transport towards the south-east corner.

The corresponding nominal diameters of the sediment characteristics described above are as follows, coarse sand $d_{50}=300\ \mu\text{m}$, fine sand $d_{50}=150\ \mu\text{m}$, very fine sand $d_{50}=75\ \mu\text{m}$ and silt $<63\ \mu\text{m}$. The critical shield stresses are calculated as described in section 4.1.1, results are displayed in Table 4.2. It can be assumed that under these conditions transport of sediment takes place.

	$d_{50}(\mu\text{m})$	Critical shear stress (N/m^2)	Critical velocity (m/s)
Coarse sand	300	0.26	0.44
Fine sand	150	0.12	0.3
Very fine sand	75	0.04	0.2

Table 4.2: Critical shear stress and velocity of the sediment samples present at river bank L, the diameters are estimated based on the samples and literature

Besides sediment samples, also samples of water were obtained from the project location to get a better understanding of the suspended sediment in the water column. The water sample taken at the tidal flat (sample 2 in Figure 4.2) contained a relatively large amount of fine sediment compared to the sample obtained at the middle of the groyne (sample 1). Sample 1 contained less suspended sediment in the water column, with the average grain size being larger than at sample 2. The higher suspended sediment concentration at location 2 can be related to the shallow water depth in combination with the sediment being brought into suspension by the small waves. Coarse sediment indicates a relatively fast settling process and high critical shear stresses for erosion. These factors can account for the presence of fine sediment in the water column at the tidal flat.

4.2.2. Visual observations

The photographs displayed in this section are all obtained from a different location. The locations of these photographs are displayed in Figure 4.5. In the left picture the areas represented in the top view photographs A and B are indicated by a dashed rectangle. In the right picture, the location (cross inside a circle) and the direction (dashed lines), and so the covered area of photographs C, D and E are displayed. The photographs are taken just after low water when the water level starts rising. In this period, the velocities inside the navigation channel are directed seawards (De Nijs et al., 2011).

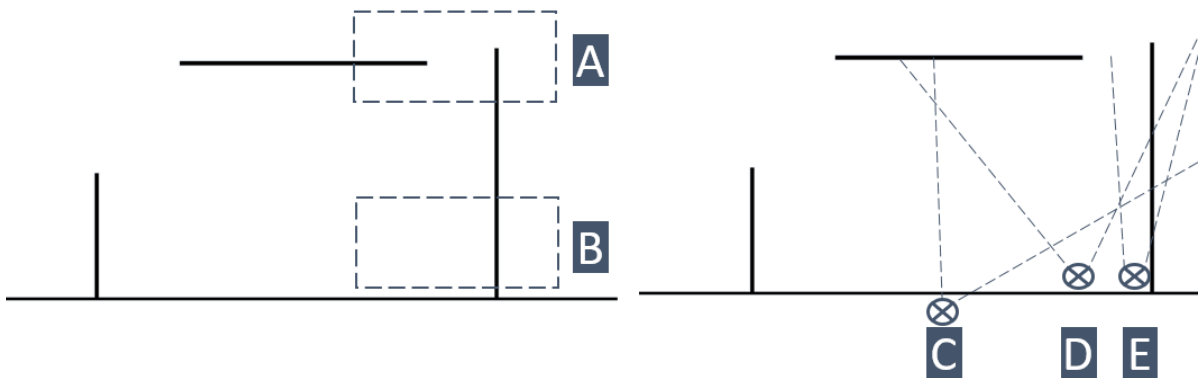


Figure 4.5: Locations of the photographs. A and B represent the top view images. For photographs C, D and E the area that is included is displayed by dashed lines.

In Figure 4.6, photograph A, the east entrance of river bank L is displayed. Observing this photograph, the high turbidity at the river bank relative to the navigation channel is clearly visible. From the pattern in the flow, visible due to the high turbidity, one can obtain that the flow is directed seawards. A small stroke of low turbidity can be indicated in this photograph in between the longitudinal wall and the groyne directing towards the south-west. This indicates the flow with low turbidity originating from the navigation channel into the river bank. The angle at which the flow enters the river bank can be derived from this photograph and is about 120 degrees with the main flow direction in the navigation channel. The high turbidity inside the groyne area originates from the high turbulence intensities resulting from obstructions of the flow and so stirring of the sediment.

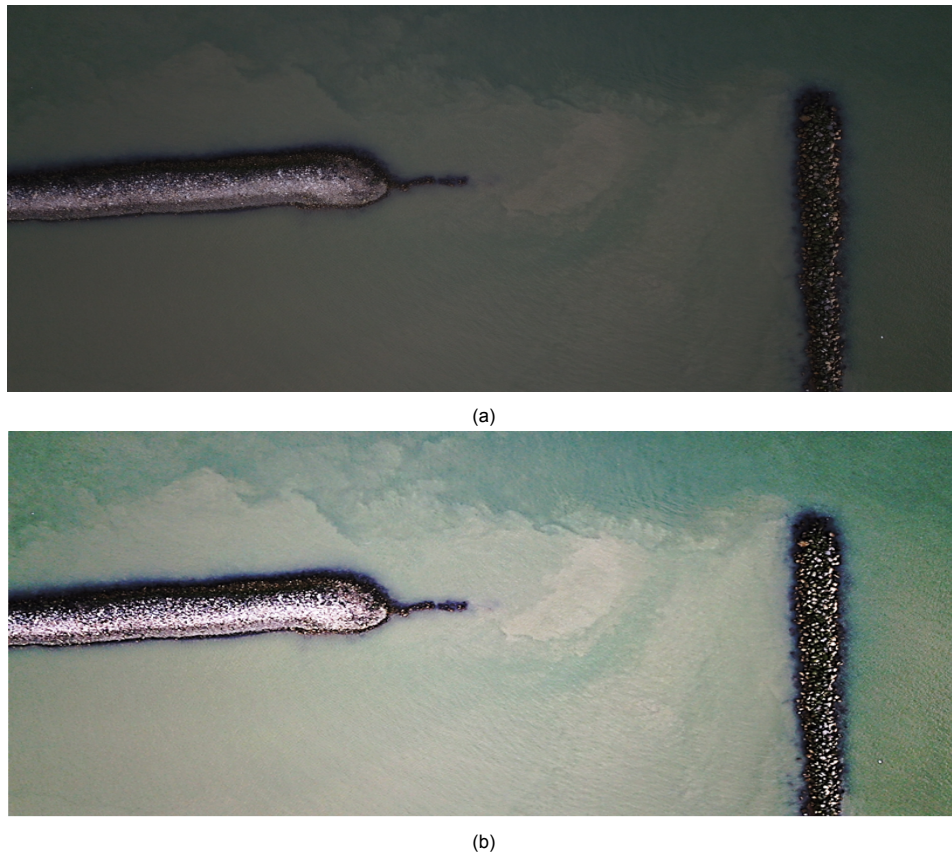


Figure 4.6: Photograph A: Top view of east entrance tidal river bank L

In Figure 4.7a, photograph B, the top view of the tidal flat present at the east corner is displayed. When following the border of the water line present in this photograph, initially the distance from the river bank up to the water line is increasing when opting from west to east. At a certain moment, this distance becomes constant, and thereafter decreases close to the groyne. The presence of lower bed levels close to the groyne is, as explained in Chapter 3, the result of the groynes being submerged for a period of time during flood. Resulting from the spiraling flow close to the groyne during high tide, sediment is stirred up and erosion takes place.

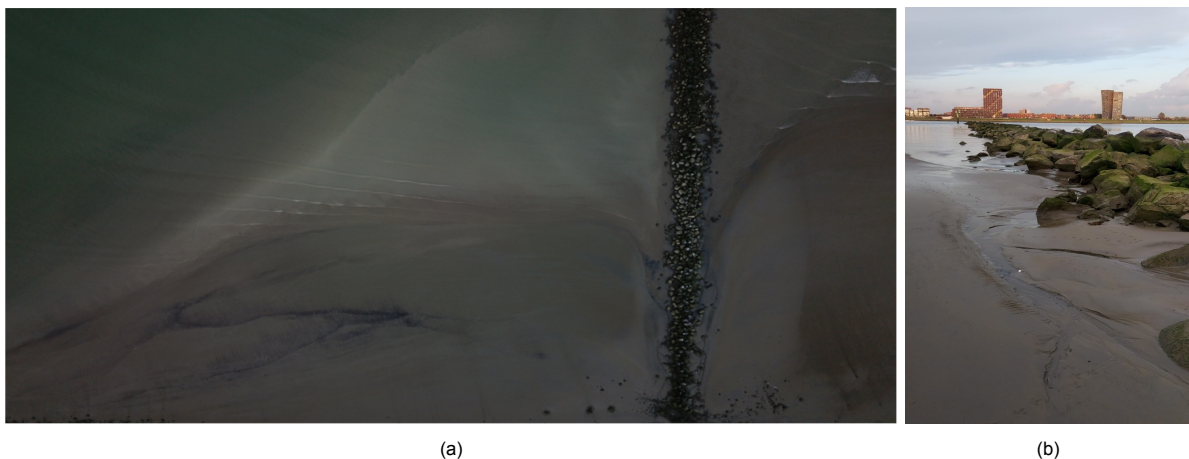


Figure 4.7: In Figure 4.7a photograph B is visualised: displaying the top view of the tidal flat at the east corner of river bank L. Figure 4.7b displays photograph E in which a tidal gully is visible close to the right groyne.

This is primarily observed close to the navigation channel, as the flow velocities are largest close to the

navigation channel and decreasing towards the river bank. However, a decrease in bed level elevation is also present closer to the start of the river bank. At this location a tidal channel is observed, displayed in Figure 4.7b, photograph E.

In Figure 4.8, photograph C, the layout of the river bank is visualized. The sloping structure of the river bank consists of concrete blocks with vegetation growth in between the blocks. There is a sudden transition from the concrete sloping dike into the tidal flat. This photograph shows a part of the intertidal area at the river bank during a water level of -0.45 m NAP. From this, it can be obtained that the height of the intertidal flat present at river bank L is relatively low.



Figure 4.8: Photograph C: Hard sloping structure of the river bank, consisting out of concrete blocks in combination with the growth of vegetation in between these blocks. Sudden transition from sloping concrete river bank into the tidal flat.

In Figure 4.9, photograph D, the secondary waves field resulting from a passing vessel is displayed. As is explained in Chapter 3, the presence of a longitudinal wall affects the wave action inside the river bank. The expected pattern drawn in the previously mentioned chapter is confirmed, the wave rays are bending around the longitudinal wall. The waves resulting from this specific vessel are short and relatively small, the magnitude depends on the dimensions and the speed of the vessel passing by. From visual observations, it was obtained that the waves resulting from the same vessel were much higher in river bank M in which no longitudinal wall is present. The presence of the longitudinal wall decreases the wave impact at the river bank significantly.

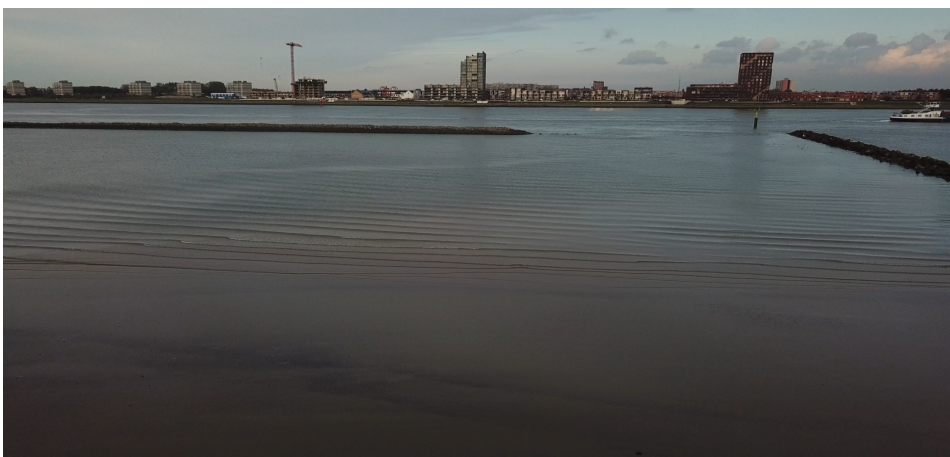


Figure 4.9: Photograph D: Secondary waves of a passing vessel entering river bank L from the east entrance

Morphology of the river banks

In this chapter, the morphological development of the river banks in the Nieuwe Waterweg over the last five years is determined. Bed level data is available from five measurement campaigns, executed with multi-beam echo sounders, in the years 2015 to 2019. The morphological development is determined by a hypsometric analysis, this is defined as the study of the distribution of ground surface area, or horizontal cross-sectional area, of a landmass with respect to elevation, according to Strahler (1952). This type of analysis is often used to describe large watersheds, but in addition for small drainage basins to determine how the mass is distributed within a basin from base to top (Strahler, 1957). This analysis can also be used for creating a hypsometric curve of the tidal flats, this method is described by De Vet et al. (2017). From this analysis it can be obtained which river banks are developing intertidal zones, and can also provide information on the effect of the geometry on the horizontal tidal asymmetry inside the river bank. In addition, this research provides information on the correlation between location of the river bank and the development of the intertidal areas inside the river bank.

5.1. Methodology

In this section the construction method of hypsometric curves is treated, initially it is elaborated what conclusions can be drawn from these curves. Two example hypsometric curves are used, one curve of a flood dominant system and one curve of an ebb dominant system. The description flood dominant system is used when the magnitude of the maximum flood flow is larger than the maximum ebb flow, for an ebb dominant system the reverse is accounted for. The geometry of the system can strengthen or weaken this difference in magnitude between the ebb and flood flow (Bosboom and Stive, 2015). A flood dominant system results in an import of sediment, and an ebb dominant system results in the export of sediment. Examples of hypsometric curves for a flood dominant system (right) and an ebb dominant system (left) are displayed in Figure 5.1. Present-day, the Rhine-Meuse area consists out of deep channels in combination with shallow river banks. This resembles the left figure, flood dominance, import of sediment which is in agreement with literature.

The geometry of the river bank can indicate whether flood or ebb dominance of the system is enhanced. One could think that when a lot of sediment is imported at the river bank, a transition can occur resulting in the small system becoming more ebb dominant, which can possibly prevent further sedimentation

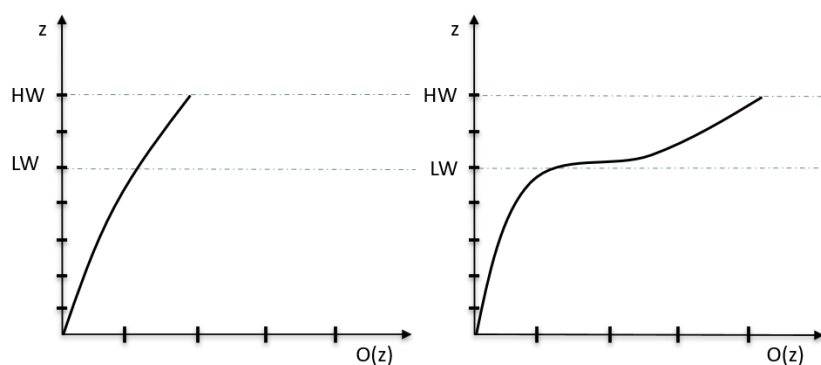


Figure 5.1: Hypsometric curves of two different basin types, left: flood dominance enhanced, right: ebb dominance enhanced (Bosboom and Stive, 2015)

of these areas. However, the geometry of the river banks is not expected to significantly affect the velocity profile inside the river bank as the velocity profile is foremost dependent on the surrounding system, the Rhine-Meuse estuary. Besides the effect of geometry on the horizontal tide, hypsometric curves clearly indicate the amount of intertidal area present and the development of the latter one. All river banks assigned with a letter in Figure 5.2 are analysed, from this the correlation between location of the river bank and the development of the intertidal area inside the river bank can be determined. The method and necessary data for conducting a hypsometric analysis is now presented.

The necessary data for constructing hypsometric curves is bed level data, and the tidal range at the area of interest. In section 3.4 the analysis of the tide present at Maassluis is treated, the resulting characteristic water levels (HAT, LAT, MLW and MHW) are used in this analysis. The available data on bed level consists of in total four years of measurements, measurements are executed in 2015, 2017, 2018, and two times in 2019. These bed level measurements are executed by multibeam echosounders and are limited to the +0.5 m NAP line and all measured with respect to NAP. The measurement interval is equal to 1 metre and thus the area represented by one measurement is assumed to be 1 m². The measurement data is visualized in Figure 5.2, from this it can be obtained that at river banks L, M, and N the data is not complete. This results from the limitation of the measurements being +0.5 m NAP and the bed levels at that location being higher than those values. The intertidal areas of these river banks will be larger than calculated by the use of this data. For are L and M, additional hypsometric curves are constructed based on the additional bed level data approximated from the AHN (Algemeen Hoogtebestand Nederland) database in combination with bed level measurements in 2019. No additional curve of river bank N is constructed regarding time consumption and large amount of bed level elevations being higher than the intertidal region (AHN, 2020). The AHN database is an application where the height relative to NAP for the Netherlands is stored. This data is based on measurements between 2014 and 2019 (AHN, 2020).

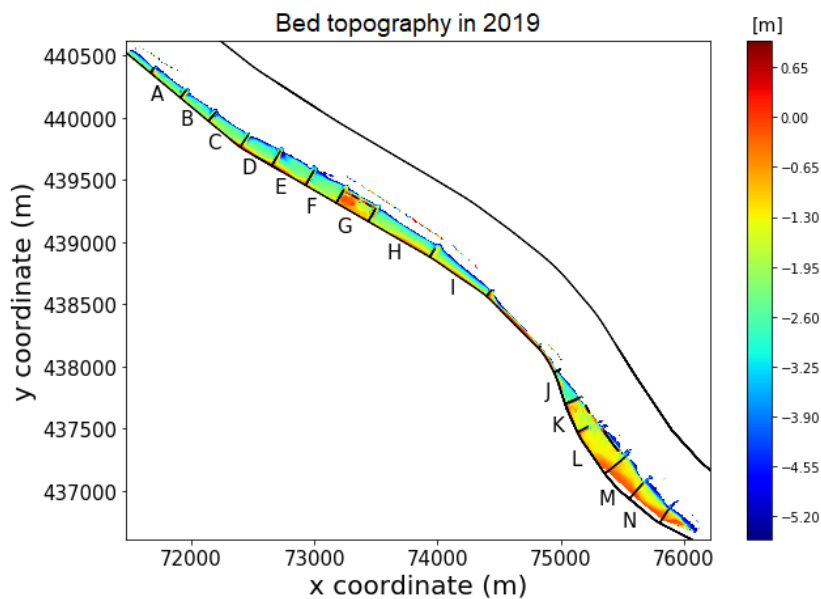


Figure 5.2: Overview of all the groyne areas being labelled by alphabetic letters

The procedure to construct the hypsometric curve is now elaborated, this procedure is obtained from De Vet et al. (2017) and thereafter adapted in order to suit this research approach.

- The data on the bed level is filtered based on the coordinates of the areas of interest, and thereafter filtered to values above -6.0 m NAP.
- The hypsometric function $A(z) = A(Z > z) - A(Z > \text{MHW})$ is obtained by multiplying the surface area per measurement with the number of measurements of which the bed level is larger than z , but smaller than MHW.

- Thereafter the same operation is done with data filtered upon the coordinates of the area of interest and in addition on being higher than MLW in order to represent the intertidal areas.

Besides the construction of the hypsometric curves, the average height of the intertidal flats is calculated, see equation 5.1. In addition to the previous steps, one more step needs to be executed, the volume distribution at the flats. This can be obtained by multiplying the bed level with the area determined in the second step.

$$h = \frac{V(Z > \text{MLW}) - V(Z > \text{MHW})}{A(Z > \text{MLW}) - A(Z > \text{MHW})} \quad (5.1)$$

5.2. Results

5.2.1. Evolution over years

In Figure 5.3, the hypsometric curves of the river banks are displayed, constructed from measurements in June 2019. The x-axis represents the relative area, a dimensionless parameter, in order to be able to compare the curves of different riverbanks independent of their size. In Figure 5.3a the hypsometric curves are displayed from -6 m NAP up to +1.0 m NAP, the maximum elevation is set to +1.0 m NAP for clarity, reason being no bed level elevations are larger than this value. In Figure 5.3b the part of the curves present in the intertidal area are visualized, represented by -0.74 m NAP.

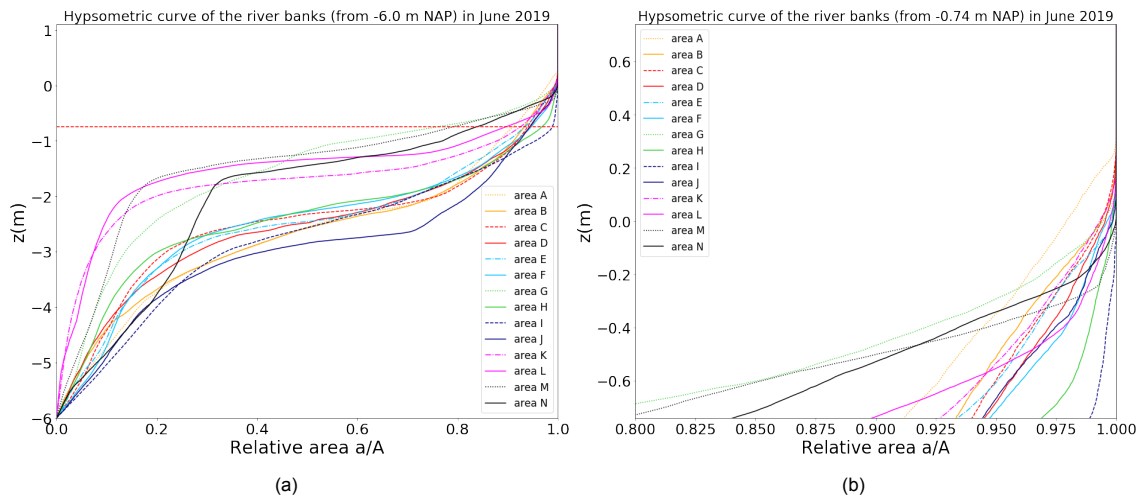


Figure 5.3: Hypsometric curves of riverbanks A to N, constructed from bed level measurements in July 2019. The left figure displays the curves from -6.0 m to +1.0 m NAP. The right figure displays the hypsometric curves of the intertidal area from -0.74 m (LAT)

Comparing the shapes of the hypsometric curves displayed in Figure 5.3a to the theory explained in section 5.1, noting that the theory applies to a tidal basin, the curves resemble a system in which flood dominance is enhanced. The intertidal areas hardly contribute to the total cross sectional area of the river banks. It is therefore expected that the flood velocities are enhanced. However, one should keep in mind that the velocities present at the river banks are foremost dependent on the surrounding system, the Rhine-Meuse estuary. The effect of the growth of intertidal areas at the river banks on the velocity profile of the total system (Rhine Meuse estuary) is expected to be negligible.

Figure 5.3a shows that besides the intertidal areas being small relative to the total area of the river bank above -6 m NAP, the shape of the hypsometric curves are quite different per riverbank. A remarkable difference is visible in the bed level elevations at which the curves display a constant line. This constant line indicates that a large area contains the same bed level elevation. River banks containing a relatively large intertidal area coincide with the high bed level elevations where the curve is constant. This indicates that river banks with relatively large intertidal areas have a mild-slope, for example river bank G, L, M and N. The contrary is accounted for river banks with a constant curve at lower bed levels, these areas contain small intertidal areas and indicate as steeper slope from this location to the

maximum bed level elevation.

The river banks A to N are ordered with increasing distance from the river mouth. The bed level elevation at which the hypsometric curve is almost constant, indicating a large area with the same elevation, is lower close to the river mouth. This indicates a trend of more sedimentation inside the river banks located further from the river mouth. It can be hypothesized that the difference in sedimentation inside the river bank is depended on the location of the river bank inside the river, since erosion of sediment takes place at the outer bend and the deposition of sediment takes place in the inner bend. This hypothesis is answered in section 5.2.2. One could also argue that the difference in sedimentation of the river banks is related to the location of the tip of the salt-wedge. This location often coincides with large sedimentation (De Nijs et al., 2011), but this is beyond the scope of this research.

Figure 5.3b displays the same curves as are presented in Figure 5.3a but focused on the intertidal area. This figure clearly shows the small amount of intertidal area present at the river banks and clarifies the differences between river banks. River bank I and H have the least intertidal area present, followed by F,D,C,E,B,K and A. These river banks all contain less than ten percent intertidal area with respect to the total area. The river banks containing more than ten percent intertidal area are, from small the largest are L,N,M, up to G. Possible reasons for these results are, river bank L, N and M being situated in the lee area behind the platform of the ferry. At river bank G a sand nourishment is placed which is the reason for the relatively large intertidal area.

As mentioned before, the evolution of the hypsometric curves over years can indicate the growth of intertidal area and thus a transition towards a possible small ebb dominant system. In order to obtain information on the evolution of the river banks, it is important that the data sets contain the same amount of measurements per year. The data set of 2019-2 contains 96 percent of the 100% data set (2019-1), for data set 2015,2017 and 2018 this equals 97 %, 98 % and 100 % respectively. These values are based on the total amount of measurement points of all the river banks, the completeness of the data set varies per river bank, this is further discussed in Appendix B. For each river bank, hypsometric curves from five measurement campaigns taken over four years are constructed, the curves are displayed in Figure 5.4. The curves indicate the total area of the river bank and how this area is distributed over the elevation of the river banks. The grey horizontal line indicates the lowest astronomical tide (LAT) of -0.74 and the black horizontal line indicates +1.1 m NAP (high water) as no bed level measurements are representing levels above +0.5 NAP. In Appendix B, Figure B.1 , the same hypsometric curves are displayed but only representing the tidal flats inside the river bank.

From Figure 5.4 the incompleteness of the data sets is visually obtained. The total cross sectional area, displayed on the x-axis should be around equal for all hypsometric curves. The data sets are initially filtered based on coordinates, determined by location of the river bank, and thereafter on exceeding the bed level elevation of -6.0 m NAP. Small deviations in cross-sectional area can occur as a result of filtering the data on bed level. In almost all riverbanks, the curves representing different measurement campaigns display the same shape up to the intertidal region. This indicates that the lack of measurement points of the river banks originate inside the intertidal area. Opting from a practical point of view, this is plausible as the data is obtained by a multibeam echosounder which might indicate difficulties obtaining data in shallow water.

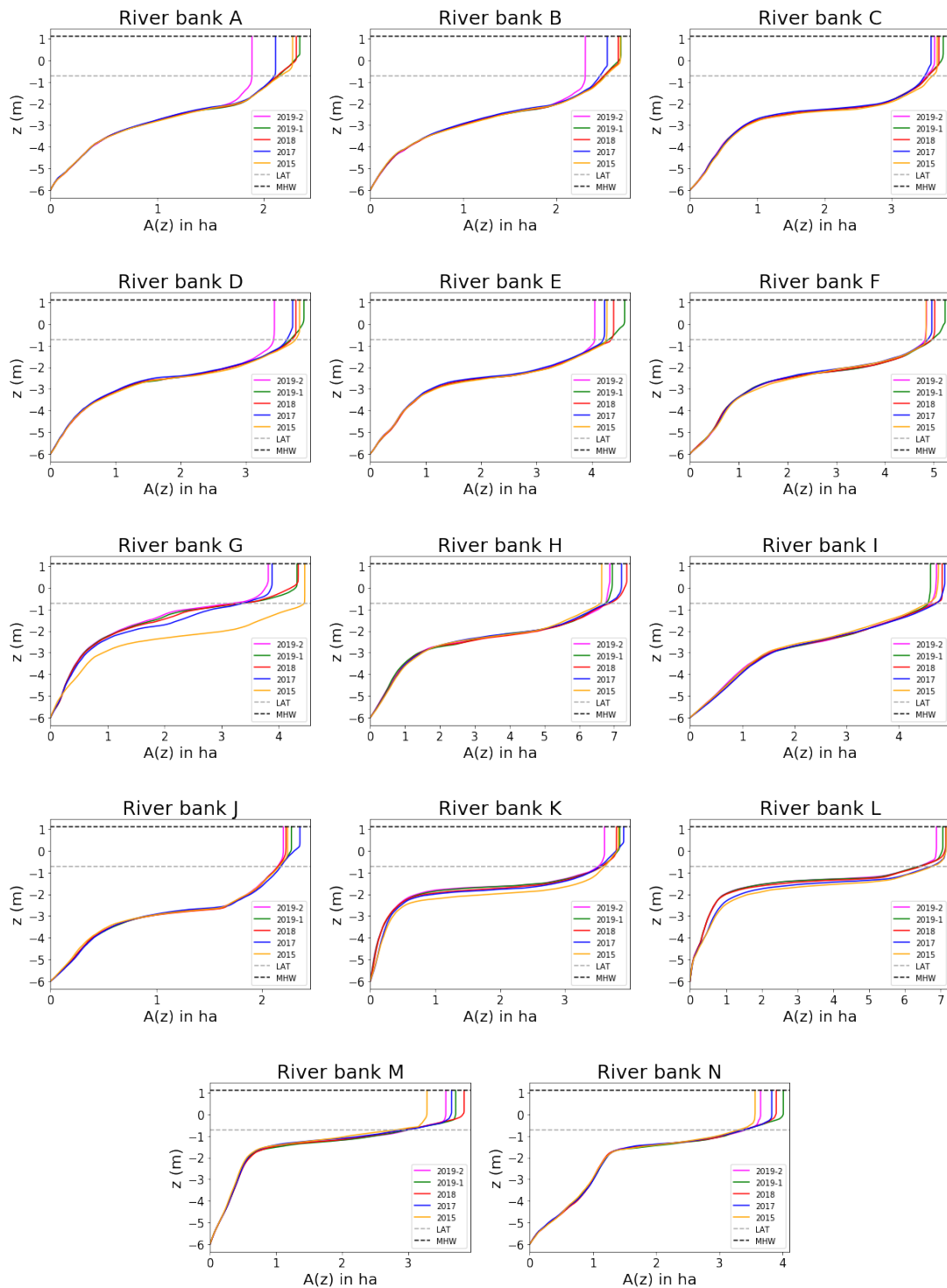


Figure 5.4: Morphological evolution of the river banks from -6.0 m NAP (ordered with increasing distance from the mouth), obtained from 5 measurement campaigns. The lines indicate the years, orange : 2015, blue : 2017, red : 2018, green : 2019-1 and pink 2019-2. For reference to location of letters, see Figure 5.2

Although the data sets are incomplete at some river, conclusions can be drawn on the morphological evolution of the river banks. In Appendix B the morphological evolution of each river bank is discussed separately. In general it can be obtained that the intertidal areas inside the Nieuwe Waterweg are increasing, either in height or in surface area. The sand nourishment at river bank G is clearly visible, as the average height of the river bank increased, from 2017-2019 the intertidal area is however de-

creasing. Most commonly the increase of the intertidal area at the river banks occurs simultaneously with an increase in bed level elevation of the river bank. Only at river bank K and L, the river banks at which longitudinal walls are constructed, a clear rise in bed level at the river banks and a clear increase in intertidal area is visible. In Figure 5.5 the evolution of the volume of the intertidal flats is visible. The increase of volume of the tidal flat is the combined effect of increase in either surface area and/or elevation. At most river banks the volume of the intertidal area is increasing. From Figure 5.5 it can be obtained that the volume of the intertidal flats present at the river bank are small, mainly at the river banks closer to sea.

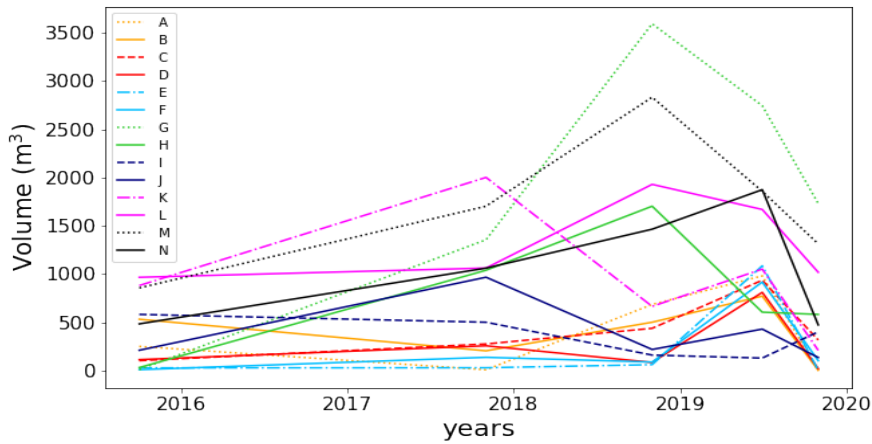


Figure 5.5: Evolution of the volume of the intertidal areas at the river banks present in the Nieuwe Waterweg

5.2.2. Location dependency

From the average height of the areas over four years in combination with their location in the river, the dependency on this factor can be visualized. In Figure 5.7 the average height of the intertidal area, the average height of the river bank (from -6 m NAP), and the average intertidal surface area are displayed. These values are averaged over four years, and displayed with respect to the overall average values of the heights/areas are the averaged values over four years.

As is explained before, the data sets are lacking data inside the intertidal area, which was clearly visible in Figure 5.2. In Figure 5.6, the corrected hypsometric curves of river bank L and M are displayed including the correction for bed levels above +0.5 m NAP with AHN data . The total intertidal area at river bank L is equal to 1.1 ha, for river bank M this is equal to 1.9 ha. The height and surface area of the intertidal area displayed in Figure 5.7 are based upon the hypsometric curves displayed in Figure 5.6. The hypsometric curve is not corrected for river bank N, at this river bank the height and surface area of the intertidal area are however also larger than obtained from the data sets and displayed in Figure 5.7d.

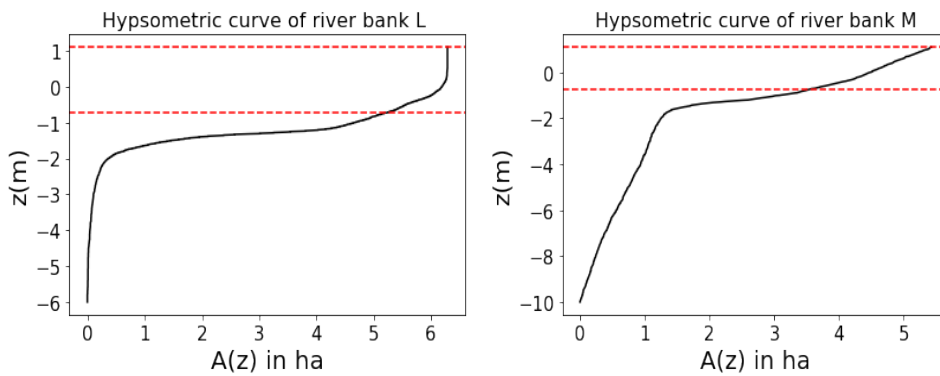


Figure 5.6: Hypsometric curves of river bank L and M, after AHN correction

Conclusion

It can be concluded that in general there is a correlation between the location of the tidal parks and the intertidal areas present at those locations. At the outer bends, the heights of the intertidal area are smaller than the average height. This is also what is expected as a result of the spiraling flow. It should be noted that the differences in height are small, and other aspects also affect the height of the intertidal areas, for instance, a sand nourishment at the river banks and/or dredging of navigation channel. Figure 5.7c shows that the groyne areas at the sea-side have a lower average river bank height, a lower surface area and height of the intertidal area. Besides, it can be obtained that at the example areas (M and N) and the river banks K and L, in which longitudinal walls are constructed, display a relatively large difference in increase in height of both the intertidal area and river bank and surface area. This can originate from the presence of the lee area behind the platform of the ferry, which obstructs the flow being directed towards these river banks. The intertidal surface area in the other river banks, except for river bank G which has a large intertidal area due to human interventions, is really small. A lot of tidal area can be gained in these river banks, however, due to the low bed levels, the process will be time-consuming.

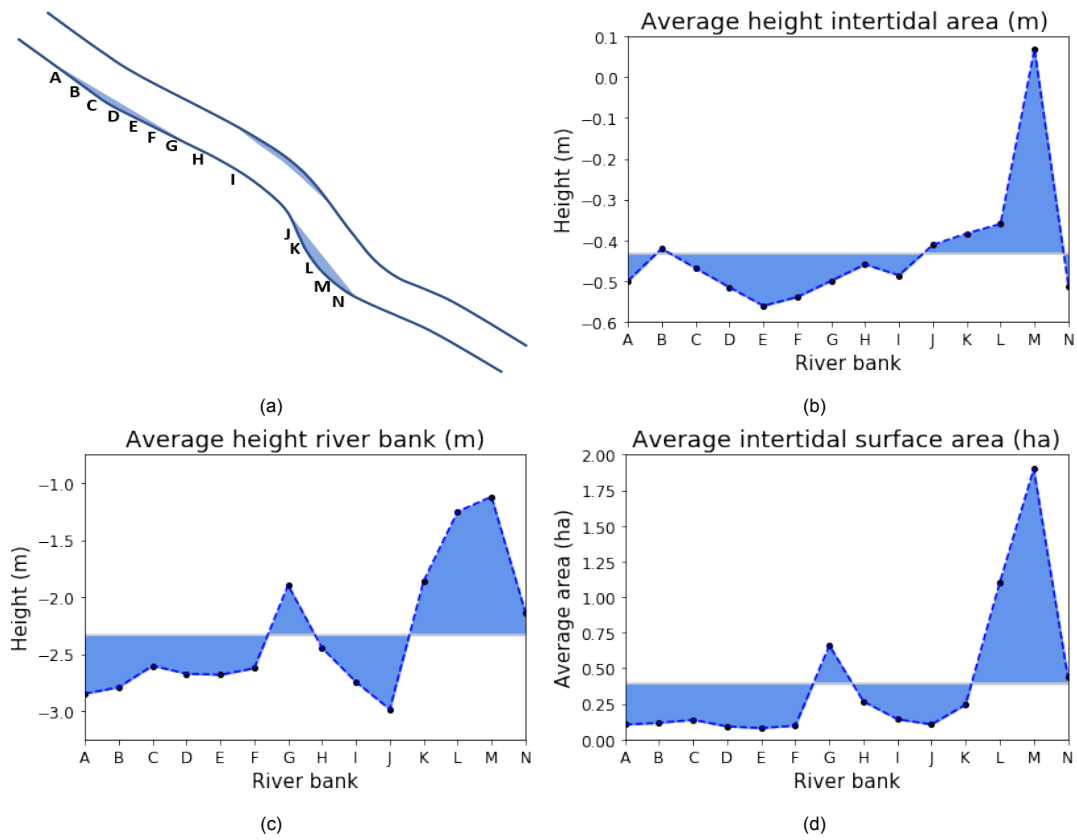


Figure 5.7: Location of the river banks indicated in combination with graphs displaying the average height of the intertidal area, the average height of the river bank from -6.0 m NAP and the average intertidal surface area obtained from averaging five years of measurements. In case of river bank M and L, the average values in these graphs are based upon data from the AHN data-base and 2019-1 measurements. The blue shaded areas in the graphs are used to indicate the difference with respect to the overall average values of the heights/areas over four years

Simulation approach and model set-up

The literature review in Chapter 3 provided insight into the effect of both hydrodynamic forcing and variations in geometry on the sediment transport at the river bank. A 2DH Delft3D model is used to investigate the latter by executing various model simulations. First, the hypotheses and modelling methodology is discussed. Secondly, the model set up is presented. The Delft3D model neglects the presence of waves and is forced by a combination of tidal forcing and a fresh water discharge. In Chapter 7, the results of the model study into the effect of hydrodynamic forcing on the sediment transport at the river bank are presented. In Chapter 8, the results of the model study into the effect of variations in geometry on the sediment transport at the river bank are discussed.

6.1. Hypotheses and modelling approach

As is stated in the problem statement, the sediment transport at the river banks in the Nieuwe Waterweg is relatively unexplored. The resulting sediment import into the river bank area is besides being related to the availability of sediment, related to both the hydrodynamic forcing of the system and human interventions. The effect of the latter is researched by implementing several variations in a developed numerical model.

6.1.1. Hydrodynamic forcing related

The effect of hydrodynamic forcing on the sediment transport on the current situation is determined by incorporating both a morphological tide, a spring tide and an extreme event: a storm surge. The incorporation of a spring tide is included as this type of forcing is responsible for large-scale erosion and re-suspension of sediment (Allen et al., 1980). It is therefore hypothesized that the incorporation will result in more sediment transport into the river bank area. In addition, it is expected that sediment will be transported further into the river bank area.

The Maeslantkering is a storm surge barrier, located in the Nieuwe Waterweg, that closes off the connection between sea and river during storm surges. The closure can however not prevent high water elevations from being present at the Nieuwe Waterweg. The presence of a storm surge often is responsible for re-suspension and transport of sediment (Yin et al., 2016). During a storm surge, the water levels inside the estuary are higher than usual. It is hypothesized that this results in more sediment deposition at the river bank as a consequence of the larger sediment availability. The simulation approach of the hydrodynamic forcing scenarios are displayed in Figure 6.4.

6.1.2. Human intervention-related

In this section, hypotheses are formulated for the different variations in geometry which are all human intervention related. The tidal parks at the Groene Poort are developed between previously existing groynes in combination with newly constructed longitudinal walls parallel to the river bank. River bank L is chosen as study location. There are four adaptations that are considered in this research that affect the sediment transport towards the river banks in the Nieuwe Waterweg.

- Varying bed topography in the groyne area
- Varying the width of the longitudinal wall
- Varying length and height of groynes
- Varying opening of the inlet

Adaptation 1: Varying bed topography

The bed topography present at river bank L is altered by years of ongoing sediment transport. To display the effect of the constructed longitudinal wall on the flow and sediment transport, a simulation is executed incorporating a constant bed level at -1.8 m NAP. This simulation displays the effect of the constructed longitudinal wall on the flow and transport excluding the effect of the already present bed topography. In addition, two simulations are executed incorporating a higher bed level than is present at river bank L. One simulation is executed incorporating a constant bed level at -1.0 m NAP. This bed topography is ought to resemble the bed level present at tidal parks the Zaayer. The third simulation incorporates a bed level at 0.0 m NAP. This simulation is executed to display the morphological development of the river bank when a nourishment is executed.

The bed level heights that are modelled are presented below in combination with the simulation number.

- 0.0 m NAP (simulation D.1)
- -1.0 m NAP (simulation D.2)
- -1.8 m NAP (simulation D.3)

Hypothesis 1: It is expected that a change in bed topography will lead to a different flow pattern. The incorporation of a constant bed level of -1.8 m and -1.0 m NAP result in an increase in tidal prism. A constant bed level of -1.8 m NAP is expected to result in higher flow velocities as a result of the increase in tidal prism and larger water depth. The velocities are expected to be higher which can result in more sediment import of sand if the critical velocities are reached. The incorporation of a constant bed level at -1.0 m NAP is expected to result in smaller velocities. Export of coarse sediment is expected close to the navigation channel.

Hypothesis 2: If the bed level at the river bank is increased up to 0 m NAP, the river bank area is only partly flooded during a tidal cycle. It is expected that this results in a decrease in velocities over the whole river bank. In addition, it is expected that this adaptation will result in the export of sediment at the groyne area, more specifically at the entrances of the groyne area.

Adaptation 2: Varying the width of the longitudinal wall in front of tidal park

Currently, the solution for enhancing sedimentation in the Groene Poort consists of constructing longitudinal walls. The length of the longitudinal wall affects the flow pattern at the river bank. The eddies formed by consecutive groynes are obstructed by the presence of a wall. Decreasing the length of the longitudinal wall ensures that this effect decreases, and the flow pattern will return to the original situation. Therefore, it is chosen to simulate multiple situations considering the length of the longitudinal wall. In the present-day situation, the length of the wall equals 228 meters. A longitudinal wall functions as a wave damper. This is explained in section 3.4.2. Longitudinal walls in combination with groynes ensure the presence of a lee area. In this area the flow velocities are small and sediment has more time to settle. It is expected that the presence of a longitudinal wall has a larger impact on the sediment transport of cohesive sediment rather than non-cohesive sediment. The variations in the length of the longitudinal wall are visualized in Figure 6.1 and listed below.

- Extended longitudinal wall (280 m), Figure 6.1b (simulation E.1)
- Shortened longitudinal walls (140 and 70 m), Figures 6.1c,6.1d (simulation E.2 and E.3)
- No longitudinal wall, Figure 6.1e (simulation E.4)

Hypothesis 1: An increase in length of the longitudinal wall is expected to increase the flow velocities present at the entrances of the river bank as the surface area of the entrances decreases. However, the flow direction from the navigation channel into the river bank area becomes more unfavourable as the longitudinal wall becomes larger. It is expected that transport of cohesive sediment into the river bank area is enhanced by an increase in the longitudinal wall. In addition, it is expected that the import of fine sediment increases compared to the base case simulation.

Hypothesis 2: A decrease in the length of the longitudinal wall is expected to result in a decrease in the magnitude of flow velocities at the entrances. As a result, less erosion is expected at the entrances.

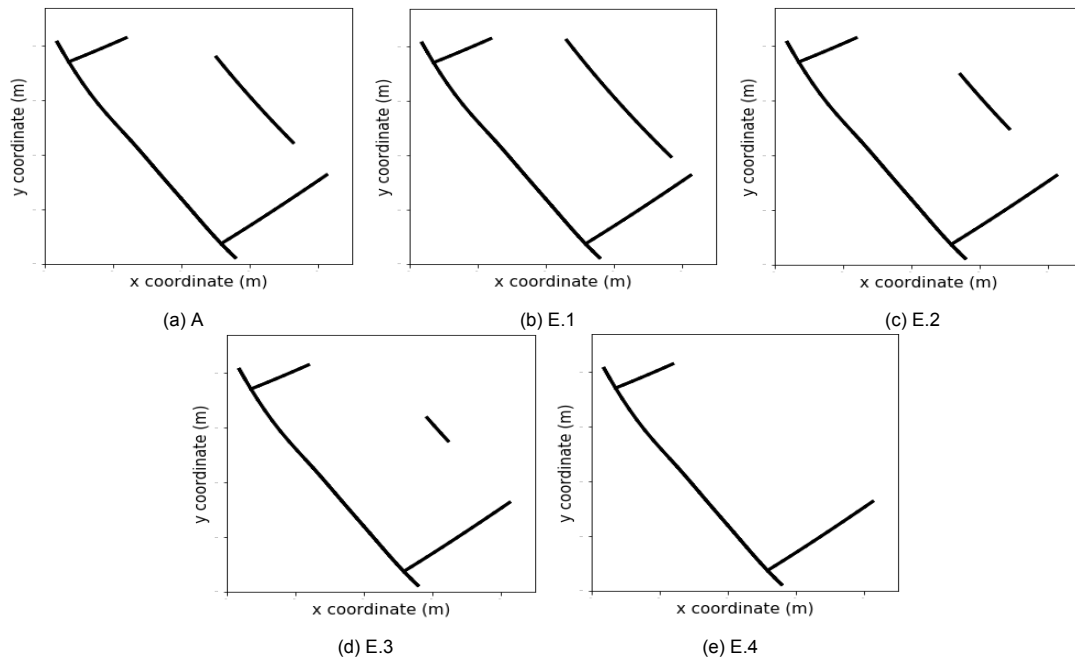


Figure 6.1: Figure displaying the simulations incorporating variations in the length of the longitudinal wall, numbers are presented in the caption.

This decrease in eroded sediment is expected to result in less sediment transport of coarse sediment into the river bank area. The mean velocity in the groyne area is expected to increase, as the flow from the navigation channel towards the river bank is less obstructed resulting from a decrease in length of the longitudinal wall. It is expected that this will result in less sedimentation of fine sediments at the river bank.

Adaptation 3: Varying length and height of groynes

As is explained in Section 3.4, the submergence and the length of the groynes affect the flow pattern in a groyne area. Submerged groynes ensure higher flow velocities which hinders the settlement of suspended sediment. By modelling various variations on submergence, the effect on flow velocities and sediment transport at the river bank area becomes clear. The submerged groynes are located at the same location as the present-day location of the groynes. The combination of increasing the length and the groynes being submerged is not considered in this research. The circulation patterns present in the groyne area are, as explained in Section 3.4, dependent on the ratio between the length of the groynes (L) to the width between the groynes (S). Changing these variables will affect the flow patterns and the sediment transport into the groyne area. When this ratio is close to one, a single eddy is present. When the width between two groynes becomes larger, a ratio of S/L 2-4, two circulation patterns are expected. When this ratio becomes too large, the main flow penetrates into the river bank area and erosion is expected Yossef and De Vriend (2010). The latter is however also affected by the presence of a longitudinal wall located in front of the river bank. The variations of the groynes in heights and length are listed below and visualized in Figure 6.2.

- Submerged groynes level -0.6 m , 0 m and +0.5 m NAP, Figure 6.2a (simulation F.1,F.2, and F.3)
- Extended left groyne, Figure 6.2b (simulation F.4)
- Shortened left groyne, Figure 6.2c (simulation F.5)
- Removal left groyne, Figure 6.2d (simulation F.6)
- Shortened left and right groyne, Figure 6.2e (simulation F.7)

Hypothesis 1: It is expected that increasing the submergence of the groynes leads to higher velocities at the groyne area. Less sedimentation is expected at the river bank compared to the original situation.

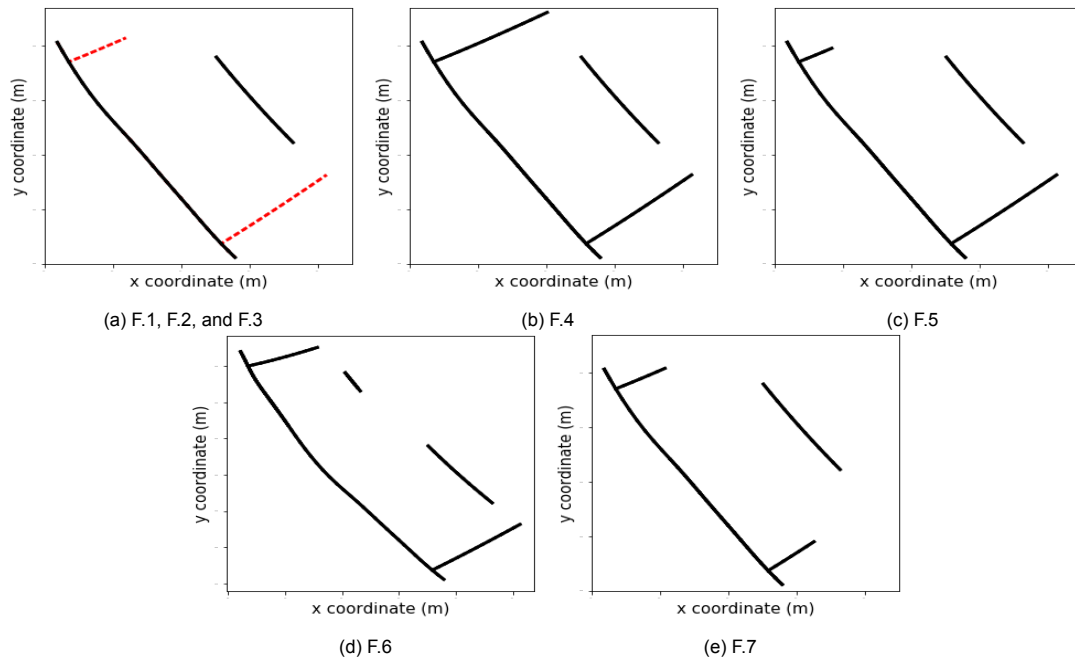


Figure 6.2: Figure displaying the simulations incorporating variations in height and length of the groynes at the tidal park, numbers are presented in the caption.

Hypothesis 2: Increasing or decreasing the length of the groyne will affect the flow pattern in the groyne area. An increase in groyne length will decrease the inlet area and therefore flow velocities are expected to increase at the inlet causing erosion which is deposited in the groyne area. In addition, the flow is expected to enter the river bank at a larger angle with the main flow direction inside the navigation channel. Leading to the flow being more directed towards the river bank. A decrease in groyne length will result in a more dynamic area, higher flow velocities and less sedimentation of fine sediment are expected

Adaptation 4: Varying inlet of the tidal park

The adaptations considered are the implementation of a sill or fully closing the inlet. Water particles follow the path of the least resistance. The presence of a sill leads to increased resistance which results in water particles being less prone to flow into the area. At the location of the sill, the flow is contracted by which the velocities are expected to be relatively high. The velocities in the area behind the sill are expected to decrease compared to the original situation. From Figure 3.15b, Chapter 3, it is obtained that for sediment to be transported over sills higher flow velocities are required. Therefore it is assumed that at locations where the sill is present there is less import of sediment originating from the navigation channel. The suspended sediment transport is less affected. When the flow is directed towards the sill originating from the river bank area, it is expected that sedimentation occurs in front of the sill. This is expected to result from the particles not experiencing enough forces in order to be transported over the sill. The adaptations that are researched are displayed in Figure 6.3. Both the options of implementing a sill at the left side (flood entrance) and at the right side (ebb entrance) are explored. When the ebb flow is decelerated and obstructed by the presence of a sill, it is expected that the velocity signal at the river bank becomes more flood dominant. The reverse is accounted for with a sill present at the flood entrance. In Figure 6.3a, 6.3b and 6.3c the sills at river bank L are visualized. Besides researching the effect of a sill which is assumed to alter the velocity profile, the effect of full closure of one of the entrances is researched. This is visualized in Figures 6.3e and 6.3d.

- Sill located at right or left entrance, Figure 6.3a, 6.3b (simulation G.1 and G.2)
- Sill located at both entrances, Figure 6.3c (simulation G.3)
- Full closure of the left or right entrance, Figures 6.3e, 6.3d (simulation G.4 and G.5)

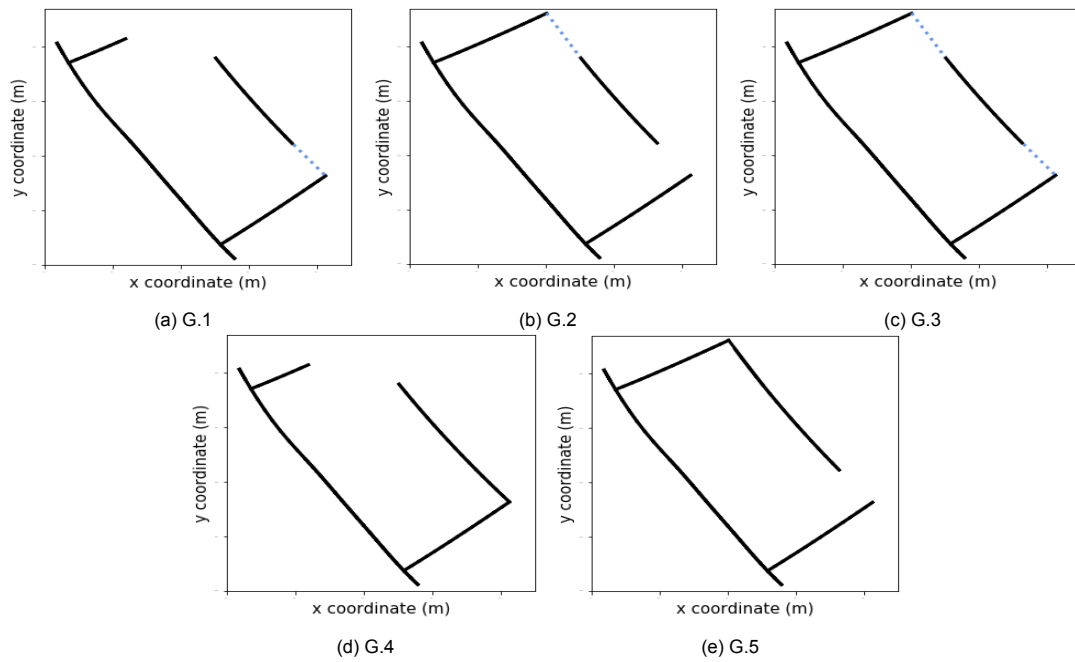


Figure 6.3: Figure displaying the simulations incorporating variations in the surface area of the inlet of the tidal park, numbers are presented in the caption.

Hypothesis 1: It is expected that the implementations of sills affect the flow pattern in terms of increasing/decreasing the ratio between the ebb and flow velocities. Besides that, the sedimentation at the river bank is ought to increase behind the sill. This only applies when the flow velocities at the river bank are large enough to transport sediment from the other entrance to this location.

Hypothesis 2: It is expected that a full closure of the groyne areas will increase/decrease the ratio between ebb and flow velocities. The magnitude of velocities present at the river bank is expected to decrease. More sedimentation is expected at the river bank as a result of the decrease in the magnitude of velocity which is expected to result in additional settlement of suspended sediment.

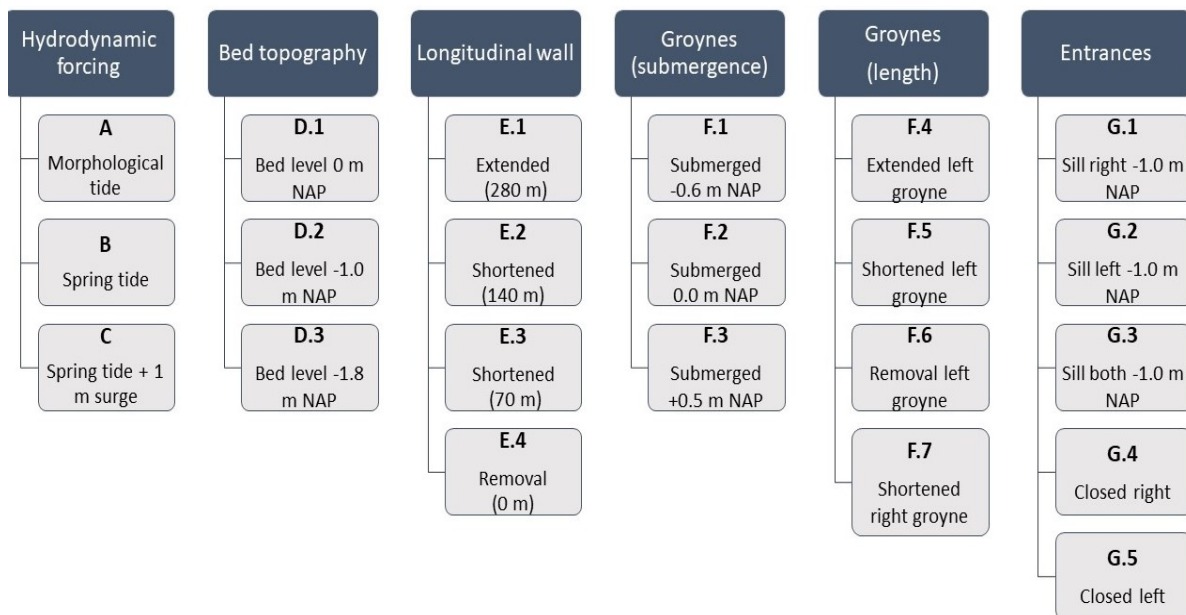


Figure 6.4: Overview of the simulations

6.2. Model set-up

In the following section the model set-up of the numerical model in Delft3D is described. This numerical model is used to answer the hypotheses formed in Chapter 3. Delft3D is a software that carries out simulations of flow, sediment transport and morphological developments Deltares (2018). Delft3D can solve both 2D (depth-averaged) and 3D flow and transport phenomena.

6.2.1. Process based model

The model is set up as a 2DH simplification of the Nieuwe Waterweg, in which the tidal park is located. The requirement for the numerical model is to include the important processes that initiate sediment transport towards the river bank. By constructing a 2DH model, the effect of the present salt wedge intruding the Nieuwe Waterweg, which affects the sediment import in the Rhine-Meuse estuary as is described by De Nijs et al. (2011), is not taken into account. For simplicity, it is assumed that the salt wedge only affects the sediment transport in the main channel and that the effect of this phenomenon on sediment transport towards the river bank can be neglected.

The Delft3D-FLOW module solves the 2D (depth-averaged) non-linear shallow water equations. These equations are derived from the 3D Navier Stokes equations under several assumptions. Two important assumptions include the Boussinesq assumption by which the fluid is seen as in-compressible, and the shallow water assumptions by which the vertical momentum equation is reduced to a hydrostatic pressure equation (Deltares, 2018). Models developed in Delft3D are nearly always stable. The time-step incorporated in the models is therefore not only depending on stability but also on the accuracy of the representation of important spatial length scales, depending on the CFL number. The CFL number is a stability number, dependent on the grid size, the velocity, and the water depth. The CFL number should not exceed a value of 10. Using a time step of 0.1 minutes, the CFL number suffices.

A large amount of data necessary for the model set-up is obtained from a model created by Deltares, the Rhine Meuse Morphological-model. This model covers the whole Rhine-Meuse estuary, see Figure 6.5. In this figure, the grid covered by the RMM-model is displayed, in combination with the grid of the developed model. The RMM-model is available both in 2- and 3-D and is used to determine the long-term effects of interventions in a certain branch, and to display the effect of the latter one on the whole system Sloff et al. (2012). The RMM-model takes various mechanisms into account, the physical modelling of the effect of the salt wedge on sediment transport, incorporation of subsoil layer information, subsoil bookkeeping, and managing the tidal boundary in the morphological river model Sloff et al. (2012). In the RMM model, the 3D effect of the salt wedge on the averaged sediment transport rates is incorporated by parametrization. This is not implemented in the constructed model. Besides, this parametrization only has a significant impact on sand transport (Sloff et al., 2012).



Figure 6.5: Grid of the RMM model indicating the location of the nested model

6.2.2. Grid and bed schematization

In Delft3D, the concept of a staggered grid is applied. This concept introduces the quantities in Delft3D, such as information on the water level and velocity components not being in the same location in the numerical grid. The water level points are defined in the center of the grid cell, the velocity points are defined at the boundaries of the grid cell and the depth is defined at the location at which grid cells intersect. This ensures that at the water level points, the velocity is unknown and vice versa. This is resolved by numerically solving the equations implicitly by the ADI method. More information is available in the Delft3D Flow manual (Deltares, 2018). In order to construct a suitable grid, the following criteria need to be fulfilled: the grid must be orthogonal and the spacing between the grid must vary smoothly. In addition, the grid should be large enough to prevent boundary disturbances from entering the area of interest. In order to resolve the horizontal circulation at the river bank, the grid size should be 10 percent of the horizontal circulation size (Deltares, 2018). Incorporating these conditions, the grid and corresponding bed topography are constructed. The bed topography in the model is constructed using available measurements by multibeam echosounders provided by Rijkswaterstaat, in combination with data from AHN in order to include the bed levels above +0.5 m NAP. Dependent on the available amount of data relative to the grid size, the data is transformed to depth values by triangular interpolation, grid cell averaging, or internal diffusion. More information on obtaining a depth file from available data can be found in the Delft3D flow manual. For morphodynamic calculations, it is important that the grid cells at the boundaries have a smooth bed topography (in both m and n direction). This in order to minimize the effect of boundary disturbances entering the domain.

The land boundaries of the computational grid are constructed using ArcGIS and thereafter implemented in RFGRID in order to construct the grid. The land boundaries, the grid, and the bed topography are displayed in Figure 6.6. The total amount of grid cells are equal to 302 and 50 in the M- and N-direction respectively. The grid is refined at the area of interest, with the area of the cell being equal to 12 x 12 m. The area of the grid cells in the surrounding areas is equal to 50 x 12 m. A smooth transition is present from fine to coarse grid cells. The bed topography near the boundaries is constant in m-direction. This results from a trial and error process during the simulations including sediment transport. These depth values deviate from the measurements at the location of the boundary but are not expected to affect the sediment transport at the river bank. The boundaries are located sufficiently far from the area of interest. In addition, the bed topography is smoothed to prevent small disturbances from being present.

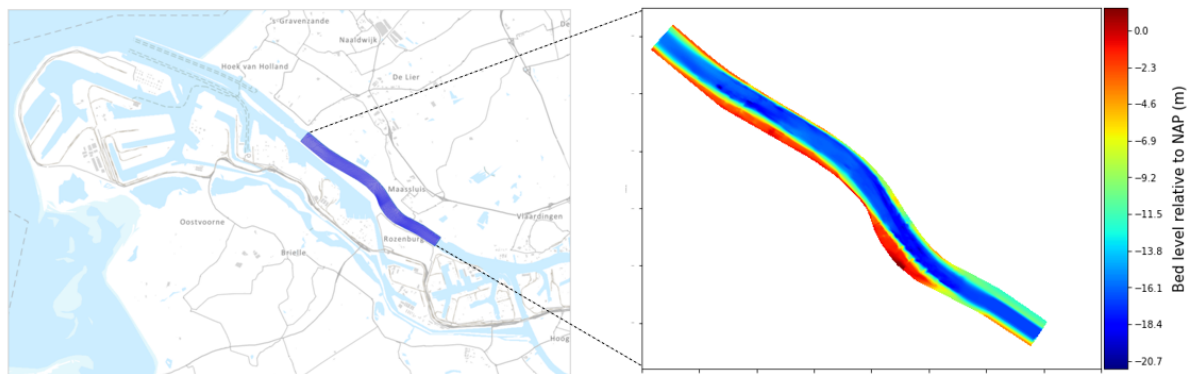


Figure 6.6: Grid and corresponding bed topography of the constructed model

6.2.3. Boundary conditions

Flow boundary conditions

At both grid boundaries, boundary conditions need to be prescribed. Several types of boundary conditions can be implemented in Delft3D: water level, velocity, Neumann, and discharge boundaries. The boundary conditions for the hydrodynamic calculations of the constructed model are obtained from the RMM-model by using the nest function of Delft3d. In Figure 6.5, both grids of the models are displayed. The hydrodynamic forcing of the RMM-model consists out of a morphological tide at the sea-side boundary of the model in combination with a constant discharge at the upstream boundary.

This discharge can be adapted to values between 1000 and 7000 m³/s. The downstream boundary is represented by a morphological tide and consists out of the M2, M4, and M6 components only. The M2 component is multiplied by 1.1 to obtain a correction for the spring-neap cycle. These conditions have been derived and validated in a previous study (Sloff et al., 2012).

Nesting can be described as the process of implementing hydrodynamic and transport boundary conditions from a larger overall model into a smaller model. This function is fully automated by Delft3D, and consists out of creating observation points in the large model at the location of the boundaries of the 'nested' model. Thereafter the hydrodynamic and transport boundaries are generated, the generated boundary conditions can only contain velocity or water level time-series (Deltares, 2018). Increasing the discharge at the upstream boundary of the RMM-model largely impacts the velocity profile. This is visualized in Figure 6.7, which displays the water level and velocity data at an observation point located at the downstream boundary of the nested model. The depth-averaged velocities are becoming more ebb dominant with increasing discharges. Which is in agreement with the described literature in Chapter 2. For obtaining the hydrodynamic transport conditions of the nested model, an upstream discharge of 1900 m³/s is implemented as the upstream boundary of the RMM-model. The yearly average discharge of the Rhine at Lobith equals about 2200 m³/s. Implementing a smaller river discharge results in a decrease in ebb dominance of the velocity profile with respect to the average discharge scenario.

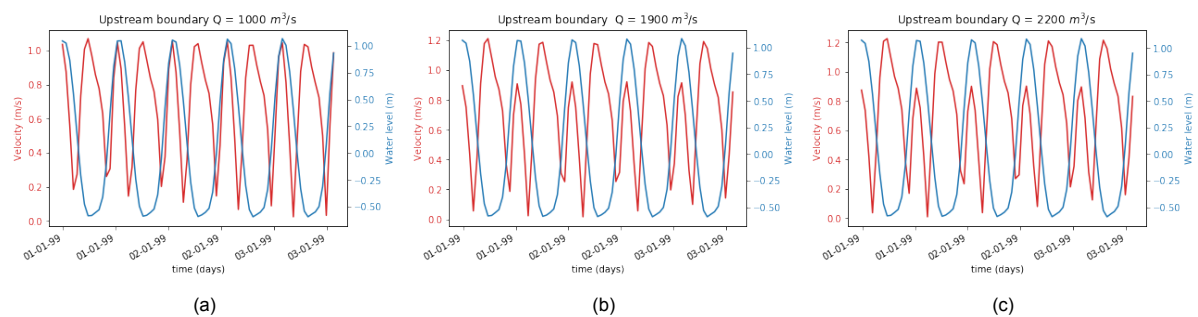


Figure 6.7: Effect of various discharges at the upstream boundary of the RMM-mode, observation point located at downstream boundary of nested model

From the nesting procedure, a water level time-series is obtained for the downstream boundary. A discharge time-series is manually obtained for the upstream boundary in order to prevent instabilities. The discharge time-series is thereafter rewritten into water-level time series. Conclusively, both boundaries of the model consist out of water-level time series resembling the situation in the RMM model. In the RMM model several domains are coupled. Therefore, it is not possible to manually adapt the downstream tidal forcing being a morphological tide into a spring-neap tidal cycle. In order to represent various hydrodynamic forcing scenarios, the water level time-series obtained from the nesting procedure are manually adapted. The hydrodynamic forcing scenarios incorporated in the model are explained in the following section.

The nested model is constructed in order to get a better understanding of the sediment dynamics on a relatively small time scale. The morphological tide is, as the name suggests, a representative boundary condition that represents the average condition for morphology (Sloff et al., 2012). Therefore, the effect of a spring tide, which is responsible for large-scale erosion and re-suspension of sediment (Allen et al., 1980), is the second hydrodynamic forcing scenario treated. The spring tide is obtained by calculating the mean water level of the time series, and thereafter using the following procedure: spring tide = (morphological water level - average) * 1.5 + average water level. The modelled spring-tide does not resemble the exact spring-tide at the location of the tidal park. From the tidal analysis executed in Chapter 3, it is obtained that the HAT and corresponding LAT were equal to +1.6 m NAP and -0.74 m NAP respectively. In the manually created spring tide, these values at the location of interest correspond to +1.54 m NAP and -0.78 m NAP respectively. Besides the effect of a spring tide, the effect of a surge on sediment transport at the area of interest is researched. This is incorporated as an additional water level rise of 1 metre, on top of the spring tide water levels. The high water levels present with a surge result in higher flow velocities, which induce more sediment transport. The three hydrodynamic boundary scenarios researched are displayed in Figure 6.8.

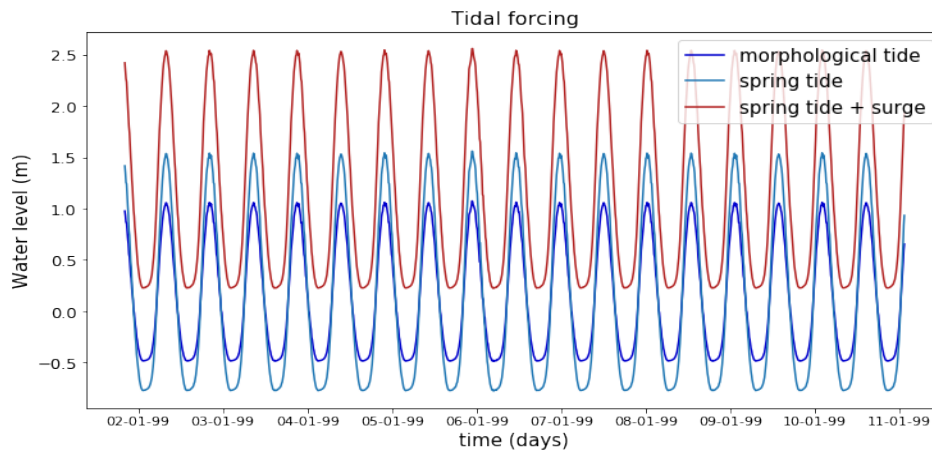


Figure 6.8: The water level elevations implemented in the model of three hydrodynamic forcing scenarios.

Transport boundary conditions

As the hydrodynamic boundary conditions are set, sediment can be added to the model. The sediment transport and morphology module supports both bed load and suspended load transport of non-cohesive sediments and suspended load of cohesive sediments. The sediment present at the Rhine-Meuse estuary consists out of both cohesive and non-cohesive sediments as is elaborated in Chapter 2. In order to get a better understanding of the differences in sediment transport between the different types of sediment into the tidal park, it is decided to model these sediment fractions separately. For the transport of non-cohesive sediment, the method of van Rijn (1993) is used. Initial conditions for the transport of non-cohesive are not required, as the sediment concentrations adapt to the equilibrium conditions very rapidly (Deltares, 2018). Concluding, it suffices to provide the model with sediment layers by which thereafter equilibrium concentrations are calculated. Cohesion is a soil property which mainly depends on the electro-chemical bond between particles (Van Rijn, 2020). Cohesive sediment is implemented in the model as being silt and thereby neglecting clay. The literature review showed that at the river banks in the Nieuwe Waterweg, the top of the bed layer mainly consists out of silt and fine sand. Therefore, it is chosen to only incorporate silt into the numerical model. The cohesive sediment transport is calculated according to the Partheniades-Krone formulations. Cohesive transport requires concentrations for the initial and boundary conditions. A lot of the sediment characteristics are implemented from the RMM-model. The diameter and the concentration of silt are not known at the area of interest. Hence, a sensitivity analysis is executed on the effect of various diameters and concentrations. These variations, in combination with the other sediment characteristics, are displayed in Table 6.1.

6.2.4. Calibration and validation

Validation is defined as the verification of model results with measured data, and the explanation of the differences and conclusions of the model performances. Calibration is defined as the comparison between measurements and computations which are thereafter used to improve the model computations (Luijendijk, 2001). The nested model is constructed using the boundary conditions of the RMM-model. This model is hydraulically verified in 2012, in which the simulations were compared to an already existing model (SOBEK-RE NB1₁). These models showed resemblances in water levels and velocities. The morphological validation of the RMM-model showed that the locations of sedimentation or erosion are correctly predicted but the magnitude deviates (Sloff et al., 2012). In this model, a representative tidal cycle is implemented (morphological tide), but it is not verified what the loss of accuracy on morphological changes are caused by this simplification. This initiated further research into this section. One should keep in mind that the RMM model is developed for erosion and sedimentation patterns on the large scale, and this research is focused on small-scale processes. More specifically, the goal is to gain insight into how sediment is transported towards the river bank, and how this transport can be affected, rather than creating a perfect resemblance of reality. Therefore, the overall morphodynamic

Table 6.1: Overview of the main model parameter settings

	Parameter	Value	Description
FLOW	t	10	Simulation time [days]
	Δt	0.1	Computational time step [min]
	ρ_w	1000	Density of water [kg/m^3]
	Roumet	W, White-Colebrook	Type of bottom friction formulation [-]
	Ccofu	0.255	Uniform bottom roughness in u-dir [m]
	Ccofv	0.255	Uniform bottom roughness in v-dir [$\text{m}^{1/2}/\text{s}$]
	Vicouv	0.5	Uniform horizontal eddy viscosity [m^2/s]
	Dicouv	0.5	Uniform horizontal eddy diffusivity [m^2/s]
	Dryflc	0.1	Threshold depth for drying and flooding [m]
Transport non-cohesive	MorFac	19.33	Morphological scale factor [-]
	MorStt	745	Spin-up interval for start of morphological changes [min]
	MorUpd	true	Update bathymetry during FLOW simulation [-]
	EqmBc	true	Equilibrium concentration profile at inflow boundaries [-]
	DensIn	false	Include effect of concentration on fluid density [-]
	D ₅₀	75/150/300	Median grain diameter [μm]
	RhoSol	2650	Specific density [kg/m^3]
	CDryB	1600	Dry bed density [kg/m^3]
	IniSedThick	15	Initial sediment layer thickness at bed [m]
	TraFrn	Vanrijn1993	Sediment transport formula [-]
Transport cohesive	MorFac	19.33	Morphological scale factor [-]
	MorStt	745	Spin-up interval for start of morphological changes [min]
	MorUpd	true	Update bathymetry during FLOW simulation [-]
	EqmBc	true	Equilibrium concentration profile at inflow boundaries [-]
	DensIn	false	Include effect of concentration on fluid density [-]
	C01	0.1 / 0.01 / 0.001	Initial concentration [kg/m^3]
	Boundary C	0.1 / 0.01 / 0.001	Boundary concentration [kg/m^3]
	RhoSol	2650	Specific density [kg/m^3]
	CDryB	500	Dry bed density [kg/m^3]
	WS0	0.15	Settling velocity fresh water [mm/s]
TraFrn	Partheniades-Krone	Sediment transport formula [-]	

performance of the RMM-model is not improved or calibrated in any way in this project. Nevertheless, the effect of a spring tide in contrary to a morphological tide on the sediment transport is treated in this research.

The hydrodynamics of the nested model represent the boundaries of the RMM-model quite well, there is however a small deviation in velocity profile at the location of interest. In the RMM-model, corresponding to a discharge of $1900 \text{ m}^3/\text{s}$, the respective flood and ebb velocities are 1.2 and 0.94 m/s. In the nested model, these velocities at the location of interest are 1.12 and 0.83 m/s respectively. This results from a difference in bed topography between the nested and the RMM-model. The bed topography of the nested model is created from measurements of multibeam echosounders in 2019, In contrary, the bed levels of RMM are obtained from measurements of the year 2009. The resulting difference is that the bed levels in the navigation channel of the nested model are on average 1.5 m lower than in the RMM-model due to dredging activities. The velocity patterns and water levels however resemble well. The obtained velocity and water level pattern also resembles the pattern obtained from measurements of Aquitec, presented in Chapter 3.

The representation of the morphological development is validated with data on bed level changes at the river banks described in Chapter 3. The calibration of several parameters is elaborated in Appendix C and contains the calibration of the bed topography, horizontal eddy diffusivity, critical shear stress and different sediment characteristics. The simulations incorporating cohesive sediment are divided into two variations, one including an erodible bed layer at the river bank and one including a non-erodible bed layer. The sensitivity analysis of cohesive sediment showed that the horizontal diffusivity and critical shear stress of the sediment implemented in the model largely affected the sediment transport. A

relatively high horizontal diffusivity ($40 \text{ m}^2/\text{s}$) was incorporated in the model. This resulted in the transport of cohesive sediment resembling the trend of bed level changes. The model is relatively sensitive to the latter, which indicates that this value should be treated carefully. Smaller values for horizontal diffusivity result in less sedimentation at the river bank. For the erodible bed layer incorporated with silt, a critical shear stress of 0.1 N/m^2 is assumed which is a common value for upper muddy layers with low strengths against erosion (Van Rijn, 2020). This is however a relatively low value for the critical shear stress of erosion for silt, and in reality, this value also varies in time and space due to consolidation processes (Van Rijn, 2020).

The simulation time of the model is 10 days, incorporating the spin-up time for morphological development and the morphological acceleration factor, the morphological run represents 6 months. Comparing the data on bed level changes with the result various runs with Delft3D incorporating a silt concentration of 0.001 kg/m^3 with different hydrodynamic forcing are visualized in Figure 6.9. The order of magnitude of sedimentation at river bank L resembles the model simulation of silt transport. Calibration of the hydrodynamics is not executed as the nesting provides stable boundary conditions.

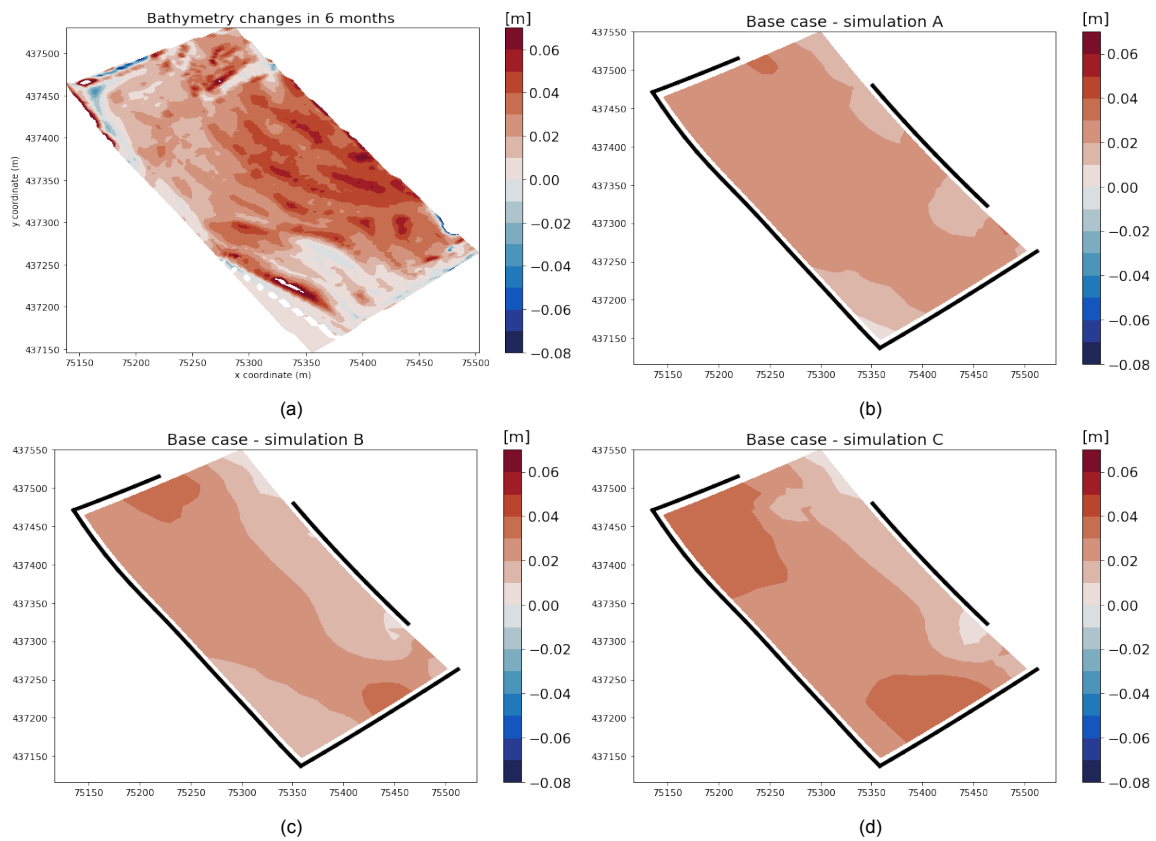


Figure 6.9: In Figure 6.9a the morphological development of the river bank is displayed after six months obtained from data. In Figure 6.9b the latter is displayed resulting from the base case scenario after six months of modelling with the calibrated model. The concentration of silt incorporated is equal to 0.001 kg/m^3 and the horizontal eddy diffusivity is set to $40 \text{ (m}^2/\text{s)}$. The critical shear stress for erosion is 0.1 N/m^2 . In Figure 6.9c and 6.9d the same is displayed but for simulation B and C respectively.

Model results of base case and varying hydrodynamic forcing

The model results of this research are separated into two chapters. In this chapter, the model results of the base case, incorporating a morphological tide, are discussed. Thereafter, the effect of varying hydrodynamic forcing on the hydro- and morphodynamics of the river bank are presented. In Chapter 8, the model results on the effect of various adaptations in the geometry of the river bank on the hydro- and morphodynamics are presented.

7.1. Base case

The tidal parks are developed between previously existing groynes in combination with newly constructed longitudinal walls parallel to the river bank. The groynes and longitudinal walls are incorporated in Delft3D as thin dams. This ensures no exchange of water and/or sediment through these grid cells. The hydrodynamic forcing scenario in the base case is a morphological tide.

7.1.1. Hydrodynamics results

In Figure 7.1, the water level and the velocity profile are displayed for the base case simulation. The tidal signal in the Nieuwe Waterweg is asymmetric, both horizontally and vertically. The tidal elevation and the tidal currents in the model with a morphodynamic tide are displayed in Figure 7.1. Slack water is a synonym for tidal flow reversal, the definition of slack water according to Bosboom and Stive (2015) is the following. The flow reversal from ebb to flood occurs around low water and is defined as low water slack, the reverse is accounted for with high water slack. The slack water periods are defined as a period of time during which the current velocities are below some threshold. From Figure 7.1 it can be obtained that the HW-slack occurs a relatively short period after high water, the LW-slack follows the low water level with a larger time difference. The periods of slack water are nearly equal.

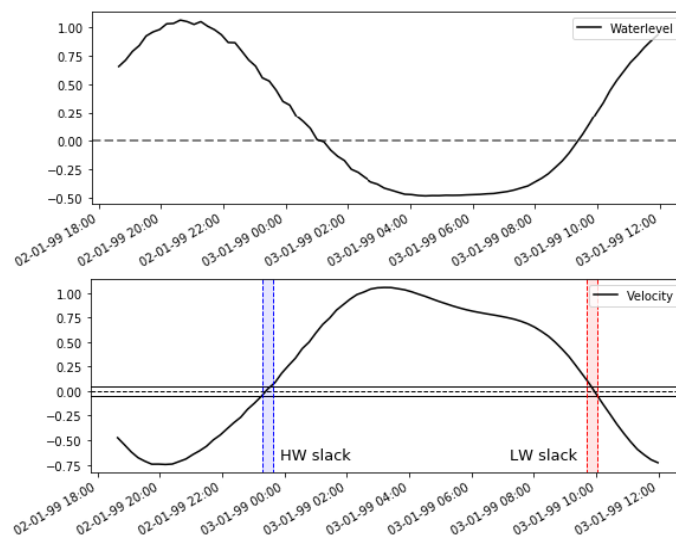


Figure 7.1: The water level (top figure) and velocity (bottom figure) in the navigation channel resulting from the base case. The slack periods are indicated with the blue and red areas indicating the high water (HW) and low water (LW) slack respectively.

The profile of the vertical tide shows that high water is further above the mean water level than low water. Also, the rise of the tide is faster than the fall of the tide. The maximum ebb and flood velocities are equal to 1.05 and -0.75 m/s respectively. The water level and velocity profile obtained by De Nijs et al. (2011) indicated that the low and high water slack periods in the Nieuwe Waterweg are almost equal. High water slack close to the bed is delayed comparing to the occurrence of high water slack high in the water column.

The effect of the hydrodynamic forcing is considered both in the navigation channel and at bank L. Four phases are considered regarding the flow pattern at the river bank, low water slack (1), flood phase (2), high water slack (3) and ebb phase (4). In Figure 7.2, velocity profiles during one tidal cycle are displayed both in the navigation channel and at the river bank (location L.2 in Figure 7.6a). Four phases of the tidal cycle are indicated by a dashed line and a corresponding number. The profile of the horizontal tide in the navigation channel obtained from the model shows many similarities with the measurements of De Nijs et al. (2011), described in Chapter 2. The velocity profile at the river bank area deviates from the velocity profile at the navigation channel. The difference in velocity profile at the river bank is explained by the small basin approach. Following this approach, it is expected that the water level immediately follows the water level outside the area of interest. This results in low and high water occurring at the same time in the entire 'small basin' (Bosboom and Stive, 2015). Theoretically, this results in velocities being zero at high and low water and the velocity profile leading the surface elevation. A similar situation is present at the tidal park, the surface elevation almost immediately follows the water levels at the navigation channel, see Figure 7.2b. During the constant period of low water, the velocity inside the groyne area is almost constantly equal to zero. When the reversal from low to high tide occurs, the velocities increase again.

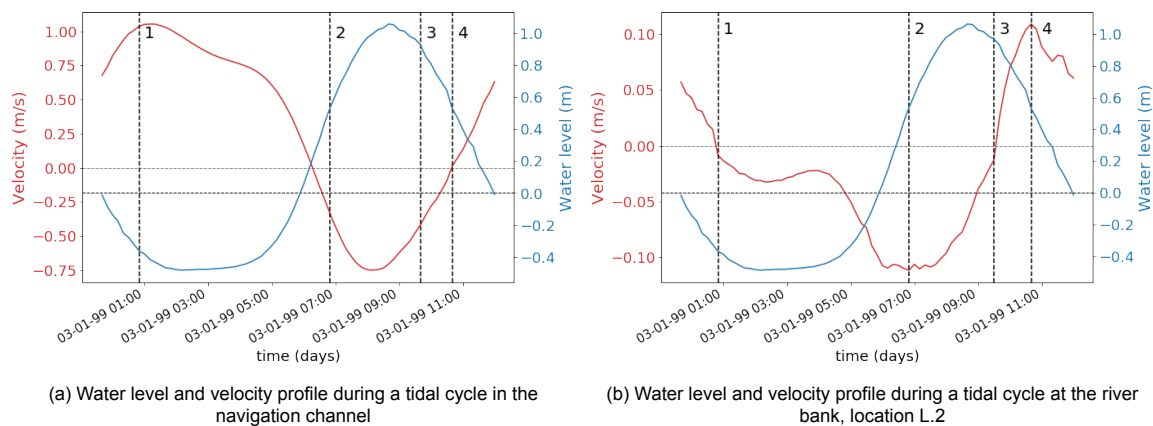


Figure 7.2: In this figure the water level elevation (blue line) in combination with the velocity (red line) is displayed. In Figure 7.2a the situation inside the navigation channel is displayed. The observation point is located in the middle of the channel just in front of river bank L. In Figure 7.2b the same is displayed but for an observation point at the river bank. The location of this observation point is displayed in Figure 7.6a, L.2. The results correspond to the base case simulation.

In Figure 7.3, a two-dimensional visualization of the flow field during four different phases in the tidal cycle is displayed. The colour bar indicates the bed level relative to NAP. Both the navigation channel and the river bank are displayed in these figures. During high and low water slack, the velocities inside the navigation channel are significant while the velocities at the river bank are almost zero. This is resulting from the small basin approach at the river bank and the velocity profile leading the water level profile inside the Rhine-Meuse estuary. Phase 1, visualizes low water slack. The velocities at the river bank are almost everywhere equal to zero with small eddies present at the entrances. Phase 2, visualizes the moment of maximum flood velocities at the river bank. This figure displays the velocities in the tidal park being significantly smaller than in the navigation channel. In Figure 7.4a, the velocity field during flood at the river bank is displayed in more detail. Phase 3, displays the situation during high water slack. The velocities at the river bank are almost equal to zero. Small eddies are present at the entrances while the velocities inside the navigation channel are relatively large. Phase 4, displays the situation in which maximum ebb velocities present. The velocities inside the navigation channel are almost equal to zero. In Figure 7.4b, the velocity field during ebb at the river bank area is displayed.

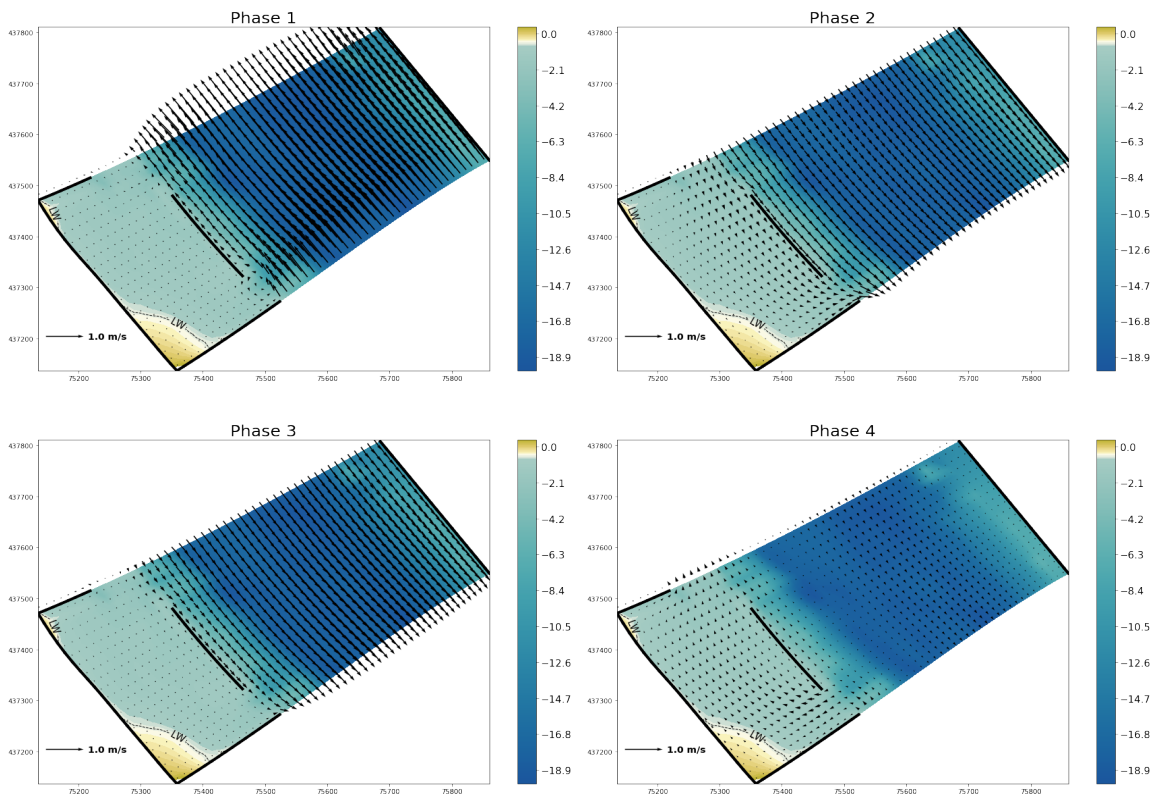


Figure 7.3: Flow field during four different phases at the navigation channel and the river bank resulting from simulation A. The time frame represented in the figures are visualized in Figure 7.2. The color bar displays the bed level elevation relative to NAP in metres. Phase 1: low water slack, phase 2: flood phase, phase 3: high water slack and phase 4: ebb phase.

In Figure 7.4, the velocity patterns inside the river bank are displayed in more detail during flood and ebb. A clear distinction can be obtained between the flow field, resulting from the geometry of the groynes and the longitudinal wall. At the west entrance, the flow can easily enter the river bank. As a result, the flow direction is in line with the flow direction inside the navigation channel. Large flow velocities are present close to the longitudinal wall. Overall, the flow is not directed towards the river bank. This is contrary to the situation present during ebb flow. As a result of the flow being contracted, the flow approaches the river bank under an angle. The direction of the flow field at the entrance is towards the landside of the river bank. The velocities present close to the landside of the river bank are larger during ebb than during flood.

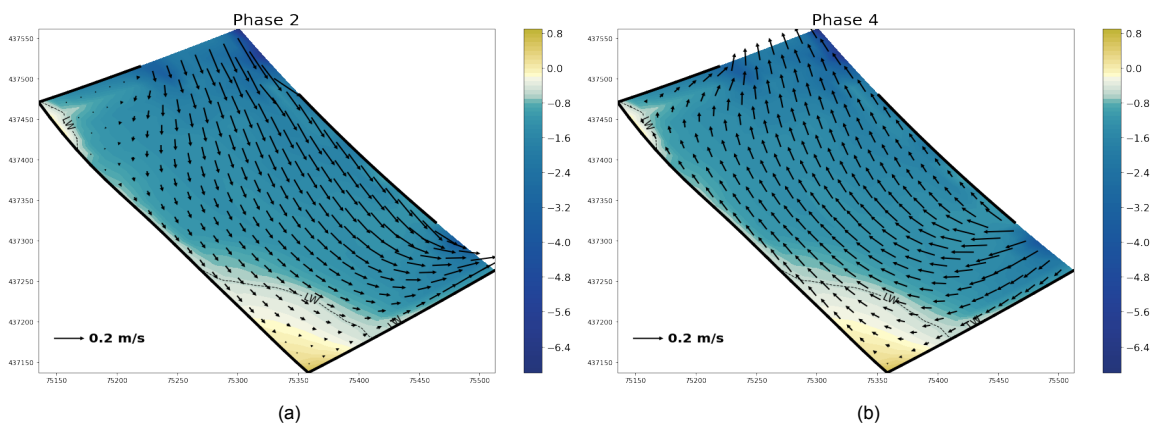


Figure 7.4: Flow field at river bank L during phase 2 (flood) and phase 4 (ebb) resulting from simulation A. The time frames in which the figures are obtained are visualized in Figure 7.2. The color bar displays the bed level relative to NAP in metres.

From literature, it was obtained that the presence of groynes ensures a certain circulation pattern at the river bank. This pattern is, among other, dependent on the length of groynes and the width between groynes. The longitudinal wall prevents the flow in the navigation channel from interacting with the flow at the river bank. Consequently, a relatively small eddy is present at the west entrance, displayed in Figure 7.5. The velocities in the circulating eddy are relatively small. Therefore the effect on the flow pattern at the river bank area is relatively small. The eddy at the west entrance is responsible for the flow at the river bank being in the opposite direction of the flow at the navigation channel.

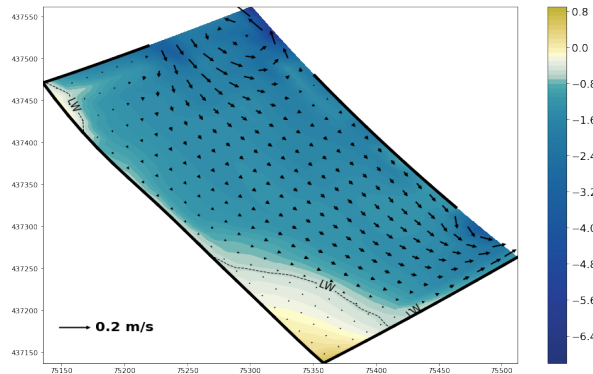


Figure 7.5: Circulation inside the river bank during the period of constant low water. At the entrances of the tidal park the eddies are clearly visible in combination with the flow being directed in the opposite direction as in the navigation channel.

In Figure 7.6 the locations of three observation points and the corresponding velocity profile obtained from simulation A are displayed. At location L.1 the velocity profile is flood dominant, the maximum flood velocity is equal to 0.25 m/s and for ebb, this equals 0.11 m/s. The opposite is accounted for at location L.3, in which the velocity profile is ebb dominant, maximum flood and ebb velocities equal 0.19 and 0.25 m/s respectively. At location L.2, located in the middle of the river bank, both the maximum flood and ebb velocities equal 0.11 m/s. The velocity profile present at observation point L.2 resembles the profile at location L.1 during flow reversal from flood to ebb. The geometry at the east entrance of the river bank ensures a flow contraction by which the flow velocity at observation point L.1 is equal to 0.25 m/s. Thereafter the magnitude of velocity quickly decreases as a result of the available flow surface and the presence of a large outlet area (west entrance).

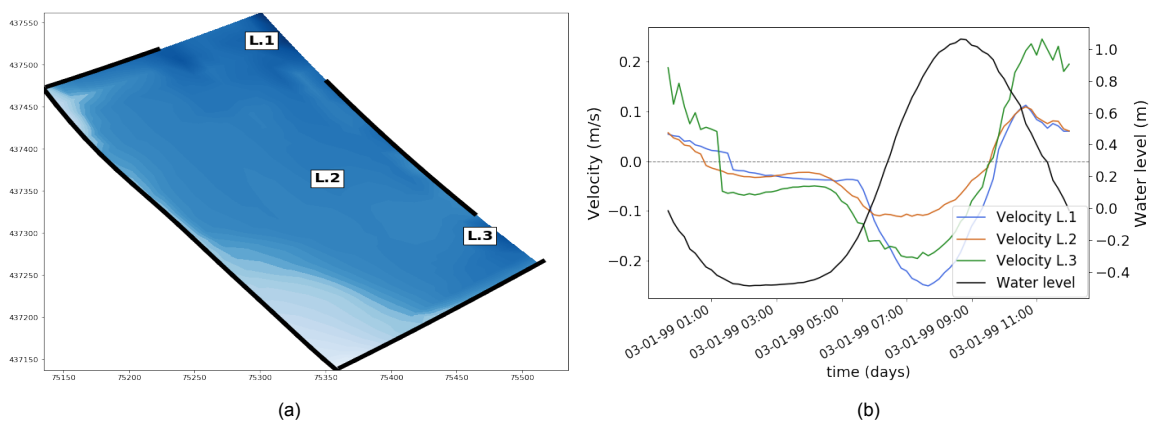


Figure 7.6: Figure 7.6a displays the location of the observation points at river bank L. Location L.1 is located closest to the sea. Figure 7.6b displays the velocity profiles at observation points displayed in Figure 7.6a resulting from simulation A.

Box plots are used to display the distribution of data sets. To gain more insight into the dynamics at the river bank, box plots are used to determine the depth-averaged velocities of the entire river bank. Three time frames are considered, a full tidal cycle, an ebb period and a flood period. The data is considered as ebb and flood period respectively if the rise or fall of the water level exceeds 0.5 centimetres per minute. In Figure 7.15c the resulting box plot is displayed for simulation A. The red diamonds indicate

the mean depth-averaged velocities of the data set considered. The magnitude in flood velocities is larger than the ebb velocities. The mean depth average velocities equal 0.055 , 0.062 and 0.078 m/s for the full tidal cycle, ebb and flood period respectively. This results in a $\frac{U_{flood}}{U_{ebb}}$ ratio of 1.26.

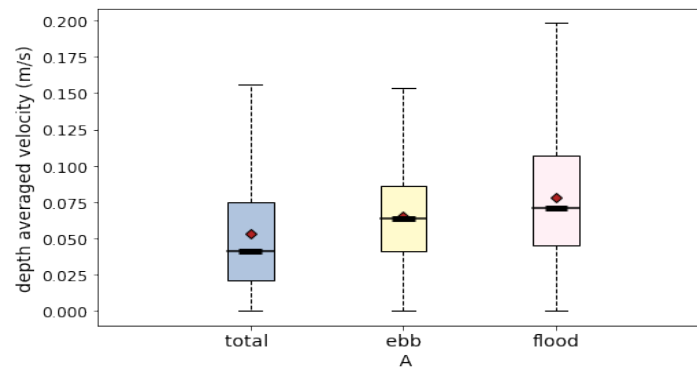


Figure 7.7: Box plot displaying the velocities at the river bank. The box plots are created for simulation A, incorporating a morphological tide. All locations inside river bank L are taken into account. The data of the box plots are created both for a full tidal cycle, an ebb period and a flood period. The data in the flood and ebb period are filtered based upon the period in which the water level rise is larger than 0.5 cm/minute

In chapter 4, the critical velocities for three sediment particles were determined. For diameters of 300, 150 and 75 μm , the critical velocities are 0.44, 0.3 and 0.2 m/s respectively. The hydrodynamic results show that the critical velocities for transport are hardly reached at the river bank. Excluding the outliers of the data sets, the velocities are not reached.

7.1.2. Morphodynamics results

The morphodynamic results of this research are separated into a section considering noncohesive sediment transport and a section considering cohesive sediment transport.

Noncohesive sediment

The transport of coarse sediment consists out of bedload transport and suspended sediment transport. The governing factors in the transport of coarse noncohesive sediment are the magnitude in relative ebb and flood flow velocities and the availability of sediment. The velocity profile at the navigation channel is ebb dominant. In Figure 7.8a the suspended sediment concentration (SSC) in combination with the velocity profile in the navigation channel in front of river bank L is displayed. The first peak represents ebb velocities and the second peak represents flood velocities. The SSC at the navigation channel is considerably higher during ebb than during flood, 37 and 9 mg/l respectively. The suspension of coarse sediment directly responds to the flow. The maximum SSC coincides with the maximum velocities. No lag effects are present. In Figure 7.8b the SSC of sand is displayed at three observation points at river bank L. The order of magnitude of the SSC at the river bank is a thousand times smaller than in the navigation channel. The maximum SSC obtained at observation point L.3 (east entrance) coincides with the maximum SSC in the navigation channel during maximum ebb velocities. At observation point L.1 (west entrance) the maximum SSC coincides with the maximum SSC in the navigation channel during maximum flood velocities. The concentration of suspended sediment quickly declines towards the river bank. At observation point L.2 no suspended sediment is observed. The amount of suspended sediment at the navigation channel is relatively high. However, the suspended sediment is not largely transported towards the river bank. This originates from multiple causes. To start with, the velocities at the river bank are not large enough to reach the critical velocity for erosion and thus suspension and transport of sediment. From the channel cross-section displayed in Chapter 3 it was observed that the transition from the navigation channel (located at around -18 m NAP) up to the start of the river bank (located at around -2 m NAP) is very steep. The sediment at the navigation channel is suspended at the bed layer and therefore the SSC are maximum close to the bed. This ensures that the suspended sediment can not easily be transported towards the river bank.

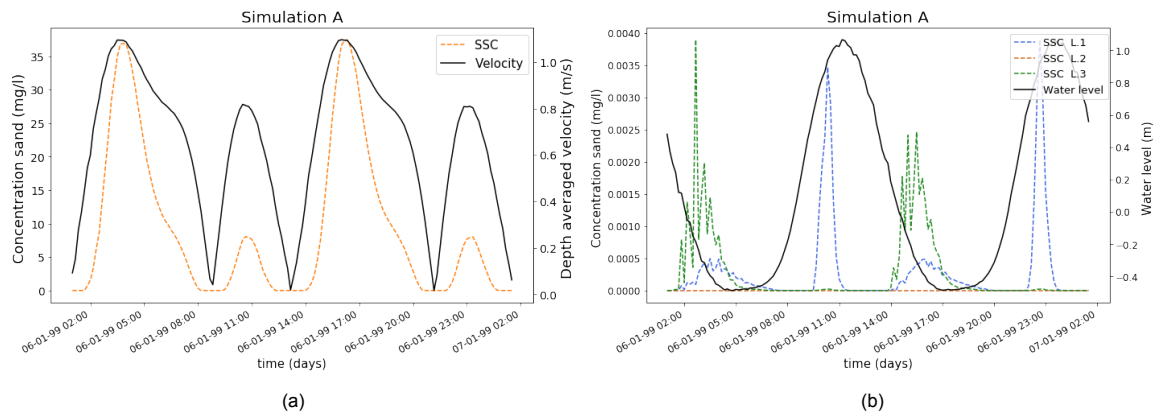


Figure 7.8: In Figure 7.8a the depth-averaged velocity and suspended sediment concentration profile in the middle of the navigation channel in front of river bank L is displayed. The initial peak in velocities corresponds to ebb velocities and the second peak corresponds to flood velocities. In Figure 7.8b the suspended sediment concentrations are displayed at three locations at the river bank, for the location it is referred to Figure 7.6a. The same period of time is displayed in both figures.

In Figure 7.17 the resulting cumulative sedimentation and erosion for three different sediment particle diameters are displayed (75, 150 and 300 μm). At the west entrance, incorporating a diameter of 75 μm , some sedimentation can be observed. A diameter of 75 μm is relatively small for sand and almost comparable with the diameters of silt. Incorporating a diameter of 150 μm in the model results in a decrease in the import of sediment compared to a diameter of 75 μm . This can be assigned to higher critical velocities for erosion by which less sediment is brought into suspension. The total import of cohesive sediment after six months of morphological modelling equals 0.5 m^3 . Erosion is observed at the west side of the longitudinal wall. Incorporating a particle diameter of 300 μm results in no sedimentation at the river bank, but a small amount of erosion is observed. More information regarding the sensitivity analysis towards different particle diameters is presented in Appendix C.

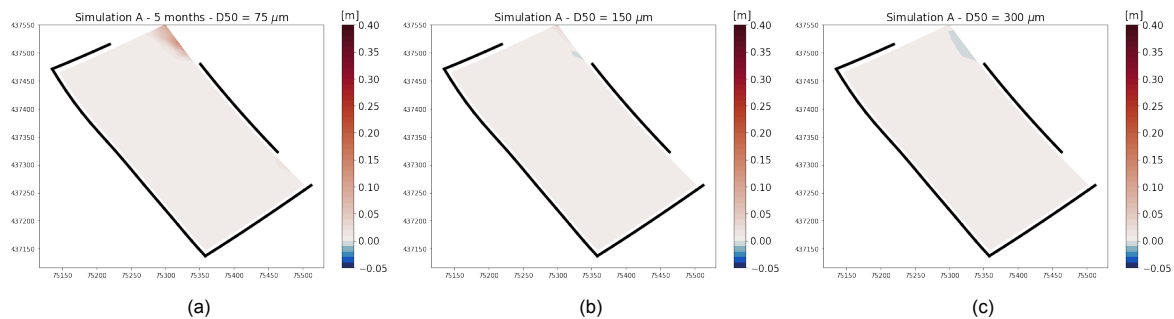


Figure 7.9: Cumulative sedimentation / erosion obtained from simulations A in combination with three gradings of sediment incorporated. The black lines in the figure indicate the locations of the longitudinal walls and groynes present at the river bank. Incorporating a diameter of 75 μm the cumulative erosion/sedimentation is displayed after a time span of 5 months. In case of the other grading the results are obtained after 6 months. In all figures the scale displayed in the color bar is the same and displays erosion or sedimentation in metres.

Cohesive sediment

In Appendix C the calibration and sensitivity analysis of the model is elaborated. This sensitivity analysis showed that the silt concentration implemented in the model only affects the magnitude of cumulative erosion and sedimentation. The sediment transport pattern did not alter. In the base case simulation a silt concentration of 0.001 kg/m^3 is incorporated and the horizontal eddy diffusivity is set to 40 (m^2/s). The critical shear stress for erosion is 0.1 N/m^2 . The transport of cohesive sediment is researched both by incorporating a non-erodible and an erodible bed layer. Information obtained from borehole drilling activities at the river banks showed that mainly sand and silt are present in the upper layer of river bank L (Schutjes and Van Leeuwen, 2013). By incorporating both an erodible and non-erodible subsoil, two extreme scenarios are simulated.

Hydrodynamic forcing largely affects the suspended sediment concentration. Tidal and neap-spring cyclic variations are dominant scales in suspended sediment dynamics (Yang et al., 2004). Cohesive sediment is mainly transported in suspension. The sediment is brought into suspension if the critical shear stress for erosion is reached. For sedimentation a high critical shear stress is implemented in the model which indicates that sedimentation occurs at all times (Winterwerp and Van Kesteren, 2004). In Figure 7.10a the SSC in combination with the depth-averaged velocity in the navigation channel is displayed for a non-erodible bed layer. The first peak represents ebb velocities and the second peak represents flood velocities. The SSC just after the maximum ebb flow is significantly higher than after flood flow. The maximum ebb velocities almost coincide with maximum silt concentrations. The maximum SSC in the flood period is lagging the peak velocity. The minimum SSC lags the moment of zero velocities. This results from lag effects. A lag effect is defined as the time scale between the particle being below a critical velocity and settlement of the particle. More information regarding lag effects can be found in Appendix A.

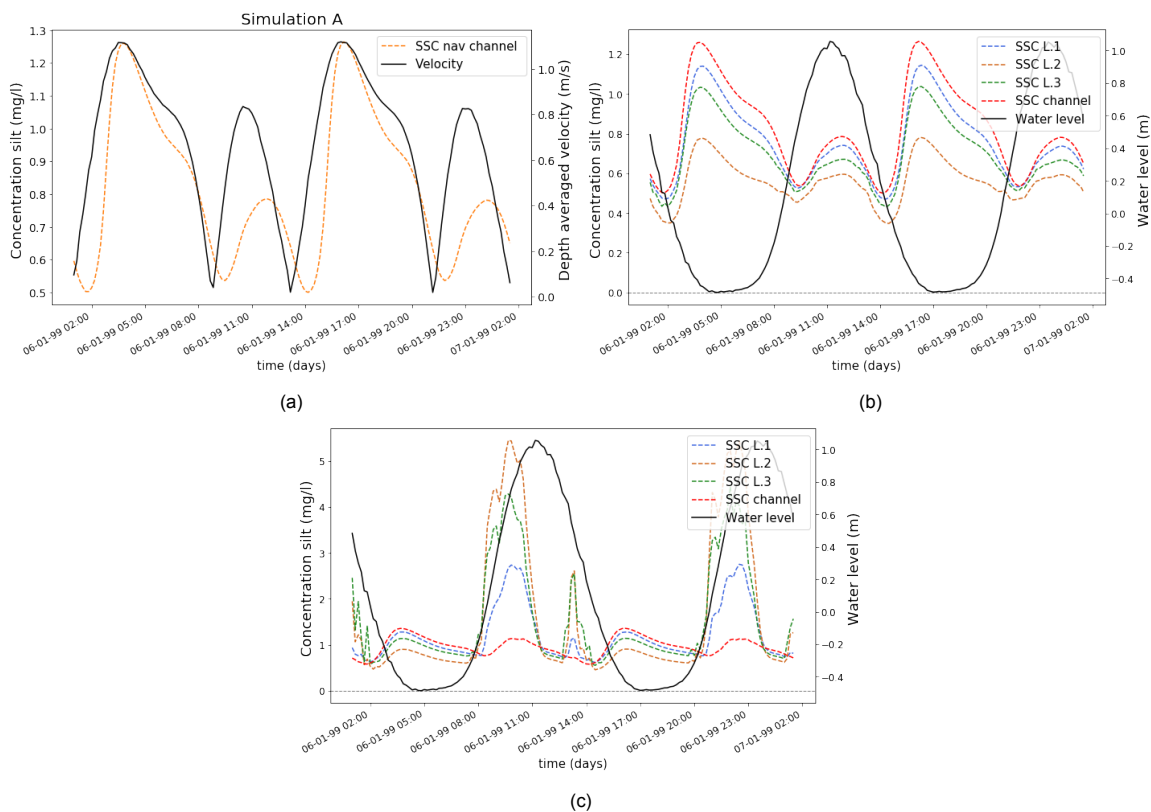


Figure 7.10: In Figure 7.10a the depth-averaged velocity and SSC profile in the middle of the navigation channel in front of river bank L is displayed incorporating a non-erodible bed layer. The initial peak in velocities corresponds to ebb velocities and the second peak corresponds to flood velocities. Figure 7.10c and 7.10b display the SSC at three observation points at the river bank (location Figure 7.6a) and at the navigation channel. The black line indicates the water level. Figure 7.10b incorporates a non-erodible bed layer and Figure 7.10c incorporates an erodible bed layer.

In Figure 7.10b the SSC at three locations at the river bank is displayed in combination with the water level variation during two tidal cycles. The flood velocities at the river bank are higher than the ebb velocities. The SSC concentration at the river bank after maximum flood velocities is lower than after maximum ebb velocities. The higher peak in concentration after maximum ebb velocities originates from the higher concentration of suspended sediment in the navigation channel. A high SSC in the navigation channel in combination with relatively small flow velocities during ebb results in large suspended sediment concentrations at the river bank. In addition, it can be obtained that the minimum suspended sediment concentration at the river bank lags the minimum velocities. Furthermore, it can be obtained that the maximum SSC lags the maximum velocities. During the period of constant low water low flow velocities (≈ 0.02 m/s) are present at the river bank. In addition, the suspended sediment concentration in the water column decreases. This can indicate the settlement of sediment particles.

However, during constant water level also eddies are visible and other flow patterns with low magnitudes. Therefore it is possible that during this time frame not all sediment is deposited but sediment is also transported into the navigation channel. From the hydrodynamic results in combination with the SSC, it is concluded that sedimentation of silt is present during ebb when the water level is constant.

In Figure 7.10c the suspended sediment concentration at the river bank is displayed incorporating an erodible bed layer. At locations with relatively high flow velocities silt is likely to erode. The erodibility of the bed layer largely affects the SSC at the river bank. Additional figures providing information on the SSC in combination with the velocity profile in both the navigation channel and observation point L.1 are provided in Appendix D in Figure D.5. The SSC profile displays three peaks. The peak in SSC during ebb with an erodible bed layer is in agreement with a non-erodible bed layer both regarding magnitude and moment in time. The other two peaks in SSC inside river bank L are governed by the suspension of the bed layer of the river bank. The peaks in concentration coincide with peaks in velocities at the river bank. The largest peaks in SSC in Figure 7.10c corresponds with the time frame of maximum flood velocities inside the river bank. The second peak thereafter corresponds with maximum ebb velocities inside the river bank. The SSC induced by erosion at the river bank overrules the SSC profile obtained incorporating a non-erodible bed layer. This also affects the time frame in which the peak in SSC occurs in the navigation channel in front of river bank L. The time frame of maximum SSC at the navigation channel during flood period corresponds with the maximum SSC at the river bank. This indicates that a large part of the suspended sediment is transported towards the navigation channel. In addition, it is observed that when incorporating an erodible bed layer, the highest concentration from three observation points is present at observation point L.2.

The mean residual transport resulting from simulation A, incorporating both a non-erodible and erodible bed layer, is displayed in Figure 7.11a and 7.11b respectively. The magnitude of mean transport in case of a non-erodible bed layer is small compared to an erodible subsoil. This is visualized in the scale of the arrow displayed in the left corner of both figures. This originates from less suspended sediment present at the river bank incorporating a non-erodible bed layer as sediment cannot be uplifted from the bed layer. The velocity profiles obtained from the hydrodynamic results are in agreement with the mean transport direction. At the east entrance, the velocities are directed towards the river bank, almost perpendicular to the east groyne. The mean transport pattern is in agreement with the latter, Figure 7.11a. At the west entrance, the flow pattern is almost in line with the flow direction at the navigation channel. However, the mean transport direction is more directed in the south-east direction. The simulation incorporating an erodible bed layer, Figure 7.11b, displays a large transport at the entrances directed towards the navigation channel. This originates from the relatively high shear stresses at these locations, leading to erosion of silt. Although the mean residual current is directed towards the navigation channel at the entrances, sediment is transported towards the river bank in the middle of the river bank.

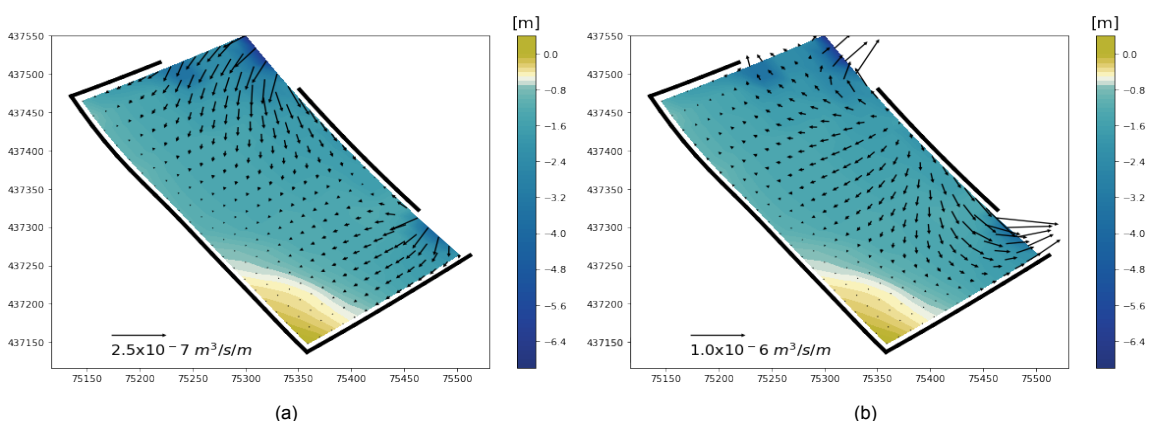


Figure 7.11: Figure displaying the mean total transport of silt at the river bank. In Figure 7.11b the subsoil is erodible and in Figure 7.11a the subsoil is non-erodible. The arrows indicate the direction of the mean transport. The scale of transport is displayed in the left bottom of the figures. Note that these scales are different. The color bar displays the bed levels in metres.

In Figure 7.12a the resulting cumulative erosion/sedimentation after six months of morphological modelling is displayed for a non-erodible bed layer. The same is displayed in Figure 7.12b for an erodible bed layer of two metres. Incorporating a non-erodible bed layer leads to no erosion at the river bank which is also visible in Figure 7.12a. Little sedimentation is present at the river bank. The magnitude of sedimentation is in agreement with what is obtained from data, see Figure 6.9. The sediment import inside the river bank resulting from a non-erodible bed layer equals 15.5 m^3 . The maximum sedimentation is present close to the groynes in the middle of the river bank. No sedimentation is visible at the southeast located corner where the intertidal area is located. At this location, no water is present in the water column during the full tidal cycle.

In Figure 7.12b the resulting sedimentation/erosion pattern is visualized incorporating an erodible bed layer. This simulation shows that a large amount of erosion is present close to the navigation channel. A small amount of sedimentation is present close to the river bank. The ratio between sedimentation and erosion present at the river bank equals 0.23. The eroded amount of sediment equals 123 m^3 and the amount of deposited sediment equals 28 m^3 . Although more suspended sediment is present in the water column, the largest amount of sediment is transported towards the navigation channel. The location of the turning point between sedimentation and erosion is in agreement with the flow pattern during maximum flood velocities, see Appendix D, Figure D.1. Again at the south corner of the river bank, the intertidal area, no sedimentation is present. In Appendix D, Figure D.6, the SSC at the south corner of river bank L is displayed incorporating an erodible subsoil. The SSC profile at the south corner almost equals the profile at observation point L.3. When no water is present at the intertidal area, the SSC concentration equals the equilibrium concentration. The results indicate that outside the time frame of constant water level not a lot of sediment is deposited. Although silt is available in the water column at the intertidal area during ebb and flood flow, according to the model results, the velocities are too high for sediment deposition.

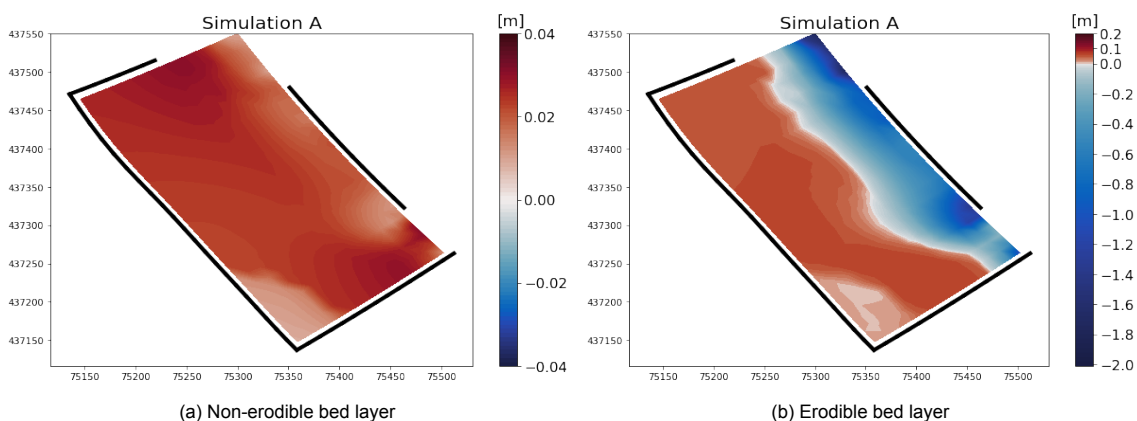


Figure 7.12: Cumulative sedimentation and erosion at river bank L after six months. In Figure 7.11a the subsoil at river bank L is modelled as being non-erodible, therefore only sedimentation is present in this Figure. In Figure 7.12b the subsoil at river bank L is modelled as being erodible. Note that the scales used in the figures are not the same.

The morphological evolution of the river bank can be displayed through hypsometric curves. The method of constructing these curves is elaborated in Chapter 5. The morphological evolution is displayed after two, four and six months for both an erodible and a non-erodible bed layer in Figure 7.13. Incorporating a non-erodible bed layer, Figure 7.13a does not display large amounts of sedimentation. When zooming in on the intertidal area, small changes in bed level elevation are visible. Sediment is mainly deposited in the area below low water (-0.48 m NAP). Below -1.0 m NAP (limit zoomed area) small increases in bed level are visible. The changes over time display a constant decrease/increase in bed level per time frame. Which indicates that a continuous process is observed. In Figure 7.13b the morphological evolution of river bank L is displayed incorporating an erodible bed layer. Erosion is present at lower bed levels. The changes over time display a constant decrease and increase in bed level per time frame. At a bed level of -1.3 m NAP , a turning point is present from erosion to sedimentation. The sedimentation present above mean low water (-0.48 m NAP) is small compared to the sediment deposition from -1.3 to -0.48 m NAP .

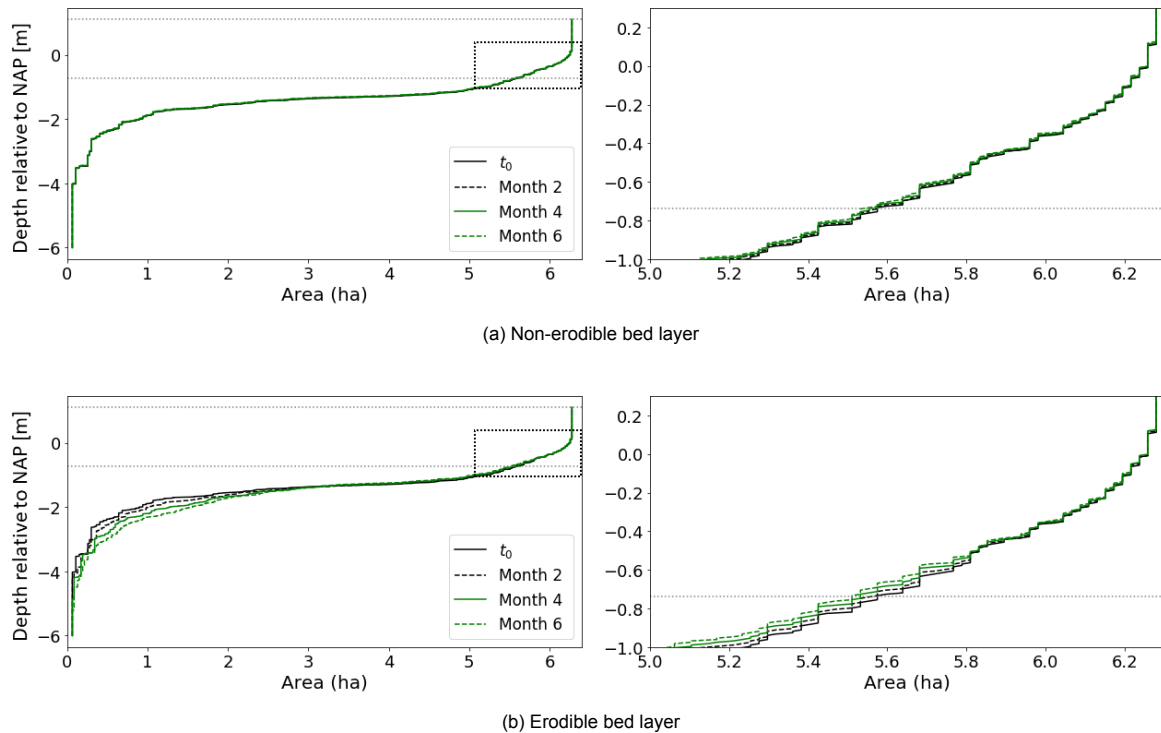


Figure 7.13: Evolution of the river bank resulting from the base case, incorporating a morphological tide. In Figure 7.13a the morphological evolution is displayed incorporating a non-erodible bed layer. In Figure 7.13b the morphological evolution of river bank L is displayed incorporating an erodible bed layer. The black dotted area indicates the shallow area (from -1.0 m NAP) of the river bank of which the hypsometric curve is visualized in the right part of the figures.

Discussion on model results

The hydrodynamic results of the base case showed that the mean depth-averaged velocities over the entire river bank equal 0.055, 0.062 and 0.078 m/s for the full tidal cycle, ebb and flood period respectively. This results in a $\frac{U_{flood}}{U_{ebb}}$ ratio of 1.26. The simulation results displayed that in a large part of the river bank the critical velocities for coarse sediment transport are not reached. Consequently, no large input of coarse sediment is present at the river bank. After six months of morphological modelling, an import of cohesive sediment of 0.5 m^3 is observed incorporating a sand diameter of $150 \mu\text{m}$.

Cohesive sediment is modelled both incorporating an erodible and non-erodible bed layer. The reason behind this simulation strategy is to display both the extreme versions to get a better view of reality, which is in between these extremes. The base case simulation showed that the incorporation of an erodible bed layer results in erosion close to the navigation channel. Besides erosion close to the navigation channel, sedimentation is observed at the river bank. The ratio between sedimentation and erosion present at the river bank equals 0.23. The eroded amount of sediment equals 123 m^3 and the amount of deposited sediment equals 28 m^3 . From this, it can be concluded that the largest part of the eroded sediment is transported into the navigation channel. Therefore, no deposition of silt is expected at the region close to the navigation channel.

The sediment import inside the river bank resulting from a non-erodible bed layer equals 15.5 m^3 . The largest amount of sedimentation is present close to the groynes in the middle of the river bank. No sedimentation is visible at the southeast located corner at the river bank. At this location, the intertidal area is located in which no water is present in the water column during the time frame of constant low water. This indicates that the period of constant low water level is responsible for the settlement of cohesive sediment, which is in agreement with the suspended sediment concentration profile.

The simulation results of the base case showed no import of cohesive sediment at the river bank. However, from borehole drilling activities at river bank L and visual observations, it is known that the latter is present at the river bank. The absence of cohesive sediment import in the model can be assigned to many reasons. The presence of waves and wind is not incorporated in the model. Although by hand calculations it is obtained that the latter result in additional shear stresses exerted on the bed layer. This can ensure the sediment being further transported into the river bank. In addition, the additional shear stresses can result in the suspension of the bed layer surrounding the river bank. Enhancement of sediment suspension close to the river bank can result in larger sediment transport towards the river bank as the source of sediment increases. Secondly, the geometry implemented in the base case model includes groynes being implemented as thin-dams which ensures no exchange of water and sediment. The literature review showed that suspended sediment can be transported over submerged groynes. Disregarding the effect of submerged groynes can account for less sedimentation of coarse sediment present at the river bank. Lastly, the base case simulation implements the geometry of the river bank present in 2019. The longitudinal wall in front of river bank L is constructed in 2018. Therefore it is likely that the sediment present at the river bank originates from the morphological evolution before the construction of the longitudinal wall.

7.2. Effect hydrodynamic forcing

In this section, the effect of different hydrodynamic forcing scenarios on the hydrodynamics and the morphodynamics at river bank L are discussed. These forcing scenarios consist of a spring tide (simulation B) and a spring tide in combination with a surge of one metre (simulation C). Initially, the effect on the hydrodynamics inside the navigation channel and the river bank are discussed. Thereafter the effect on morphodynamics is elaborated.

7.2.1. Hydrodynamic results

The base case incorporates a morphological tide, also referred to as simulation A. The effect of different boundary conditions is noticeable in both the navigation channel as well as inside the river bank. This is displayed in Figure 7.14, in which the velocity profiles are displayed with simulation B and C respectively. In simulation A, the maximum ebb and flood velocities inside the navigation channel are equal to 1.05 and -0.75 m/s respectively ($\frac{U_{flood}}{U_{ebb}} = 0.71$). When altering the tidal signal into a spring tide, simulation B, the maximum ebb and flood velocities are equal to 1.29 m/s and -1.0 m/s respectively ($\frac{U_{flood}}{U_{ebb}} = 0.77$). Incorporating a spring tide in combination with a surge, the maximum ebb and flood velocities at the navigation channel are equal to 1.34 m/s and -1.03 m/s ($\frac{U_{flood}}{U_{ebb}} = 0.77$). Both boundary conditions lead to an increase in both ebb and flood velocities relative to simulation A. In addition, a small decrease in inequality of the magnitude differences between ebb and flood flow is observed. The velocity profile is becoming more flood dominant in the navigation channel.

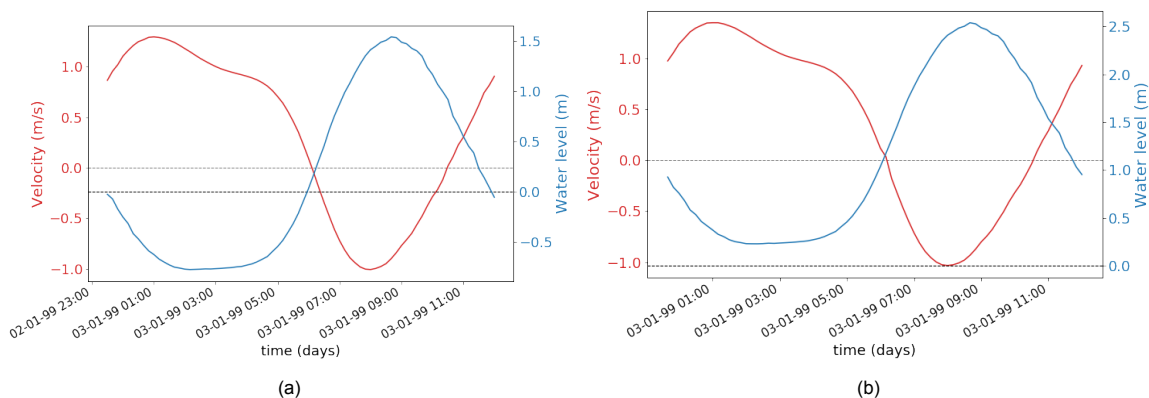


Figure 7.14: In this figure the water level elevation (blue line) in combination with the velocity (red line) is displayed. The velocity profiles are obtained in the middle of the channel just in front of river bank L. Figure 7.14a displays the situation resulting from simulation B. Figure 7.14b displays the situation resulting from simulation C.

In Figure 7.15a the velocities at location L.2 at the river bank are displayed for simulations A, B, and C. For the location of observation point L.2 it is referred to Figure 7.6a. Negative velocities are land-ward directed (flood) and positive velocities are sea-ward directed (ebb). Comparing simulation B with simulation A, it can be obtained that both the maximum ebb and flood velocities increase. The duration of the ebb period decreases and the peak in ebb velocity is shifted to the left. Besides the maximum velocity during flood, the velocity profile of simulation B is in agreement with simulation A. This indicates that the small basin approach is applicable and velocities remain the same order of magnitude during constant low water level. Comparing simulation C with simulation B, the effect of the additional surge of one metre on the velocity profile is determined. During constant low water level, the velocities at the river bank are larger compared to simulation B. This is resulting from the large change in low water elevation as incorporating an additional surge results in a low water level +0.2 m NAP. In addition, the maximum flood velocity increases and the maximum ebb velocity remains the same compared to simulation B. The ebb period is decreasing significantly inside the navigation channel comparing simulation C with simulation A. The maximum ebb and flood velocities at the river bank exactly coincide with zero velocity present inside the navigation channel in simulation C.

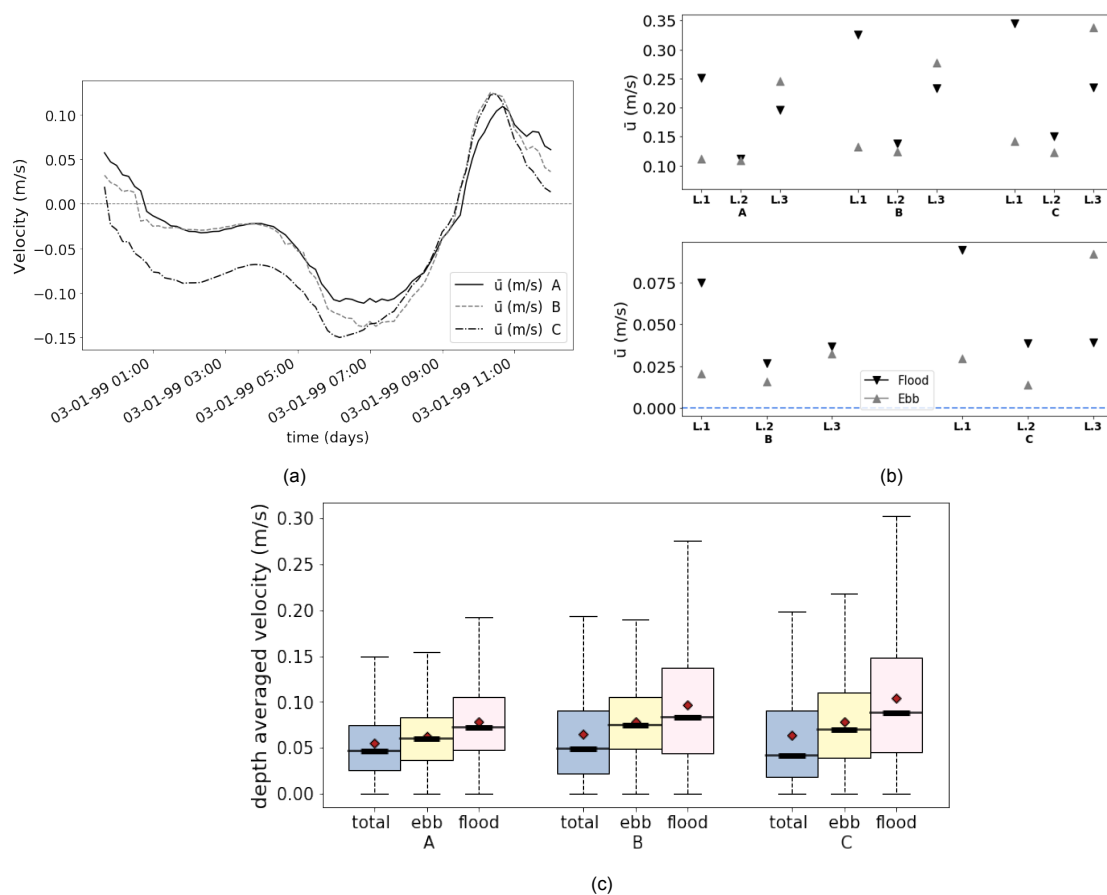


Figure 7.15: In Figure 7.15a the velocity profile at observation point L.2, in the middle of river bank L of simulations A, B, and C are displayed. Negative velocities are landward directed (flood) and positive velocities are seaward directed (ebb). In Figure 7.15b the maximum ebb and flood velocities obtained at three locations from simulations A, B and C are displayed in the top figure. The bottom figure displays the difference relative to simulation A. For the location of the observation points, it is referred to Figure 7.6a. Figure 7.15c displays the box plot on the depth-averaged velocities inside the river bank. The box plots are created for simulation A, B, and C. All locations inside river bank L are taken into account. The data of the box plots are created both for a full tidal cycle, an ebb period and a flood period. The data in the flood and ebb period are filtered based upon the period in which the water level rise is larger than 0.5 cm/minute for simulation A and larger than 0.7 cm/minute for simulation B and C. The red diamond indicates the mean of the data set and the black lines inside the box indicate the median of the data set. The coloured range indicates the 25 to 75 percentile of the data set and the dotted lines indicate the lowest and largest data point excluding outliers.

In the top of Figure 7.15b the maximum ebb and flood velocities obtained at three locations for simulations A, B and C are displayed. The black triangles indicate the maximum flood velocities and the grey triangles display the maximum ebb velocities. Similarities can be obtained both regarding the location-related ebb and flood dominance. In general, the velocities are increasing at the river bank from simulation A to C. The ebb dominance and flood dominance at the sea-ward (L.1) and land-ward (L.3) entrance respectively are visible in all three simulations. Furthermore, it can be obtained that at the sea-ward entrance the relative flood dominance is increasing from simulation A to C. The ebb dominance at the east entrance only increased incorporating an additional surge of one meter resulting from a significant increase in ebb velocities. The maximum velocities at the middle of the river bank (L.2) remain small. A relatively large increase in velocities inside the navigation channel does not largely affect the velocity profile further into the river bank. A clear ebb or flood dominance is hardly visible at observation point L.2 with simulation A. From simulation B and C, a flood dominant profile is observed at the middle of the river bank (location L.2). This is in agreement with the velocities becoming relatively more flood dominant at observation points L.1 and L.3.

In Figure 7.15c the box plot providing information on the velocities in the entire river bank during three time frames are displayed for simulation A, B and C. Resulting from simulation B, incorporating a spring tide, the mean velocity during a full tidal cycle increased from 0.055 to 0.065 m/s compared to simulation A. Both the mean velocities of ebb and flood, averaged over the river bank, increased from 0.062 to 0.078 m/s and 0.078 to 0.097 m/s respectively. The $\frac{U_{\text{flood}}}{U_{\text{ebb}}}$ ratio equals 1.23 for simulation B. Although the velocity profile inside the navigation channel has increased in flood dominance, the depth-averaged velocity profile over the river bank has become less flood dominant compared to the base case. The box plot shows that the range in velocities increased in both the ebb and flood period. Simulation C results in an increase in mean velocity during a full tidal cycle from 0.055 to 0.065 m/s compared to simulation A. Both the mean velocities of ebb and flood, averaged over the river bank, increased from 0.062 to 0.078 m/s and 0.078 to 0.101 m/s respectively. The $\frac{U_{\text{flood}}}{U_{\text{ebb}}}$ ratio equals 1.32 for simulation C. The increase in the magnitude of the ebb and flood velocities originate from the additional surge. Mean low water is present at +0.2 m NAP.

7.2.2. Morphodynamics results

Noncohesive sediment

The transport of noncohesive sediment is modelled incorporating three different diameters of sediment separately to obtain information on the possible transport of different grading of sediment into the river bank. The three variations in diameters are modelled in simulation A, B and C leading to nine simulations. The result of this sensitivity analysis is fully elaborated in Appendix C. In this section, only the key points are discussed. In Figure 7.16 the velocities present inside the navigation channel in combination with the suspended sediment concentrations of noncohesive sediment with a diameter of 150 μm are displayed. The first velocity peak represents the ebb velocities and the second peak represents the flood velocities. A relatively small change in velocity leads to a significant difference in suspended sediment concentration. The difference in SSC between ebb and flood declines as the velocity profile becomes more flood dominant in the navigation channel.

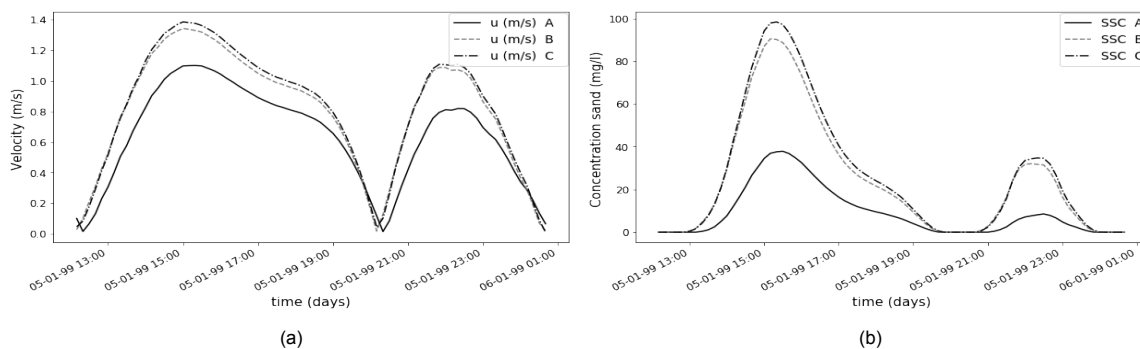


Figure 7.16: Figure 7.16a displays the velocity profile in the navigation channel in front of river bank L for simulation A,B and C. In Figure 7.16b the corresponding suspended sediment concentrations of sand (150 μm .) are displayed

In Figure 7.17 the resulting cumulative sedimentation and erosion for nine simulations are displayed. The effect of incorporating a more 'extreme' boundary condition leads to more sedimentation inside the navigation channel for diameters of 75 and 150 μm . Simulations including a larger sediment diameter resulting in a smaller distance to which the sediment transported into the river bank. From Figure 7.17 it can be obtained that an increase in hydrodynamic forcing leads to the sediment being transported further into the river bank. The velocities present at the river bank remain too small for sediment transport towards the corners of the river bank. Although the SSC in the navigation channel largely increased with increasing velocities, the sedimentation inside river bank L is not largely increasing. Noncohesive sediment in the order of 300 μm is not likely to deposit at the river bank. In addition, coarse sediment present as bed layer is also likely to erode. This is in agreement with literature, from which it is obtained that at the tips of groynes erosion pits are likely to occur resulting from flow contractions in combination with large turbulence intensities (Schierreck and Verhagen, 2016). Medium coarse sediment is only likely to enter the river bank incorporating a spring tide, as the velocities present both at the river bank and the navigation channel increase. This sensitivity analysis is in agreement with literature, as spring tide results in increased sedimentation at intertidal areas. This research shows that large input of coarse sand is not expected at the river bank.

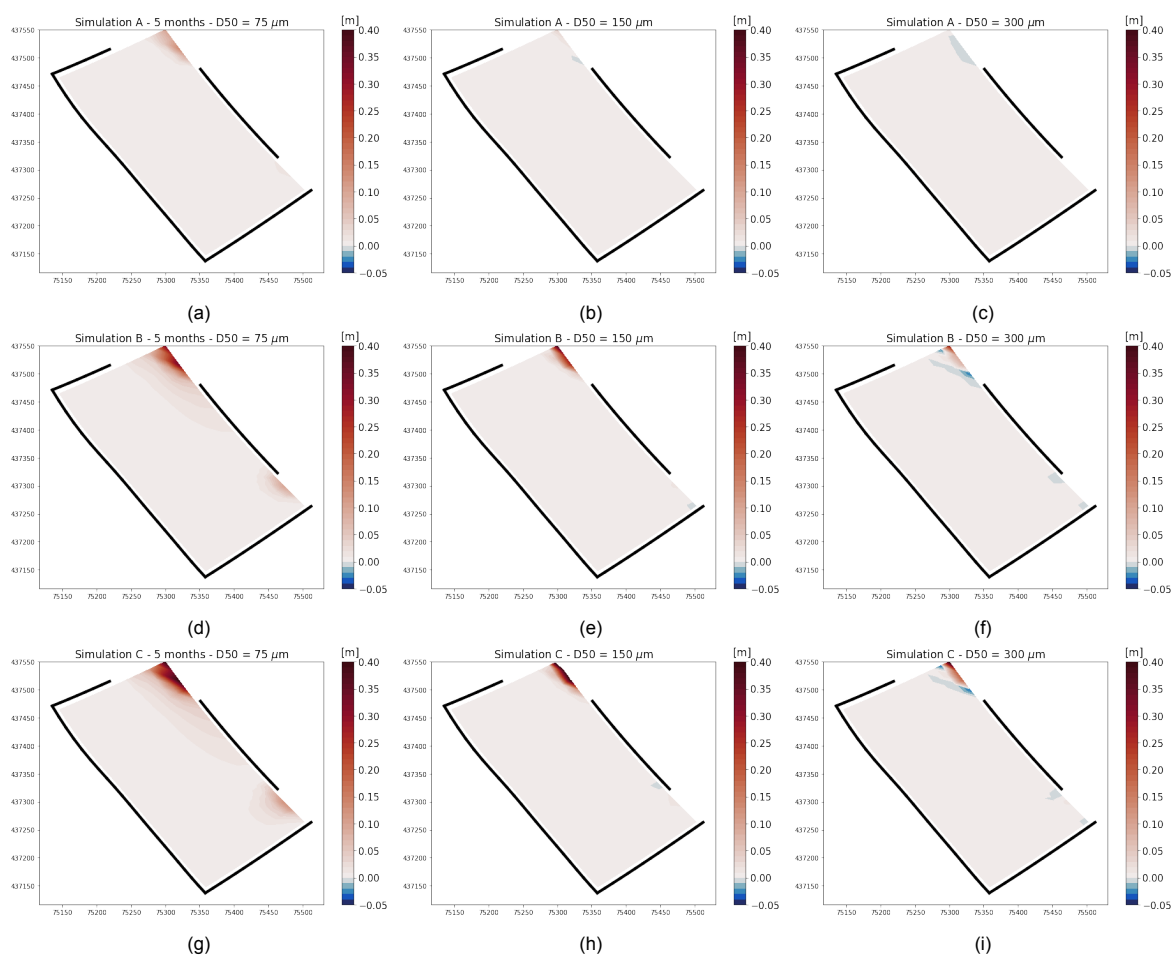


Figure 7.17: Cumulative sedimentation and erosion in metres obtained from simulations A,B and C in combination with three gradings of sediment. The black lines in the figure indicate the locations of the longitudinal walls and groynes at the river bank. For a diameter of 75 μm the cumulative erosion/sedimentation is displayed after a time span of 5 months. In case of the other grading the results are obtained after 6 months. The used scale in the color bar is equal for all figures.

Cohesive sediment

In this section, the effect of hydrodynamic forcing on the transport of cohesive sediment is discussed. In Figure 7.18 the velocities and the concentration of silt in kg/m^3 are displayed for simulations A, B and C in the navigation channel in front of river bank L. Note that the tidal cycle of simulation A is slightly

shifted towards the right in Figure 7.18. Although the incorporation of a spring tide (simulation B) or a spring tide in combination with a surge (simulation C) results in higher ebb and flood velocities at the navigation channel, only an increase in suspended sediment concentration in the flood period is visible. The SSC during ebb flow even slightly decreases. The minimum concentration in the navigation channel has increased from simulation A to B and C respectively. The change in SSC in the navigation channel results from the increasing velocities and a relatively larger tidal prism in simulations B and C. Simulation C shows the highest minimum SSC. Silt is implemented in the numerical model by imposing an initial concentration and concentrations of silt at the boundary. As a result, the effect of higher velocities and or an additional surge of one meter (simulation C) does not highly impact the SSC in the navigation channel.

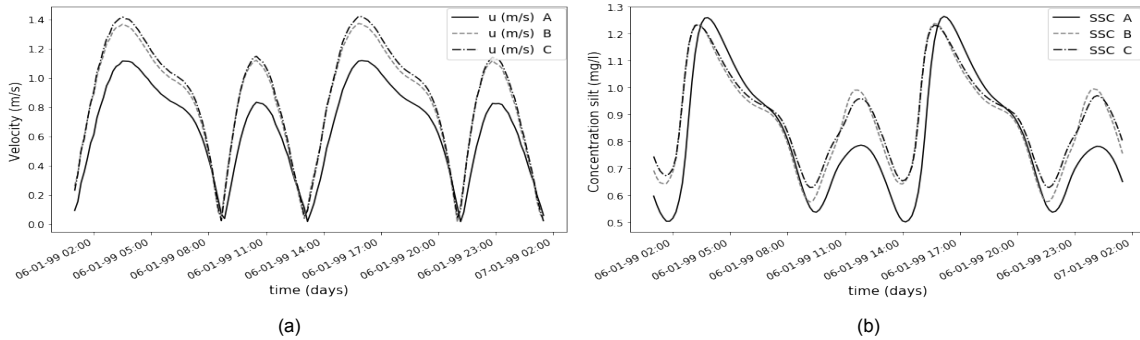
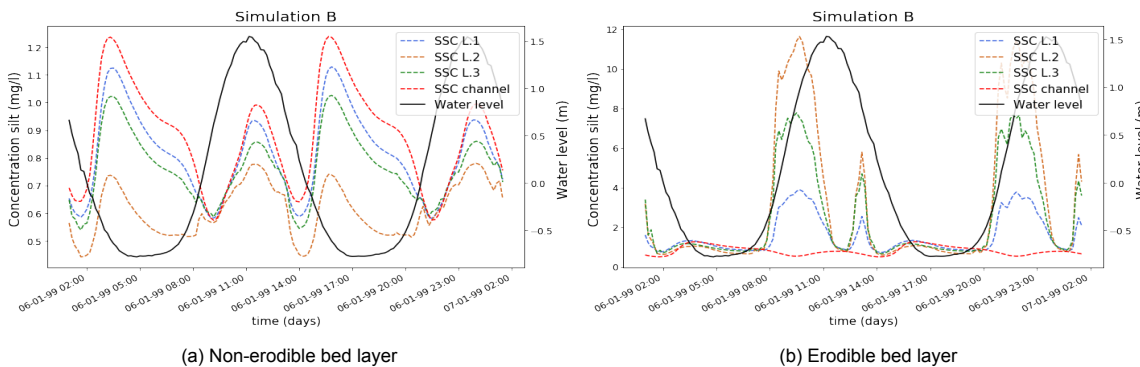


Figure 7.18: Figure 7.18a displays the depth-averaged velocity profile in the middle of the navigation channel in front of river bank L for simulation A,B and C. The initial peak of velocities are ebb velocities and the second peak represents the flood velocities. In Figure 7.18b the corresponding suspended sediment concentrations of silt are displayed. The bed layer is non-erodible.

The suspended sediment concentrations at three locations of river bank L are displayed in Figure 7.19 for simulations B and C. The SSC at the navigation channel increased during the flood period and decreased during the ebb period resulting from simulations B and C. Figure 7.19, incorporating a non-erodible bed layer, displays that the SSC profile at the river bank follows the SSC in the navigation channel. As a consequence, the SSC in the flood period increased at all locations of the river bank. In addition, the minimum concentrations at the river bank increased. Resulting from a spring tide, simulation B, a decrease is obtained in SSC during ebb, in which the largest decrease in SSC is obtained in the middle of the river bank (location L.2). Simulation B and C display almost equal SSC profiles. The additional surge results in a larger suspended sediment concentration at the middle of the river bank during ebb. This is in agreement with the hydrodynamic results, which showed that the presence of an additional surge leads to relatively higher ebb velocities. When an erodible bottom is incorporated, the peaks in SSC are correlated with the velocity profile at the river bank. Both simulations B and C showed increased magnitudes of velocities compared to simulation A. Simulation C resulted in increased velocities further into the river bank. However, the maximum velocities present at the west entrance are larger during flood resulting from simulation B compared to C. Therefore the SSC resulting from simulation B is higher, as more sediment is brought into suspension at the entrances.



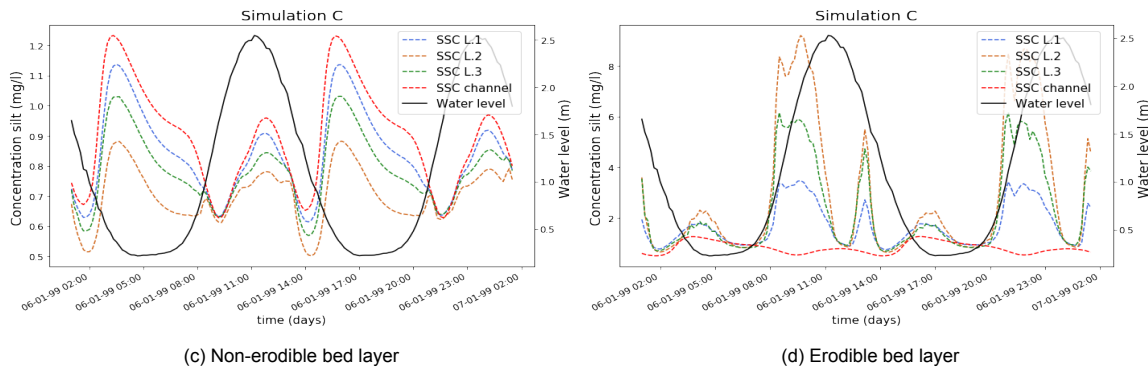


Figure 7.19: The suspended sediment concentrations of silt at three locations at river bank L obtained from simulations A,B and C. The left figures display the concentrations in combination with the water levels present at the river bank. The right figures display the SSC in combination with the depth-averaged velocity present at location L.1 (left entrance of the river bank).

The resulting cumulative erosion/sedimentation patterns for simulation B and C are displayed in Figure 7.21. The sediment budgets for simulations A, B, and C incorporating both an erodible and non-erodible bed layer are displayed in Figure 7.22. A sediment budget provides information on sediment transport on a more general level. In order to determine the sediment budget at river bank L, the river bank is split up into 8 smaller slices. The slices and their corresponding number are indicated in Figure 7.20. Number 1 up to 8 all represent a slice of the river bank, it should however be noted that the areas of the slices are not all equal. For these slices, the cumulative import/export of sediment is determined after six months of morphological modelling. Lastly, the morphological development of the river bank is displayed for simulation A, B, and C in Figure 7.23. First, the results of simulation B are discussed. Thereafter simulation C is treated.

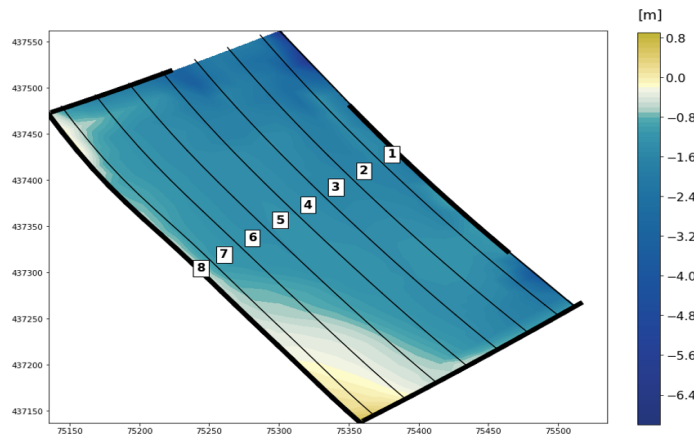


Figure 7.20: The areas displayed in which the sediment budget is obtained indicated with numbers. The sediment budget is determined by cumulative total transport over the cross-sections displayed with black lines

Simulation B

Incorporating a spring tide, simulation B, results in an equal amount of sediment import when an erodible bed layer is incorporated. A sedimentation / erosion ratio $\frac{S}{E}$ of 0.11 is observed, a ratio of 0.23 is observed for the base case simulation. This decrease in ratio originates from an increase in erosion close to the navigation channel. The total amount of eroded sediment at the river bank increased from 123 to 256 m³ compared to the base case. The presence of a spring tide increases the magnitudes of velocity present at the river bank. This results in the turning point between erosion and sedimentation being present closer to the land side of the river bank, Figure 7.21b. From Figure 7.22a it can be observed that the presence of a spring tide is responsible for large erosion present close to the navigation channel. The largest amount of eroded sediment is transported towards the navigation channel, as little additional sediment deposition is observed at area 7 and 8 (shallow area). Although a decrease in total import of silt is observed, increased import is observed at the intertidal areas. In Figure 7.23 the

morphological evolution of the river bank after six months is displayed. A large increase of erosion is present at lower bed levels compared to simulation A. In addition, sediment deposition increased from ≈ -0.56 m NAP compared to simulation A.

Incorporating a non-erodible bed layer in combination with a spring tide results in a decrease in the import of silt at the river bank compared to simulation A. The import of cohesive sediment is equal to 15.5 m^3 for simulation A. For simulation B this equals 13.9 m^3 . From Figure 7.21a it can be obtained that less silt is deposited close to the navigation channel, but silt is transported further into the river bank compared to simulation A. In Figure 7.22b the sediment budget is displayed incorporating a non-erodible bed layer. From this figure, it can be obtained that no additional import of sediment is present close to the intertidal area (area 7 and 8) compared to the base case simulation. The incorporation of a spring tide results in larger velocities present at the entrances and close to the longitudinal wall by which sediment deposition is hindered.

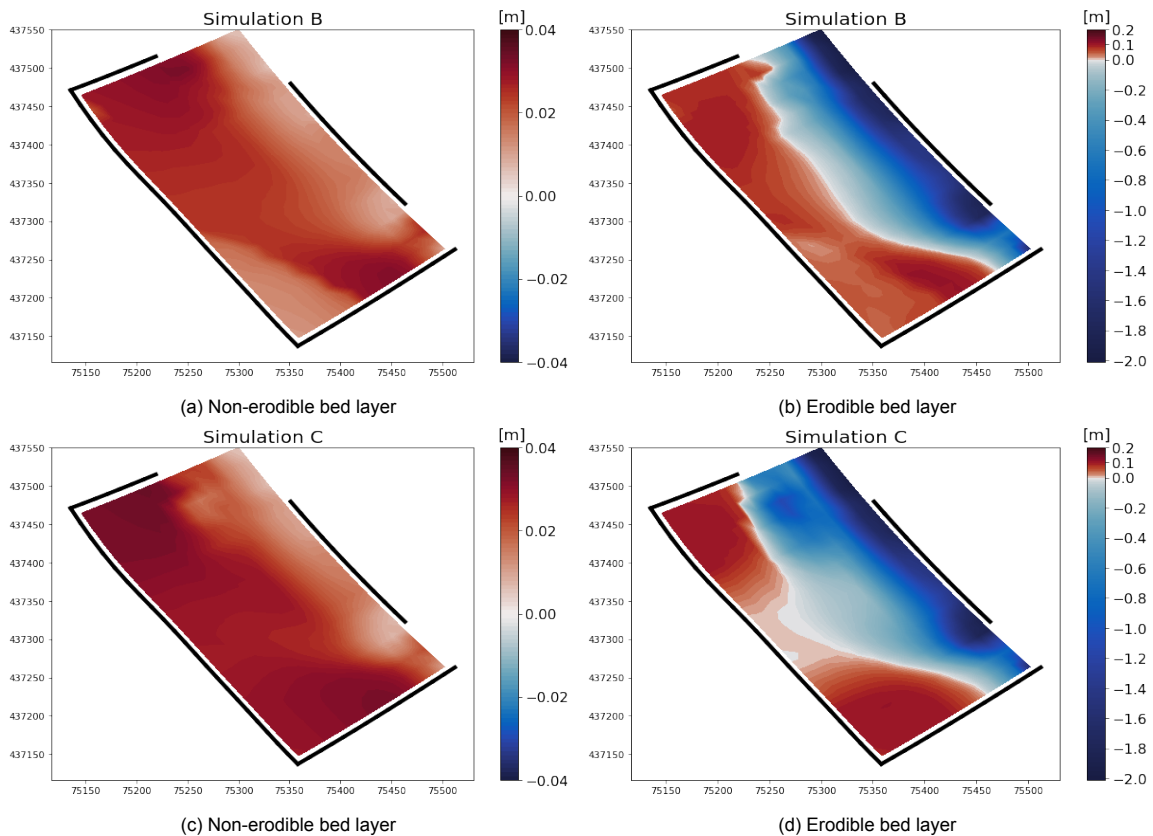


Figure 7.21: Cumulative sedimentation and erosion at river bank L after six months resulting from simulation B and C. The black lines in the figure indicate the locations of the longitudinal walls and groynes preset at the river bank. In all figures the scale displayed in the color bar is the same and displays erosion or sedimentation in metres. Note that the scale of Figure 7.21b and 7.21d is different than in Figure 7.12b in which the base case (simulation A) is displayed.

Simulation C

Incorporating a spring tide in combination with a surge, simulation C, results in a decrease in sediment import when an erodible bed layer is implemented compared to the base case. A sedimentation / erosion ratio $\frac{S}{E}$ of 0.06 is observed. The amount of erosion present at the river bank increased from 123 to 270 m^3 compared to the base case. The amount of sedimentation decreased from 28 to 17 m^3 . A spring tide in combination with a surge additionally increases the magnitude of velocity present at the river bank compared to simulation B. In addition, a higher magnitude of velocity is present over a larger surface area compared to simulation B and A, see Figure D.3 and D.4 (Appendix D, Section D.1). This results in the turning point between erosion and sedimentation being present closer to the land side of the river bank. The turning point almost coincides with the land-side in the middle of the river

bank, Figure 7.21d. This is in agreement with the observed bed topography present at the river bank. In Figure 7.22a the sediment budget is displayed for simulation C incorporating an erodible bed layer. From this, it can directly be obtained that erosion is present over a larger surface area compared to simulation A and B. The increased amount of eroded sediment is transported towards the navigation channel. No large increase in sedimentation is present at area 7 and 8 (shallow area). In Figure 7.23 the morphological evolution after six months of morphological modelling is displayed for simulation C. An increase in sedimentation is observed in bed levels above -0.48 m NAP bed level elevation compared to simulation A and B. The presence of a surge is responsible for additional sediment deposition in the intertidal area present at the corners of the river bank.

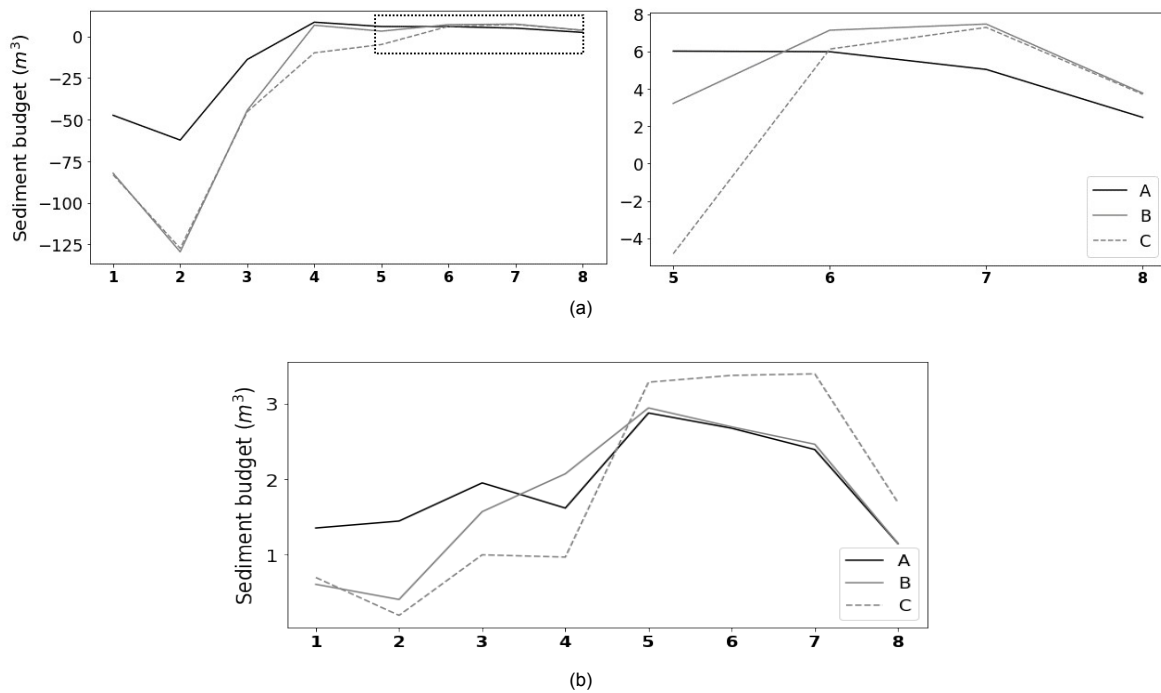


Figure 7.22: Figures displaying the sediment budget after six months of morphological modelling. The simulations in this figure incorporate a difference in hydrodynamic forcing. A represents the morphological tide, B represents a spring tide and C a spring tide in combination with one meter surge. Negative values indicate export of sediment (erosion) and positive values indicate import of sediment (sedimentation). The sediment layer present at the river bank is erodible for Figure 7.22a. In the left part of Figure 7.22a the sediment budget for the entire river bank is displayed, from 1 to 8. The black dotted area indicates the shallow area of the river bank of which the sediment budget is visualized in the right part of Figure 7.22a. In Figure 7.22b the sediment budget is visualized resulting from a non-erodible bed layer at the river bank. Only positive values are present in the y-axis as no erosion can occur. Note that the areas indicated by number are not equally sized.

Incorporating a non-erodible bed layer results in combination with a spring tide and surge in a decrease in import of silt at the river bank compared to simulation A. The import of cohesive sediment is equal to $14.6 m^3$ for simulation C. Less silt is deposited close to the navigation channel compared to simulation A. In addition, sediment is transported further into the river bank, towards the landside. The model results of simulation A displayed no sedimentation at the southeast corner of the river bank. This is contrary to what is observed from simulation C. This can be assigned towards the increase of mean low water to $+0.2$ m NAP. During the period of constant low water, in which cohesive settlement is observed, water is present in the water column at the southeast corner.

In Figure 7.24 several parameters regarding the hydrodynamics and morphodynamics present at river bank L are displayed resulting from different hydrodynamic boundary conditions.

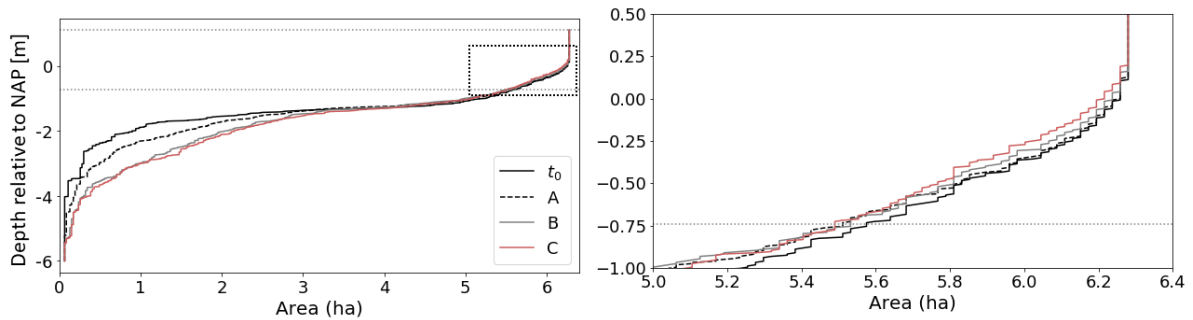


Figure 7.23: In the left part of the figure the resulting morphological evolution is displayed after six months for variations in hydrodynamic forcing (simulation A,B and C). The black dotted area indicates the shallow area (from - 1.0 m NAP) of the river bank of which the hypsometric curve is visualized in the right part of the figure.

	A	B	C
\bar{u} (m/s)	0.055	0.064	0.064
$\frac{u_{flood}}{u_{ebb}}$	1.26	1.23	1.32
S non cohesive (m ³)	0.5	6.5	10.9
E cohesive erodible (m ³)	123	256	271
S cohesive erodible (m ³)	28	28	17
S/E cohesive erodible (-)	0.23	0.11	0.06
S cohesive non erodible (m ³)	15.5	13.9	14.6

Figure 7.24: Table displaying the effect of changes in hydrodynamic forcing on several parameters regarding the hydrodynamics and morphodynamics present at river bank L. \bar{u} represents the mean depth-averaged velocity over a full tidal cycle at the river bank. The $\frac{u_{flood}}{u_{ebb}}$ ratio provides information on the relative ebb and flood dominance of the velocity signal at the river bank. The third parameter represents the sediment input of noncohesive sediment incorporating a diameter of 150 μm . The fourth and fifth parameter represents the eroded and deposited sediment respectively for an erodible bed layer. The sixth parameter, S/E, represents the ratio between sedimentation and erosion present at the river bank incorporating an erodible bed layer. The last parameter represents the sediment input of cohesive sediment incorporating a non-erodible bed layer

Discussion on model results

To conclude this section, the sub-question displayed below is answered. First, the effects on the hydrodynamics are discussed and thereafter morphodynamics of noncohesive and cohesive sediment is treated.

How do changes in the hydrodynamics affect the morphodynamics in the tidal parks according to the developed model?

The hydrodynamic results of the base case (morphological tide) showed that mean depth average velocities for the entire river bank equal 0.055, 0.062 and 0.078 m/s for the full tidal cycle, ebb and flood period respectively. The velocity profile inside the river bank is flood dominant ($\frac{u_{flood}}{u_{ebb}} = 1.26$). This originates from the geometry present at the river bank as the velocity profile inside the navigation channel is ebb dominant. From the model results, it is obtained that the incorporation of a spring tide or a spring tide in combination with a surge increases the dynamics present at the river bank. Incorporating

a spring tide results in an increase in mean velocity from 0.055 to 0.065 m/s compared to simulation A. The velocity profile at the river bank has become less flood dominant ($\frac{U_{flood}}{U_{ebb}} = 1.23$), although the velocity profile in the navigation channel has increased in flood dominance. Increase in $\frac{U_{flood}}{U_{ebb}}$ from 0.71 to 0.77 compared to the morphological tide. The increase in the magnitude of the mean velocity originates from an increase in the magnitude of velocity at the entrances. As a result, higher velocities are present over a large part of the river bank. The presence of an additional surge to the spring tide does not result in an additional rise of the depth-averaged mean velocity for the entire river bank. An additional increase in magnitude of the flood velocities inside the river bank is observed as a result of the additional surge ($\frac{U_{flood}}{U_{ebb}} = 1.32$). The increase in the magnitude of the flood velocities originates from the larger volume of water present in the water column.

The increase in dynamics at the river bank, mainly the increase in velocity present at the west entrance, is responsible for enhanced sedimentation of coarse sediment towards the river bank. Although the transport of coarse sediment into the river bank increases with increasing hydrodynamic forcing and smaller grain sizes, large input of noncohesive sediment is not observed. Incorporating a grain diameter of 150 μm , the total import of cohesive sediment after six months of morphological modelling equals 0.5 m^3 incorporating a morphological tide. The import is equal to 6.5 and 10.9 m^3 resulting from a spring tide and an additional surge of one metre respectively. The input of noncohesive sediment is only visible at low bed levels (close to the entrance). This originates from the critical velocities for sediment transport not being reached inside the river bank ($u_* : 0.2 - 0.44\text{m/s}$).

Cohesive sediment is transported further into the river bank resulting from an increase in hydrodynamic forcing. The incorporation of a spring tide results in additional sediment deposition at the intertidal area from ≈ -0.56 m NAP. The presence of an additional surge of one metre is responsible for additional sediment deposition in the intertidal area present at the corners of the river bank, above -0.48 m NAP.

The simulation results showed that the coarse sediment is not likely to deposit inside the river bank resulting from additional hydrodynamic forcing. The same discussion point holds for the base case simulation, the absence of waves and wind incorporated in the model. These effects will result in additional shear stresses on the bed layer by which sediment is brought into suspension. From the hydrodynamic results, it is obtained that an increase in hydrodynamic forcing in the navigation channel leads to increased dynamics at the river bank. Higher flow velocities are observed. The additional stresses resulting from wave action, in combination with the shear stresses from the simulation results, are therefore expected to be large enough for initiation of sediment transport towards the river bank.

An estuary is a dynamic system in which the spring-neap tidal cycle in combination with varying fresh-water discharge is responsible for constantly changing dynamics. In this research, the effect of a constant spring tide and a constant spring tide in combination with an additional surge of one metre is researched. The time series for the spring tide is constructed by manually adapting the boundary conditions in the developed model. From the tidal analysis executed in Chapter 3, it was obtained that the HAT and corresponding LAT were equal to +1.6 NAP and -0.74 NAP respectively. In the manually created spring tide, these values at the location of interest correspond to +1.54 NAP and -0.78 NAP respectively. This induces deviations in the velocity profile obtained from the simulation results in comparison with what would be present during a spring tide in reality. In simulation C, an additional water level of one metre is added to the hydrodynamic boundary conditions. A constant forcing leads to the system being less dynamic. The results obtained from this research show the effect of the presence of a constant spring tide over a large time frame. From these results, the effect of a spring tide, or a spring tide in combination with a surge on the sediment transport at the river bank can be determined. However, they do not represent the dynamic spring-neap tidal cycle in which constantly changing water level and velocity profiles are visible.

Model results of effects of human interventions

In the previous chapter, the sediment transport towards the river bank resulting from different hydrodynamic forcing scenarios is discussed. In this chapter, the effect of various adaptations in geometry on the sediment transport towards the river bank is researched. The results of the numerical model both regarding the hydrodynamics and morphodynamics are elaborated per adaptation in separate sections. The sections are concluded by evaluating and discussing the proposed hypotheses in Chapter 6.

8.1. Varying bed topography

The effect of a different bed topography both affects the magnitude and pattern of the flow inside the river bank, and consequently impacts the sediment transport. Three simulations are executed, incorporating a constant bed level of 0 m NAP (simulation D.1), -1.0 m NAP (simulation D.2), and -1.8 m NAP (simulation D.3). The last simulation is almost similar to the bed topography of the base case, but the shallow area close to the shore is not incorporated. The change in bed topography is visualized in Figure 8.1. The resulting bed topography inside the river bank is presented in Appendix D, Figures D.7, D.8 and D.9.

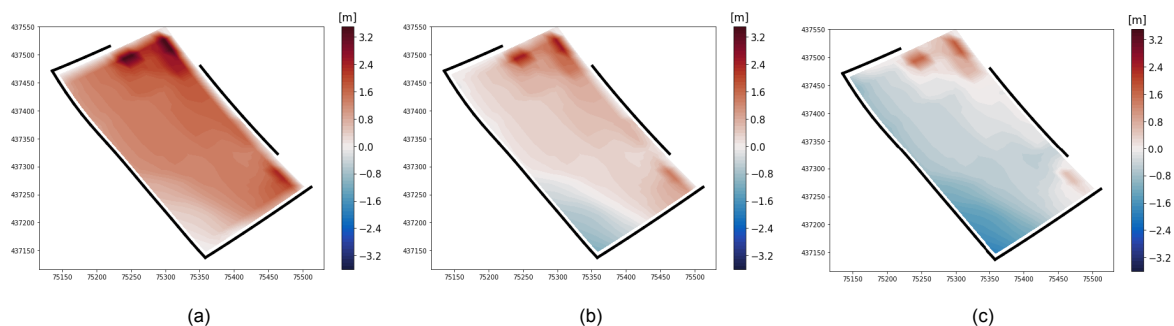


Figure 8.1: Relative increase or decrease in bed level with respect to the base case bed topography. Positive values, displayed in red in the color bar, represents an increase in bed level relative to the base case. Negative values, displayed in blue in the color bar, represents a decrease in bed level relative to the base case. The color bar indicates the change in bed topography in meters. Figure 8.1a, 8.1b, and 8.1c represent simulation D.1, D.2 and D.3 respectively.

Hydrodynamic results

The computed hydrodynamics inside the river bank resulting from simulation A, D.1, D.2 and D.3 are displayed in Figure 8.2. In Figure 8.2a the changes in 1D velocity profile are displayed at observation point L.2. In Figure 8.2b the maximum ebb and flood velocities are indicated, obtained from three observation points at river bank L. In Figure 8.2c, a box plot is displayed which is constructed based on data on the depth-averaged velocities in the entire river bank. Additional figures on the flow pattern during both ebb and flood, in combination with the changes in magnitude and direction of the flow of the simulations relative to base case simulation A can be found in Appendix D, Figures D.7, D.8 and D.9.

Simulation D1

Incorporating a bed level of 0.0 m relative to NAP in the entire river bank ensures that during a large period of time (≈ 6 hours) no water is present in the water column. This can also be obtained from Figure 8.2a, as zero velocities are present during this time frame. In addition, the velocity profile shows a decrease in magnitude of velocities during the full tidal cycle compared to the base case. Besides,

from Figure 8.2b it can be obtained that at all locations the velocity decreased. In addition, a distinct decrease in velocity is present over the entire river bank, see Figure 8.2c. The largest decrease in velocity present in the box plot is during the flood period. The time frames for both ebb and flood are determined based on a relative increase or decrease of 0.5 cm/minute. In terms of the flood period, the time frame includes a small period of time in which zero velocities are present resulting from zero water depth. As a result, the observed decrease in velocity in the flood period is larger than during the ebb period compared to simulation A. The mean velocities of ebb and flood averaged over the entire river bank decreased from 0.062 to 0.039 m/s and 0.078 to 0.035 m/s respectively. The mean velocity over the entire river bank, for a full tidal cycle, decreased from 0.055 to 0.028 m/s. The relatively large decrease in the magnitude of velocity compared to simulation A can be assigned to the larger effect of friction on the flow resulting from smaller water depths. Simulation A, incorporating the bed topography present in 2019, results in a tidal prism of 100 000 m³ incorporating the mean tidal range (-0.52 to +1.09 m NAP). A constant bed level of 0 m NAP significantly decreases the tidal prism to 73 000 m³. The bed levels close to the groynes and thin dams are lower than the assigned constant bed level. This ensures a larger flow towards the northwest corner of the river bank and an increase in magnitude at this location relative to simulation A during flood. The 2D flow pattern at the river bank is not largely affected by a change in bed topography, only the magnitude is largely affected.

Simulation D2

Incorporating a bed level of -1.0 m relative to NAP in the entire river bank ensures a decrease in velocity of the full tidal cycle at observation point L.2, Figure 8.2a. Besides, from Figure 8.2b it can be obtained that at all locations L.1 and L.2 the velocity decreased, disregarding observation point L.1 (sea-ward entrance). At observation point L.1 an increase in velocity is obtained, this can be assigned towards an increase in the tidal prism. The tidal prism increased from 100 000 m³ in the base case towards 101 000 m³, incorporating the mean tidal range (-0.52 to +1.09 m NAP). This results from no intertidal area being present at the river bank incorporating a constant bed level of -1.0 m NAP. A decrease in velocity is present over the entire river bank, as can be obtained from Figure 8.2c, the third column (D.2). The mean velocity during a full tidal cycle decreased from 0.055 to 0.051 m/s compared to the base case simulation. The decrease in magnitude is assigned to increased frictional effects on the flow resulting from the shallow water depth. Figure 8.1b displays the relatively large increase in initial bed level from simulation A to D.2. The mean velocities of ebb and flood averaged over the entire river bank decreased from 0.062 to 0.058 m/s and 0.078 to 0.073 m/s respectively. No significant differences in flow patterns are observed relative to simulation A. Small changes in flow direction can be observed at the river bank. During flood, the flow is slightly more directed away from the land boundary of the river bank (eastwards) compared to the base case. During maximum ebb velocities, the flow is altered in direction towards the west, the land boundary of the river bank.

Simulation D3

Incorporating a bed level of -1.8 m relative to NAP at the entire river bank results in the velocity profile at observation point L.2 being almost equal to the base case, see Figure 8.2a. A decrease of 0.015 m/s is observed during the ebb period. From Figure 8.2b it can be obtained that the maximum velocities during both ebb and flood increased at observation point L.1, this increase equals 0.02 m/s. From Figure 8.1c it is observed that a large decrease in initial bed level is observed from simulation A to D.3. The same increase in tidal prism is observed as in simulation D.2. This, in combination with the larger water depths, accounts for the increase in velocity observed at observation point L.1. The mean velocities at the river bank, both during ebb and flood period are not significantly affected compared to the base case. The mean velocity during a full tidal cycle increased from 0.055 to 0.056 m/s compared to the base case simulation. The mean velocities in the ebb period remained the same, and an increase from 0.078 m/s to 0.079 m/s is obtained during the flood period. The increase in the magnitude of velocity originates from less friction present inside the river bank. This originates from the removal of the shallow water areas present in the base case. The flow patterns resulting from simulation D.3 during the maximum flood and ebb velocities displayed in Figure D.9, Appendix D. Differences in flow direction are observed during the fall of the tide. In this period, the direction of the flow close to the east entrance is almost perpendicular with the flow direction present inside the navigation channel. This effect was also visible in the base case simulation but enhanced in simulation D.3 as less friction is present resulting from changes in bed topography.

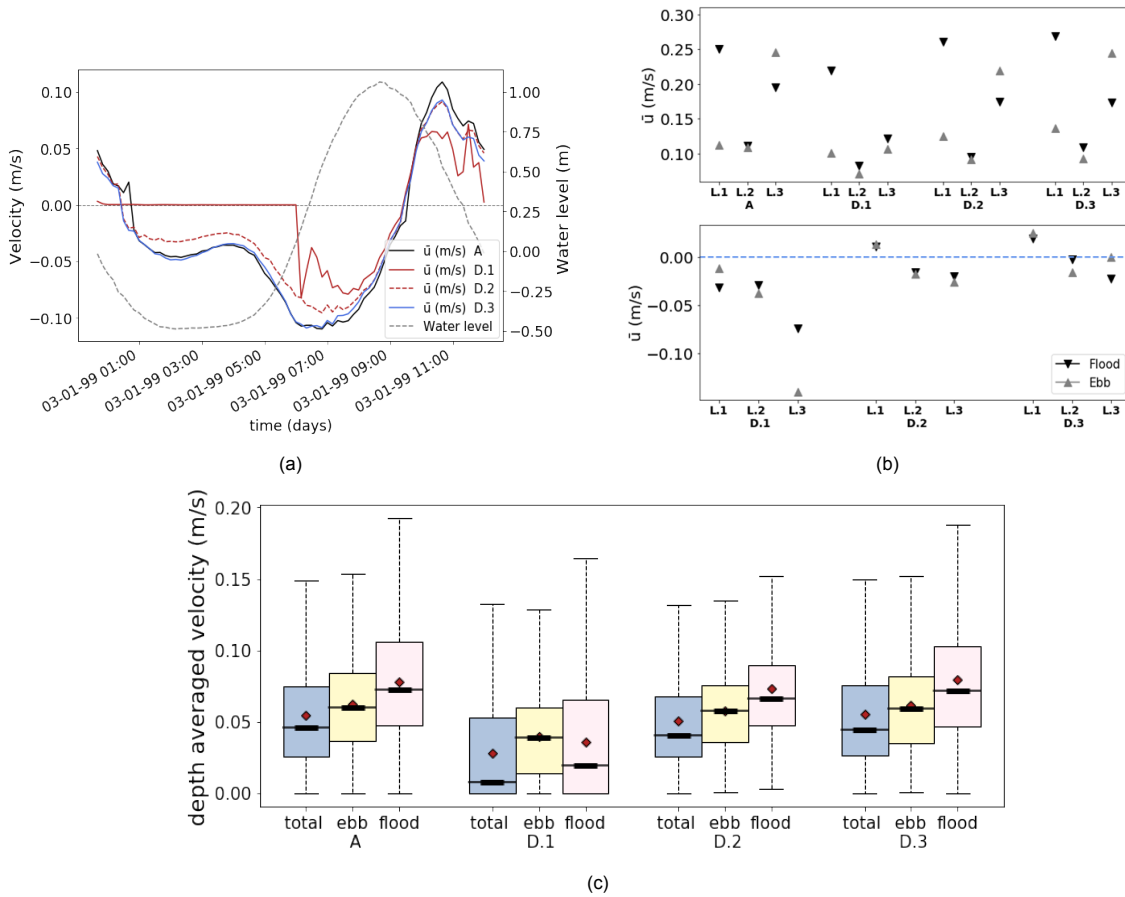


Figure 8.2: In Figure 8.2a the velocity profile at observation point L.2, in the middle of river bank L of simulations A, D.1, D.2 and D.3 are displayed. In Figure 8.2b the maximum ebb and flood velocities obtained at three locations from simulations A (morphological tide), D.1, D.2 and D.3 are displayed in the top figure. The bottom figure displays the difference relative to simulation A. The variation in simulations is a different bed topography inside the river bank for each run. For the location of the observation points, it is referred to Figure 7.6a. Figure 8.2c displays the box plot on the depth-averaged velocities inside the river bank. The box plots are created for simulations A, D.1, D.2, and D.3. All locations inside river bank L are taken into account. The data of the box plots are created both for a full tidal cycle, an ebb period, and a flood period. The data in the flood and ebb period are filtered based upon the period in which the water level rise is larger than 0.5 cm/minute. The red diamond indicates the mean of the data set and the black lines inside the box indicate the median of the data set. The coloured range indicates the 25 to 75 percentile of the data set and the dotted lines indicate the lowest and largest data point excluding outliers.

Morphodynamics results

The effect of variations in bed topography at river bank L on the morphological evolution of the river bank is separated into two parts. First, the effect on the transport of non-cohesive sediment is treated and thereafter the effect on the transport of cohesive sediment is treated. The resulting cumulative erosion and sedimentation patterns of the variations are displayed in Appendix E, Section E.1. In Figure 8.5 several parameters regarding the hydrodynamics and morphodynamics at river bank L are displayed resulting from changes in bed topography.

Noncohesive sediment

The results of the adaptations are compared to the base case simulation. The base case simulation, incorporating a nominal diameter of 150 μm , results in a total sediment input of 0.5 m^3 . In Figure E.1, Appendix E, Section E.1, the resulting cumulative sedimentation and erosion patterns of simulations D.1, D.2 and D.3 are displayed after six months of morphological modelling. No significant differences are observed regarding the sedimentation of sediment. The total input of non-cohesive sediment at river bank L, resulting from six months of morphological modelling, is equal to 0.5, 0.43, and 0.51 m^3 for simulations D.1, D.2 and D.3 respectively.

Cohesive sediment

All simulations incorporating the sediment transport of silt were both executed with either an erodible or non-erodible bed layer. The resulting cumulative erosion and sedimentation patterns for the latter are displayed in Figure E.3 and E.2 (Appendix E, Section E.1). The sediment budgets for simulations D.1, D.2, D.3 and A, incorporating both an erodible and non-erodible bed layer are displayed in Figure 8.4. In addition, the morphological evolution of the river banks is displayed for simulations D.1, D.2 and D.3 in Figure 8.3.

Simulation D.1, incorporating a bed level at 0.0 m NAP, in both cases (erodible / non-erodible), results in smaller silt input compared to the base case simulation. Incorporating an erodible bed layer, results in a sedimentation / erosion ($\frac{S}{E}$) ratio of 0.03. The total amount of sedimentation and erosion observed is equal to 2.5 and 88 m³ respectively after six months of morphological modelling. Over almost the entire river bank, export of the silt bed layer is observed. This originates from the flow being less directed into the river bank. Therefore, almost all the sediment brought into suspension by the flow is transported into the navigation channel. From Figure 8.4 it can be observed that the export of silt is smaller close to the navigation channel relative to simulation A. This originates from the decrease in velocity. In addition, the export of silt is visible close to the land-side of the river bank. From the hypsometric analysis, it is observed that the magnitude of erosion is decreasing. This indicates that the erosion process is flattening. In addition, sedimentation is observed close to the river bank although overall export of sediment is observed in this area (area 8, Figure 8.4). The simulations incorporating a non-erodible bed layer are in agreement with the latter, the import of cohesive sediment is reduced by approximately 50 percent compared to simulation A, from 15.5 m³ to 7.1 m³. From Figure 8.4b it is observed that the largest accumulation of sediment is present close to the entrance. Thereafter the import of sediment significantly decreased.

Simulation D.2, incorporating a bed level at -1.0 m NAP, in both cases (erodible / non-erodible), results in smaller input of silt compared to the base case simulation. Incorporating an erodible bed layer results in an $\frac{S}{E}$ of 0.24, which almost equals the ratio for simulation A (0.23). The total amount of sedimentation and erosion observed is equal to 27.53 and 114 m³ respectively after six months of morphological modelling. Import of silt is observed from the land-side of the river bank up to the location to which the west groyne is extended. At the east side of the river bank import of silt is observed further towards the navigation channel. The locations in which sediment is deposited are in agreement with the flow pattern observed from the hydrodynamic results. From the sediment budget in Figure 8.4 it can be obtained that the turning point from export to import of sedimentation is at the same location for simulations D.2 and A. In addition, a small increase in sedimentation is observed close to the land side of the river bank. Figure 8.3 shows that the magnitude of erosion is decreasing and the magnitude of sedimentation is constant. A large amount of silt is exported into the navigation channel. From Figure 8.4b it can be observed that the largest accumulation of sediment is present in areas 5,6 and 7 in the case of a non-erodible bed layer. Although the pattern of sediment import resembles simulation A, a decrease in total input is observed from 15 to 12.8 m³.

Simulation D.3, incorporating a bed level at -1.8 m NAP, in both cases (erodible / non-erodible), results in an almost equal input of silt compared to the base case simulation. Incorporating an erodible bed layer results in an $\frac{S}{E}$ of 0.22, which almost equals the ratio for simulation A (0.23). The total amount of sedimentation and erosion observed is equal to 28 and 128 m³ respectively. Import of silt is observed from the land-side of the river bank up to the location to which the west groyne is extended. At the east side of the river bank import of silt is observed further towards the navigation channel. The ebb flow at the west entrance is more directed towards the southeast corner than observed in the base case. As a result, at this location the turning point of sedimentation/erosion at the river bank is caved, see Figure E.3, Appendix E, Section E.1. From the sediment budget in Figure 8.4 it can be obtained that the turning point from export to import of sedimentation is at the same location for simulations D.3 and A. An increase in sedimentation is observed in area 8. From the morphological evolution of the river bank, Figure 8.3, it can be obtained that the magnitude of erosion is decreasing and the magnitude of sedimentation is constant. A large amount of the eroded silt is transported into the navigation channel.

Incorporating a non-erodible bed layer shows that the largest accumulation of sediment is present in areas 5,6, and 7, Figure 8.4b. Although the pattern of sediment import resembles simulation A, a decrease in total input is observed from 15 to 14.7 m³. This originates from a decrease in sediment input close to the navigation channel, as the input of sediment at areas 7 and 8 (landside) increased. The decrease in import close to the navigation channel originates from the increase in bed level close to both entrances in simulation D.3 compared to the base case.

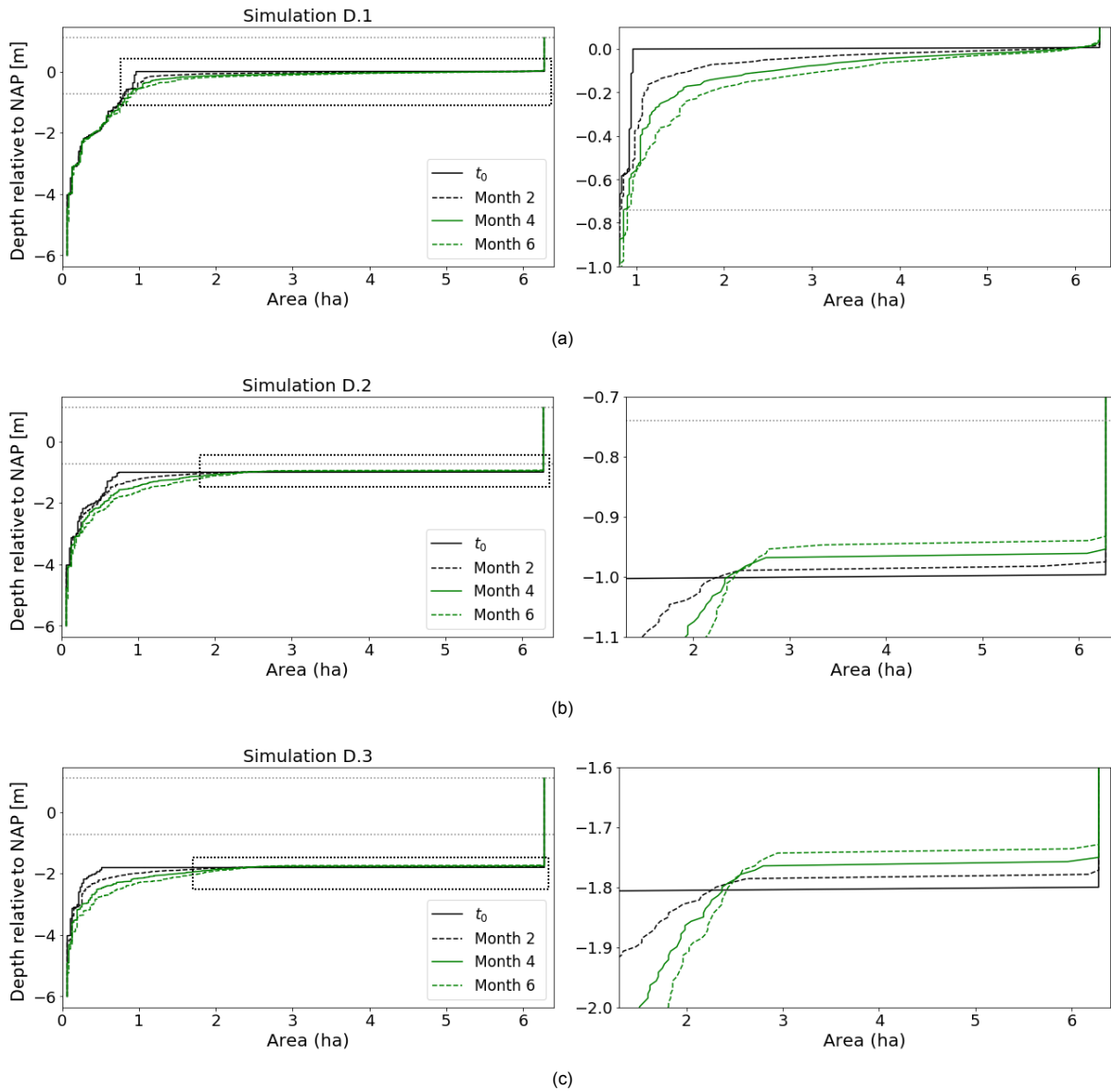


Figure 8.3: Morphological evolution over six months of river bank L, resulting from variations in initial bed topography at the river bank. In the left part of the figures, the full hypsometric curve is displayed. The black dotted area is visualized in the right figure.

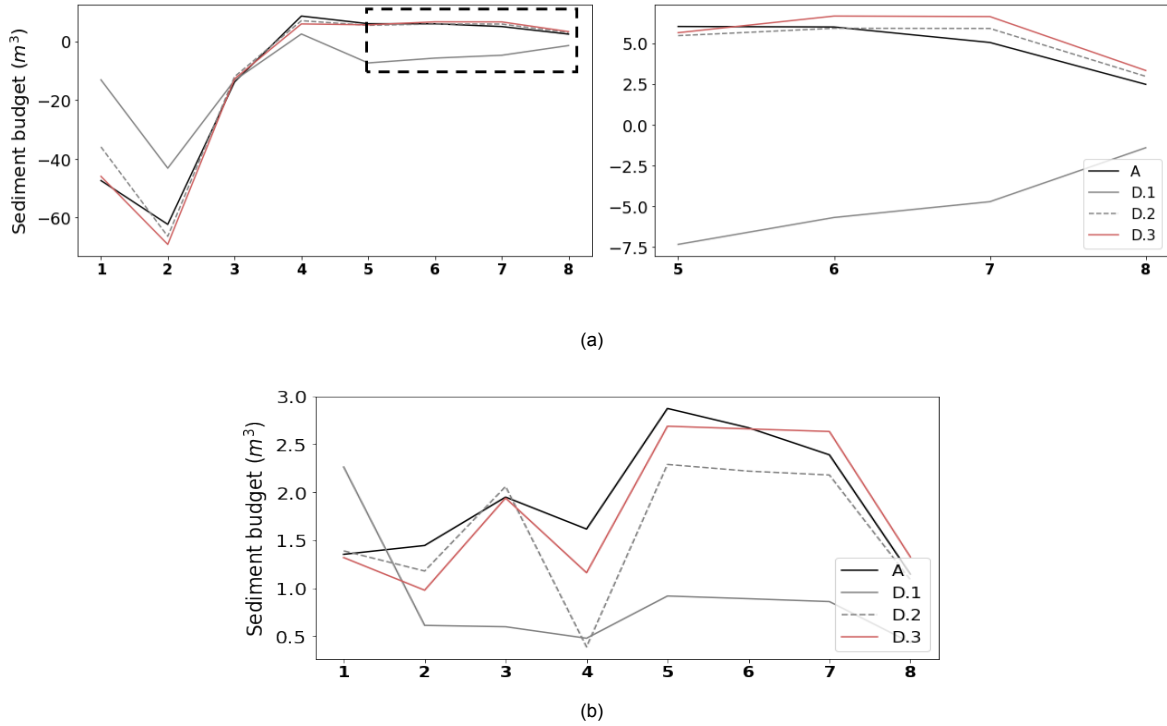


Figure 8.4: Figures displaying the sediment budget after six months of morphological modelling. The simulations in this figure incorporate a different bed topography compared to the base case. In addition, base case simulation A is displayed. Negative values indicate export of sediment (erosion) and positive values indicate import of sediment (sedimentation). The sediment layer at the river bank is erodible for Figure 8.4a. In the left part of Figure 8.4a the sediment budget for the entire river bank is displayed, from 1 to 8. The black dotted area indicates the shallow area of the river bank of which the sediment budget is visualized in the right part of Figure 8.4a. In Figure 8.4b the sediment budget is visualized resulting from a non-erodible bed layer at the river bank. Only positive values are present in the y-axis as no erosion can occur. Note that the areas indicated by number in the above figures and visualized in Figure 7.20 are not equally sized. Area 1 represents the area closest to the navigation channel and area 8 is the area closest to the land-side of the river bank.

	A	D.1	D.2	D.3
\bar{u} (m/s)	0.055	0.028	0.051	0.056
$\frac{u_{flood}}{u_{ebb}}$	1.26	0.9	1.26	1.29
S non cohesive (m ³)	0.5	0.5	0.43	0.51
E cohesive erodible (m ³)	123	89	114	128
S cohesive erodible (m ³)	28	2.5	27	28
S/E cohesive erodible (-)	0.23	0.03	0.24	0.22
S cohesive non erodible (m ³)	15.5	7.1	12.8	14.7

Figure 8.5: Table displaying the effect of changes in bed topography at the river bank on several parameters regarding the hydrodynamics and morphodynamics at river bank L. \bar{u} represents the mean depth-averaged velocity over a full tidal cycle at the river bank. The $\frac{u_{flood}}{u_{ebb}}$ ratio provides information on the relative ebb and flood dominance of the velocity signal at the river bank. The third parameter represents the sediment input of non-cohesive sediment incorporating a diameter of 150 μ m. The fourth and fifth parameter represents the eroded and deposited sediment respectively for an erodible bed layer. The sixth parameter, S/E, represents the ratio between sedimentation and erosion at the river bank incorporating an erodible bed layer. The last parameter represents the sediment input of cohesive sediment incorporating a non-erodible bed layer

Discussion on model results

To conclude this section, the proposed hypotheses in Chapter 6 are evaluated. Thereafter the results of cohesive sediment transport are concluded. On the forehand, no hypotheses are written on the latter, due to complexity regarding both hydrodynamics and the amount of suspended sediment available in the water column.

1: It is expected that a change in bed topography will lead to a different flow pattern. The incorporation of a constant bed level of -1.8 m and -1.0 m NAP increases the tidal prism. A constant bed level of -1.8 m is expected to result in higher flow velocities as a result of the increase in tidal prism and larger water depth. The velocities are expected to be higher which can result in more sediment import of sand if the critical values are reached. The incorporation of a constant bed level at -1.0 NAP is expected to result in smaller velocities. Export of coarse sediment is expected close to the navigation channel.

The simulation results partly confirm the hypothesis. Incorporating a constant bed level of -1.8 m NAP, removing the intertidal area present in the base case simulation, results in an increase in mean velocity over the river bank in the order of 0.001 m/s. The intertidal area present in the base case simulation is relatively small, by which the tidal prism only increased with 1000 m³. The flow pattern, both during ebb and flood, is more directed towards the southeast corner (location of the intertidal area was present in the base case simulation) compared to the base case. Resulting from the removal of the intertidal area, the flow is less obstructed due to a decrease in frictional effects. The effect of the change in bed level did not impact the import of coarse sediment compared to the base case. This is contrary to what was expected. The increase in velocity is not large enough to reach the critical velocities for transport. A decrease in import of cohesive sediment is observed resulting from a constant bed level at -1.8 m NAP. This results in a relative increase in bed level close to the entrances. A relative increase in sedimentation is observed close to the river bank, as the flow is more directed towards the river bank resulting from the removal of the intertidal area. In addition, an increase in volume present in the water column at those locations is obtained during a full tidal cycle. This directly implies a larger amount of suspended sediment at those locations.

Incorporating a constant bed level of -1.0 m NAP, results in an increase in tidal prism of 1000 m³/s. The relatively small water depth results in more frictional effects by which the mean magnitude in velocity over the river bank decreased from 0.055 m/s to 0.051 m/s. The flow pattern, both during ebb and flood, is more directed towards the southeast corner compared to the base case. The import of coarse sediment decreased, but no export of coarse sediment is visible. Less import of cohesive sediment is observed compared to the base case.

2: If the bed level at the river bank is increased up to 0 m NAP, the river bank area is only partly flooded during a tidal cycle. It is expected that this results in a decrease in velocities over the whole river bank. In addition, it is expected that this adaptation will result in the export of sediment at the groyne area, more specifically at the entrances of the groyne area.

The simulation results partly confirm the hypothesis. Incorporating a constant bed level of 0.0 m NAP, results in a decrease of mean velocity at the river bank from 0.055 to 0.028 m/s compared to the base case. The decrease in velocity originates from a decrease in tidal prism of 27 000 m³, in combination with an increase in frictional effects at the river bank. The flow is less directed towards the river bank. An equal amount of coarse sediment import is observed compared to simulation A, contrary to the expected export of coarse sediment. The simulation results of cohesive sediment transport showed that river banks incorporating higher bed levels experience less input of cohesive sediment. This originates from relatively small mean depth-averaged velocities, in combination with no water present during low water. In addition, an increasing bed level results in erosion being present over a larger surface area of the river bank.

The implementation of a constant bed level at the river bank resulted in small deviations between the desired constant bed level at the river bank and the resulting bed level present in the simulation. The initial bed level at the river bank is adapted by changing the depth values of the relevant grid nodes present in Delft3D. Interpolation of these depth points with the surrounding depth points is necessary in order to provide the grid with bed levels by which it is possible to numerically compute the water and

sediment transport. As a result, the bed levels at the river bank are almost equal to the inserted depth value, except at the boundaries of the river bank, i.e. close to the groynes and the longitudinal wall. At these locations, the bed levels are interpolated between the inserted depth values and the surrounding depths. This predominantly leads to lower bed levels at the boundaries of the river bank than was desired. This affects the flow pattern observed from the simulations. The largest effect is noticeable at simulation D.1, incorporating a bed level of 0 m, which shows the flow is directed into the decreased bed levels present close to the groynes.

The variations in bed topography did not largely affect the sediment import of coarse sediment at river bank L. The magnitude of flow velocities did not increase up to the limit of critical velocity (0.3 m/s). Sedimentation of non-cohesive sediment is only present close to the entrance (only the first row of grid cells). At these locations, the bed levels are almost equal in simulations D.1, D.2, D.3 and D.4 resulting from the error in bed topography. Consequently, the effect of changes in bed topography on coarse sediment transport is hardly affected. The hydrodynamic boundary condition incorporated in the model is a morphological tide. The presence of a spring tide results in larger velocities at the entrances. Assuming the effect of changes in bed topography on the velocity profile being equal, it is expected that a bed level at -1.8 NAP will result in an increase in the import of coarse sediment. The transport of cohesive sediment is affected by the difference between the expected simulated bed level and the simulated bed topography for simulation D.1. Accumulation of silt is present at lower bed levels close to the entrance. At these locations, water is present in the water column and able to settle during a tidal cycle, predominantly during constant low water. In the sediment budget, the area close to the navigation channel (area 1) is taken into account. Therefore, simulation D.1 displays a larger import of cohesive sediment than what would have been observed if the bed levels were equal to the constant value over the entire river bank.

The present geometry enhances sedimentation towards the southeast of the corner in terms of cohesive sediment transport. It was expected that the resulting sedimentation pattern from simulation D.3, incorporating a constant bed level at -1.8 m would resemble the sediment pattern as observed in reality. The resulting cumulative sedimentation and erosion pattern does not fully resemble the bed topography present in 2019 in which higher bed levels are present at the southeast and the southwest corner. The increase in bed level in the middle of the river bank close to the land side, observed in simulation D.3, is not observed in the data analysis. In addition, the bed levels present at the southeast corner are higher than at the southwest corner. The changes between the model and data are related to the hydrodynamics at the river bank. In the current simulation, a morphological tide is implemented, a spring tide will result in higher velocities present further into the river bank. The velocities at the southeast and southwest corner of the river bank remain small. This leads to re-suspension of the sediment in the middle of the area. This sediment is either transported into the navigation channel or towards the southeast and southwest corner.

8.2. Varying longitudinal wall

The presence of a longitudinal wall affects the flow pattern inside river bank L. Four variations are tested in this research. An extension of the longitudinal wall up to 280 meters (simulation E.1). Two variations on a shortened longitudinal wall, 140 meters (simulation E.2) and 70 meters (simulation E.3). Lastly, the flow pattern and sediment transport patterns are tested in case of no longitudinal wall present (simulation E.4). Which was the geometry present before the construction of the longitudinal wall in 2018.

Hydrodynamic results

The computed hydrodynamics inside the river bank resulting from simulations A, E.1, E.2, E.3 and E.4 are displayed in Figure 8.6. In Figure 8.6a the changes in 1D velocity profile are displayed at observation point L.2. In Figure 8.6b the maximum ebb and flood velocities are indicated, obtained from three observation points at river bank L. In Figure 8.6c, a box plot is displayed which is constructed based on data on the depth-averaged velocities in the entire river bank. Additional figures on the flow pattern during both ebb and flood, in combination with the changes in magnitude and direction of the flow from the simulations relative to base case simulation A are available in Appendix D, Figures D.10, D.11, D.12 and D.13.

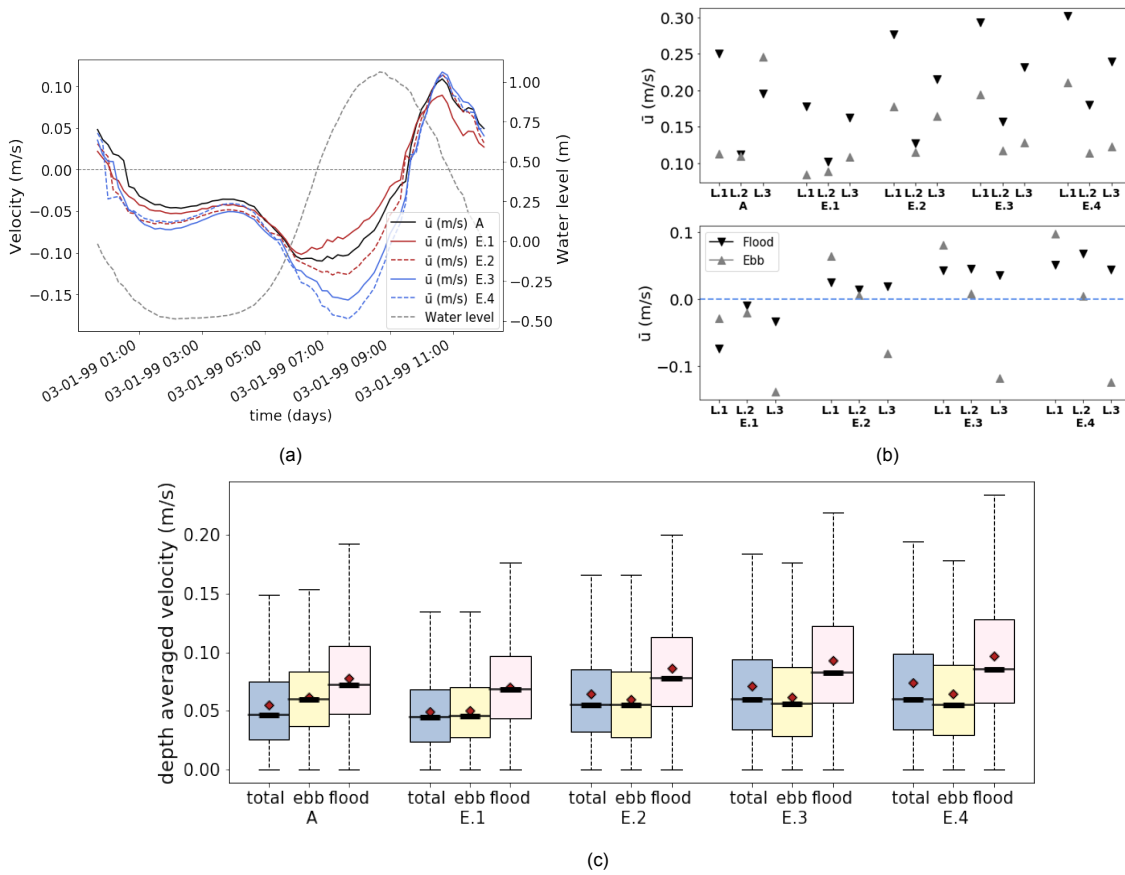


Figure 8.6: In Figure 8.6a the velocity profile at observation point L.2, in the middle of river bank L of simulations A, E.1, E.2, E.3 and E.4 are displayed. In Figure 8.6b the maximum ebb and flood velocities obtained at three locations from simulations A (morphological tide), E.1, E.2, E.3 and E.4 are displayed in the top figure. The bottom figure displays the difference relative to simulation A. The variation in simulations is a different length of the longitudinal wall located in front of river bank L. For the location of the observation points it is referred to Figure 7.6a. Figure 8.6c displays the box plot on the depth-averaged velocities inside the river bank. The box plots are created for simulations A, E.1, E.2, E.3, and E.4. All locations inside river bank L are taken into account. The data of the box plots are created both for a full tidal cycle, an ebb period, and a flood period. The data in the flood and ebb period are filtered based upon the period in which the water level rise is larger than 0.5 cm/minute. The red diamond indicates the mean of the data set and the black lines inside the box indicate the median of the data set. The coloured range indicates the 25 to 75 percentile of the data set and the dotted lines indicate the lowest and largest data point excluding outliers.

Extending the longitudinal wall

Extending the longitudinal wall in front of river bank L results in smaller velocities at observation point L.2, obtained from Figure 8.6a. During the largest part of the tidal cycle, a decrease in velocity is present. The velocity during constant water level slightly increased. From Figure 8.6b it can be observed that at all three observations a decrease in maximum velocity is obtained, both ebb and flood. The increase of longitudinal wall results in a decrease in surface area of the entrances of the river bank. Water flows into the direction in which it experiences the least friction. Extending the dam leads to the flow experiencing more friction when travelling towards the river bank. This can be observed from the box plot, Figure 8.6c, as the velocities decreased in all three periods of time. The mean velocity during a full tidal cycle decreased from 0.055 to 0.049 m/s compared to the base case simulation. The velocity profile averaged over the entire river bank has become more flood dominant, the $\frac{U_{flood}}{U_{ebb}}$ ratio increased from 1.26 (base case) to 1.4. The mean velocities of ebb and flood averaged over the entire river bank decreased from 0.062 to 0.050 m/s and 0.078 to 0.070 m/s respectively. A larger decrease in ebb velocities is observed as the surface area of the east entrance relatively decreased more than the west entrance. From the changes in 2D flow pattern, Figure D.10 Appendix D, it is observed that during

flood the flow approaches the river bank with a larger angle relative to the main flow direction inside the navigation channel than in the initial situation. In other words, the flow is slightly more directed towards the land-side of the river bank. The opposite is observed during ebb, the velocities at this location are smaller resulting from a smaller entrance. As a result, the flow is less directed towards the land-side of the river bank. The flow approaches the river bank with a smaller angle relative to the main flow direction inside the navigation channel than in simulation A.

Shortening of the longitudinal wall

Simulations E.2, E.3 and E.4 are three simulations considering shortening of the longitudinal wall, in which simulation E.4 incorporates no longitudinal wall in front of river bank L. Shortening of the longitudinal wall results in larger velocities at observation point L.2 (middle of the river bank), Figure 8.6a. The increase in the magnitude of velocity results from the flow being less hindered by the presence of an obstruction. A larger increase in flood velocities is observed rather than in ebb velocities. The increase in the magnitude of the ebb velocities resulting from simulations E.2, E.3, and E.4 is really small and almost equal in magnitude at observation point 2. In Figure 8.6b the maximum velocities at three observation points are displayed for all simulations incorporating a shortening of a longitudinal wall. This figure shows that at observation point L.1 (sea-ward entrance) the magnitude in flow velocity increased both during ebb and flood. The increase in magnitude relative to the base case increases with a decreasing length of the longitudinal wall. In the base case, the flow was contracted through a relatively small inlet which resulted in relatively large velocities present during ebb. A decrease in the length of the longitudinal wall results in the flow being less contracted. As a result, a decrease in magnitude in ebb velocity is observed at observation point L.3 (east entrance) resulting from simulation E.2, E.3, and E.4, Figure 8.6b. This decrease in the magnitude of maximum ebb velocity becomes larger relative to the base case with a decrease in length of the longitudinal wall.

In Figure 8.6c the resulting magnitudes in velocity are presented from data on the depth-averaged velocities at river bank L. The mean velocity during a full tidal cycle increased from 0.055 to 0.065 m/s resulting from a decrease in length of the longitudinal wall of 90 meters compared to base case simulation. The velocity profile averaged over the entire river bank has become more flood dominant. The $\frac{U_{\text{flood}}}{U_{\text{ebb}}}$ ratio increased from 1.26 (base case) to 1.44. The mean velocities of ebb and flood averaged over the entire river bank decreased and increased from 0.062 to 0.060 m/s and 0.078 to 0.086 m/s respectively. A decrease in the length of the longitudinal wall of 160 meters results in an increase in mean velocity from 0.055 to 0.071 m/s. The velocity profile at the river bank has become more flood dominant. The mean velocities for ebb remained constant and an increase in magnitude is obtained during the flood period from 0.078 to 0.093 m/s compared to the base case. Removal of the longitudinal wall results in an increase in mean velocity from 0.055 to 0.075 m/s compare to simulation A. Both the mean velocities of ebb and flood, averaged over the river bank, increased from 0.062 to 0.065 m/s and 0.078 to 0.096 m/s respectively. An increase in dynamics is observed resulting from a decrease in the length of the longitudinal wall. In Figure D.11, D.12, D.13 (Appendix D) the flow patterns are visualized of simulation E.2, E.3 and E.4. The removal of the longitudinal wall results in the flow being more directed towards the river bank during flood compared to simulation A. The angle between the main flow direction inside the navigation channel and the flow towards the river bank becomes larger with a decreasing longitudinal wall. The longitudinal wall hinders the exchange of water and sediment over the full length. When this length decreases, the flow can enter the river bank at more locations and so large differences in flow direction are observed at the location of the original longitudinal wall. In addition, a large decrease in the magnitude of velocity is observed at the location of the landward entrance, as the flow is less contracted at this location.

Morphodynamics results

The effect of variations in the longitudinal wall in front of river bank L on the morphological evolution of the river bank is separated into two parts. First, the effect on the transport of non-cohesive sediment is treated and thereafter the effect on the transport of cohesive sediment is treated. The resulting cumulative erosion and sedimentation patterns of the variations are displayed in Appendix E, Section E.2. In Figure 8.9 several parameters regarding the hydrodynamics and morphodynamics at river bank L are displayed resulting from variations in the length of the longitudinal wall.

Noncohesive sediment

The results of the adaptations are compared to the base case simulation. The base case simulation, incorporating a nominal diameter of $150 \mu\text{m}$, results in a total sediment input of 0.5 m^3 . In Figure E.4, Appendix E, Section E.2, the resulting cumulative sedimentation and erosion patterns of simulations E.1, E.2, E.3, and E.4 are displayed resulting from six months of morphological modelling. The decrease in length of the longitudinal wall results in more import of non-cohesive sediment at river bank L. The reverse is accounted for with an increase in the length of the longitudinal wall. No significant differences are observed regarding the sedimentation of sediment. The total input of non-cohesive sediment at river bank L, resulting from six months of morphological modelling, is equal to 0.9, 1.09, 1.18 and 1.26 m^3 for simulations E.1, E.2, E.3, and E.4 respectively. Compared to the import of non-cohesive sediment for the base case being equal to 0.5 m^3 this increase is significant. The resulting cumulative erosion pattern display that, in addition to the import of sediment, the bed topography at the original location of the longitudinal wall becomes more smooth. This is obtained from the alternating erosion and sedimentation patterns.

Cohesive sediment

All simulations incorporating the sediment transport of silt were executed with either an erodible or non-erodible bed layer. The resulting cumulative erosion and sedimentation patterns for the latter are displayed in Figure E.6 and E.5 (Appendix E, Section E.2). The sediment budgets for simulations E.1, E.2, E.3, and E.4 incorporating both an erodible and non-erodible bed layer are displayed in Figure 8.7. In addition, the resulting morphological development after six months of morphodynamic modelling is displayed for simulations E.1, E.2, E.3, E.4 in Figure 8.8.

Extending the longitudinal wall in front of the river bank by 50 meters, in both cases (erodible / non-erodible), results in a smaller import of silt compared to the base case. Incorporating an erodible bed layer, results in a sedimentation / erosion ($\frac{S}{E}$) ratio of 0.43. The amount of sedimentation relative to the erosion increased, however, the absolute values for sedimentation and erosion decreased from 28 to 16 m^3 and 123 to 37 m^3 compared to the base case. Less erosion is observed close to the longitudinal wall. The turning point from sedimentation to erosion shifted towards the navigation channel compared to simulation A. Silt can accumulate over a larger part of the river bank resulting from the decrease in the magnitude of velocity at the river bank. From Figure 8.7a it can be observed that the export of silt is smaller close to the navigation channel and the import of silt close to the land side is smaller relative to simulation A. From the morphological evolution, Figure 8.8, it can be obtained that the relative erosion of silt at the river bank is small compared to simulation A. As a consequence, less sediment is brought into suspension and less sedimentation is observed at the intertidal area. Incorporating a non-erodible bed layer results in a decrease from 15.5 to 13.1 m^3 compared to the base case. The sediment budget in Figure 8.7b displays the same pattern in sediment budget per area, only a decrease in magnitude is obtained from simulation E.1. From the hydrodynamic results, it was obtained that water is less prone to flow into the river bank. Cohesive sediment is mainly transported in suspension, therefore, a decrease in discharge into the river bank results in a decrease in the magnitude of silt deposition.

Decreasing the length of the longitudinal wall present in front of river bank L results in an increase in the import of silt incorporating a non-erodible bed layer. Incorporating an erodible bed layer results in a decrease in sediment import and an increase in sediment export. Three simulations are executed regarding the decrease in length of a longitudinal wall, E.2 (dam = 140 m), E.3 (dam = 70 m) and E.4 (dam = 0 m). The sedimentation/erosion ratio ($\frac{S}{E}$) decreased with a decreasing length of the longitudinal wall. The ratio equals 0.14, 0.08, and 0.07 for simulation E.2, E.3 and E.4 respectively. This results from both an increasing amount of erosion and decreasing amount of sedimentation by decreasing the length of the longitudinal wall. In addition, the turning point between sedimentation and erosion is traveling further into the river bank by decreasing the length of longitudinal wall, see Figures E.6 (Appendix E, Section E.2) and 8.7a. This originates from increased dynamics at the river bank.

The difference between simulation E.3 and E.2 is a decrease in the length of the longitudinal wall of 70 meters, same is accounted for between simulation E.4 and E.3. From Figure 8.7a it can be observed that the difference in erosion between simulation E.2 and E.3 is larger than between E.3 and E.4, al-

though the absolute value of the decrease in length of the longitudinal wall is equal. The sedimentation of silt at area 8, the intertidal area, increases with decreasing length of the longitudinal wall. In Figure 8.8 the morphological evolution of the river bank after six months is displayed. This confirms that additional erosion is flattening by decreasing the length of the longitudinal wall. Additional sedimentation of silt at the shallow area (6-8) is flattening by decreasing length. The observed cohesive transport relations are in agreement with the hydrodynamic results, which also display a flattening increase of dynamics inside the river bank by a decreasing length of the longitudinal wall.

Incorporating a non-erodible bed layer, decreasing the length of the longitudinal wall results in an increase of cohesive sediment import. The import of cohesive sediment is equal to 15.5 m^3 for simulation A. For simulation E.2, E.3, E.4 and E.4 this is equal to 16.6, 16.8 en 16.5 m^3 respectively. The sediment budget in Figure 8.7b shows that a decrease in length of longitudinal wall results in enhanced sedimentation in areas 3 to 8, in combination with a decrease in sedimentation close to the navigation channel. This results from the increase in velocity present in the area close to the longitudinal wall. This enhances re-suspension of deposited sediment and consequently, the sediment is transported further into the river bank.

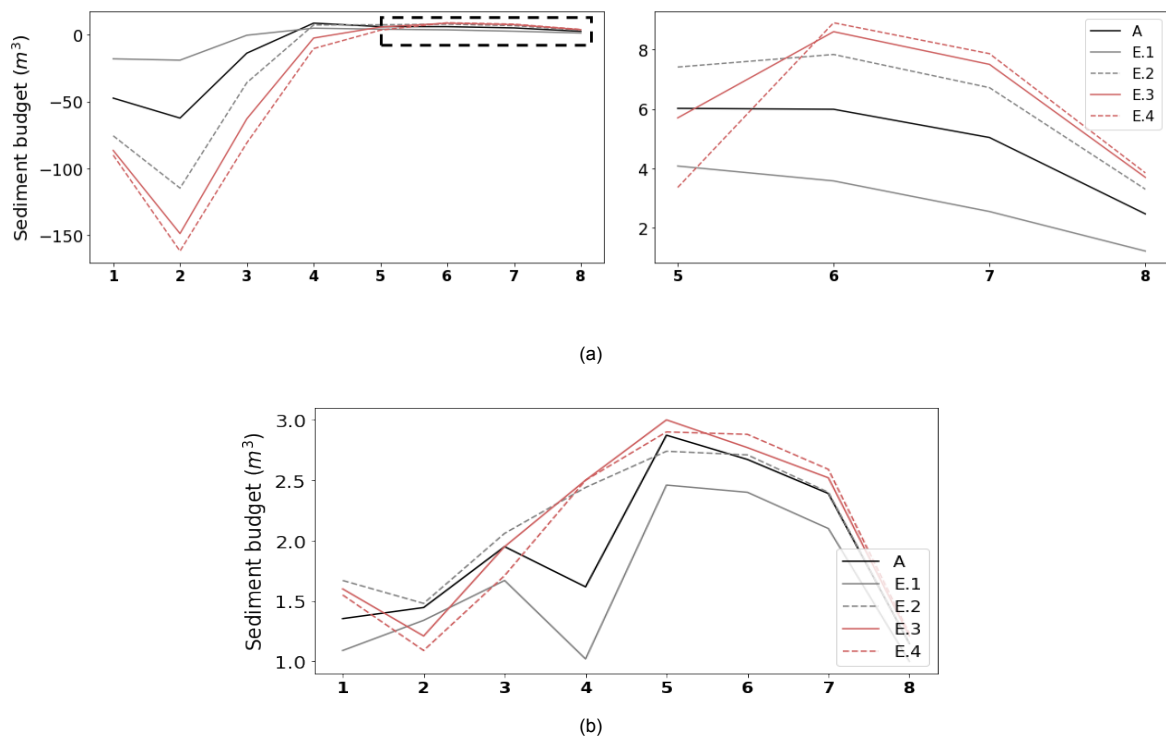


Figure 8.7: Figures displaying the sediment budget after six months of morphological modelling. The simulations displayed contain different lengths of the longitudinal wall located in front of river bank L. In addition, base case simulation A is displayed. Negative values indicate export of sediment (erosion) and positive values indicate import of sediment (sedimentation). The sediment layer at the river bank is erodible for Figure 8.7a. In the left part of Figure 8.7a the sediment budget for the entire river bank is displayed, from 1 to 8. The black dotted area indicates the shallow area of the river bank of which the sediment budget is visualized in the right part of Figure 8.7a. In Figure 8.7b the sediment budget is visualized resulting from a non-erodible bed layer at the river bank. Only positive values are present in the y-axis as no erosion can occur. Note that the areas indicated by number in the above figures and visualized in Figure 7.20 are not equally sized. Area 1 represents the area closest to the navigation channel and area 8 is the area closest to the land-side of the river bank.

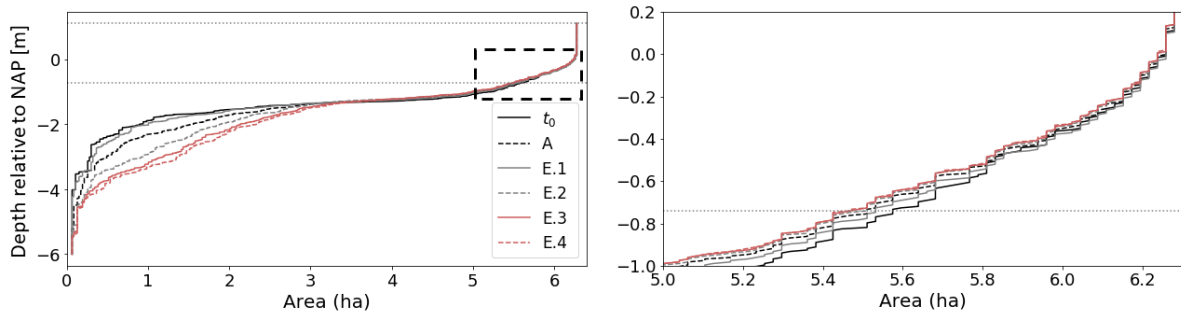


Figure 8.8: In the left part of the figure the resulting morphological evolution is displayed after six months for variations in length of the longitudinal wall. The black dotted area indicates the shallow area (from 1.0 m NAP) of the river bank of which the hypsometric curve is visualized in the right part of the figure.

	A	E.1	E.2	E.3	E.4
\bar{u} (m/s)	0.055	0.049	0.065	0.071	0.074
$\frac{u_{flood}}{u_{ebb}}$	1.26	1.40	1.44	1.50	1.50
S non cohesive (m ³)	0.5	0.49	1.09	1.18	1.26
E cohesive erodible (m ³)	123	38	226	300	343
S cohesive erodible (m ³)	28	16	33	26	24
S/E cohesive erodible (-)	0.23	0.43	0.14	0.08	0.07
S cohesive non erodible (m ³)	15.5	13.1	16.6	16.8	16.5

Figure 8.9: Table displaying the effect of different lengths of the longitudinal wall present in front of the river bank on several parameters regarding the hydrodynamics and morphodynamics at river bank L. \bar{u} represents the mean depth-averaged velocity over a full tidal cycle at the river bank. The $\frac{u_{flood}}{u_{ebb}}$ ratio provides information on the relative ebb and flood dominance of the velocity signal at the river bank. The third parameter represents the sediment input of non-cohesive sediment incorporating a diameter of 150 μm . The fourth and fifth parameter represents the eroded and deposited sediment respectively for an erodible bed layer. The sixth parameter, S/E, represents the ratio between sedimentation and erosion at the river bank incorporating an erodible bed layer. The last parameter represents the sediment input of cohesive sediment incorporating a non-erodible bed layer

Discussion on model results

To conclude this section, the proposed hypotheses in Chapter 6 are evaluated.

1: *An increase in length of the longitudinal wall is expected to increase the flow velocities present at the entrances of the river bank as the surface area of the entrances decreases. However, the flow direction from the navigation channel into the river bank area becomes more unfavourable as the longitudinal wall becomes larger. It is expected that the transport of cohesive sediment into the river bank area is enhanced by an increase in the longitudinal wall. In addition, it is expected that the import of fine sediment increases compared to the base case simulation.*

The simulation results do not confirm the hypothesis. The velocities at the entrances of river bank L, in combination with the mean velocities over the entire river bank decrease as a result of an increase in length of the longitudinal wall. The mean velocity over the river bank decreased from 0.055 to 0.049 m/s. The additional friction experienced by the flow, results in a smaller discharge entering the river bank, although the tidal prism is constant. This results from the discharge flowing through the river bank not only being dependent on the tidal prism but also on the velocity profile present in the navigation channel. The additional friction effects are dominant over the possible increase in flow velocity resulting from the contraction of the flow. Consequently, the import of coarse sediment decreased from

0.5 to 0.49 m³. The import of silt decreased as a result of the increase in length of the longitudinal wall of 90 meters from 15.5 to 13.1 m³. Cohesive sediment is mainly transported in suspension, therefore, a decrease in discharge into the river bank results in a decrease in the magnitude of silt deposition. The deposition of silt is present over a larger part of the river bank compared to the base case, as the velocities for erosion are only reached close to the navigation channel. Extending the longitudinal wall results in the river bank being less sensitive to erosion.

2: A decrease in the length of the longitudinal wall is expected to result in a decrease in the magnitude of flow velocities at the entrances. As a result, less erosion is expected at the entrances. This decrease in eroded sediment is expected to result in less sediment transport of coarse sediment into the river bank area. The mean velocity in the groyne area is expected to increase, as the flow from the navigation channel towards the river bank is less obstructed resulting from a decrease in length of the longitudinal wall. It is expected that this will result in less sedimentation of fine sediments at the river bank.

The simulation results do not confirm the hypothesis. The decrease in length of longitudinal wall results in both an increase in mean depth-averaged velocity at the river bank, as well as an increase in velocity at the entrances. Disregarding the maximum ebb velocities at the eastward entrance. A decrease in the length of the longitudinal wall results in the flow being less contracted at the west entrance. The decrease in the magnitude of ebb velocity at the eastward entrances becomes larger relative to the base case with a decrease in the length of the longitudinal wall. The increase in the magnitude of velocity results in an increase in the import of non-cohesive sediment. A decrease in length of the longitudinal wall of 90, 170, and 230 meters result in import of 1.09, 1.18, and 1.26 m³ respectively, resulting from six months of morphological modelling. (Base case import non-cohesive sediment equals 0.5 m³). In addition, the import of cohesive sediment increased with a decreasing length of the longitudinal wall. The enhanced sedimentation is present close to the land-side of the river bank. This results from the increase in velocity present in the area close to the longitudinal wall. This enhances re-suspension of deposited sediment and consequently, the sediment is transported further into the river bank.

The hypotheses regarding simulations incorporating changes in the length of the longitudinal wall showed some deviations from which is obtained with simulation results. At the moment that the hypotheses were written, it was not expected that the hydrodynamics present surrounding river bank L largely impacted the discharge flowing into the river bank. It was assumed that the discharge entering the river bank would remain constant, as the tidal prism remains equal. Model results showed the latter not being confirmed. The hypotheses would be valid if a close basin was considered with a constant discharge flowing in and out, as the balance $Q = u \cdot A$ would be applicable.

Disregarding the hypotheses, results obtained from the simulations introduce discussion points. As has been discussed in Chapter 3, the effect of a longitudinal wall largely impacts the wave action at the river bank. The presence of waves and wind is neglected in this research. It is expected that the implementation of wind and wave effects results in additional suspension and advection of the sediment at the river bank. By this, it is expected that the sediment is transported further into the river bank. The presence of a longitudinal wall decreases the wave action at the river bank. The simulation results display a decrease in sedimentation of both non-cohesive and cohesive sediment for an increase in length of the longitudinal wall. Besides, it is obtained that the turning point between erosion and sedimentation is close to the navigation channel, which indicates that over a large part of the river bank sedimentation is present. Additional sediment transport induced by waves is expected to decrease by an increase in the length of the longitudinal wall. A decrease in the length of the longitudinal wall is expected to result in more wave-induced sediment transport. Therefore, it is expected that enhanced import of cohesive sediment is present close to the land-side of the river bank compared to the simulation results. From the simulation results, it is obtained that eroded cohesive sediment in areas 1,2, and 3 (close to the navigation channel) is mainly transported towards the navigation channel. It is expected that by including the effect of waves, a larger part of the eroded sediment is transported towards the land-side of the river bank. In addition, further transport of the deposited sediment at the river bank is expected towards the intertidal area (areas 7 and 8).

8.3. Varying groyne heights/lengths

The presence of groynes affects the flow pattern inside river bank L. The variations in groynes are separated into the submergence of the groynes in the present situation, and the adaptation of the lengths of the groynes. First, the effect of the submergence of groynes (F.1 to F.3) is discussed and thereafter the variation in length (F.4 to F.7) is discussed.

8.3.1. Submergence of groynes

Hydrodynamic results

The groynes being submerged results in the flow being less hindered to flow towards the river bank during the time frame in which the water level is above the level of the groynes. The groyne levels tested are -0.6 m NAP (simulation F.1), 0.0 m NAP (simulation F.2) and +0.5 m NAP (simulation F.3). The groynes being submerged is only tested in combination with the geometry (length/location) in the current situation (simulation A). The computed hydrodynamics inside the river bank resulting from simulations A, F.1, F.2 and F.3 are displayed in Figure 8.10. In Figure 8.10a the changes in 1D velocity profile are displayed at observation point L.2. In Figure 8.10b the maximum ebb and flood velocities are indicated, obtained from three observation points at river bank L. In Figure 8.10c, a box plot is displayed which is constructed based on data on the depth-averaged velocities in the entire river bank. Additional figures on the flow pattern during both ebb and flood, in combination with the changes in magnitude and direction of the flow from simulations F.1, F.2 and F.3 relative to base case simulation A can be found in Appendix D, Figures D.14, D.15, D.16.

From Figure 8.10a, it can be obtained that by decreasing the groyne height, an increase in magnitude in velocity is obtained. A larger ebb period is observed from simulation F.1 when the groynes present are at -0.6 m NAP. During almost constant low water, the velocities at observation point L.2 are almost equal to zero resulting from simulation F.1. In this time frame, the ebb velocities inside the navigation channel are still significant, see Section 7.1. The presence of the large flow velocities in the navigation channel, in combination with a small amount of water being able to flow over the submerged groynes, results in large eddies at the entrances of the river bank. In simulations F.2 and F.3, no large differences in 1D velocity profile are obtained during constant water level. For simulation F.3 (+0.5 m NAP), the 1D velocity profile displays a small period in which the flow velocities are constant with the increasing water level. When the water level reaches 0.5 m, the velocity profile displays an increase in velocity. This results from the water flowing over the groynes, instead of following the path indicated by the entrances. In addition, a slight decrease in ebb velocity is observed at observation point L.2 for simulation F.3.

In Figure 8.10b the maximum velocities for both ebb and flood flow are displayed at three observation points for simulations A, F.1, F.2 and F.3. A larger increase in flood velocities is observed resulting from the submergence of groynes rather than in ebb velocities at observation point L.1 (left entrance). A decrease in ebb velocity is even observed at the right entrance (L.3), as the flow is less contracted by the presence of submerged groynes.

In Figure 8.10c box plots incorporating the depth-averaged velocities at river bank L for three periods of time resulting from simulations A, F.1, F.2, and F.3 are displayed. A decrease in groyne height increases the velocities at the river bank. If a groyne height of -0.6 m NAP is incorporated in the model, simulation F.1, the mean velocity during a full tidal cycle increases from 0.055 to 0.085 m/s compared to the base case simulation. The velocity profile averaged over the entire river bank is less flood dominant than resulting from the base case simulation, the $\frac{\bar{u}_{\text{flood}}}{\bar{u}_{\text{ebb}}}$ ratio decreased from 1.26 (base case) to 1.01. The mean velocities of ebb and flood averaged over the entire river bank increased from 0.062 to 0.103 m/s and 0.078 to 0.104 m/s respectively. This originates from the velocity profile at the river bank being more affected by the velocity profile inside the navigation channel, as the flow is less obstructed by the groynes. Close to the entrances, at observation points L.1, L.2 and L.3 the velocity profile became more flood dominant relative to the base case.

By incorporating a groyne height of 0.0 m NAP in the model, simulation F.2, the mean velocity during a full tidal cycle increases from 0.055 to 0.071 m/s compared to the base case simulation. The $\frac{\bar{u}_{\text{flood}}}{\bar{u}_{\text{ebb}}}$ ratio

increased from 1.26 (base case) to 1.27. The mean velocities of ebb and flood averaged over the entire river bank increased from 0.062 to 0.074 m/s and 0.078 to 0.094 m/s respectively. The increase in magnitude is smaller than observed in simulation F.1, as the flow is experiencing more friction from an increased groyne height. The increase in ebb magnitude is smaller than the flood magnitude resulting from the inequality in groyne length. The east groyne is extended further into the navigation channel, as a result, the ebb flow is experiencing more friction compared to the flood flow by an increasing groyne height. Close to the entrances, at observation points L.1, L.2 and L.3 the velocity profile became more flood dominant relative to the base case.

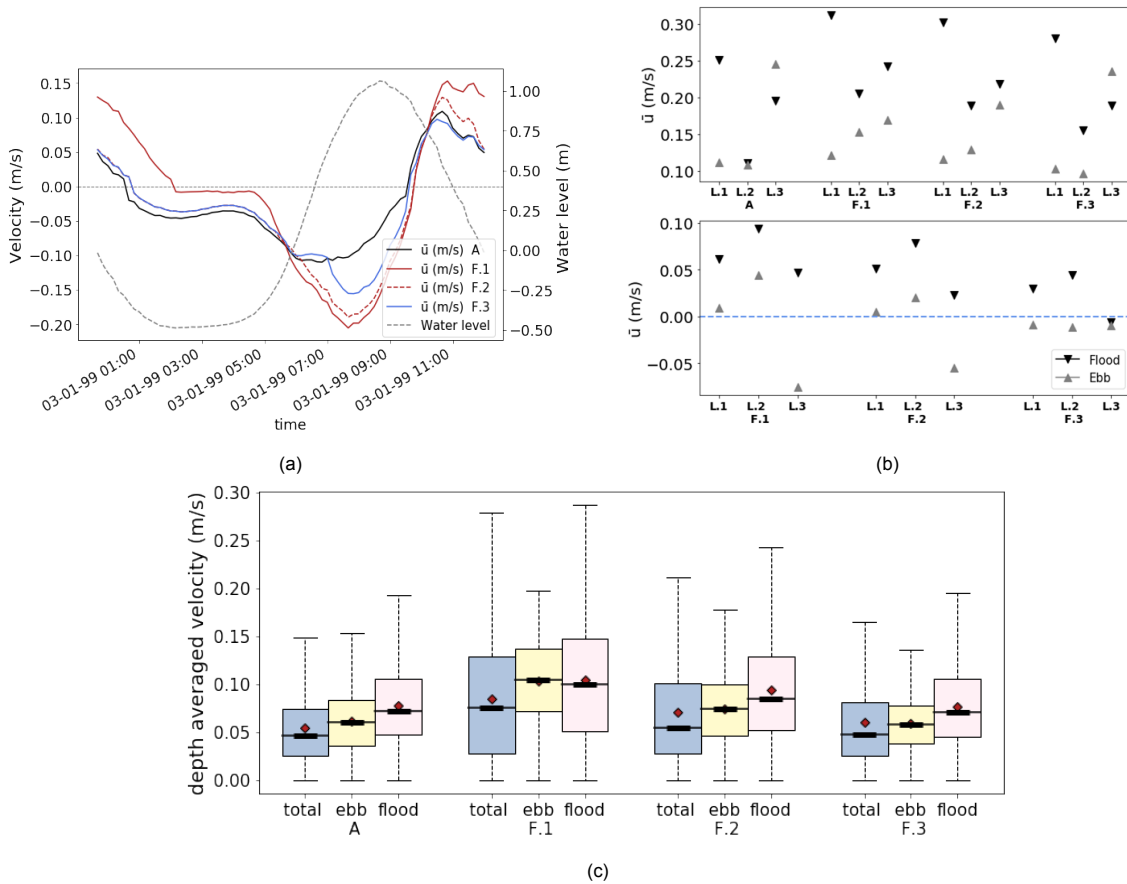


Figure 8.10: In Figure 8.10a the velocity profile at observation point L.2, in the middle of river bank L of simulations A, F.1,F.2, and F.3 are displayed. In Figure 8.6b the maximum ebb and flood velocities obtained at three locations from simulations A (morphological tide), F.1,F.2, and F.3 are displayed in the top figure. The bottom figure displays the difference relative to simulation A. The variation in simulations is a height of the groynes at river bank L. For the location of the observation points it is referred to Figure 7.6a. Figure 8.6c displays the box plot on the depth-averaged velocities inside the river bank. The box plots are created for simulations A, F.1,F.2, and F.3. All locations inside river bank L are taken into account. The data of the box plots are created both for a full tidal cycle, an ebb period and a flood period. The data in the flood and ebb period are filtered based upon the period in which the water level rise is larger than 0.5 cm/minute. The red diamond indicates the mean of the data set and the black lines inside the box indicate the median of the data set. The colored range indicates the 25 to 75 percentile of the data set and the dotted lines indicate the lowest and largest data point excluding outliers.

Simulation F.3, incorporating a groyne height of +0.5 m NAP, results in the mean velocity during a full tidal cycle increasing from 0.055 to 0.060 m/s compared to the base case simulation. The $\frac{U_{flood}}{U_{ebb}}$ ratio increased from 1.26 (base case) to 1.29. The mean velocities of ebb and flood averaged over the entire river bank decreased from 0.062 to 0.060 m/s and 0.078 to 0.077 m/s respectively. Although observation points L.1 and L.2 located at the seaward side of the river bank, show an increase in both ebb and flood velocities.

In Figure D.14, D.15 and D.16 in Appendix D the flow patterns observed from simulations F.1, F.2, and F.3 are visualized. In combination with the differences observed in direction and magnitude. A change in direction is mainly observed close to the groynes. In the base case, relatively small velocities are present directed parallel to the groynes. In the case of submerged groynes, the direction is perpendicular to the groynes. The moment of time in which the flow patterns (both ebb and flood) are displayed at +0.55 m relative to NAP. Although the groynes are submerged, and the water can flow over the groynes, the friction present in combination with the small obstruction ensures that the main flow stream still originates from the entrance during flood. The water flowing over the groynes enters the river bank with a relatively small velocity during flood. This velocity decreases with an increasing groyne height. During the ebb period, the flow over the submerged groynes at the east location is larger as the entrance of the river bank at ebb-location is smaller compared to the west entrance. The magnitude of velocity flowing over the right groyne during ebb is significantly decreasing with increasing groyne height.

Morphodynamic results

Noncohesive sediment

The results of the adaptations are compared to the base case simulation. The base case simulation, incorporating a nominal diameter of 150 μm , results in a total sediment input of 0.5 m^3 . In Figure E.7, Appendix E, Section E.3, the resulting cumulative sedimentation and erosion patterns of simulations F.1, F.2 and F.3 are displayed resulting from six months of morphological modelling. A decreasing height of the groynes results in larger velocities at the river bank. The total input of non-cohesive sediment at river bank L, resulting from six months of morphological modelling, is equal to 0.78, 0.78, and 0.71 m^3 for simulations F.1, F.2, and F.3 respectively. Compared to the import of non-cohesive sediment for the base case being equal to 0.5 m^3 a small increase in import of non-cohesive sediment is observed. The resulting cumulative erosion pattern display that, in addition to the import of sediment, an increasing erosion pit at the west side of the longitudinal wall is observed by decreasing the height of the groynes.

Cohesive sediment

All simulations incorporating the sediment transport of silt are executed with either an erodible or non-erodible bed layer. The resulting cumulative erosion and sedimentation patterns for the latter are displayed in Figure E.9 and E.8 (Appendix E, Section E.3). The sediment budgets for simulations F.1, F.2, and F.3 incorporating both an erodible and non-erodible bed layer are displayed in Figure 8.11. In addition, the resulting morphological development after six months of morphodynamic modelling is displayed for simulations F.1, F.2, and F.3 in Figure 8.12.

Decreasing the height of the groynes results in a decrease in the import of silt incorporating a non-erodible bed layer. Incorporating an erodible bed layer results in an increase of both sediment import and export into the river bank compared to the base case. Three simulations are executed regarding the submergence of groynes. F.1 (groyne level = -0.6 m NAP), F.2 (groyne level = 0.0 m NAP), and F.3 (groyne level = +0.5 m NAP). The simulations are ordered from with an increasing groyne height. The sedimentation/erosion ratio ($\frac{S}{E}$) is decreasing with decreasing height of the groyne. The ratio equals 0.11, 0.16, and 0.24 for simulations F.1, F.2 and F.3 respectively. A decreasing groyne height leads to both an increase in erosion and a decrease in sedimentation comparing simulations F.1 to F.3. The volume of eroded sediment equals 398, 288, and 191 m^3 for simulations F.1, F.2, and F.3 respectively after six months of morphological modelling. In the base case, incorporating groynes in which no exchange of water or sediment is possible, the amount of erosion equals 123 m^3 . Compared to the base case, the amount of sedimentation increased by incorporating submerged groynes. The imported volume after six months of morphological modelling equals 43, 47, 46, and 28 m^3 for simulations F.1, F.2, F.3, and A.

The cumulative sedimentation and erosion patterns of cohesive sediment obtained from the incorporation of the submergence of groynes are largely affected, Figure E.9 (Appendix E, Section E.3). From the hydrodynamic results, it is obtained that the flow velocities at the east groyne are larger compared to the flow velocities over the west groyne during flood. This originates from the location of river bank L inside of the Nieuwe Waterweg and on the lengths of the groynes in combination with the surface

areas of the entrances. As a result of the above, the largest accumulation of sediment is present at the southwest corner of the river bank. The turning point between sedimentation and erosion is present from the tip of the west groyne towards the southeast corner of river bank L for simulation F.1 (groyne level = -0.6 m NAP). An increasing groyne height results in the sedimentation being spread over a larger part of the southwest corner, but also in an increase in erosion at the southeast corner.

From the sediment budget incorporating an erodible bed layer, Figure 8.11a it is observed that a decreasing groyne height does not only increase the magnitude of erosion but it also increases the surface area over which erosion is present. A decreasing groyne height results in an increase in sedimentation at locations including higher bed levels (areas 7 and 8). From the morphological evolution, Figure 8.12 it is observed that a decrease in groyne height results in a decrease in the intertidal area at river bank L compared to simulation A. This originates from the erosion of the intertidal area at the eastward groyne as a result of the higher magnitude of velocities at this location compared to the base case simulation. The submergence of groynes enhances the re-suspension of cohesive sediment at the intertidal areas at river bank L.

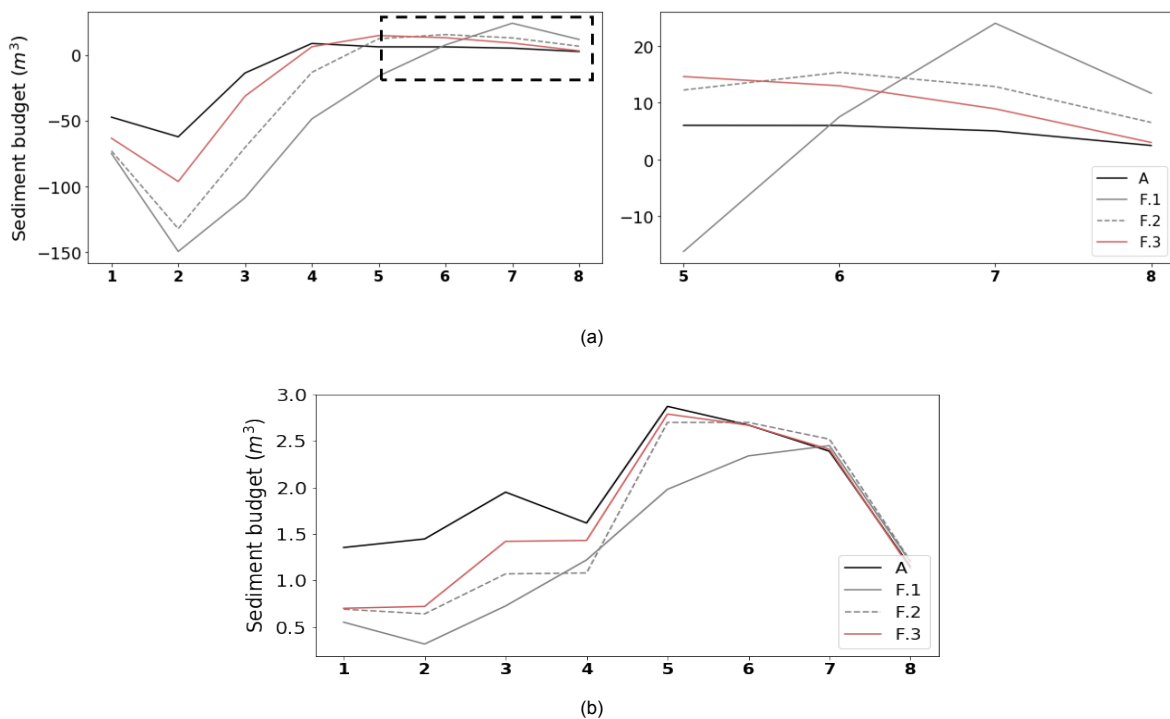


Figure 8.11: Figures displaying the sediment budget after six months of morphological modelling. The simulations displayed contain varying heights of the groynes at river bank L. In addition, base case simulation A is displayed. Negative values indicate export of sediment (erosion) and positive values indicate import of sediment (sedimentation). The sediment layer at the river bank is erodible for Figure 8.11a. In the left part of Figure 8.11a the sediment budget for the entire river bank is displayed, from 1 to 8. The black dotted area indicates the shallow area of the river bank of which the sediment budget is visualized in the right part of Figure 8.11a. In Figure 8.11b the sediment budget is visualized resulting from a non-erodible bed layer at the river bank. Only positive values are present in the y-axis as no erosion can occur. Note that the areas indicated by number in the above figures and visualized in Figure 7.20 are not equally sized. Area 1 represents the area closest to the navigation channel and area 8 is the area closest to the land-side of the river bank.

Incorporating a non-erodible bed layer results, with a decreasing height of the groynes, in a decrease in cohesive sediment import. The import of cohesive sediment is equal to 15.5 m^3 for simulation A. For simulation F.1, F.2 and F.3 this is equal to 10.8 , 12.6 and 13.3 m^3 respectively. The sediment budget in Figure 8.7b shows a large decrease in sediment import close to the longitudinal wall. In addition, no increase in sediment import is observed in areas 7 and 8 (shallow area). The decrease in sediment deposition at the river bank resulting from decreasing groyne heights can be accounted for by an increase in dynamics.

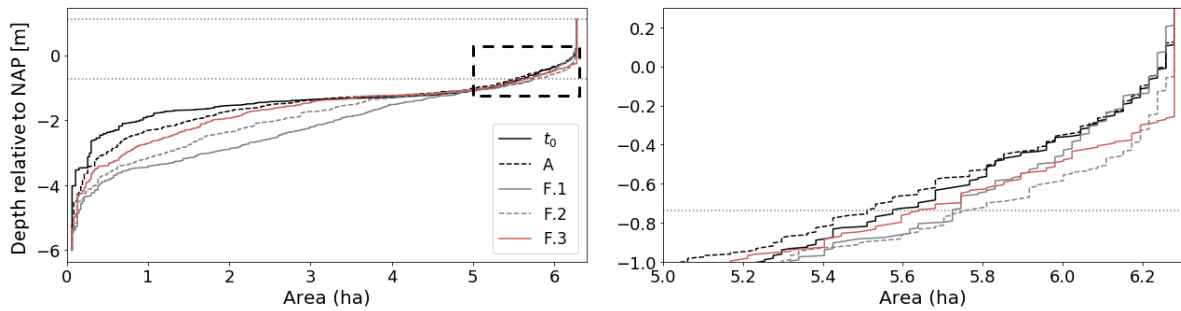


Figure 8.12: In the left part of the figure the resulting morphological evolution is displayed after six months for variations height of the groynes at river bank L. The black dotted area indicates the shallow area (from 1.0 m NAP) of the river bank of which the hypsometric curve is visualized in the right part of the figure.

8.3.2. Varying length of groynes

Hydrodynamic results

Four simulations are tested all incorporating a different groyne length. Simulation F.4 incorporates an extended left groyne, simulation F.5 incorporates a shortened left groyne, simulation F.6 incorporates the removal of the left groyne and simulation F.7 incorporates a decrease in length of the right groyne. For more information regarding the lengths, it is referred to the simulation approach, Chapter 6.

The computed hydrodynamics inside the river bank resulting from simulations A, F.4, F.5, F.6 and F.7 are displayed in Figure 8.13. In Figure 8.13a the changes in 1D velocity profile are displayed at observation point L.2. In Figure 8.13b the maximum ebb and flood velocities are indicated, obtained from three observation points at river bank L. In Figure 8.13c, a box plot is displayed which is constructed based on data on the depth-averaged velocities in the entire river bank. Additional figures on the flow pattern during both ebb and flood, in combination with the changes in magnitude and direction of the flow from simulations F.1, F.2 and F.3 relative to base case simulation A can be found in Appendix D, Figures D.17, D.18, D.19 and D.20.

Extension left groyne

Extending the left groyne decreases the magnitude in ebb and flood velocities compared to the base case, Figure 8.13a. Extending the left groyne decreases the surface area of the flood entrance. The flow into the river bank is more obstructed relative to the base case, and so less prone to enter the river bank. As a result, smaller flow velocities are observed inside the river bank. In Figure 8.13b the maximum ebb and flood velocities are displayed at three observation points for all simulations. A decrease in magnitude is observed at all locations resulting from simulation F.4 compared to simulation A. In addition, at both entrances, the flow ebb dominant, in agreement with the profile in the navigation channel. The same can be observed in Figure 8.13c, from which it becomes clear that in the total river bank the velocities are ebb dominant. In contrary to base case simulation A. The mean depth-averaged velocity over the full river bank decreased from 0.055 to 0.048 m/s compared to the base case simulation. The $\frac{U_{\text{flood}}}{U_{\text{ebb}}}$ ratio increased from 1.26 (base case) to 1.07. The mean velocities of ebb and flood averaged over the entire river bank decreased from 0.062 to 0.052 m/s and 0.078 to 0.056 m/s respectively. A significant decrease in the magnitude of flood velocities is observed resulting from the decrease in surface area of the entrance. From Figure D.17 in Appendix D it can be obtained that the extended left groyne ensures an eddy formation close to the groyne during flood. In addition, the flow is more directed towards the middle of the river bank. During ebb, the flow is more directed towards the navigation channel at the west entrance resulting from the extended groyne.

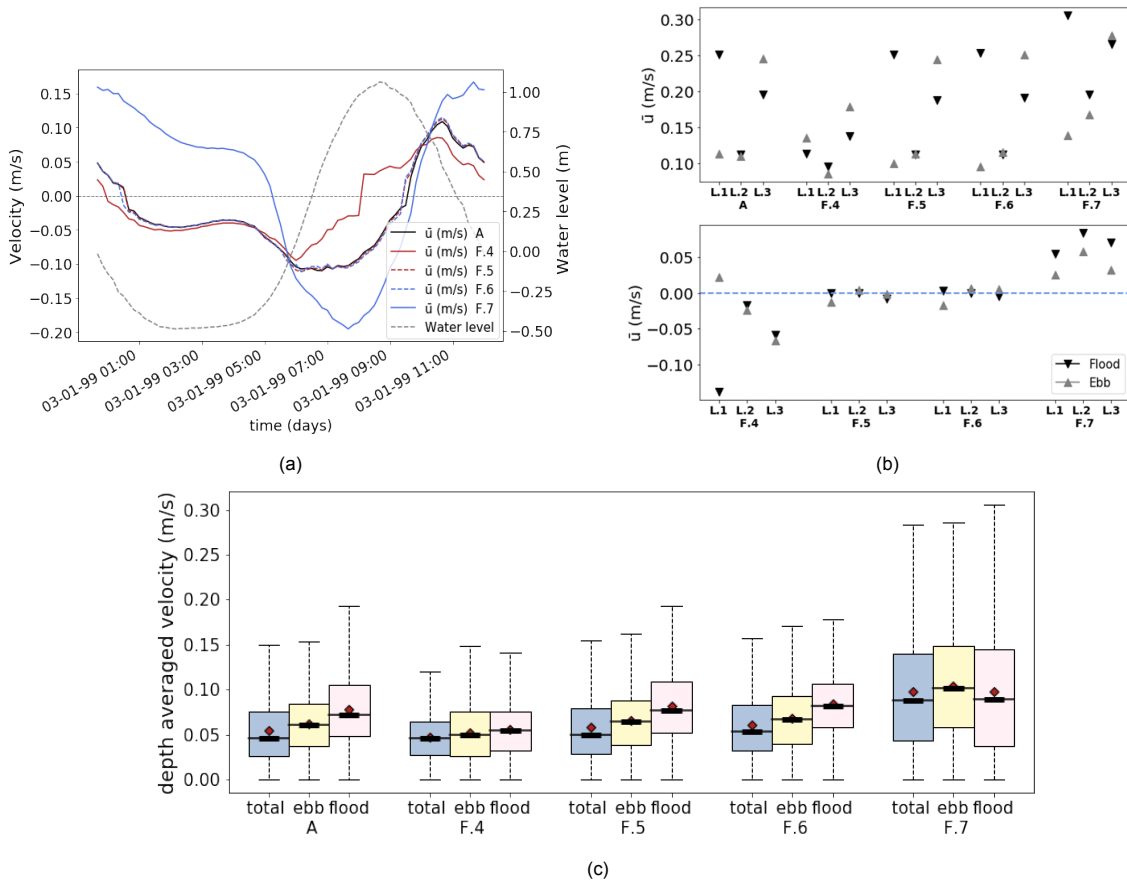


Figure 8.13: In Figure 8.13a the velocity profile at observation point L.2, in the middle of river bank L of simulations A, F.4, F.5, F.6 and F.7 are displayed. In Figure 8.13b the maximum ebb and flood velocities obtained at three locations from simulations A (morphological tide), F.4, F.5, F.6 and F.7 are displayed in the top figure. The bottom figure displays the difference relative to simulation A. The variation in simulations is a different length f the groynes at river bank L. For the location of the observation points, it is referred to Figure 7.6a. Figure 8.13c displays the box plot on the depth-averaged velocities inside the river bank. The box plots are created for simulations A, F.4, F.5, F.6 and F.7. All locations inside river bank L are taken into account. The data of the box plots are created both for a full tidal cycle, an ebb period and a flood period. The data in the flood and ebb period are filtered based upon the period in which the water level rise is larger than 0.5 cm/minute. The red diamond indicates the mean of the data set and the black lines inside the box indicate the median of the data set. The coloured range indicates the 25 to 75 percentile of the data set and the dotted lines indicate the lowest and largest data point excluding outliers.

Decrease length of west groyne

The decrease in length of the left groyne is simulated in two simulations, F.5 (shortened west groyne) or F.6 (removal of the west groyne). The decrease in length of the westward groyne does not impact the velocity profile at observation point L.2, Figure 8.13a. From Figure 8.13b it can be obtained that the magnitude in observed velocities at all three observation points are not largely affected by the decrease in length of the left groyne. In Figure 8.13c, the effect of the simulations on the depth-averaged velocities in the full river bank are displayed. A decrease in length of the left groyne (simulation F.5) results in an increase in mean depth-averaged velocity from 0.055 to 0.065 m/s compared to the base case. The magnitude of ebb and flood velocities increased from 0.062 to 0.065 m/s and 0.078 to 0.081 m/s respectively. Resulting from this proportional increase in magnitude, the $\frac{U_{flood}}{U_{ebb}}$ ratio decreases from 1.26 to 1.24 compared to the base case. The simulation results of the absence of the west groyne show an increase in mean depth-averaged velocity from 0.055 to 0.061 m/s compared to the base case. The magnitude of ebb and flood velocities increased from 0.062 to 0.068 m/s and 0.078 to 0.084 m/s respectively. Resulting from this proportional increase in magnitude, the $\frac{U_{flood}}{U_{ebb}}$ ratio almost remains equal, a decrease from 1.26 to 1.25 is observed. The relatively small effect of the decrease in groyne length on the velocities inside the river bank can be accounted for by the following. River bank K is situated on the west side of river bank L, in front of this river bank a longitudinal wall is present. Therefore, the flow

velocities at the west side of the left groyne are relatively small as this area is located in the lee area of river bank K. In addition, the direction of the flow from the navigation channel towards the river bank is not orthogonal to the left groyne. This also results from river banks K, and L being located in the lee area of the main flood flow direction, see Figure 3.4, Chapter 3. Although the magnitude in velocities are not much affected, the flow pattern is affected, see Figure D.18 and D.19 in Appendix D. The flow becomes more perpendicular to the land-side of the river bank for a longer distance by a decreasing length of the west groyne both during ebb and flood.

Decrease in the length of the left and right groyne

In simulation F.7, groynes on either side of river bank L are decreased in length. This largely impacts the velocity profile at the river bank, Figure 8.13a. The 1D velocity profile resembles the profile in the navigation channel, only including significantly smaller velocities. Compared to simulation A, the maximum flood, as well as the maximum ebb velocity, increased. Furthermore, an increase in ebb period is observed. Comparing the maximum velocities at three observation points, Figure 8.13b, it can be obtained that overall the velocities increased. The velocity profile at the west entrance becomes more flood dominant and the velocity profile at the east entrance both higher ebb and flood velocities are observed. From the previous section, it is obtained that a decrease in groyne length of the west groyne does not largely impact the velocities inside the river bank. However, the latter in combination with a decrease in groyne left at the east entrance results in large velocity differences, see Figure 8.13c. The simulation results show an increase in mean depth-averaged velocity from 0.055 to 0.097 m/s compared to the base case. The magnitude of ebb and flood velocities increased from 0.062 to 0.102 m/s and 0.078 to 0.097 m/s respectively. The overall velocity profile at the river bank has become ebb dominant $\frac{U_{flood}}{U_{ebb}} = 0.94$. The large increase in ebb velocities can be accounted for as the east entrance area largely increased in combination with the ebb flow in the navigation channel being more directed towards river bank L. In addition, the flood flow entering the river bank is experiencing less friction than in the base case simulation as the eastward groyne is partly removed. This combined leads to a large increase in the magnitude of velocities relative to simulation A for both ebb and flood, Figure 8.13c.

Morphodynamic results

Non-cohesive sediment

The results of the adaptations are compared to the base case simulation. The base case simulation, incorporating a nominal diameter of 150 μm , results in a total sediment input of 0.5 m^3 . In Figure E.10, Appendix E, Section E.4, the resulting cumulative sedimentation and erosion patterns of simulations F.4, F.5, F.6, and F.7 are displayed resulting from six months of morphological modelling. The total input of non-cohesive sediment at river bank L, resulting from six months of morphological modelling, is equal to 0.22, 0.51, 0.51, and 1.22 m^3 for simulations F.4, F.5, F.6, and F.7 respectively. Compared to the import of non-cohesive sediment for the base case being equal to 0.5 m^3 . An increase in length of the west groyne (F.4) decreases the flow magnitudes at the river bank compared to simulation A. Therefore, a smaller import of non-cohesive sediment is observed. The decrease of the west groyne (F.5 and F.6) does not significantly impact the sediment import of non-cohesive sediment at the river bank. This originates from the magnitude of velocities at the river bank not being largely affected by a decrease in length of the west groyne. A decrease in length of the east and west groyne (simulation F.7) results in an increase in sediment import compared to the base case. Sediment is deposited at the west entrance, in which the maximum flood velocity largely increased compared to the base case. This in combination with no significant increase of the ebb velocities at this location results in an increased import of non-cohesive sediment at this location compared to the base case.

Cohesive sediment

All simulations incorporating the sediment transport of silt were both executed with either an erodible or non-erodible bed layer. The resulting cumulative erosion and sedimentation patterns for the latter are displayed in Figure E.12 and E.11 (Appendix E, Section E.4). The sediment budgets for simulations F.4, F.5, F.6, and F.7 incorporating both an erodible and non-erodible bed layer are displayed in Figure 8.14. In addition, the resulting morphological development after six months of morphodynamic modelling is displayed for simulations F.4, F.5, F.6, and F.7 in Figure 8.15.

Simulation F.4, incorporating an increase in length of the west groyne results in an increase of cohesive sediment import incorporating a non-erodible bed layer. A decrease in sediment import resulting from an erodible bed layer is observed compared to the base case simulation. Incorporating an erodible bed layer results in an increase in the ratio between sedimentation and erosion ($\frac{S}{E}$) from 0.23 to 1.7. The total amount of erosion and sedimentation observed equals 7 and 12 m³ respectively after six months of morphological modelling. For the base case these this equals 123 and 28 m³ for erosion and sedimentation respectively. A large decrease in erosion is observed. This affects the amount of suspended sediment in the water column and therefore directly impacts the possible sedimentation at the river bank. From Figure E.12 (Appendix E, Section E.4) it is obtained that erosion is only observed at the entrances of the river bank. From Figure 8.14a it can be observed that the export of sediment is close to zero over the full river bank. This results from the decrease in the magnitude of velocity at the river bank, by which the critical shear stress for erosion (0.1 N/m²) is hardly reached. In addition, a decrease in sediment import in the shallow water area is observed compared to the base case. From the hypsometric analysis, Figure 8.15, it can be obtained that the river bank did not experience a significant change in morphological evolution as a result of the increased west groyne. Up to -0.55 m NAP, an increase in bed level is observed compared to the initial state (t_0). Above -0.55 m NAP, a decrease in bed level is observed compared to the initial state (t_0). This results from the erosion of the intertidal area at the southeast corner of the river bank. The simulations incorporating a non-erodible bed layer display an increase in sediment import of cohesive sediment relative to the base case simulation. The import of cohesive sediment has increased from 15.5 m³ in the base case to 17.9 m³ resulting from simulation F.4. Figure 8.14b shows that the additional import of sediment compared to simulation A is present in areas 1-5, located close to the longitudinal wall. The increase in sediment deposition at this location is related to the decrease in the magnitude of velocity at the river bank.

Simulation F.5 and F.6 result in an equal amount of sediment import of cohesive sediment incorporating an erodible bed layer as was obtained from the base case. Incorporating a non-erodible bed, simulations F.5 and F.6 result in a smaller import of sediment compared to the base case simulation. Incorporating an erodible bed layer results in a decrease in the ratio between sedimentation and erosion ($\frac{S}{E}$) from 0.23 to 0.22 for both simulation F.5 and F.6 compared to the base case simulation. The total amount of erosion observed after six months of morphological modelling equals 128, 131 and 123 m³ for simulations F.5, F.6 and A respectively. The total amount of sedimentation observed after six months of morphological modelling equals 28, 29 and 28 m³ for simulations F.5, F.6 and A respectively. The removal of the west groyne does not largely affect the sediment transport of cohesive sediment at river bank L. From Figure 8.14a it can be observed that the sediment budget is almost equal for simulations F.5, F.6, and A. A small increase in import of sediment is observed in the shallow area of river bank L (areas 7 and 8) resulting from a decreasing groyne length. The decrease in length of the west groyne does not significantly affect the morphological evolution of river bank L, see Figure 8.15. The relatively small impact of a decrease in west groyne length originates from the hydrodynamics at the river bank not being largely affected by the latter. The simulations incorporating a non-erodible bed layer display a decrease in sediment import of cohesive sediment relative to the base case simulation. The import of cohesive sediment is decreased from 15.5 m³ in the base case to 14.1 m³ for both simulation F.5 and F.6. Figure 8.14b shows that the decrease in import of sediment compared to the base case is present in areas 5-8.

Simulation F.7, incorporating a decrease in length of both the east and west groyne results in a decrease of cohesive sediment import incorporating a non-erodible bed layer. An increase in sediment import resulting from an erodible bed layer is observed compared to the base case simulation. Incorporating an erodible bed layer, results in a decrease in the ratio between sedimentation and erosion ($\frac{S}{E}$) from 0.23 to 0.13. The total amount of erosion and sedimentation observed equals 372 and 49 m³ respectively after six months of morphological modelling. For the base case these this equals 123 and 28 m³ for erosion and sedimentation respectively. The erosion observed has tripled and the sedimentation at the river bank has almost doubled compared to the base case. From Figure E.12 (Appendix E, Section E.4) it is obtained that the turning point between erosion and sedimentation is at the imaginary line between the shortened west and east groyne. The increase in velocity magnitude, in combination with the adapted flow pattern, is responsible for the latter. From Figure 8.14a the relocation of the turning

point between sedimentation and erosion from simulation A to F.7 is observed. The morphological evolution resulting from simulation F.7 significantly differs from the base simulation, Figure 8.15. Besides the large erosion at the relatively low bed levels, a significant increase in bed levels is observed above -1.2 m NAP. The simulations incorporating a non-erodible bed layer display a decrease in sediment import of cohesive sediment relative to the base case simulation. The import of cohesive sediment has decreased from 15.5 m³ in the base case to 10.7 m³ for simulation F.7 resulting from six months of morphological modelling. From Figure E.11 (Appendix E, Section E.4) it is observed that almost no sediment deposits at the east side of the river bank resulting from relatively large velocities observed compared to the base case. Relatively more sediment is deposited at the west side of the river bank, including the southwest corner. This results from higher bed levels present close to the groynes at river bank K (west) compared to river bank M (east). Figure 8.14b shows that the decrease in import of sediment compared to the base is present in the areas close to the longitudinal wall (1-4).

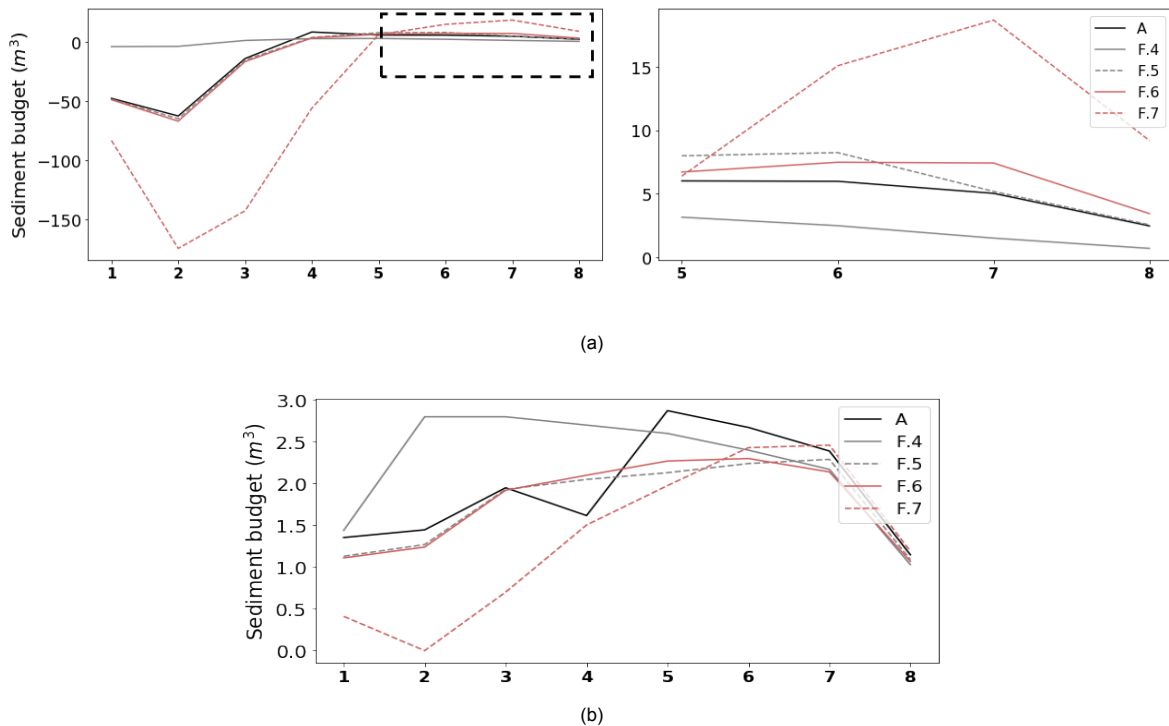


Figure 8.14: Figures displaying the sediment budget after six months of morphological modelling. The simulations displayed contain varying lengths of the groynes at river bank L. In addition, base case simulation A is displayed. Negative values indicate export of sediment (erosion) and positive values indicate import of sediment (sedimentation). The sediment layer at the river bank is erodible for Figure 8.14a. In the left part of Figure 8.14a the sediment budget for the entire river bank is displayed, from 1 to 8. The black dotted area indicates the shallow area of the river bank of which the sediment budget is visualized in the right part of Figure 8.14a. In Figure 8.14b the sediment budget is visualized resulting from a non-erodible bed layer at the river bank. Only positive values are present in the y-axis as no erosion can occur. Note that the areas indicated by number in the above figures and visualized in Figure 7.20 are not equally sized. Area 1 represents the area closest to the navigation channel and area 8 is the area closest to the land-side of the river bank.

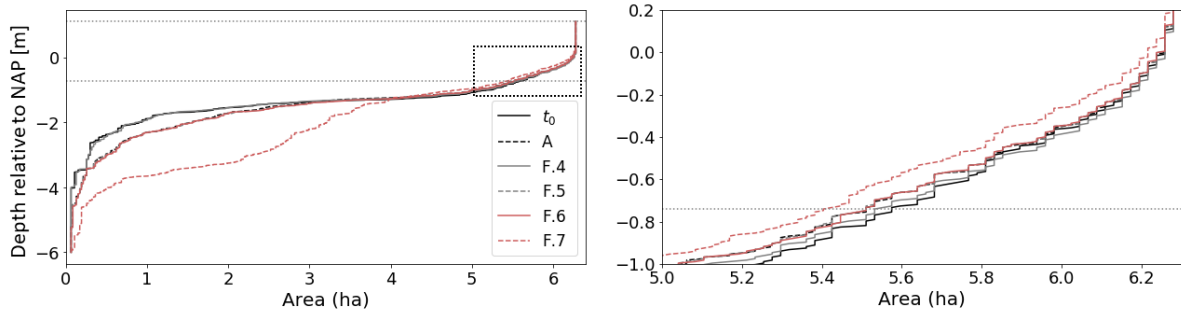


Figure 8.15: In the left part of the figure the resulting morphological evolution is displayed after six months for variations in length of the groynes at river bank L. The black dotted area indicates the shallow area (from 1.0 m NAP) of the river bank of which the hypsometric curve is visualized in the right part of the figure.

	A	F.1	F.2	F.3	F.4	F.5	F.6	F.7
\bar{u} (m/s)	0.055	0.085	0.071	0.060	0.048	0.058	0.061	0.097
$\frac{u_{flood}}{u_{ebb}}$	1.26	1.01	1.27	1.29	1.07	1.24	1.25	0.94
S non cohesive (m ³)	0.5	0.78	0.78	0.71	0.22	0.51	0.51	1.22
E cohesive erodible (m ³)	123	397	288	191	7	128	132	372
S cohesive erodible (m ³)	28	43	47	46	12	28	29	49
S/E cohesive erodible (-)	0.23	0.11	0.16	0.24	1.7	0.22	0.22	0.13
S cohesive non erodible (m ³)	15.5	10.8	12.6	13.3	17.9	14.1	14.1	10.7

Figure 8.16: Table displaying the effect of different lengths and heights of the groynes surrounding the river bank in front of the river bank on several parameters regarding the hydrodynamics and morphodynamics at river bank L. \bar{u} represents the mean depth-averaged velocity over a full tidal cycle at the river bank. The $\frac{u_{flood}}{u_{ebb}}$ ratio provides information on the relative ebb and flood dominance of the velocity signal at the river bank. The third parameter represents the sediment input of non-cohesive sediment incorporating a diameter of 150 μ m. The fourth and fifth parameter represents the eroded and deposited sediment respectively for an erodible bed layer. The sixth parameter, S/E, represents the ratio between sedimentation and erosion at the river bank incorporating an erodible bed layer. The last parameter represents the sediment input of cohesive sediment incorporating a non-erodible bed layer

Discussion on model results

To conclude this section, the proposed hypotheses in Chapter 6 are evaluated.

1: It is expected that increasing the submergence of the groynes leads to higher velocities at the groyne area. Less sedimentation is expected at the river bank compared to the original situation.

The simulation results confirm the hypothesis. The hydrodynamic results show that a decrease in height of the groynes results in an increase in mean depth-averaged magnitude at the river bank. A magnitude of 0.085, 0.071 and 0.06 m/s is obtained for simulations incorporating a groyne height of -0.6 m, 0.0 m and +0.5 m relative to NAP. Decreasing the groyne height results in the velocity profile more resembling the velocity profile inside the navigation channel which is ebb dominant. The import of non-cohesive sediment at the river bank increased resulting from decreasing groyne height. The total input of non-cohesive sediment at river bank L, resulting from six months of morphological modelling, is equal to 0.78, 0.78, and 0.71 m³ for simulations F.1, F.2, and F.3 respectively. Compared to the import of non-cohesive sediment for the base case being equal to 0.5 m³ a small increase in import of

non-cohesive sediment is observed.

A decrease in import of cohesive sediment is observed resulting from a decreasing groyne height. The import of cohesive sediment is equal to 15.5 m^3 for simulation A. For simulation F.1, F.2 and F.3 this equals 10.8 , 12.6 en 13.3 m^3 respectively. This results from the enhanced dynamics at the river bank resulting from the presence of submerged groynes. The presence of submerged groynes results in a decrease of the intertidal area at river bank L, incorporating an erodible bed layer. This originates from erosion at the intertidal area located at the eastward groyne as a result of the increasing magnitude of velocities compared to the base-case simulation. The submergence of groynes enhances the re-suspension of cohesive sediment at the intertidal areas at river bank L.

2: Increasing or decreasing the length of the groyne will affect the flow pattern in the groyne area. An increase in groyne length will decrease the inlet area and therefore flow velocities are expected to increase at the inlet causing erosion which is deposited in the groyne area. In addition, the flow is expected to enter the river bank at a larger angle with the main flow direction inside the navigation channel. Leading to the flow being more directed towards the river bank. A decrease in groyne length will result in a more dynamic area, higher flow velocities and less sedimentation of fine sediment are expected

The simulation results partly confirm the hypothesis. The hydrodynamic results show that an increase in length of the left groyne decreases the magnitude of flow velocities at the river bank. The mean depth-averaged magnitude at the river bank decreased from 0.055 to 0.048 m/s . The velocity profile inside the river bank has become more ebb dominant. This results from the decrease in surface area of the west entrance ($\frac{U_{\text{flood}}}{U_{\text{ebb}}} = 1.07$). The observed flow pattern confirms the hypothesis regarding the change in the flow direction, which approaches the river bank at a larger angle with the main flow direction inside the navigation channel compared to the base case simulation. The import of non-cohesive sediment at the river bank decreased resulting from an increasing groyne length, from 0.5 to 0.22 m^3 . An increase in import of cohesive sediment is observed resulting from an increase in groyne length. 17.9 m^3 is imported after six months of morphological modelling compared to 15.5 m^3 for the base case simulation. The increase in sediment deposition at this location is related to the decrease in the magnitude of velocities at the river bank. More specifically, a decrease in the maximum velocities at the entrances of the river bank. Possible erosion of cohesive sediment is present at the entrances of the river bank.

A decrease in length of the west groyne does not significantly affect the hydrodynamics at the river bank. The mean depth-averaged velocities inside the river bank from 0.055 to 0.061 m/s resulting from the removal of the west groyne. In addition, the morphological evolution of the river bank is not significantly affected by the decrease in length of the west groyne. A decrease in length of both groynes results in an increase in mean depth-averaged velocities from 0.055 to 0.097 m/s . The velocity profile at the river bank is ebb dominant ($\frac{U_{\text{flood}}}{U_{\text{ebb}}} = 0.94$), which is in agreement with the velocity profile present in the navigation channel. The import of non-cohesive sediment resulting from six months of morphological modelling increased from 0.5 to 1.22 m^3 compared to the base case. The simulations incorporating a non-erodible bed layer display a decrease in sediment import of cohesive sediment relative to the base case simulation of 15.5 m^3 to 10.7 m^3 . Less sediment is deposited close to the longitudinal wall as a result of the increased velocities. Large erosion of cohesive sediment is present resulting from the decrease in length of the east groyne.

From the data analysis, it is obtained that the largest sedimentation at river bank L is present in the southeast corner of the river bank. Model simulations show, incorporating submerged groynes, that cohesive sediment at the southeast corner of the river bank is eroding. The submergence of groynes leads to the velocity profile inside the river bank more resembling the velocity signal in the navigation channel in the model. The velocity signal in the navigation channel is ebb dominant with longer ebb periods present. From literature, it is known that the velocity profile inside the Rhine-Estuary is predominantly flood dominant. This can account for the reversed patterns observed from the simulation results of the developed model.

The expected spiralling pattern in the bed layer originating from the presence of submerged groynes is not observed from the simulation results incorporating both non-cohesive and cohesive sediment. This can be accounted towards the grid size at the river bank not being large enough to represent the relatively small scale pattern. The simulation results show that incorporating an erodible bed layer of cohesive sediment results in erosion of sediment close to the groyne. This erosion is however present over the entire eastward corner, and not only close to the submerged groynes. The simulation results incorporating noncohesive sediment did not display the spiralling flow in the river bed. This can be assigned towards the critical velocities for the erosion of sediment with a diameter of $150\ \mu\text{m}$ at these locations not being reached. An increased hydrodynamic forcing, such as a spring tide, possibly results in erosion close to the groyne. However, a spiral pattern can not be observed as the grid size is too large.

By adapting the groynes, both in height and in length, the effect of the bed levels present in the neighbouring river banks becomes more important. In the simulations incorporating an erodible bed layer, only the bed layer at river bank L is erodible. The suspension of cohesive sediment at the neighbouring river banks (K and M) is important for the morphological evolution of river bank L. The simulation results indicated that at the west side of the river bank, sediment is more likely to deposit. This results from the obstruction of further transport by relatively high bed levels present close to the location of the original groyne at river bank K. It is expected that when an erodible bed layer is implemented in both river banks K and M, the increased sedimentation at the southwest corner relative to the southeast corner decreases.

8.4. Varying inlet

The surface area of the inlet largely impacts the amount of water flowing towards the river bank. In this research, five variations in the surface area of the entrances of the river bank are tested. The surface area of the inlets is either decreased by the implementation of a sill or by fully closing the inlet. In simulation G.1 a sill is implemented at the right entrance at $-1\ \text{m}$ NAP. Simulation G.2 incorporates a sill at $-1\ \text{m}$ NAP at the left entrance in combination with the extension of the left groyne. Simulation G.3 includes a sill at $-1\ \text{m}$ NAP both at the left and the right entrance in combination with the extension of the left groyne. In simulation G.4 the right entrance of the river bank is fully closed and in simulation G.5 the left entrance of the river bank is fully closed.

Hydrodynamic results

The computed hydrodynamics inside the river bank resulting from simulation A, G.1, G.2, G.3, G.4, and G.5 are displayed in Figure 8.17. In Figure 8.17a the changes in 1D velocity profile are displayed at observation point L.2. In Figure 8.17b the maximum ebb and flood velocities are indicated, obtained from three observation points at river bank L. In Figure 8.17c, a box plot is displayed which is constructed based on data on the depth-averaged velocities in the entire river bank. Additional figures on the flow pattern during both ebb and flood, in combination with the changes in magnitude and direction of the flow from simulations G.1, G.2, G.3, G.4 and G.5 relative to base case simulation A can be found in Appendix D, Figures D.21, D.22, D.23, D.24 and D.25.

Sill at east entrance

The presence of a sill at the entrance ensures more friction, and so a local increase and thereafter a decrease in velocity. In Figure 8.17a the 1D velocity profile at observation point L.2 is displayed. In simulation G.1, implementation of sill at the east entrance, a slight decrease in velocities is obtained both in ebb and flood compared to simulation A. The time frame in which the maximum velocities are present is equal for simulations A and G.1. The periods of ebb and flood flow inside the river bank at observation point L.2 are not affected by the implementation of a sill at the right. From Figure 8.17b it is observed that the maximum ebb and flood velocities at the left entrance (L.1) and the middle of the river bank (L.2) are not much affected by the implementation of a sill at the right entrance. At observation point L.3, close to the east entrance, a distinct decrease in ebb velocity is obtained. The sill ensures more friction on the flow entering the river bank, and therefore a decrease in ebb velocity is

obtained. The mean velocity during a full tidal cycle decreased from 0.055 to 0.048 m/s compared to the base case simulation. The velocity profile averaged over the entire river bank, has become more flood dominant, the $\frac{U_{\text{flood}}}{U_{\text{ebb}}}$ ratio increased from 1.26 (base case) to 1.31. The mean velocities of ebb and flood averaged over the entire river bank decreased from 0.062 to 0.053 m/s and 0.078 to 0.070 m/s respectively. A larger decrease in ebb velocities is observed as the surface area of the east entrance decreased by the presence of a sill. A decrease in the magnitude of the mean flood velocities is observed as the flow experiences additional friction originating from the presence of a sill at the east entrance, which obstructs the outflow. In Appendix D, Figure D.21, the flow patterns are displayed resulting from simulation G.1 during maximum flood and ebb velocities inside the river bank. This figure shows that the flow pattern inside the river bank is not much affected. Close to the west entrance, the direction of the flow is not altered but a decrease in velocity is obtained during ebb, Figure D.21f.

Sill at west entrance

Simulation G.2 is a combination of the implementation of a sill at the left entrance with an extended left groyne. Figure 8.17a and 8.17b both display a significant decrease in both maximum flood and ebb velocities compared to the base case simulation. From simulation F.4, incorporating an extended left groyne, it was obtained that the mean depth-averaged velocity over the full river bank decreased from 0.055 to 0.048 m/s compared to the base case simulation. The mean velocities of ebb and flood averaged over the entire river bank decreased from 0.062 to 0.052 m/s and 0.078 to 0.056 m/s respectively resulting from an extended groyne. The presence of a sill results in an additional decrease in velocity magnitude, which results in a mean depth-averaged velocity over the full river bank of 0.038 m/s. The mean velocities of ebb and flood averaged over the entire river bank decreased from 0.052 to 0.041 m/s and 0.056 to 0.039 m/s respectively compared to simulation F.4. The $\frac{U_{\text{flood}}}{U_{\text{ebb}}}$ ratio decreased from 1.07 (simulation F.4) to 0.96. The decrease in dynamics is visualized in Figure 8.17c by means of a box plot incorporating the depth-averaged velocities of the river bank. From the flow patterns obtained during maximum ebb and flood velocities, Figure D.22, Appendix D, large differences are obtained compared to the base case. These changes are in agreement with the changes in flow pattern obtained from simulation F.4. The changes in direction are mainly originating from the elongation of the left groyne. In comparison with simulation F.4, an additional decrease in the magnitude of velocity is obtained during ebb at the east entrance.

Sill at both entrance

In simulation G.3, in addition to simulation G.2, a sill is incorporated at the right entrance. The velocity profile at observation point L.2, Figure 8.17a is not much affected. A decrease in the magnitude of velocity during ebb is obtained, which originates from the presence of the sill at the east (ebb) entrance. In Figure 8.17b the additional decrease in maximum ebb velocity at observation point L.3, comparing G.3 to G.2, is observed. Figure 8.17c, displaying the box plot of the depth-averaged velocities for all simulations, shows that the additional sill at the right entrance (simulation G.3) does not largely affect the velocities inside the river bank compared to simulation G.2. The mean depth-averaged velocity over the full river bank equals 0.035 m/s, which indicates a decrease of 0.004 m/s compared to simulation G.2. The $\frac{U_{\text{flood}}}{U_{\text{ebb}}}$ ratio equals 0.99, which indicates a decrease in ebb dominance as a result of the presence of a sill at the east entrance. From the flow patterns in Figure D.23 it is obtained that the decrease in the magnitude of velocity during the ebb period is noticeable further into the river bank resulting from simulation G.3, relative to G.2.

Closure of entrance

The closure of one entrance of the river bank, results in full blockage of exchange in water and sediment. In simulation G.4 the right entrance of the river bank is fully closed and in simulation G.5 the left entrance of the river bank is fully closed. In Figure 8.17a the velocity profiles obtained at observation point L.2, resulting from simulation G.4 and G.5 show that almost at all times the velocities are close to zero. The maximum ebb and flood velocities at three observation points, 8.17b, display a decrease in velocity where the entrances are 'open' relative to the base case. At the other two observation points, the maximum velocities are almost equal to zero. The decrease in magnitude at the entrance that is not fully blocked is obtained due to the water particles experiencing more friction when flowing towards the river bank. Therefore, less water is flowing towards the river bank and the velocities further

into the river bank significantly decrease compared to the base case. From Figure 8.17c, a large decrease in the magnitude of velocity, both during the full tidal cycle, ebb and flood period is obtained for both simulations compared to the base case. Simulation G.4, closure of the right entrance, displays a decrease in mean velocity during a full tidal cycle from 0.055 to 0.015 m/s compared to the base case simulation. The velocity profile averaged over the entire river bank, has become more flood dominant, the $\frac{\bar{U}_{flood}}{\bar{U}_{ebb}}$ ratio increased from 1.26 (base case) to 1.48. The mean velocities of ebb and flood averaged over the entire river bank decreased from 0.062 to 0.014 m/s and 0.078 to 0.021 m/s respectively. Simulation G.5, closure of the left entrance, displays a decrease in mean velocity during a full tidal cycle from 0.055 to 0.015 m/s compared to the base case simulation. The velocity profile averaged over the entire river bank, has become more flood dominant, the $\frac{\bar{U}_{flood}}{\bar{U}_{ebb}}$ ratio increased from 1.26 (base case) to 1.09. The mean velocities of ebb and flood averaged over the entire river bank decreased from 0.062 to 0.014 m/s and 0.078 to 0.015 m/s respectively.

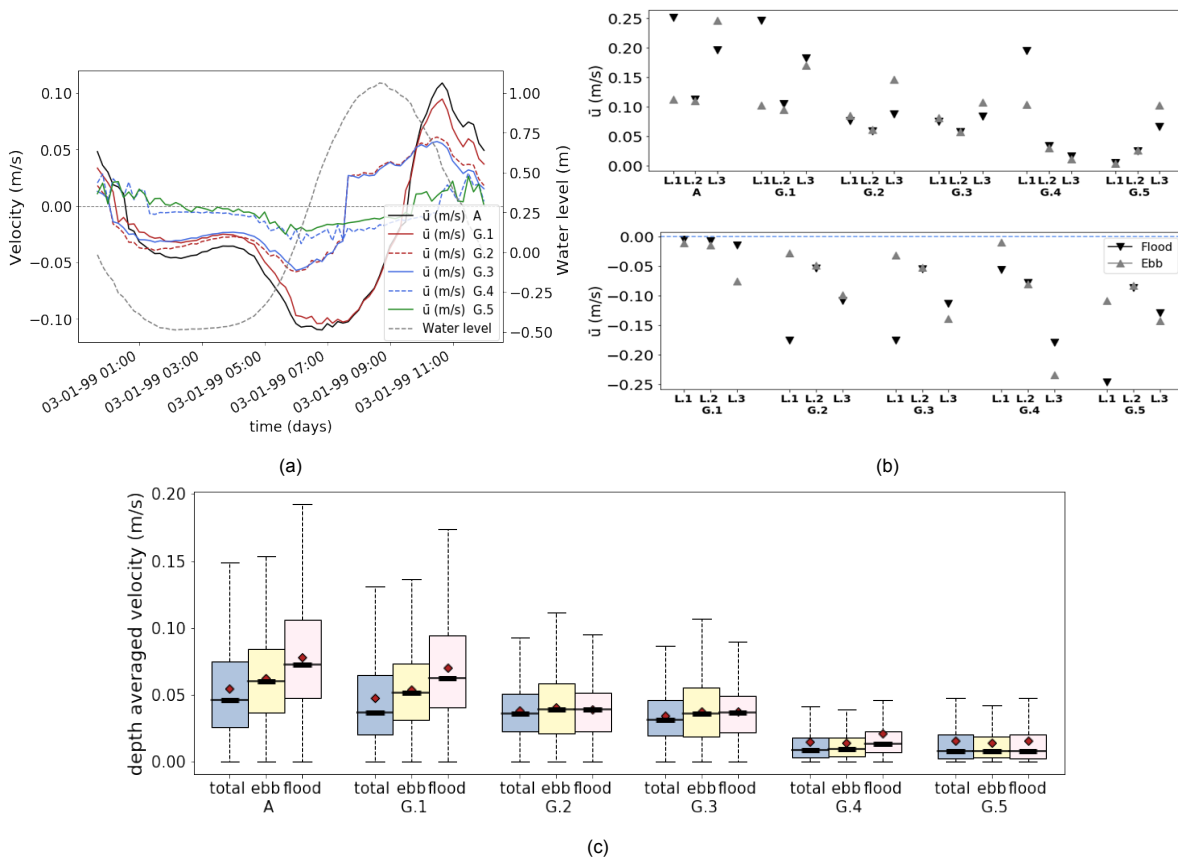


Figure 8.17: In Figure 8.17a the velocity profile at observation point L.2, in the middle of river bank L of simulations A, G.1, G.2, G.3, G.4 and G.5 are displayed. In Figure 8.17b the maximum ebb and flood velocities obtained at three locations from simulations A (morphological tide), G.1, G.2, G.3, G.4 and G.5 are displayed in the top figure. The bottom figure displays the difference relative to simulation A. The variation in simulations is a different surface area of the entrances at the river bank. For the location of the observation points, it is referred to Figure 7.6a. Figure 8.17c displays the box plot on the depth-averaged velocities inside the river bank. The box plots are created for simulations A, G.1, G.2, G.3, G.4 and G.5. All locations inside river bank L are taken into account. The data of the box plots are created both for a full tidal cycle, an ebb period and a flood period. The data in the flood and ebb period are filtered based upon the period in which the water level rise is larger than 0.5 cm/minute. The red diamond indicates the mean of the data set and the black lines inside the box indicate the median of the data set. The coloured range indicates the 25 to 75 percentile of the data set and the dotted lines indicate the lowest and largest data point excluding outliers.

The flow patterns of simulation G.4, closure of right entrance, are displayed in Figure D.24, Appendix D. The flood flow is able to enter the river bank, although the magnitude in velocities is quickly decreasing further into the river bank. The ebb flow is not able to enter the river bank at the right entrance. At the left entrance, the flow is propagating into the river bank but the flow is directed towards river bank K. In

Figure D.25, Appendix D, the flow patterns are displayed for simulation G.5. During the flood period, the flow can enter the river bank at the left entrance. As a result, a large eddy is visible at the tip of the longitudinal wall (right side). The flood flow is prone to enter the river bank as the east groyne is extended further into the navigation channel than the longitudinal wall. The ebb flow is entering the river bank with small velocities, both resulting from the large friction due to the blockage of the east entrance and the geometry of the right groyne in combination with the longitudinal wall.

Morphodynamics results

The effect of variations in surface area of the entrances at river bank L on the morphological evolution of the river bank is separated into two parts. Initially, the effect on the transport of non-cohesive sediment is treated and thereafter the effect on the transport of cohesive sediment is treated. The resulting cumulative erosion and sedimentation patterns of the variations are displayed in Appendix E, Section E.5.

Non-cohesive sediment

The results of the adaptations are compared to the base case simulation. The base case simulation, incorporating a nominal diameter of $150 \mu\text{m}$, results in a total sediment input of 0.5 m^3 . In Figure E.13, Appendix E, Section E.5, the resulting cumulative sedimentation and erosion patterns of simulations G.1 to 5 are displayed. Blockage of the entrance, either the west or east entrance, results in a reduction in sediment input of non-cohesive sediment. The presence of a sill at -1.0 m NAP leads to a reduction of coarse sediment input. The effect of a sill present at the west entrance is larger than at the east entrance, as initially, the largest amount of sedimentation is observed at the west entrance resulting from the base case. The total input of non-cohesive sediment at river bank L, resulting from six months of morphological modelling, is equal to 0.45, 0.23, 0.2, 0.35, and 0.05 for simulations G.1, G.2, G.3, G.4, and G.5 respectively. Either fully closing or partly closing the westward entrance results in the largest decrease in sediment import.

Cohesive sediment

In Figure E.14 and E.15, Appendix E, Section E.5 the resulting cumulative erosion and sedimentation patterns are displayed for all simulations incorporating a non-erodible and erodible bed layer. In Figure 8.18, the sediment budget for simulation A, G.1, G.2, G.3, G.4 and G.5, incorporating both a non-erodible and erodible bed layer is displayed. In addition, in Figure 8.19, the morphological evolution of simulation A, and G.1 to 5 is displayed incorporating an erodible bed layer.

Sills at entrances

Simulation G.1, including a sill at -1.0 m NAP at the east entrance, results in a decrease in cohesive sediment import incorporating both a non-erodible and erodible bed layer. Incorporating an erodible bed layer results in an increase in the ratio between sedimentation and erosion ($\frac{S}{E}$) from 0.23 to 0.28. The total amount of erosion and sedimentation observed equals 88 and 25 m^3 respectively after six months of morphological modelling. For the base case these this equals 123 and 28 m^3 for erosion and sedimentation respectively. A large decrease in erosion is observed resulting from the presence of a sill. From Figure E.15 (Appendix E, Section E.5) it is observed that the decrease in the magnitude of erosion is resulting from less erosion at the east entrance. The presence of a sill decreases the magnitude in which the ebb flow enters the river bank, which decreases the amount of erosion. In addition, the presence of a sill decreases the outflow of cohesive sediment. From Figure 8.18a it can be observed that the decrease in erosion is present in areas 1-4. In addition, a decrease in sediment import is observed in the shallow area (area 6-8) resulting from the presence of a sill. From the hypsometric analysis, Figure 8.19, it can be obtained that the morphological evolution of the river bank is not much affected by the presence of a sill at the east entrance. A smaller amount of erosion at low bed levels and a smaller amount of sedimentation at higher bed levels is present resulting from simulation G.1 compared to simulation A. The simulations incorporating a non-erodible bed layer display a decrease in sediment import of cohesive sediment relative to the base case simulation. The import of cohesive sediment has decreased from 15.5 m^3 in the base case to 14.5 m^3 resulting from simulation G.1. Figure 8.18b shows that the decrease in import of sediment is equally spread over all eight areas. The presence of a sill results in less import of cohesive sediment but the same pattern of sediment deposition is observed. No increased sediment deposition is present just in front of the sill.

Simulation G.2, including a sill at -1.0 m NAP at the west entrance in combination with an extended left groyne, results in a decrease in cohesive sediment import incorporating both a non-erodible and erodible bed layer. Incorporating an erodible bed layer results in an increase in the ratio between sedimentation and erosion ($\frac{S}{E}$) from 0.28 to 153. The total amount of erosion and sedimentation observed equals 0.09 and 13.77 m³ respectively after six months of morphological modelling. For the base case these this equals 123 and 28 m³ for erosion and sedimentation respectively. Almost no erosion is observed resulting from an implementation of a sill at the west entrance. To determine the effect of the presence of a sill at the west entrance, the simulation results are compared with simulation F.4. In this simulation, the west groyne is elongated up to the same extent as incorporated in simulation G.2. The eroded and deposited volume equals 7.24 and 12.34 m³ after six months of morphological modelling resulting from simulation F.4. The additional presence of the sill decreases the amount of erosion observed at the river bank and in addition the imported amount of sediment has increased compared to simulation F.4. This originates from both a large decrease in the magnitude of the velocity and the blockage of sediment-rich water by the presence of a sill. The erosion observed from simulation G.2 is observed at the intertidal area and both at the west and east entrances. It is likely that the eroded sediment is deposited inside the river bank and not transported into the navigation channel. This results from the enhanced sedimentation present close to the entrances in comparison with the surrounding surface area of the river bank. From Figure 8.18a it is observed that hardly any sediment import or export is observed at river bank L. The resulting morphological evolution of simulation G.2 displays that below -0.55 m NAP a relatively smaller increase in bed level is observed compared to simulation A. Above -0.55 m NAP a decrease in bed level is observed compared to the initial situation (t_0), which indicates the erosion of the intertidal area.

The simulations incorporating a non-erodible bed layer display an increase in sediment import of cohesive sediment relative to the base case simulation. The import of cohesive sediment has increased from 15.5 m³ in the base case to 18.1 m³ resulting from simulation G.2. From Figure E.14(Appendix E, Section E.5) it is observed that enhanced sedimentation is present at the entrances compared to the base case simulation. This originates from the decrease in the magnitude of flow velocities by which further transport of sediment into the river bank is obstructed. In addition, re-suspension and thereby export of the sediment is obstructed by the presence of a sill. From the sediment budget in Figure 8.18b the increase in sediment import close to the longitudinal wall (area 1 -4) is observed. A decrease in import of cohesive sediment close to the landside of the river bank is obtained (area 5 - 8) relative to the base case.

Simulation G.3 is a combination of simulation G.1 and G.2, incorporating a sill at -1 m NAP at both sides and an extended west groyne. The simulation results display an increase in cohesive sediment import compared to the base case incorporating a non-erodible bed layer. The import of cohesive sediment resulting from an erodible bed layer has decreased compared to simulation A. Incorporating an erodible bed layer results in an increase in the ratio between sedimentation and erosion ($\frac{S}{E}$) from 0.28 to 86 compared to the base case. This significant decrease in ratio compared to simulation G.2 results from a slight increase in erosion which equals 0.17 m³ resulting from six months of morphological modelling of simulation G.3. The resulting import of cohesive sediment equals 14.7 m³. From Figure E.15(Appendix E, Section E.5) it is observed that the additional presence of a sill at the right entrance results in less erosion at the east entrance. The sediment budget in Figure 8.18a shows that the sediment budget resembles the budget observed from simulation G.2. The same is accounted for regarding the morphological evolution of the river bank, Figure 8.19.

The simulations incorporating a non-erodible bed layer display an increase in sediment import of cohesive sediment relative to the base case simulation. The import of cohesive sediment has increased from 15.5 m³ in the base case to 18.1 m³ resulting from simulation G.3. This amount equals the import of cohesive sediment obtained from simulation G.2. From Figure E.14(Appendix E, Section E.5) it is observed that the exact same sedimentation pattern is observed as from simulation G.2. The sediment budget in Figure 8.18b also displays the same budget as was observed from simulation G.2. This indicates that the additional implementation of a sill at the east entrance does not largely affect the

sediment import at the river bank. This originates from the magnitudes of velocity already being small. As a result, the effect of an additional sill at the east entrance is almost negligible.

Full closure of entrances

In simulation G.4 the right entrance of the river bank is fully closed and in simulation G.5 the left entrance of the river bank is fully closed. Both simulations resulted in a decreased import of cohesive sediment incorporating both an erodible and non-erodible bed layer. In simulation G.4 the eastward entrance of the river bank is closed. Incorporating an erodible bed layer results in an increase in the ratio between sedimentation and erosion ($\frac{S}{E}$) from 0.28 to 6. The total amount of erosion and sedimentation observed equals 16 and 9 m³ respectively after six months of morphological modelling. For the base case these this equals 123 and 28 m³ for erosion and sedimentation respectively. This large decrease in erosion is observed from the significant decrease in magnitudes of velocity at the river bank. Due to the closure of the entrance, the river bank is no longer contributing to the cross-sectional area through which a part of the discharge can flow. From the cumulative erosion and sedimentation pattern, it is observed that erosion is present at the west entrance. At this location, the magnitudes in flow velocity, both ebb and flood, are large enough for the erosion of cohesive sediment. Part of the eroded sediment is transported towards river bank K (west neighbouring river bank) and a part of the eroded sediment is transported into river bank L. The sediment budget in Figure 8.18a shows the small amount of erosion present compared to the base case simulation. In addition, it is observed that the import of cohesive sediment in the shallow area is small compared to simulation A. The same is accounted for regarding the morphological evolution of the river bank, Figure 8.19. Smaller increases in bed level are obtained below -0.55 NAP compared to simulation A. In addition, erosion is observed above -0.55 NAP which originates from the erosion of the intertidal area present in the southeast corner.

The simulations incorporating a non-erodible bed layer display a decrease in sediment import of cohesive sediment relative to the base case simulation. The import of cohesive sediment has decreased from 15.5 m³ in the base case to 10.3 m³ resulting from simulation G.4 after six months of morphological modelling. From Figure E.14(Appendix E, Section E.5) it is observed that the largest sedimentation is present close to the west entrance and is thereafter decreasing in magnitude into the river bank. From the sediment budget in Figure 8.18b it can be observed that a decrease in sediment import is observed over the entire river bank compared to simulation A. The effect of the full closure of the right entrance results in a decrease in sediment import. In addition, the cohesive sediment is not transported further into the river bank as a result of the velocities being close to zero.

In simulation G.5 the west entrance of the river bank is closed. Incorporating an erodible bed layer results in an increase in the ratio between sedimentation and erosion ($\frac{S}{E}$) from 0.28 to 8. The total amount of erosion and sedimentation observed equals 0.6 and 5 m³ respectively after six months of morphological modelling. For the base case these this equals 123 and 28 m³ for erosion and sedimentation respectively. The geometry at the river bank displays that the tip of the east groyne is located further into the navigation channel than the longitudinal wall. As a result, the flow during the flood period is more prone to flow into the river bank. From the cumulative erosion and sedimentation pattern, it is observed that a negligible amount of erosion is present at the entrance. The same is observed from the sediment budget, as no significant export or import of sediment is present.

The simulations incorporating a non-erodible bed layer display a decrease in sediment import of cohesive sediment relative to the base case simulation. The import of cohesive sediment has decreased from 15.5 m³ in the base case to 10.9 m³ resulting from simulation G.5 after six months of morphological modelling. From Figure E.14(Appendix E, Section E.5) it is observed that the largest sedimentation is present close to the east entrance and is thereafter decreasing in magnitude into the river bank. From the sediment budget in Figure 8.18b it can be observed that the sediment import of cohesive sediment is almost equally spread over the river bank. The effect of the full closure of the left entrance results in a decrease in sediment import. In addition, the cohesive sediment is not transported further into the river bank as a result of the velocities being close to zero.

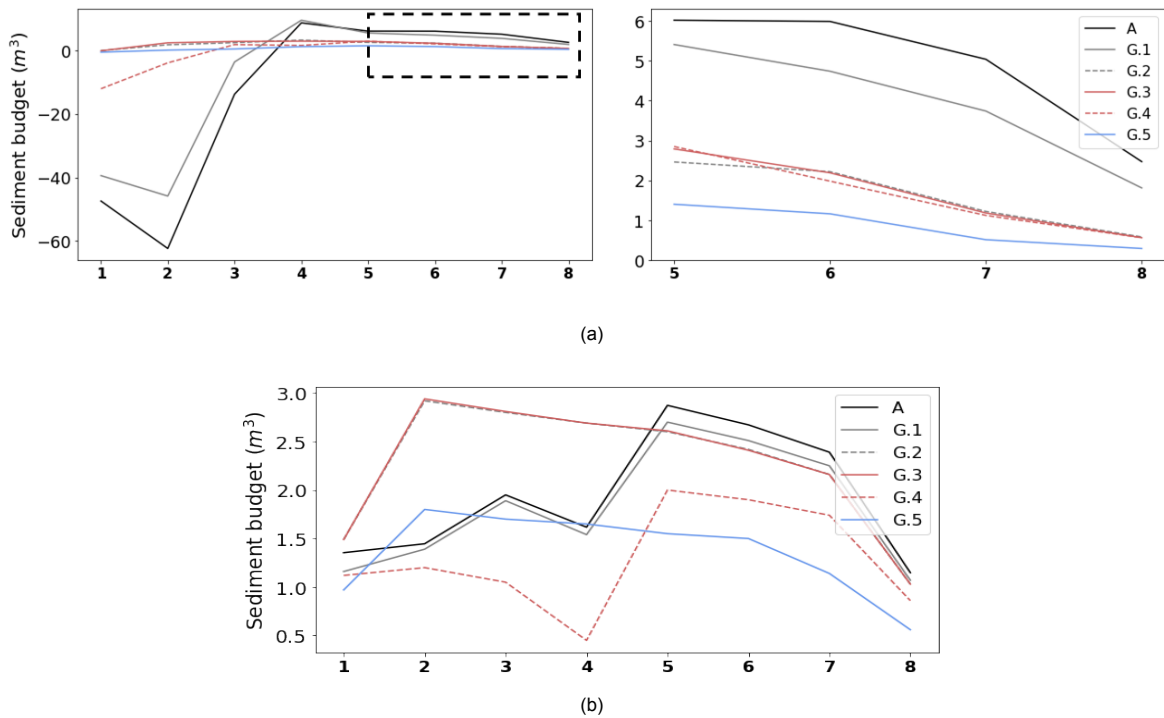


Figure 8.18: Figures displaying the sediment budget after six months of morphological modelling. The simulations displayed contain a varying surface area of the entrances at river bank L. In addition, base case simulation A is displayed. Negative values indicate export of sediment (erosion) and positive values indicate import of sediment (sedimentation). The sediment layer at the river bank is erodible for Figure 8.18a. In the left part of Figure 8.18a the sediment budget for the entire river bank is displayed, from 1 to 8. The black dotted area indicates the shallow area of the river bank of which the sediment budget is visualized in the right part of Figure 8.18a. In Figure 8.18b the sediment budget is visualized resulting from a non-erodible bed layer at the river bank. Only positive values are present in the y-axis as no erosion can occur. Note that the areas indicated by number in the above figures and visualized in Figure 7.20 are not equally sized. Area 1 represents the area closest to the navigation channel and area 8 is the area closest to the land-side of the river bank. Note that simulation G.2 (grey dotted line) and G.3 (red line) almost display the same results by which the distinction between the two simulation is difficult to observe.

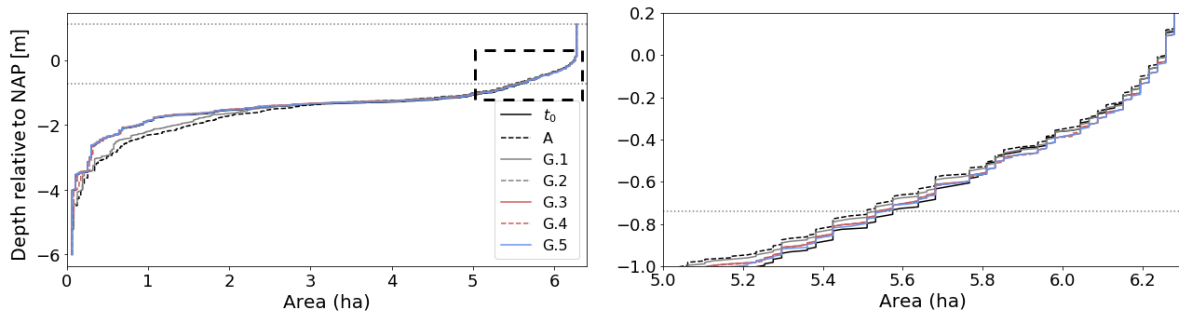


Figure 8.19: In the left part of the figure the resulting morphological evolution is displayed after six months for variations in surface area of the river bank entrances. The black dotted area indicates the shallow area (from 1.0 m NAP) of the river bank of which the hypsometric curve is visualized in the right part of the figure.

	A	G.1	G.2	G.3	G.4	G.5
\bar{u} (m/s)	0.055	0.048	0.038	0.035	0.015	0.015
$\frac{u_{flood}}{u_{ebb}}$	1.26	1.31	0.96	0.99	1.48	1.09
S non cohesive (m ³)	0.5	0.45	0.23	0.20	0.35	0.05
E cohesive erodible (m ³)	123	88	0.09	0.17	16	0.6
S cohesive erodible (m ³)	28	25	14	15	10	5
S/E cohesive erodible (-)	0.23	0.28	153	86	0.6	8.23
S cohesive non erodible (m ³)	15.5	14.5	18.1	18.1	10.3	10.9

Figure 8.20: Table displaying the effect of different surface areas of the entrances at the river bank on several parameters regarding the hydrodynamics and morphodynamics at river bank L. \bar{u} represents the mean depth-averaged velocity over a full tidal cycle at the river bank. The $\frac{u_{flood}}{u_{ebb}}$ ratio provides information on the relative ebb and flood dominance of the velocity signal at the river bank. The third parameter represents the sediment input of non-cohesive sediment incorporating a diameter of 150 μm . The fourth and fifth parameter represents the eroded and deposited sediment respectively for an erodible bed layer. The sixth parameter, S/E, represents the ratio between sedimentation and erosion at the river bank incorporating an erodible bed layer. The last parameter represents the sediment input of cohesive sediment incorporating a non-erodible bed layer

Discussion on model results

To conclude this section, the proposed hypotheses in Chapter 6 are evaluated.

1: It is expected that the implementations of sills affect the flow pattern in terms of increasing/decreasing the ratio between the ebb and flow velocities. Besides that, the sedimentation at the river bank is ought to increase behind the sill. This only applies when the flow velocities at the river bank are large enough to transport sediment from the other entrance to this location.

The simulation results confirm the hypothesis. The effect of the implementation of a sill has a large impact on the velocity profile observed close to the sill but is less noticeable further into the river bank. The implementation of a sill at the east entrance results in a decrease in the magnitude of both ebb and flood velocities. The mean velocity during a full tidal cycle (\bar{u}) decreased from 0.055 to 0.048 m/s compared to the base case simulation. The velocity profile averaged over the entire river bank, has become more flood dominant, the $\frac{u_{flood}}{u_{ebb}}$ ratio increased from 1.26 (base case) to 1.31. In addition, The mean velocities of ebb and flood averaged over the entire river bank decreased from 0.062 to 0.053 m/s and 0.078 to 0.070 m/s respectively. A decrease in the magnitude of the mean flood velocities is observed as the flow experiences additional friction originating from the presence of a sill at the east entrance, which obstructs the outflow. The incorporation of a sill at the west entrance, in combination with an extended west groyne, leads to an ebb dominant velocity profile. The $\frac{u_{flood}}{u_{ebb}}$ ratio equals 0.97. This ratio is equal to 1.07 when only an extended west groyne is implemented, from which it can be concluded that the presence of a sill leads to an increased ebb dominance. The mean depth-averaged velocity over the entire river bank equals 0.038 m/s.

From the simulations incorporating an erodible bed layer, it is observed that the presence of sills results in less erosion at the entrance in which a sill is implemented. In addition, a decrease in sediment import is observed at the river bank. The import of cohesive sediment, incorporating a non-erodible bed layer resulted in a decrease in sediment import from 15.5 to 14.5 m³ compared to the base case from the implementation of a sill at the east entrance. Incorporating a sill at the west entrance results in an increase of 0.3 m³ compared to the simulation including the elongation of the west groyne only. The enhanced sedimentation is present just behind the sill. From the sedimentation pattern, it is observed that resulting from the implementation of sills at either the west or east entrance, just behind the sill

increased sedimentation is observed as a result of the lower dynamics present in this area. From the simulation results, it is obtained that the increase in sedimentation behind the sills is not resulting from sediment originating from the opposite entrance. The presence of increased sedimentation close to the sills originates from a decreased magnitude of velocity close to the sill.

2: It is expected that a full closure of the groyne areas will increase/decrease the ratio between ebb and flow velocities. The magnitude of velocities present at the river bank is expected to decrease. More sedimentation is expected at the river bank as a result of the decrease in the magnitude of velocity which is expected to result in additional settlement of suspended sediment.

The simulation results partly confirm the hypothesis. The results of fully blocking the west or east entrance showed that the velocities at the river bank significantly decreased to being almost zero. The mean depth-averaged velocity over the entire river bank \bar{u} decreased from 0.055 to 0.015 m/s for either full closure of the west or east entrance compared to the base case. Full closure of the east entrance resulted in a relatively more flood dominant velocity profile, $\frac{\bar{u}_{\text{flood}}}{\bar{u}_{\text{ebb}}}$ ratio increased from 1.26 to 1.48. Full closure of the west entrance resulted in a relatively less flood dominant velocity profile, $\frac{\bar{u}_{\text{flood}}}{\bar{u}_{\text{ebb}}}$ ratio decreased from 1.26 to 1.09.

Less sedimentation of cohesive sediment is observed at the river bank resulting from the closure of either the west or east entrance. Fully closing one entrance of the river bank results in a significant decrease in velocity magnitudes. This results from the large increase in friction that is experienced by the flow by which a smaller volume of water is flowing into the river bank. This results in a smaller import of cohesive sediment into the river bank, and the cohesive sediment not transporting further into the river bank resulting from the velocities being close to zero. The total import of cohesive sediment import into the river bank decreased from 15.5 to 10.3 and 10.8 m³ for either full closure of the east or west entrance compared to the base case. The sediment deposits near the open entrances. No erosion of cohesive sediment is visible as the critical shear stress for erosion is not reached. This leads to the river bank functioning as a sediment trap.

The sills present in this research are implemented as a weir in Delft3D. These are incorporated into the numerical model by an empirical estimation of the energy loss over the weir and thereafter converted into an effective friction coefficient. The friction that is experienced by the flow depends on the slope of the hydraulic structures. Although the possibility exists of calibrating the effective friction coefficient this is not included in this research due to time consideration. According to literature, the slope of the sill present is important for the sediment transport that can flow over the sill. Therefore, it is often recommended to implement a sill into the bed topography by which this slope can be incorporated. This requires a small grid size implemented in the model. This is not executed due to time limitations. From the literature review, it is obtained that the presence of a sill is ought to introduce an eddy formation behind the sill. In addition, it is expected that flow from the navigation channel approaches the river bank with a different angle as is resulting from the base case simulation. Both are not obtained from simulation results. The grid size resolution at the river bank is responsible for the absent eddy circulation. The slope of the sill affects the sediment transport over the sill, therefore it is assumed that neglecting the sloping effect is responsible for the absence of a change in the flow direction. The presence of a sill reduces the sediment transport of non-cohesive sediment into the river bank, which confirms that the presence of a sill hinders bedload transport into the river bank. The ratios of S/E are largely affected by small changes in sedimentation and erosion. For simulations G.2 and G.3, these ratios equal 153 and 87. This displays that using this ratio to compare solutions is not always applicable as the latter is very sensitive to changes.

Discussion

Before establishing the main conclusions resulting from the literature review, data analysis, and modelling results, a reflection is presented. This chapter provides a discussion on four levels. First, the assumptions of the broad research into all tidal parks in the Rhine-Meuse estuary are discussed. Secondly, the uncertainty in the executed data analysis is discussed. Thirdly, the choices and their effect on the results of the Delft3D schematization are discussed. Lastly, the interpretation of the model results is discussed.

9.1. Literature review on tidal parks

The literature review on all tidal parks in the Rhine-Meuse estuary resulted in a table summarizing many aspects of the tidal parks. The parks located in the Dordtse Biesbosch were not taken into consideration due to time constraints. The overview table was based on literature, but not all information was obtained from scientific articles. In addition, a large amount of information in the table originates from personal communication with an ecologist of Zuid-Hollands Landschap. This interview provided information on the sediment present at multiple tidal parks. The sediment found in tidal parks is expected to differ spatially. Only one sediment type was provided. However, the spatial distribution of sediment provides useful insights into sediment transport at tidal parks. Besides, information on the sediment, problems occurring and past maintenance at tidal parks were often lacking. These are considered important parameters in the literature review.

9.2. Insights from measurements

The data analysis in this research consists of three parts. The morphological evolution of the river banks, the analysis of velocity measurements at the Groene Poort obtained from a pilot project by Aquitec, and sediment samples retrieved from the tidal park.

The morphological development of the river banks in the Nieuwe Waterweg is determined based on data obtained by multibeam echosounders. As a result, the bed level measurements are limited to depths below +0.5 m NAP, by which already some data points in the intertidal zone are omitted. To determine the morphological evolution of a riverbank, it is of great importance that the data sets contain approximately an equal number of data points. The latter is not the case in this research. The evolution is researched over 4 years, spread over 5 datasets. The incompleteness of the datasets varies per river bank ranging to only representing 81 % of the '100 %' data set. By this inequality in data sets, the conclusions derived from the morphological evolution of bed levels above ≈ -0.7 m NAP are affected by uncertainties and inaccuracies. Data on the velocity measurements by a pilot project are analyzed. Even though the velocity measurements had limited temporal coverage and had some quality issues, they still provided valuable insight into the velocity magnitudes in this area. Thirdly, visual observations of the sediment at several locations at river bank L are available. The sediment samples were obtained close to the land side of the river bank arbitrarily and in the upper layer ± 5 cm of the intertidal area. A higher frequency of sediment sampling, in combination with sampling further below bed level, would increase the certainty of obtained sediment transport patterns at the river bank.

9.3. Insights from numerical model simulations

In this section, the choices and assumptions in the Delft3D model schematization are discussed. Disregarding the shortcomings, the model well represents the hydrodynamics at the river bank resulting from the combination of tidal forcing and freshwater discharges. The velocity profile at the river bank

in the numerical model resembles the measurements executed by Aqitec. In addition, the model can represent the morphological development of the river bank to different hydrodynamic forcing and variations in geometry.

Impact of depth-averaged assumption

In line with computational time, it was chosen to use a 2DH numerical model. It was assumed that in the area of interest, 3D effects were of minor importance. Using a 2DH numerical model results in the salt wedge in the Nieuwe Waterweg not being included. The salt wedge in the Rhine-Meuse estuary results from the interference of water bodies with different densities: freshwater inflow from the Rhine and Meuse and the salt water entering from the North Sea. This density-driven flow largely affects the estuarine circulation, and also the 3D velocity profile in the Nieuwe Waterweg (De Nijs et al., 2011). From the river mouth, a few kilometres inwards including the location of tidal park the Groene Poort, the velocity signal is flood dominant near the bottom. Import of sediment is observed. The developed model, including a freshwater discharge of 1900 m³/s, shows ebb dominant velocities and export of sediment in the navigation channel. Although the processes in the navigation channel are not the main focus of this research, the latter affects the amount of sediment being suspended in the water column. In this research, larger amounts of SSC are obtained during ebb rather than during flood as this is much related to the observed velocities (37 mg/l and 7 mg/l respectively (morphological tide $d_{50}=150 \mu\text{m}$)). In reality, the presence of the salt wedge induces, during a large part of the tidal cycle, flood dominant velocities near the bottom. This affects the variation in SSC during a tidal cycle which is not included in the numerical model. Besides the salt wedge affecting the velocity profile and so the amount of suspended sediment, the exchange flows caused by density differences often result in the accumulation of sediment at the tip of the salt wedge. Therefore, the assumption of neglecting three-dimensional flow processes can result in an underestimation of the import of fine sediment. The exchange flows caused by density differences between the channel and the groyne are expected to increase the import of fine sediment at the groyne area.

Impact of hydrodynamic boundary conditions

The hydrodynamic boundary conditions of the developed model originate from the Rhine-Meuse Morphological model (Sloff et al., 2012). In this RMM model, a discharge can be manually implemented as an upstream boundary condition and the downstream boundary condition is a tidal signal. The tidal signal is simulated as a repeated morphological tide, which implies that variations in terms of spring-neap cycles are not accounted for. The freshwater discharge entering the Nieuwe Waterweg is constantly varying, with high discharges between approximately December and July and low discharges during the other time frame (Linde and Aerts, 2008). The fresh-water discharge implemented in the model is equal to 1900 m³/s for a simulation period of six morphological months. The combination of variable tidal forcing and freshwater discharges leads to a dynamic system with constantly changing flow directions and magnitudes. This is contrary to the model's representation. As this was regarded as a significant downside of the model, two additional scenarios were modelled incorporating a spring tide and a spring tide in combination with a surge. The adapted time series again include a constant varying water level, as the time series were manually adapted. This leads to the dynamic system not being well represented. However, the exact solution is not considered to be important in this research, but the general tendency resulting from different types of forcing scenarios. This research provides insights into the morphological development of the tidal park under different hydrodynamic forcing conditions.

Impact of morphodynamic initial and boundary conditions

For simplicity and interpretation reasons, cohesive and non-cohesive sediment were modelled separately. In reality, a combination of both is present in the Rhine-Meuse estuary, and also the interaction between the two sediment types is present. Combining the results of both simulations provides insights into the sediment transport in the tidal park which resembles reality. Important factors of the transport of non-cohesive sediment are the magnitudes of relative ebb and flood velocities as well as the available sediment. The source of sediment in the numerical model originates from the sediment present as bed layer in the nested model. In reality, during flood marine sediment is brought into the estuary along with the flow while fluvial sediment is brought into the estuary with the freshwater inflow. This is neglected in the developed numerical model. It is expected that this does not largely affect the sediment transport into the river bank but only the sediment transport in the navigation channel. Non-cohesive sediment

is implemented as a single grain size applied for the entire grid. In reality, there is a large variation in sediment in the estuary as was elaborated in Chapter 2. Including multiple grain diameters at once, might provide a more realistic result of reality. As base case for variations in geometry, a diameter of $150\ \mu\text{m}$ is incorporated, which is in the same order of magnitude as the representative nominal diameter in the navigation channel at the location of interest. Therefore, it is expected that the simulation results well represent reality, disregarding the effect of implementing multiple grain sizes.

Sensitivity of the numerical model

Numerical models require the representation of complex processes by often empirical formulas including a limited number of parameters. These parameters often cannot be obtained by measurements. In this research, the following parameters are of importance: the horizontal diffusivity and the critical shear stress for the erosion of silt. These parameters largely affect the morphological development of the river bank.

Model limitations regarding important physical processes

The effect of waves and wind were not incorporated in the numerical model. Results of this research indicate that the additional shear stresses originating from waves play an important role in sediment transport further into the river bank area. Coarse sediment deposits close to the entrance although this sediment is mainly located at the left corner of the river bank. The additional shear stresses originating from wind and vessel-induced waves at the area of interest were calculated by hand and ranged from 0.02 to $0.24\ \text{N/m}^2$. The effect is significant and can stir up sediment and increase transport towards the land-side of the river bank. In addition, the wind stresses exerted on the water surface can play an important role in sediment transport. The latter can result in the set-up of the water level and reverse the flow, dependent on the geometry and surface area of the estuary (Colosimo et al., 2020). At the location of this tidal park, river bank L, the largest wind speeds originate from the direction in which the wind is largely obstructed by dikes, buildings, and trees. Therefore, it is expected that the effect of wind at the location of interest is relatively small. However, a combination of both waves and wind effects is likely to be responsible for the re-suspension and advection of sediment towards the river bank.

Limitations of implementation of hydraulic structures in Delft3D

The changes in geometry in this model consist of, among other, varying lengths of the groynes and longitudinal walls. These are modelled as thin-dams in Delft3D. Thin dams ensure no exchange of water and sediment and are defined at velocity points that prohibit flow exchange between two adjacent computational cells (Deltares, 2018). This limits the location of the hydraulic structures. In addition, no slopes of the structures can be implemented. As a result, the surface area of the entrances on both sides deviate from reality. Smaller entrances are present in the numerical model, and therefore the flow velocities inside the river bank area are likely smaller than what is obtained in reality. This effect is however assumed to be relatively small. The variations regarding the submergence of groynes and sills were modelled by implementing a weir in Delft3D. The latter was incorporated in the model by an empirical estimation of the energy loss over the weir and thereafter converted into an effective friction coefficient. The friction that is experienced by the flow depends on the slope of the hydraulic structures. Although the possibility exists of calibrating the effective friction coefficient, this was not included in this research due to time constraints. The hydrodynamic results of the structures were in agreement with the hypothesis and therefore it is assumed that results are sufficient.

Overall, improvements are possible in the numerical model and recommendations for the latter are presented in Chapter 11.

9.4. Integration of the results

Numerical models always go hand in hand with simplifications of reality. This also applies to the case study into sediment transport in tidal park the Groene Poort. However, the results of the numerical model can be used to determine the overall response of the area to a changes in hydrodynamics and geometry. Even though the prediction can still deviate from reality, a lot can be learned on the processes that play an important role in sediment transport in tidal parks.

In Figure 9.1 the interpretation of the base-case is visualized. This interpretation is based on a combination of the model results and visual observations at the river bank. These are in agreement with each other, taking into account several assumptions, by which a schematization of the sediment transport in the tidal park can be presented. In this schematization, the effect of vessel induces waves are taken into account. These waves approach the river bank at an angle of 55 deg, indicated in the figure. In Figure 9.1a and 9.1b the sediment transport of non-cohesive sediment is displayed during flood and ebb respectively. Non-cohesive sediment is incorporated in the figure with coarse sand particles (dark yellow) and fine sand particles (light yellow). Coarse sediment immediately deposits near the entrances of the river bank as the velocities further inside the river bank do not reach the critical velocities for transport according to the developed model. Coarse sediment is visible at the corners of the river bank (visual observations), which indicates that further transport into the river bank area originates from the effect of wind and waves. This confirms the importance of waves in tidal park the Groene Poort. Fine sediment is supposed to deposit further into the river bank area, as the critical velocity is smaller.

The transport of cohesive sediment is displayed in Figure 9.1c and 9.1d. Low dynamic areas are indicated with blue dots. The settlement of silt in this figure is indicated as if it would occur during periods of ebb and flood. Simulation results showed that sediment deposits during the period of constant low water and in the slack periods. During these time frames, sediment can settle over a large part of the river bank. Excluding the locations of the eddies close to the groynes. However, over a large part of the river bank, the velocities are large enough to reach the critical shear stresses for re-suspension of the sediment. The main part is transported towards the navigation channel. A small part is transported towards the areas indicated with the blue dots. The effect of vessel induced waves is expected to be responsible for additional transport towards these areas. Besides, the velocities at the low dynamic areas are not large enough for re-suspension of the sediment. Therefore, the sediment deposited at these locations is not expected to erode.

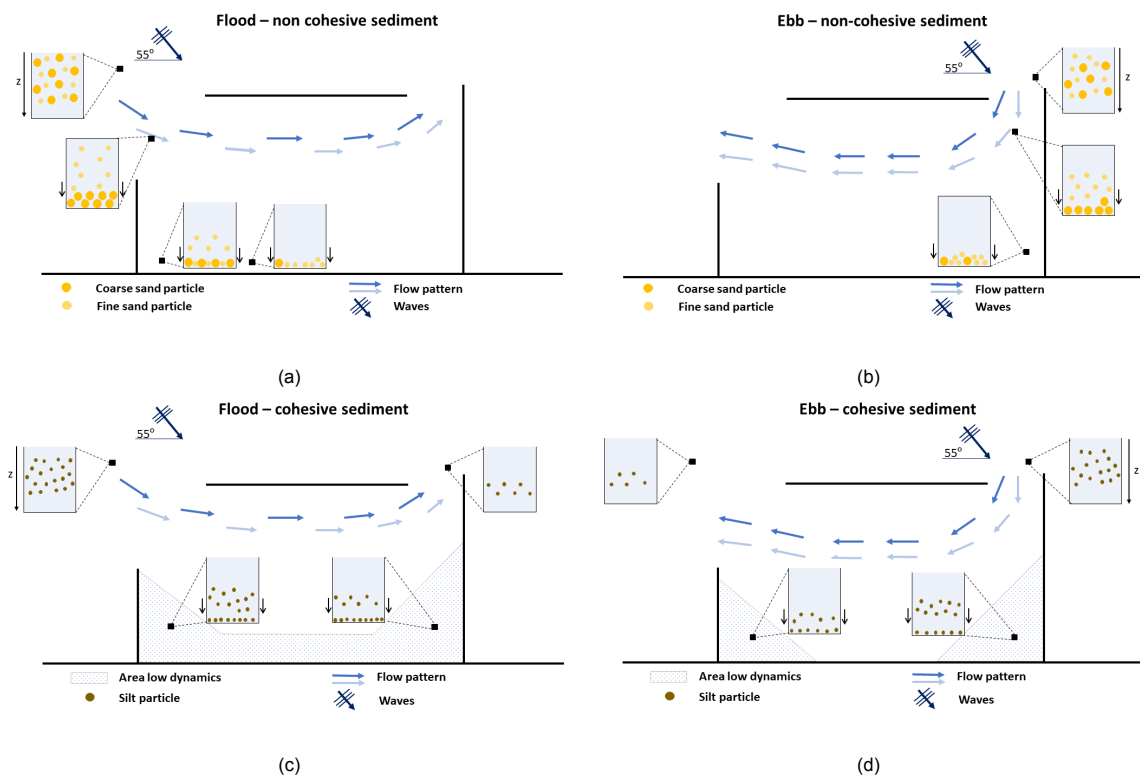


Figure 9.1: Schematization of the sediment transport of cohesive and non-cohesive sediment during flood and ebb in the absence of wind and wind waves. The blue arrows indicate the flow pattern. The light blue rectangles indicate the water column at the indicated location (black rectangle). The colored circles represent sediment grains.

This research was focused upon river bank L, which is an area of 220 x 230 meters. In terms of numerical modelling, this is a relatively small area that results in difficulties for including all the governing processes. It was thought to generalize the model results to make them applicable to other river banks inside the Nieuwe Waterweg as in the near future more tidal parks consisting of longitudinal walls and groynes will be constructed. This generalization of the results should be interpreted with caution, as this research showed that the surrounding area of the river bank is an important factor in the resulting sediment transport into the river bank area. Therefore, one cannot directly use the results obtained in this research and use them as if they are applicable for every river bank inside the Nieuwe Waterweg. Although the gross results will be equal, the effect of neighbouring river banks, being in the 'lee' area of another obstruction, and the location inside the river (outer or inner bend) affect the sediment transport.

To use the model in a manner that will provide useful insights, initially, the present-day situation both regarding bed topography and geometry was modelled. These results were compared with past trends obtained from changes in bed level obtained from data. From the simulations including non-cohesive sediment, it was directly obtained that this type of sediment could not enter the river bank resulting from currents only, as the sediment immediately deposits close to the entrance. As discussed, the effect of wind and vessel-induced waves play an important role in the latter. The transport of silt is modelled both incorporating a non-erodible and an erodible bed layer at river bank L. The reality is somewhere in between both simulations, and should also be considered as such. To deal with the limitations of the model regarding sediment transport, the results of the simulations including variations in hydrodynamic forcing and geometry have to be interpreted compared to the base case. This ensures that the relative effects of the variations can still be determined. Results from the base case show that both the velocities and sediment import at the river bank area are relatively small. When comparing the results in ratios, for instance $\frac{U_{flood}}{U_{ebb}}$ and sediment import over export ($\frac{S}{E}$), the effects of variations in geometry seem significant. It should be noted that the ratios are sensitive, as the base-case magnitudes are relatively small.

Conclusions

The objective of this research was to obtain a comprehensive understanding of the physical processes that are of importance in constructed tidal parks in the Rhine-Meuse estuary. In addition, it aims to determine the morphodynamic response of a tidal park to different hydrodynamic forcing scenarios as well as changes in the geometry of the tidal park.

The two main forcing mechanisms present in the Rhine-Meuse estuary governing the estuarine circulation are the tide and the freshwater inflow. Currently, 22 tidal parks are present in the Rhine-Meuse estuary which are created for nature or recreational purposes. Here, local forcing mechanisms become more important. The accumulated sediment found in tidal parks mainly consists of silt. This indicates that sediment is mainly transported in suspension and that critical velocities for non-cohesive sediment are not often reached.

The case study in this research is focused on tidal park the Groene Poort, located at the river banks of the navigation channel of the Port of Rotterdam. The processes that affect the hydro- and morphodynamics in this tidal park are the tidal forcing (mean tidal range -0.52 m to $+1.09$ m relative to MSL) in combination with the incoming river discharge in the Nieuwe Waterweg which is regulated to be ≈ 1500 m³/s. The waves originating from passing vessels in the Nieuwe Waterweg are important for sediment transport towards the river bank, as additional shear stresses are exerted. In addition, the geometry of the river bank affects the hydro- and morpho-dynamics. The geometry ensures that the velocity profile at the river bank deviates from the navigation channel. The effect of groynes and the longitudinal wall are observed in the morphological development of river bank L. At the east groyne, a spiralling pattern is observed in the bed indicating a submerged groyne. Moreover, before the construction of the longitudinal wall ripples were observed in the bed resulting from wave-induced transport. These ripples disappeared after the construction of the longitudinal wall. This indicates that sediment transport in the tidal park is largely affected by the decrease in wave action. Field observations show that the sediment present at river bank L mainly consists of fine sand and silt. This indicates that either the velocities are not large enough for coarse sediment transport, or that there is no source of the latter.

At most river banks in the Nieuwe Waterweg, the intertidal areas are increasing. This increase occurs simultaneously with an increase in bed level elevation of the entire river bank. At the outer bends, the height of the intertidal area is smaller than the average height. This indicates the importance of spiralling flow in river bends. River banks closer to the sea contain a lower average river bank height. The intertidal areas are lower in height as well as smaller in surface area. It should be noted that the differences in height are in the order of 10 cm. Other aspects, nourishing the river bank or dredging the navigation channel for example, also affect the height of the intertidal areas.

The mean depth-averaged velocities for the entire river bank are smaller than 0.1 m/s resulting from a morphological tide. The incorporation of a spring tide or in combination with a surge increases the dynamics present at the river bank. The mean depth-averaged velocities at the river bank increased by 17 percent and higher velocities are present over a larger part of the river bank. The increase in dynamics at the river bank, mainly the increase in velocity at the west entrance, is responsible for enhanced transport of coarse sediment towards the river bank. The transport of coarse sediment into the river bank area increases with increasing hydrodynamic forcing and smaller grain sizes. However, no significant import of coarse sediment is observed and the latter is only present at low bed levels This originates from the critical velocities for sediment transport not being reached at the river bank ($u_* :$

0.2 - 0.4 m/s). Cohesive sediment is transported further into the river bank area resulting from an increase in tidal range. The incorporation of a spring tide results in additional sediment deposition at the intertidal area above ≈ -0.56 m NAP. The presence of an additional surge of one metre is responsible for additional sediment deposition in the intertidal area at the corners of the river bank, above -0.48 m NAP. An increase in hydrodynamic forcing ensures that the critical velocities for silt are reached over a larger part of the river bank. The presence of a spring tide solely, or in combination with a surge, is responsible for the erosion of deposited silt at the river bank close to the longitudinal wall.

Adaptations in geometry largely affect the hydrodynamics present at the river bank, both spatially and temporally. The effect of the variations in geometry on the sediment transport of coarse, non-cohesive sediment is negligible. The bed levels at the river bank largely affect the flow magnitudes observed in the tidal park. Higher bed levels decrease the flow magnitudes as a result of an increase in frictional effects and a possible decrease in tidal prism. An increase in bed level reduces the import of cohesive sediment. This originates from relatively small mean depth-averaged velocities, in combination with no water present during low water. In addition, an increase in bed level results in erosion in a larger part of the surface area of the river bank.

A decrease in the length of the longitudinal wall increases the mean depth-averaged velocities at the river bank. Hence, the import of non-cohesive sediment increases. The increase in velocity magnitudes over the entire river bank enhances the re-suspension of deposited cohesive sediment and the sediment being further transported towards the landside of the river bank. The majority of the eroded sediment at the river bank is transported into the navigation channel. The quantity increases with decreasing length of the longitudinal wall. Increasing the length of the longitudinal wall prevents erosion of deposited sediment and ensures the sedimentation being spatially spread over the river bank.

A decrease in groyne height at river bank L increases the magnitude of mean depth-averaged velocities, thereby decreasing the import of cohesive sediment. Besides, the submergence of groynes enhances re-suspension thus erosion of the cohesive sediment at the intertidal areas at river bank L. The length of the groynes is of great importance regarding the ebb or flood dominance at the river bank. A decrease in west (sea-ward) groyne hardly impacts the flow pattern and sediment transport at the river bank, resulting from being in the lee area of neighbouring river bank K. A decrease in length of both the east and west groyne significantly increases the velocity at the river bank and thereby cohesive sediment erodes over a large part of the river bank. The main part of the eroded sediment is transported into the navigation channel, but also a significant increase in intertidal area is observed (0.2 ha).

The implementation of a sill at the entrance of the river bank decreases the magnitude of velocities at the river bank. A decrease in import of non-cohesive sediment import is observed in combination with a decrease in erosion potential. Besides, cohesive sediment deposits behind the sill resulting from a decreased magnitude of velocity. Either fully blocking the west or right entrance results in a significant decrease in the magnitude of velocity. The velocities are almost equal to zero during the full tidal cycle. The import of both non-cohesive and cohesive sediment decreases. The cohesive sediment deposits near the open entrances and no erosion is visible at the river bank. This leads to the river bank accumulating sediment.

This research showed that embedding in the surrounding area, including the location in the river greatly impacts the hydrodynamics and morphological development of tidal parks. When considering possible adjustments to the design in terms of groynes, longitudinal walls and the surface area of entrances, it is important to consider not only the additional amount of sediment import but also the additional amount of erosion. These often go hand in hand. This research showed that the sedimentation process in the Groene Poort is corresponding to a large time frame. In terms of maintenance, this indicates that the river bank remains a dynamic changing area by which maintenance by means of dredging the tidal park is not expected in near future. The presence of a surge can be considered as 'natural maintenance'. Tables are included providing the important parameters both with respect to the hydro- and morpho-dynamics of various adaptations in geometry (Table 8.5, 8.9, 8.16 and 8.20). These tables provide a guide into relatively small adaptations in geometry that will enhance or decrease the natural processes of sedimentation and erosion in the tidal park. These tables can be used in future design and adaptations of already constructed tidal parks.

Recommendations

Morphological modelling always goes hand in hand with simplifications of reality. This also applies to this research on sediment transport in tidal parks. This introduces limitations of the developed model and hence recommendations for further research using a numerical model. In addition, general recommendations on the construction and future research of tidal parks are presented in this section. This chapter is concluded by presenting recommendations for tidal parks in the Nieuwe Waterweg.

11.1. Further research on tidal park the Groene Poort

This was the first study executed with numerical simulations of tidal parks in the Nieuwe Waterweg. Simplifications were therefore made to explore the sensitivity of the system. Based on these simulations, we would recommend extending future simulations by accounting for the following processes.

- To begin with the effect of ship induced waves. This study showed that the sediment transport towards the river bank is not adequately represented by the model. It is recommended to investigate the effect of including waves in the model. In Chapter 3, wave-induced sediment transport and the direction of sediment transport resulting from diffraction are explained. Waves do not only bring sediment into suspension but also exert high shear stresses on the bottom. Therefore, including waves in the model is expected to increase the sediment transport towards the river banks.
- Secondly, the hydrodynamic conditions incorporated in the numerical model are represented by a morphological tide at the seaside boundary. It is recommended that in future research a full spring-neap tidal cycle is implemented such that the daily variation is captured. The boundary conditions implemented in the model should be obtained from a more recently developed model in which the sea-side boundary conditions can be adapted. Besides, in the used RMM-model, a representative tide is incorporated but the effect on the loss of accuracy in morphological changes by replacing the spring-neap tide with a representative tide has not been verified yet.
- Thirdly, it is recommended to perform the simulations in a three-dimensional model. By this, the depth-averaged assumption can be verified and the baroclinic effects on the morphological development of the river bank can be determined.

Some additional recommendations are presented for future numerical modelling of tidal parks.

- In this research, the transport of coarse sediment and silt is treated in separate models. In reality, both coarse sediment and silt are present simultaneously and interact with one another. Therefore it is recommended that in future research they are incorporated into the model simultaneously. In addition, the exclusion of the salt wedge in combination with an ebb dominant velocity signal leads to the export of sand in the nested model. In reality, import of sediment is present at this specific area in the Rhine-Meuse estuary. Although this research showed that bedload transport of sand into the river bank is unlikely, it is recommended that a more flood dominant tidal signal is implemented as this also affects the suspended sediment concentration.
- It is recommended to execute simulations incorporating a longer time frame. In this research, simulations are executed for six morphological months. This period is small in terms of morphological development as the studied changes occur gradually over long time frames.

11.2. General recommendations

Monitoring

In terms of tidal parks in general, there is a lack of data on abiotic factors. Although bed level measurements are executed by multibeam echosounders, these measurements are limited to +0.5 m NAP. This indicates that important information on the intertidal area is not included to its full extent. Therefore it is recommended that bed level measurements are obtained using the LiDAR technology. Information on important factors determining sediment transport could not be validated during this research. These factors include the amount of suspended sediment in the water column and information on the flow velocities and waves (period/height) at the river bank. It would be interesting to set up a measurement campaign, including at least one spring-neap tidal cycle, preferably also including a varying discharge upstream. This could be obtained by a measurement campaign both in April and October. In this measurement campaign, the focus should be on measuring the hydrodynamics (currents and waves) but also the suspended sediment concentration in the tidal park. Preferably the measurements are executed at multiple locations at the river bank for fourteen days. However, this is both time-consuming and costly. If this is not possible as a consequence of the above-mentioned reasons, it is advised to monitor during a spring tide and a neap tide. These represent the extreme scenarios. The locations at which monitoring should be executed is preferably close to both entrances, at each corner of the river bank and in the middle of the river bank. This provides useful information on both the spatial variation, as well as variation in time.

Research other tidal parks

This research started with a broad literature review on all the tidal parks from which it was obtained that some tidal parks are experiencing problems related to sediment transport. There are several tidal parks on which research into the latter could be very useful. It is recommended to research the effect of adaptations in geometry, such as considered in this research, on the effect of sediment transport at those tidal parks. Combining these results will provide a more comprehensive understanding of the sediment transport in tidal parks, and the relative differences between the latter in various tidal parks in more detail. Numerical modelling provides useful insights in terms of the hydrodynamics and the morphological development of the tidal park. In addition, the effect of various adaptations in the geometry of tidal parks is well represented by the use of a numerical model. Therefore, in the future, it is recommended to use numerical models as a tool when constructing or adapting tidal parks. Furthermore, it is suggested to combine the use of a numerical model with monitoring such as described in the previous section. By this, conclusions from the numerical model can be drawn with more certainty regarding the effect of adaptations on both the hydro- and morpho-dynamics.

11.3. Recommendation for tidal parks in the Nieuwe Waterweg

From this research, recommendations can be defined for adaptations of the already present tidal parks in the Nieuwe Waterweg and for the tidal parks that will be constructed in the near future incorporating the same construction method. In the Nieuwe Waterweg, coarse sediment is not responsible for large sediment import in tidal parks located in river bank areas. Even extreme events in combination with relatively small grain sizes did not display large import of sediment. This originates from a lack of hydrodynamic forcing, and consequently, adaptations in geometry do not significantly enhance the sediment transport of coarse sediment into the river bank. Therefore, when the import of coarse sediment (sand) is desired, it should be provided through a nourishment. This research showed that increasing the bed level of the river bank, corresponding to the implementation of a nourishment, does not result in large erosion of sediment present at the river bank (coarse sediment $d_{50} = 150 \mu\text{m}$). A nourishment consisting of cohesive sediment (silt) is not expected to remain at the river bank. Only a small fraction of the eroded nourished sediment is transported towards the river bank and the main part is transported towards the navigation channel. Concluding, it is recommended that when executing a nourishment of sediment a relatively large particle diameter is chosen. Although, from an ecological point of view, taking into account that the desire for creating tidal nature is to enlarge the ecological value, one should be cautious as research showed that ecological values get harmed by a nourishment.

Adaptations in geometry affect the sediment transport of cohesive sediment into the tidal park. At the tidal parks in the Groene Poort, measures are sought which can result in enhanced sedimentation in the tidal parks. The adaptations which result in enhanced sedimentation, and are thus recommended for use in constructed tidal parks, are elaborated in the following section.

A lower groyne height results in increased erosion of sediment at the river bank. More importantly, this research showed that a decrease in height of the groyne results in erosion of the intertidal area at the river bank. This indicates that heightening the groynes up to a level above MHW or even HAT will decrease the erosion potential of the intertidal area. Consequently, when enhanced sedimentation is desired, it is recommended to increase the height of the groynes. The effect of the raise of the groynes on the flood discharge in the Nieuwe Waterweg should be researched before execution. A raise in groyne height above MHW ensures a local decrease in the cross-sectional area of the river at the location of river bank L. Research from Crosato and Kuijper (2002) showed that the increase in height of the groynes present in the bend of Maassluis results in a decrease in horizontal tidal volume. Besides, the increased hydraulic roughness resulting from energy dissipation by the presence of eddies will result in an increased water level in the upstream area of the tidal parks. The effect of heightening the groynes on flood safety should be researched in more detail in further research.

This research showed that the inequality of the length of groynes greatly impacts the flow pattern observed at the river bank. Decreasing the length of the groynes increases the dynamics. This directly implies less import of silt as a consequence of the increased velocities. The import of coarse sediment does not increase significantly resulting from a decrease in groyne length. This indicates that shortening the length of groynes is not a useful adaptation to enhance the import of sediment. Increasing the length of the groyne lowers the dynamics. As a consequence, less erosion is present and mainly sedimentation is present, spread over the full river bank. It is therefore recommended that the length of the west groyne is increased up to the longitudinal wall to enhance sedimentation of cohesive sediment in the tidal park. Although the effect of a surge or spring tide probably erodes the deposited sediment, the presence of wave forcing, in reality, can already be responsible for the transport of sediment close to the longitudinal wall towards the intertidal area of the river bank. At these locations, the enhanced velocities occurring during a spring tide do not result in increased erosion.

The construction of a longitudinal wall in front of the river bank results in the sedimentation at the river bank being more spatially spread and less sensitive to erosion. By increasing the length of the longitudinal wall the above-mentioned effects also increase. In addition, no significant erosion pits are observed close to the longitudinal wall as the velocities present at the entrances decrease by increasing the length of the longitudinal wall. Concluding, when constructing tidal parks it is advised that the longitudinal wall is constructed with the largest length possible as no hinder is observed both regarding the hydrodynamics and morphodynamics. However, the tidal park should remain connected with the river at both sides.

The presence of a sill decreases the erosion potential of the river bank. Furthermore, it ensures that sediment-rich water entering the riverbank is hindered from leaving the river bank when a sill is present. It is advised to locate the sill at the entrance in which incoming water contains the smallest suspended sediment concentration. It is advised that through monitoring, it is determined which flow, relative ebb or flood flow, contains the highest suspended sediment concentration. Using this information the desired location of the sill can be determined.

Lastly, a full closure of the entrance of the river bank could be considered as the last measure for the enhancement of sedimentation. This adaptation significantly decreases the erosion potential of the sediment at the river bank. In addition, the building forces of sediment transport towards the river bank decrease. The combination of a relative decrease in sedimentation and no erosion results in the river bank accumulating sediment. In terms of maintenance, the latter is not recommended as only accretion of sediment is present. In addition, a full closure of one entrance of the river bank results in a significant decrease in the cross-sectional area of the river. Before considering this adaptation, it is recommended to further investigate the effect on the water elevation in the surrounding areas and the corresponding flood safety.

References

- AHN (2020). Arcgis. URL <https://www.ahn.nl/ahn-viewer>.
- Allen, G.P. , Salomon, J.C. , Bassoullet, P. , Du Penhoat, Y. , and De Grandpré, C. (1980). Effects of tides on mixing and suspended sediment transport in macrotidal estuaries. *Sedimentary Geology*, 26(1):69–90. ISSN 0037-0738. doi: [https://doi.org/10.1016/0037-0738\(80\)90006-8](https://doi.org/10.1016/0037-0738(80)90006-8). URL <https://www.sciencedirect.com/science/article/pii/0037073880900068>.
- ARK Natuurontwikkeling (2016). Klein profijt. URL <https://www.ark.eu/gebieden/de-delta/ijsselmonde/klein-profijt>.
- Baptist, M.J. , Tamis, J.E. , Borsje, B.W. , and van der Werf, J.J. (2008). *Review of the geomorphological, benthic ecological and biogeomorphological effects of nourishments on the shoreface and surf zone of the Dutch coast*. Number C113/08 in Report / IMARES. IMARES / Deltares.
- Beygipoor, G. , Bajestan, M. , Kaskuli, H.A. , and Nazari, S. (2013). The effects of submerged vane angle on sediment entry to an intake from a 90 degree converged bend. *Advances in Environmental Biology*, 7:2283–2292.
- Bijlmer, A. , Gozuberk, I. , Mosselaar, A. , Willems, H. , Wienke, R. , Andela, M , and Ruter, D. (2014). Leenheerengorzenpolder Goudswaard wijzigingsplan Deltanatuur. *Dienst Landelijk Gebied*, (NL.IMRO.0588.BPBGA13wp0114-VG01).
- Bomar, B. , Janssen, B. , and Mol, B. (2017). Landschapsplan quarantaineterrein Rotterdam. Technical report, BVR adviseurs. 170926-BVR.
- Bosboom, J. and Stive, M.J.F (2015). *Coastal Dynamics*, volume Part 1 (version 2015-0.5). VSSD. Lecture Notes CT4305. Delft University of Technology.
- Bouwmeester, J. (1987). *Flexibele waterbouwkundige constructies*. Collegediktaat f4. Delft University of Technology.
- Chavarrias, V. , Sloff, K. , and Mosselman, E. (2020). Final evaluation longitudinal training walls wp10: Morphology, operation and maintenance - draft. Technical report, Deltares, Delft. 11204644-012-ZWS-0001.
- CIRI, CETMEF , CUR (2007). *The Rock Manual, the use of rock in hydraulic engineering*. C683, CIRIA, London, 2nd edition.
- Colosimo, I. , de Vet, P.L.M. , van Maren, D.S. , Reniers, A.J.H.M. , Winterwerp, J.C. , and van Prooijen, B.C. (2020). The impact of wind on flow and sediment transport over intertidal flats. *Journal of Marine Science and Engineering*, 8(11):1–26. ISSN 20771312. doi: 10.3390/jmse8110910.
- Copeland, R.R. (1983). *Bank protection techniques using spur dikes*. Hydraulics Laboratory : U.S. Army Engineers Waterways Experiment station. Miscellaneous Paper HL-83-1.
- Crosato, A. and Kuijper, C. (2002). Hydromorfologische effecten van kribaanpassingen in de bocht van Maassluis. Technical report, Delft Hydraulics. Z3426.
- De Boo, M. (2008). Zoetwatergetijdenatuur keert terug op Tiengemetten. *De levende natuur*, 1:22–26.
- De Haan, W. (2020). Ontwerpnota referentieontwerp Sophiapolder. Technical report, RPS advies- en ingenieursbureau bv. 1505053A50-R20-386.
- De Nijs, M.A.J. (2012). *On sedimentation processes in a stratified estuarine system*. PhD thesis, Delft University of Technology.

- De Nijs, M.A.J. , Pietrzak, J.D. , and Winterwerp, J.C. (2011). Advection of the salt wedge and evolution of the internal flow structure in the Rotterdam Waterway. *Journal of Physical Oceanography - J PHYS OCEANOGR*, 41:3–27. doi: 10.1175/2010JPO4228.1.
- De Vet, P.L.M. , Prooijen, B.C. , and Wang, Z.B. (2017). The differences in morphological development between the intertidal flats of the Eastern and Western Scheldt. *Geomorphology*, 281. doi: 10.1016/j.geomorph.2016.12.031.
- Deltares (2018), Delft3D-FLOW user manual version 3.15 - Simulation of multi-dimensional hydrodynamic flows and transport phenomena including sediments. pages 1–694.
- DELVA Landscape Architects / Urbanism (2019). *Ruimtelijk raamwerk merwe - vierhavens Rotterdam : Toekomst in de maak*. DLA-M4H-17028.
- Dinkla, L. (2018). Data measurement buoy Groene Poort, Aqitec.
- Dinteren, J. (2005). Tussen stad en haven - rotterdam stadshavens. *PropertyImagazine*, 5:65–69.
- Eertman, R.H.M. (2000). Ecologisch herstel rijn-maas-monding- mogelijkheden voor natuurontwikkeling op tien locaties in het Rotterdams havengebied. Technical report, Rijkswaterstaat.
- Freijns, C. (2020). Creating a sandy beach in the rijnhaven - workplan. Master's thesis, Delft University of Technology.
- Gatto, M. , Prooijen, B.C. , and Wang, Z.B. (2017). Net sediment transport in tidal basins: quantifying the tidal barotropic mechanisms in a unified framework. *Ocean Dynamics*. doi: 10.1007/s10236-017-1099-3.
- Gemeente Rotterdam (2018). De rivier als getijdenpark groeidocument 2018. URL <https://www.rotterdam.nl/wonen-leven/getijdenpark/>.
- Gemeente Rotterdam (2019a). De nieuwe maas als stedelijk parklandschap - Levendig, aantrekkelijk en natuurlijk! - Programma rivieroevers Toekomstperspectief binnenstedelijke nieuwe maas. URL <https://www.rotterdam.nl/wonen-leven/programma-rivieroevers/>.
- Gemeente Rotterdam (2019b). Rivieroevers Rotterdam - Uitvoerigsprogramma 2019-2022. URL <https://www.rotterdam.nl/wonen-leven/programma-rivieroevers/>.
- Gemeente Rotterdam (2020). Masterplan Rijnhaven. URL <https://www.rotterdam.nl/wonen-leven/rijnhaven/>.
- Gemeente Schiedam (n.d.). Getijdenpark Wilhelminahaven. Technical report, Gemeente Schiedam.
- Hal, R. , Bos, O. , and Jak, R. (2011). Noordzee: systeemodynamiek, klimaatverandering, natuurtypen en benthos : achtergronddocument bij natuurverkenning 2011. Wageningen : Wettelijke Onderzoekstaken Natuur en Milieu (WOt-werkdocument 255) - 108.
- Hiddema, P. , Zwakhals, W. , Van Leeuwen, J. , and Van Zonneveld, G. (2013). Groene Poort Waterweg - Van grijs naar groen: ontwerpbeschrijving. Technical report, Rijkswaterstaat.
- Hoeksche Waard Nieuws (2017). Natuurgebied leenheerengorzenpolder nabij goudswaard toegankelijk voor publiek. URL <https://www.hoekschnieuws.nl/2017/06/30/natuurgebied-leenheerengorzenpolder-goudswaard-toegankelijk-publiek/>.
- Holland National Parks (n.d.). New bliek bird island in the haringvliet inlet. URL <https://hollandnationalparks.com/en/current/new-bliek-bird-island-haringvliet-inlet>.
- Huisman, Y. and Hoitink, A.J.F. (2017). Towards control over Rhine-Meuse Delta channel network: a historical overview and contemporary research needs. *Advances in Water Resources (submitted)*.
- IVN Natuureducatie (n.d.). Tiendgorzen. URL <https://www.ivn.nl/afdeling/voorne-putten-rozenburg/tiendgorzen>.

- Jammers, S.M.M. (2017). Sediment transport over sills of longitudinal training dams. Master's thesis, Delft University of Technology.
- Kimball, M. and Able, K. (2007). Tidal utilization of nekton in Delaware bay restored and reference intertidal salt marsh creeks. *Estuaries and Coasts*, 30:1075–1087. doi: 10.1007/BF02841397.
- Klijn, F., De Bruijn, K., Knoop, J.M., and Kwadijk, J. (2012). Assessment of the Netherlands' flood risk management policy under global change. *Ambio*, 41:180–92. doi: 10.1007/s13280-011-0193-x.
- Linde, A. and Aerts, J. (2008). Simulating flood-peak probability in the Rhine basin and the effect of climate change. *Flood Risk Management: Research and Practice*, pages 1729–1736. doi: 10.1201/9780203883020.ch205.
- Luijendijk, A. (2001). Validation, calibration and evaluation of Delft3D-FLOW model with ferry measurements. Master's thesis, Delft University of Technology.
- Meijers, E. and Icke, J. (2006). Zwevende stof rijn-maasmonding. Technical report, WL Delft Hydraulics. Q4201.
- Ministerie van Infrastructuur en Milieu (2015). Stroomgebiedbeheerplan rijn 2016-2021. URL <https://www.helpdeskwater.nl/onderwerpen/wetgeving-beleid/kaderrichtlijn-water/2016-2021/>.
- Natuurvereniging IJsselmonde (n.d.). Stormpoldervloedbos. URL <https://www.natuurvereniging-ijsselmonde.nl/stormpoldervloedbos/>.
- Nuesink, N. and Veraart, J.A. (2019). Gebruik kennis over sociale waarden bij besluitvorming en ontwerp van natuurherstel- en ontwikkelingsprojecten: lessen geleerd uit LIFE IP Delta-Natuur, Wageningen University and Research.
- OMA architects and LOLA landscape architects (2019). Feyenoord city masterplan. URL <https://feyenoord-city.nl/masterplan/>.
- Pritchard, D. and Hogg, A.J. (2003). Cross-shore sediment transport and the equilibrium morphology of mudflats under tidal currents. *Journal of Geophysical Research C: Oceans*, 108:11–1.
- Prooijen, B.C. (2019). Sediment dynamics : Chapter 8 - horizontal transport barotropic processes. Delft University of Technology.
- Ratchakom, N. (2019). Assessment of the development of wetlands in Rhine-Meuse estuary. Master's thesis, HZ University of Applied Sciences.
- Reker, J., Litjens, G., and Linnartz, L. (2018). *Natuurlijke Oevers Oude Maas - Herinrichting en beheer Noordelijke Visserijgriend*. Bureau Strooming.
- Rijkswaterstaat (2011a). Beschrijving huidige situatie haringvliet. Technical report, Rijkswaterstaat.
- Rijkswaterstaat (2011b). Linker oever profielen tbv verkenning Groene Poort, Rijkswaterstaat Zuid-Holland- Meet en Informatiedienst.
- Rijkswaterstaat (2018a). Doelen herstel van leefgebied gors van de Lickebaert. Technical report, Rijkswaterstaat.
- Rijkswaterstaat (2018b). Haringvliet: Haringvlietssluisen op een kier. Technical report, Rijkswaterstaat.
- Rijkswaterstaat (2018c). Vernieuwd natuurgebied de Zaag en kunstwerk beverbrug geopend. URL <https://www.rijkswaterstaat.nl/nieuws/2018/02/vernieuwd-natuurgebied-de-zaag-en-kunstwerk-beverbrug-geopend.aspx>.
- Rijkswaterstaat (2018d). Vijfsluizerhaven: kijken hoe Nederland er vroeger uitzag. URL <https://www.rijkswaterstaat.nl/nieuws/2018/10/vijfsluizerhaven-kijken-hoe-nederland-er-vroeger-uitzag.aspx>.

- Rijkswaterstaat (2019a). Blankenburgverbinding :strekdam in het scheur. URL <https://blankenburgverbinding.nl/actueel/1451280.aspx>.
- Rijkswaterstaat (2019b). Proef: dam van oude rioolbuizen bij rozenburg. URL <https://www.rijkswaterstaat.nl/nieuws/2019/11/proef-dam-van-oude-rioolbuizen-bij-rozenburg.aspx>.
- Rijkswaterstaat (2019c). Doelen realisatie Getijdenpark Maashaven. Technical report, Rijkswaterstaat.
- Rijkswaterstaat (2020a). Projectplan waterwet (waterstaatswerken) natuurvriendelijke oevers op het eiland van brienenoord. Technical report, Rijkswaterstaat.
- Rijkswaterstaat (2020b). Nieuwe maas: natuurvriendelijke oever Wilhelminahaven. Technical report, Rijkswaterstaat.
- Schiereck, G.J. and Verhagen, H.J. (2016). *Introduction to Bed, bank and shore protection*. VSSD. ISBN 9789065624031.
- Schutjies, H. and Van Leeuwen, E.R (2013). Milieukundig bodemonderzoek Groene Poort te Rotterdam. Technical report, Gemeente Rotterdam.
- Sloff, K. , Van Der Sligte, R. , Huismans, Y. , and Fuhrhop, H. (2012). Morphological model of the rhine-meuse delta. Technical report, Deltares, Delft. 1205961-001.
- Sloff, K. , van Spijk, A. , Southamer, E. , and Sieben, A. (2013). Understanding and managing the morphology of branches incising into sand-clay deposits in the dutch rhine delta. *International Journal of Sediment Research*, 28(2):127 – 138. ISSN 1001-6279. doi: [https://doi.org/10.1016/S1001-6279\(13\)60025-6](https://doi.org/10.1016/S1001-6279(13)60025-6). URL <http://www.sciencedirect.com/science/article/pii/S1001627913600256>.
- Snippen, E. , Fioole, H. , A.and Geelen, Kamsteeg, A. , van Spijk, A. , and Visser, T. (2005). Sediment in (be)weging, sedimentbalans rijn-maasmonding periode 1990-2000. Technical report, Rijkswaterstaat. RIZA rapport ; 2005.023.
- Stevens, M. , Neucker, T. , Gelaude, E. , Baeyens, R. , Jacobs, Y. , Mouton, A. , Buysse, D. , and Coeck, J. (2011). Onderzoek naar de trekvissoorten in het Schelde-estuarium. voortplantings- en opgroei habitat van rivierprik en fint. Technical report, Instituut voor Natuur- en Bosonderzoek. ISSN: 1782-9054.
- Stichting Toegepast Onderzoek Waterbeheer (2018). *Referenties en maatlatten voor natuurlijke wateren voor de Kaderrichtlijn Water 2015-2021*. STOWA. ISBN 978.90.5773.813.5.
- Stiftung Lebensraum elbe (2020). Elbe habitat foundation - 'lifeline kirchwerder'(hamburg). URL <https://www.stiftung-lebensraum-elbe.de/english-summary.html>.
- Stolk, R. , De La Haye, M. , and Kers, B. (2015). Toestand en herstel unieke getijdennatuur langs de nieuwe waterweg. *Vakblad - natuur bos landschap*, (120).
- Strahler, A.N (1952). Hypsometric (area-altitude) analysis of erosional topgraphy. *GSA Bulletin*, 63 (11):1117–1142. ISSN 0016-7606. doi: 10.1130/0016-7606(1952)63[1117:HAAOET]2.0.CO;2. URL [https://doi.org/10.1130/0016-7606\(1952\)63\[1117:HAAOET\]2.0.CO;2](https://doi.org/10.1130/0016-7606(1952)63[1117:HAAOET]2.0.CO;2).
- Strahler, A.N. (1957). Quantitative analysis of watershed geomorphology. *Transactions, American Geophysical Union*, 38(6):913–920. doi: 10.1029/TR038i006p00913.
- Ten Brinke, W.B.M (2003). De sedimenthuishouding van kribvakken langs de waal. *RIZA*, rapport 2003.002.
- Uijtewaal, W. , Lehmann, D. , and Mazijk, A. (2001). Exchange processes between a river and its groyne fields: Model experiments. *Journal of Hydraulic Engineering-asce - J HYDRAUL ENG-ASCE*, 127. doi: 10.1061/(ASCE)0733-9429(2001)127:11(928).

- Van Delden, M.C. (2019). Constructed tidal marshes- an analysis on how model configurations influence accretion. Master's thesis, Delft University of Technology.
- Van den Broek, T. and de Wit, J. (2006). Inrichtingsplan voor natuureiland Sophiapolder - ruimte voor getij. Technical report, Royal HaskoningDHV. 9R8832a0.
- Van Den Burg, C. (2018). Natuurmonumenten trotse eigenaar van spuimonding-west. URL <https://www.natuurmonumenten.nl/nieuws/natuurmonumenten-trotse-eigenaar-van-spuimonding-west>.
- Van der Deijl, M. , E.and Perk and Middelkoop, H. (2018). Pathways of water and sediment in thebiesbosch freshwater tidal wetland. *Wetlands*, 39. doi: 10.1007/s13157-018-1071-0.
- Van Der Werf, J. , Reinders, J. , Van Rooijen, A. , Holzhauer, H. , and Ysebaert, T. (2015). Evaluation of a tidal flat sediment nourishment as estuarine management measure. *Ocean and Coastal Management*, 114. doi: 10.1016/j.ocecoaman.2015.06.006.
- Van Dort, I. and Houben, B. (2015). Uitgezette steuren hebben baat bij Groene Poort. URL <https://www.naturetoday.com/intl/nl/nature-reports/message/?msg=22066>.
- Van Holland, G , Verheyen, B , Jacobs, S , Vandenbruwaene, W , Temmerman, S , Meire, P , Peeters, P , and De Schutter, J (2010). Simulation of hydrodynamics and transport of fine sediments in vegetated polders with a controlled reduced tide: pilot project Lippenbroek. *8th International Symposium on ecohydraulics 2010 (ISE 2010): bridging between ecology and hydraulics and leading the socieER - TY's new need - living with nature, September 12-16, 2010, Coex, Seoul, Korea. Proceedings [CD-ROM]*, (Imdc):1775–1782.
- Van Linge, B.W (2017). Hydraulic evaluation of longitudinal training dams. Master's thesis, Delft University of Technology.
- Van Rijn, L. C. (2020). Literature review of critical bed-shear stresses for mud-sand mixtures. URL www.leovanrijn-sediment.com.
- Van Spijk, A. (2009). Restdebieten Rijn-Maasmonding berekent met SOBEK.
- Veldkamp, B. (2020). Ontwerpnotitie-Getijdenpark Maassluis en langsdam de Zaayer. Technical report, Arcadis.
- Vellinga, N. , Van Der Vegt, M. , and Hoitink, T. (2014). Hydrodynamics of tidal waves in the rhine-meuse river delta network. Technical report, Utrecht University - Depatment of Physical Geography.
- Verlaan, P. and Spanhoff, R. (2000). Massive sedimentation events at the mouth of the rotterdam waterway. *Journal of Coastal Research*, 16:458–469.
- Waterwinst (2018). Crezéepolder, terug naar een zoetwatergetijdengebied. URL <https://www.waterwinst.nl/project/crezeepolder-terug-naar-een-zoetwatergetijdengebied/>.
- Wensveen, M. (2014). Kwaliteit Onderhoudsbaggerspecie, Resultaten Monstercampagne Rotterdamse havens en vaarwegen. Port of Rotterdam. Technical report, Port of Rotterdam.
- Wesseling, M. (2019). Het is weer drasser dan dras in de korendijkse slikken, Trouw. URL <https://www.trouw.nl/duurzaamheid-natuur/het-is-weer-drasser-dan-dras-in-de-korendijkse-slikken~b2586462/>.
- Winterwerp, J.C. and Van Kesteren, W.G.M. (2004). *Introduction to the physics of cohesive sediment in the marine environment*, volume Developments in Sedimentology. Elsevier. ISBN 978-0-444-51553-7.
- WWF (2019). Opening blik: laat de vogels en vissen maar komen! URL <https://www.wwf.nl/wat-we-doen/resultaten/updates/opening-blik-laat-de-vogels-en-vissen-maar-komen>.

- Yang, S. L. , Zhang, J. , and Zhu, J. (2004). Response of suspended sediment concentration to tidal dynamics at a site inside the mouth of an inlet: Jiaozhou Bay (China). *Hydrology and Earth System Sciences*, 8(2):170–182. doi: 10.5194/hess-8-170-2004.
- Yin, Kai , Xu, Sudong , and Huang, Wenrui (2016). Modeling sediment concentration and transport induced by storm surge in hengmen eastern access channel. *Natural Hazards*, 82. doi: 10.1007/s11069-016-2200-9.
- Yossef, M.F.M. (2002). The effect of groynes on rivers - literature review. Technical report, Delft University of Technology.
- Yossef, M.F.M. (2004). The effect of the submergence level on the resistance of groynes an experimental investigation. *Advances in Hydro-science and-Engineering, Proc. of the 6th Int. Conf. on Hydro-science and-Engineering CD-ROM, Brisbane, Australia*.
- Yossef, M.F.M. (2005). *Morphodynamics of Rivers with Groynes*. PhD thesis, Delft University of Technology.
- Yossef, M.F.M. and De Vriend, H.J. (2010). Sediment exchange between a river and its groyne fields: Mobile-bed experiment. *Journal of Hydraulic Engineering-asce - J HYDRAUL ENG-ASCE*, 136. doi: 10.1061/(ASCE)HY.1943-7900.0000226.
- Yossef, M.F.M. and Uijtewaal, W.S.J. (2003). On the dynamics of the flow near groynes in the context of morphological modelling. *Proceedings of the 30th IAHR Congress*, pages 361–368.
- Zuid-hollands landschap (n.d.). Ridderkerkse griend. URL https://www.zuidhollandslandschap.nl/gebieden/ridderkerkse-griend?gclid=CjwKCAjwh472BRAGEiwAvHVfGh3Le2gFlRVnpJmO2ISvKEW0gkA1HsZcT-_16LITS_wT5B7cgf2OVRoCNH4QAvD_BwE.
- Zuidland (n.d.). Spuimonding west. URL <https://www.zuidland.net/natuur-en-recreatie/spuimonding-west/>.

Tidal parks in the Rhine-Meuse estuary

As is mentioned in the introduction, there are quite a lot of tidal parks in the Netherlands that are already constructed or are still under construction. This literature review aims to display the various characteristics of the tidal parks present in the Rhine Meuse estuary. The location of the tidal parks are displayed in Figure A.1. From this figure it can be seen that the locations of the tidal parks are quite far from each other from which it follows that different physical processes are playing a bigger role than the other.

In this chapter, the tidal parks that are described are categorized by the river in which they are constructed. Starting the tidal parks in the Haringvliet and thereafter the tidal parks in the 'Nieuwe waterweg', the Scheur, the 'Oude Maas', the 'Nieuwe Maas' and the 'Noord'. Thereafter the results will be presented in a table. In this section, a short description is given of each tidal park. The summary of these descriptions can be found in table 2.3. Secondly, a table is presented in which the problems and corresponding maintenance of already constructed tidal parks are reviewed. Most of this information is obtained from personal communication with Menno de Jong, an ecologist from Zuid-Hollands landschap. Lastly, the tidal range of observation points close to the tidal parks is determined, in order to provide an estimation of the tidal range at the tidal parks.

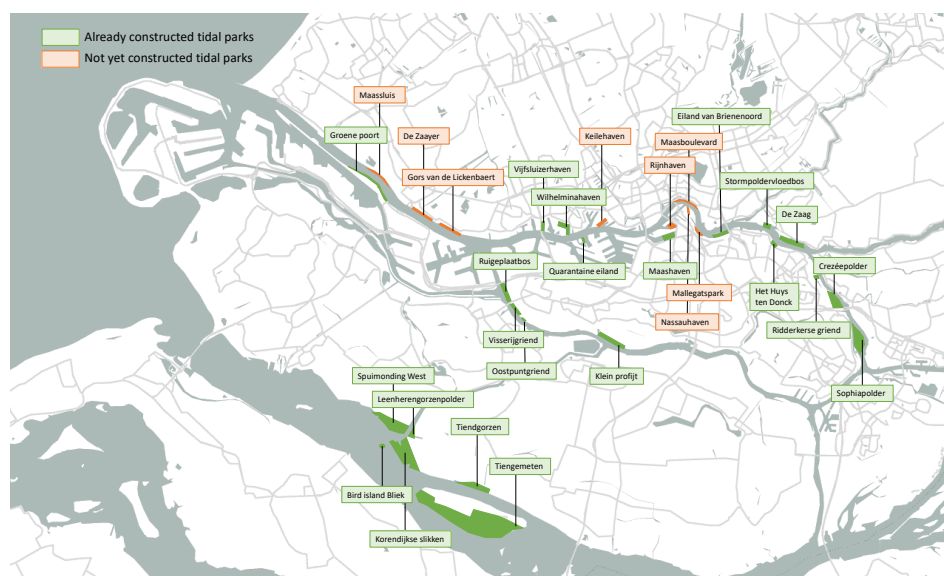


Figure A.1: Tidal parks in the Rhine-Meuse estuary which are treated in this research. The locations of the tidal parks are indicated. The colors indicate if the tidal parks in construction / design phase = orange and already constructed = green

A.1. Short description of tidal parks

A.1.1. Tidal parks in the Haringvliet

Due to the closure of the Haringvliet in 1970 by the construction of a dam, the occurring tidal amplitude at the areas in which now tidal parks are constructed became smaller and so the previous dynamic areas became less dynamic and even led to dry areas (WWF, 2019). By creating tidal parks a natural link can be made between the Biesbosch and the North sea coast (Van Den Burg, 2018). In addition, since the Haringvliet sluice is partly opened the tidal range will increase in the Haringvliet. This could

result in the development of tidal nature, if in combination with adaptations in geometry.

Tiengemeten

The island of Tiengemeten was transformed into a tidal park around 2005, in a large part of the island tidal creeks were dug to improve the ecosystem values and to create tidal marshes. Resulting from the closure of the Harinvliet, the tidal amplitude decreased significantly. The water present surrounding the tidal park is not brackish, but freshwater due to discharges originating from the upstream rivers (De Boo, 2008). From the Dinoloket and the sediment balance by Snippen et al. (2005), it is obtained that the sediment present in this area consists out of silt in combination with sand. This accounts for all tidal parks in the Haringvliet except Voegeleiland Bliet

Tiendgorzen

Tiendgorzen is a tidal park close tot the island of Tiengemeten, and consists out of a dynamic delta. In this tidal park the original quay wall was partly removed and tidal creeks were dug (IVN Natuureducatie, n.d.).

Korendijkse slikken

Originally a tidal marsh was present at Korendijkse slikken, however, due to the closure of the Haringvliet dam problems arose in this tidal marsh. Water was no longer flowing into the tidal creeks as the tidal amplitude at the Haringvliet decreased from around 150 cm to 30 cm. In order to restore the tidal nature, a large part of the Korendijkse slikken (15 ha) was excavated. The tidal creeks were deepened and gate culverts were constructed to ensure that the water entering the area has a longer residence time during flood. These constructions were executed in 2019 (Wesseling, 2019).

Spuimonding west

Tidal park Spuimonding west initially was polder Berningerwaard (Zuidland, n.d.). In 2013 and 2014 the polder was transformed into a tidal area with space for nature and recreation. The tidal park is connected to the Spui river by an opening in the dam which was already present between the Spui and the polder. Originating from this opening a tidal creek is dug providing a large part of the area with tidal inflow (Zuidland, n.d.)

Bird island Bliet

A new island has been created in the Haringvliet in 2018 (Holland National Parks, n.d.). As the Haringvliet sluices are partially opened, there is a need for vital food and breeding areas to suit the incoming fish and birds. As the other tidal parks were not yet in such a stadium to serve as such a source, the tidal park Bliet was constructed. This island consists of a sandy 'beach' being surrounded by longitudinal walls covering around 2/3 of the perimeter.

Leenherengorzenpolder

The Leenherengorzenpolder is a polder of 19 ha located above the 'Korendijkse Slikken' and next to river the Spui (Bijlmer et al., 2014). This area has been under the effect of river and the tide over the past thousand years. Before the construction of the tidal park, the situation was not dynamic anymore as dikes prevented the polder from flooding. The tidal park is obtained by constructing tidal creeks and creating an opening in the quay wall which separated the Spui and the Leenherengorzenpolder. The construction of the tidal park was finished in June 2017 (Hoeksche Waard Nieuws, 2017)

A.1.2. Tidal parks in the 'Noord'

Ridderkerkse Griend

The Ridderkerkse Griend is a tidal park with as main function willow tree growth (Zuid-hollands landschap, n.d.). The tide can flow in and out of this area by a small inlet which is also the origin of a tidal creek. The inlet of this tidal park is partly blocked by trees hanging over the creek. As a result, coarse sediment like sand is deposited in front of this 'barrier', inside the tidal creek mainly silt is found. Every once in three years the willow trees are cut, together with this operation the small creek system inside this area is dredged (M.van Lopik (Zuid-Hollands Landschap), personal communication, May 19, 2020).

Crezéepolder

The Crezeepolder was an agricultural landscape of 72 ha surrounded by dikes to prevent the river from flowing into the polder. This area was transformed into a tidal park in 2017. A tidal creek was dug and a dike was partly opened to ensure fresh water inflow on the rhythm of the tide (Waterwinst, 2018). Problems are occurring related to sedimentation/erosion are already noticeable. These problems consist out of sedimentation of the tidal channels and erosion of the banks (M.van Lopik (Zuid-Hollands Landschap), personal communication, May 19, 2020)

Sophiapolder

The Sophiapolder is a tidal park near the city of Dordrecht. Previously this area was a polder used for agriculture but it is transformed into a tidal park by digging two tidal channels with several bifurcations in 2011 (Van den Broek and de Wit, 2006). There is a large input of sediment in this area, especially at the shallow channels, but not much sediment transport is transported towards the tidal flats at which reed and brushes were expected to grow, which is not happening. Besides that large amounts of erosion is taking place at the entrances and the quay walls of the tidal park (De Haan, 2020). To solve these problems, maintenance is required in form of sand nourishment at the quay wall and possible dredging of the channels (De Haan, 2020).

A.1.3. Tidal parks in the Nieuwe Waterweg

Groene Poort

Tidal park the Groene Poort is located at the headland of Rozenburg. For a distance of 5 kilometers tidal parks are being constructed. At this river bank, groyne are already present. By placing longitudinal walls in front of the area between the groyne, a calm area is created in which sediment is ought to deposit (Gemeente Rotterdam, 2018). If enough sediment is deposited, a sloping tidal flat is created. Because of sustainability, the longitudinal walls are constructed of stones and soil which are reused from other projects in the area. (Rijkswaterstaat, 2019b) As a result, the construction of the longitudinal walls is not going as fast as planned, that is why currently there are ongoing experiments of constructing the breakwaters of sewer pipes (Rijkswaterstaat, 2019b).

The time scale in which sediment is deposited behind the longitudinal walls is too large according to Rijkswaterstaat, and a solution is researched which can enhance sedimentation behind the breakwaters.

Maassluis

The tidal park at Maassluis is not yet constructed, there is however a design laid out by a design bureau. The location of this tidal park is on the opposite side of the 'Groene Poort' and is located in the bend at Maassluis. The tidal park will consist of a tidal creek behind the longitudinal wall in which water can flow only in and out during high water but always a pool filled with water is always present for the fish. The dam will consist of 'hard' material so that waves can not pass the dam but fishes can. As mentioned before the design is already made, this design is however made by landscape architects but detailed modelling of sedimentation and erosion occurring in the tidal park are not yet researched by engineers. The quality of the soil present at the location of tidal park Maassluis is contaminated and it is not sure if this tidal park is going to be constructed, as the construction of this tidal park goes arm in arm with a lot of soil excavations. The cost of treating the contaminated soil may result in high cost for the construction of the tidal park.

De Zaayer

Tidal park the Zaayer is not yet constructed and is in the design phase. The concept is the same as of the tidal park the Groene Poort but around 2 kilometers upstream of the Nieuwe Waterweg on the opposite side at rkm 1016,5 -1018,2 (Veldkamp, B., 2020). This tidal parks is located 500 meters downstream of the tidal park Gors van de Lickebaert. At this river bank, groyne are present in combination with shallow areas in between the groyne. The design of these tidal parks consists out of constructing longitudinal walls in front of the area between the groyne. The length of the longitudinal walls is still under research. One important aspect that should be taken into account is the pump station the Zaayer, which is located at the land side of the tidal park and discharges freshwater inflow into the Nieuwe Waterweg (Veldkamp, B., 2020).

A.1.4. Tidal parks in the Scheur

Gors van de Lickebaert

Tidal park Gors van de Lickebaert is not yet constructed, it is however stated by Rijkswaterstaat that 750 meters of environmentally friendly shore are created in near future (Rijkswaterstaat, 2018a). Since 2018 the construction of the Blankenburg tunnel has started, this is a tunnel that goes underneath the Scheur and through Lickebaert park (Rijkswaterstaat, 2019a). In order to built this tunnel, a storage area was created by building a longitudinal wall and filling up the area behind with a nourishment. When the construction of the Blankenburg tunnel is finalized, the longitudinal wall stays in place and the area behind is excavated. In this area nature can develop, and tidal park Gors van de Lickebaert is created. This design resembles tidal park the Groene Poort.

Vijfsluizerhaven

Tidal park Vijfsluizerhaven was an old port basin, this park is constructed by reconnecting the port basin to the Nieuwe Maas and shallow the basin area (Gemeente Rotterdam, 2018). The park is constructed in 2015, the tide is clearly visible in this area and a large amount of silt deposits in this area (Rijkswaterstaat, 2018d). A problem occurring in this tidal park is the extensive growth of vegetation, this was not the aim of the design of this park which included the presence of a tidal flat only. The vegetation in the tidal park is removed, by this the natural processes in this park are interrupted (Rijkswaterstaat, 2018d).

A.1.5. Tidal parks in the Nieuwe Maas

Tidal parks that are constructed in the Nieuwe Maas are mostly concentrated at old port basins. Due to the construction of the Maasvlakte, a large amount of port activities moved to the Maasvlakte and port basins at the Nieuwe Maas are no longer in use (Dinteren, 2005).

Wilhelminahaven

The construction of the tidal park Wilhelminahaven started in September 2019 (Gemeente Schiedam, n.d.). This tidal park is designed with both a recreational and nature development function. The Wilhelmina haven is an old port basin and the surroundings of this basin consist of quay walls. Additional quay walls are constructed 20 meters into the basin, behind this quay wall a sloping foreshore is created in which vegetation can grow (Rijkswaterstaat, 2020b). Besides that, sidewalks are created to implement the recreation function. The area in which the tidal park area is constructed is already a sheltered area with low dynamics (Rijkswaterstaat, 2020b). A problem that might arise in the future is not only trapping large amounts of sediments but also trapping plastics. Research is executed into this topic (Rijkswaterstaat, 2020b).

Keilehaven

The tidal park that is going to be constructed at the old port basin Keilehaven is part of a larger project 'M4H', in which recreation, living, business, and environment are combined (DELVA Landscape Architects / Urbanism, 2019). This tidal park is designed to have a recreational function only. The design consists out of stairs, constructed from the shore up to some point in the port basin. These stairs will flood during high water and are fully visible during low water (Gemeente Rotterdam, 2018). As this is not a tidal park that is used for nature creation, sedimentation and erosion are important only for the stability and use of the stairs.

Quarantaine eiland

Tidal park Quarantaine island consists out of a sandy beach. This beach area is constructed in the nineties by a sand nourishment (Bomar et al., 2017). This tidal park is designed to improve ecological values and to provide a location for recreation.

Maasboulevard

The Maasboulevard is located in the outer bend of the Nieuwe Maas and currently consists of concrete quay walls. The tidal park that will be constructed in this area will consist of an ecologically friendly shore in combination with locations for recreation (Gemeente Rotterdam, 2019a). As the boulevard is located in the outer bend a hard structure, such as a longitudinal wall, is needed to prevent the tidal park from eroding and wave action (Gemeente Rotterdam, 2019a).

Maashaven

The Maashaven together with the Rijnhaven were the basis of the growth of Rotterdam into a world port city (Gemeente Rotterdam, 2020). As mentioned before the construction of the Maasvlakte brought a lot of port activities outside the city of Rotterdam, and as a result, the Maashaven port basin is partly available for re-design. The Maashaven tidal park is being constructed in different phases and phase 1 is already finished, which is the relocation of the jetties and replacing the contaminated silt with clean sediment that was available from dredging the Nieuwe Waterweg (Gemeente Rotterdam, 2019b). The tidal park will consist of an ecologically friendly shore including a tidal creek (Rijkswaterstaat, 2019c), the length of this shore is around 1 km. By constructing this tidal park the living quality of surrounding residential areas is improved (Gemeente Rotterdam, 2019b).

Rijnhaven

The Rijnhaven is an old port basin which is going to be developed into a 'new center of Rotterdam (Gemeente Rotterdam, 2020). The design concept consists of high-rise buildings neighboring a tidal park. The park will consist of floating structures, a regular park including recreational areas, and a sandy beach (Gemeente Rotterdam, 2020). The aim of this design is that the sandy beach is sloping and can be used for swimming without endangering the lives of humans. A problem that might occur in this tidal park is the sandy beach being replaced with silt, or the beach being eroded in a few years. This topic is currently being researched (Freijns, 2020).

Nassauhaven

The Nassauhaven is an old port basin, which is re-designed as an area consisting of 18 floating houses and an ecologically friendly shore (Gemeente Rotterdam, 2019b). This shore has been created in July 2019 and consists of a sloping shore in which vegetation is placed. By constructing this ecologically friendly shore, the experience and value of the park increases, and therefore the living environment (Gemeente Rotterdam, 2018).

Mallegatspark

The Mallegatspark is a tidal park that is part of a big reconstruction of a neighborhood in the city of Rotterdam, Feyenoord City. The origin of the name of this neighborhood is from the football club stadium located in this area (OMA architects and LOLA landscape architects, 2019). The whole area surrounding the stadium is re-designed, including a new stadium, many houses, and a tidal park to improve the living environment. The Mallegatspark is located in the outer bend of the Nieuwe Maas. The tidal park consists out of longitudinal walls which are placed in front of the dam in order to create a calm area behind these dams where tidal nature can develop. This tidal park is possibly connected to the neighboring tidal park Eiland van Brienoord which is located a few kilometers eastwards. This connection will be obtained by the construction of a longitudinal wall.

Brienoord

The island of Brienoord is an already existing tidal park. This tidal park is however adapted, introducing 1750 meters of ecologically friendly shore and land reclamation on the west side of the island (Rijkswaterstaat, 2020a). The original park consisted out of a green area with a lot of trees present and on the east side of the island, there were some tidal channels present (Nuesink and Veraart, 2019). By the adaptations of the tidal park in the future, it is expected that tidal nature becomes more present in this park. In the design of this park, tidal channels are not dug but it is assumed that these will be formed by natural processes (Rijkswaterstaat, 2020a).

Stormpoldervloedbos

The Stormpoldervloedbos is an already existing tidal park which has been constructed in 1993 by the Zuid-Hollands Landschap (Natuurvereniging IJsselmonde, n.d.). Before this area was designed as a tidal park it was used to grow willow trees. The construction of this tidal park consisted of a small dam around the polder including inlets in which the tide can flow in and out. Next to that, tidal creeks were dug in the polder to ensure that tidal flow can enter the area which improves the growth of tidal vegetation in the area (Natuurvereniging IJsselmonde, n.d.). A student from the TU Delft, Maud van Delden, researched the effect of several parameters on sedimentation/erosion in the Stormpoldervloedbos.

She executed this research by modeling the area in a 1D hydrodynamic model called Sobek, for more information it is referred to her thesis (Van Delden, 2019).

De Zaag

The location in which tidal park the Zaag is constructed was already an area with a lot of nature present. In 2018 this nature area was reconstructed into a large tidal park. This park consists of an intertidal area of ten ha and four kilometers of ecologically friendly shore (Rijkswaterstaat, 2018c). In the intertidal area, tidal creeks are present.

Het Huys ten Donck

Tidal park Het Huys ten Donck is located in front of the historical house: 'Huys ten Donck'. The tidal park is not yet constructed, but it will consist out of the construction of a longitudinal wall in front of the forecourt of Huys ten Donck. Behind this longitudinal wall, there is room for tidal nature development (Gemeente Rotterdam, 2018).

A.1.6. Tidal Parks in the Oude Maas

In the Oude Maas a lot of tidal parks are located, mostly these parks used to be or are still partly 'Grienden'. Grienden are areas that are used for growing willow trees (Reker et al., 2018).

Ruigeplaatbos

Tidal park Ruigeplaatbos is located close to the bifurcation of the Oude maas and the Scheur. This tidal park has a surface area of 60 ha and contains a lot of willows and reed. This tidal park is a small stroke of intertidal area between the wood of Ruigeplaatbos and the river de Oude Maas (Reker et al., 2018).

Visserijgriend

The Visserijgriend is a tidal park of 8 ha which originally was a so-called 'griend' area in which willows were grown (Reker et al., 2018). In 2008 a tidal creek was dug to improve the tidal dynamics in this area. The soil in this area mainly consists of clay, however, locally silt is found at the top of the soil layers (Reker et al., 2018).

Oostpuntgriend

Tidal park the Oostpuntgriend is an area in which willow trees are grown. The tide can flow in through a culvert which is placed underneath the dike, this ensures a small delay relative to the tide in the river. (M.van Lopik (Zuid-Hollands Landschap), personal communication, May 19, 2020)

Klein Profijt

The Klein Profijt is a tidal park consisting out of tidal creeks surrounded by willow trees (ARK Natuurontwikkeling, 2016). It is stated that during flood silty and turbid water flows into the creeks and during ebb crystal clear water flows in opposite directions in the creeks. This ensures that at the Klein Profijt a silty layer is present at the top layer (ARK Natuurontwikkeling, 2016).

Tidal park	Problems	Maintenance
Groene Poort	Time scale sediment import too large	Sand nourishment inside tidal parks
Vijfsluizerhaven	Too much vegetation growth	Removing unwanted vegetation
Eiland van Brienoord	Sedimentation of tidal channels	-
Stormpoldervloedbos	Sedimentation of tidal channels	-
De Zaag	Sedimentation of tidal channels	Reconstruction in 2018 including deepening of tidal channels
Crezeepolder	Sedimentation of tidal channels and erosion of the banks	-
Sophiapolder	Sedimentation tidal channels, erosion of dikes , erosion pit at entrance	Maintenance 12 years after construction due to increased sedimentation
Ridderkerkse griend	Sedimentation of the channel	Once every 3 years dredging of channels
Ruigeplaatbos	Erosion of the outer dike and sedimentation of tidal channels	Dredging activities are planned in future
Visserijgriend	Sedimentation of the channels	Dredging of the channels for water storage
Oostpuntgriend	Sedimentation of the channels	-
Klein Profijt	Sedimentation of the channels	Once every 30 years the lake inside the tidal park is dredged

A.2. Determination of tidal ranges at tidal park

The tidal ranges at the tidal parks are of importance in order to get an estimate on the tidal inflow in the tidal parks. The observation points are not located at the same location as the tidal parks. Therefore, in Figure A.2 the locations of both the tidal parks and the observation points are displayed to indicate the distances between the two locations. At these observation points, the astronomical tide of two spring neap tidal cycles are analysed, the result is displayed in Figure A.3. The difference between mean low water and mean high water is the tidal range displayed in Table A.2.

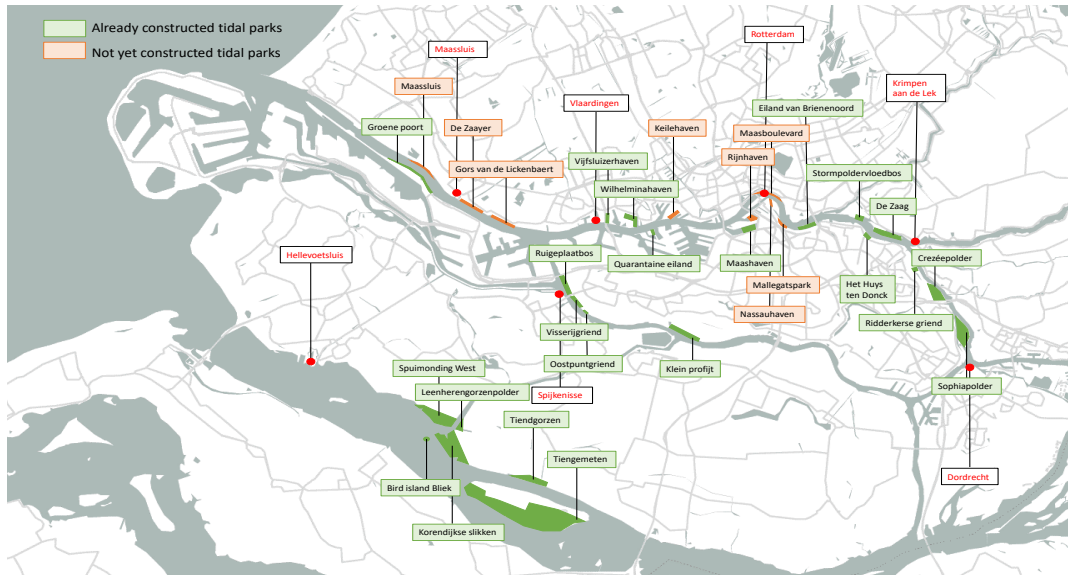


Figure A.2: Locations of the tidal parks in combination with the location of the observation points from which data on the astronomical tide is obtained

	Maassluis	Vlaardingen	Rotterdam	Krimpen aan de Lek	Dordrecht	Spijkensisse	Hellevoetsluis
LAT (m)	-0.77	-0.69	-0.60	-0.23	0.10	-0.58	0.33
HAT (m)	1.30	1.50	1.59	1.32	1.08	1.34	0.71
MLW (m)	-0.51	-0.44	-0.36	-0.05	0.18	-0.38	0.38
MHW (m)	1.06	1.21	1.27	1.15	0.95	1.11	0.64
Tidal range (m)	1.57	1.66	1.63	1.20	0.76	1.50	0.27

Table A.1: The lowest astronomical tide, highest astronomical tide, mean low water, mean high water and the average tidal range at observation points inside the Rhine Meuse estuary, locations are displayed in Figure A.2

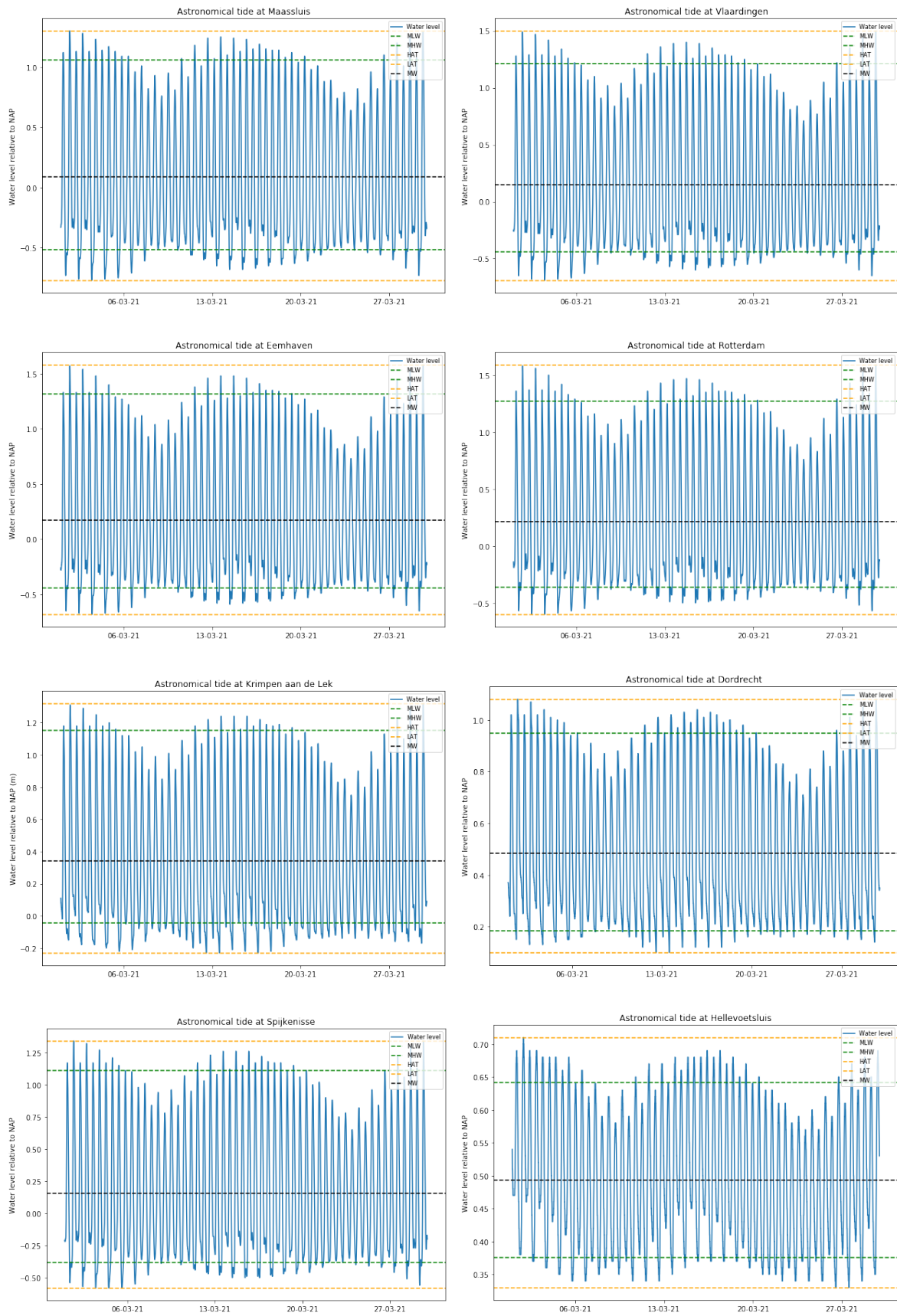


Figure A.3: Tidal analysis locations



Sediment transport in tidal regions

A.1. Sediment transport

It is very important to define the mechanisms leading to sediment transport in the Nieuwe Waterweg. For this research it is chosen to only take into account barotropic processes and thus neglecting the sediment transport as a result from baroclinic processes. This choice is based upon the fact that sediment transport as a result from salt wedge intrusion results in sediment transport near the bed, from a cross-section of the Nieuwe Waterweg, see Figure A.1 (Rijkswaterstaat, 2011b), it can be seen that this type of transport mechanism is far from the river banks at which the tidal parks are concentrated.

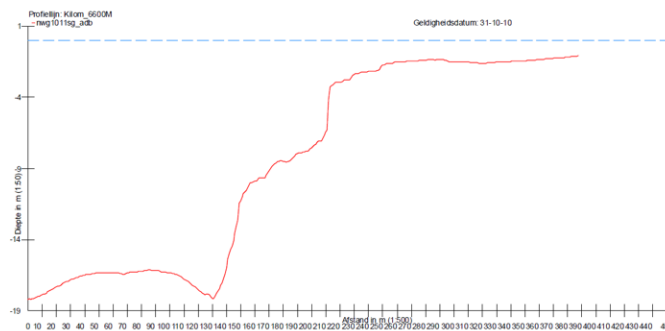


Figure A.1: Cross section of the Nieuwe Waterweg present at study location Rijkswaterstaat (2011b)

Sediment transport can both be qualified using the Lagrangian method and the Forward Eulerian approach, see Figure A.2. The Lagrangian approach assumes that one particle can represent a mean direction of the sediment transport, the frame of references moves with the sediment particle (Gatto et al., 2017). Clearly explained by Gatto et al. (2017): 'The trajectory is defined according to threshold velocities (bed-shear stresses) for erosion (U_e or t_e) and deposition (U_d or t_d). The particle starts on the bed at the beginning of the flood tide ($U < U_e$); it is then picked up from the bed ($U \geq U_e$) and horizontally transported landward by the current; it starts settling ($U \leq U_d$) while still traveling with the water motion, until it reaches the bed again. The same sequence of entrainment, transport, and deposition happens in seaward direction during ebb tide. At the end of the tidal cycle, the direction of residual transport is defined according to whether the particle is displaced landward or seaward with respect to its initial position.'

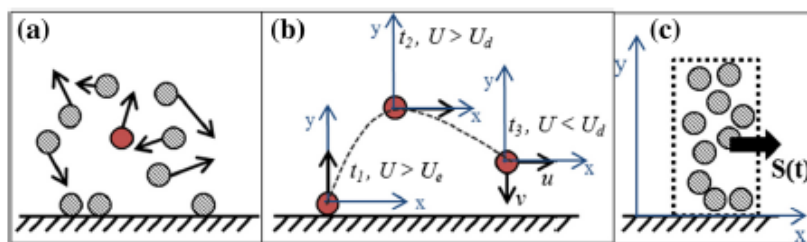


Figure A.2: Schematic representation of suspended sediment transport, a: Chaotic trajectories of particles in real world. b: Lagrangian framework c: Eulerian framework (Gatto et al., 2017)

In the Eulerian Forward method the focus is upon a specific location in space where a concentration field is considered in which the properties are observed for a control volume as a function of time (Gatto et al., 2017), see Figure A.2c. The sediment transport is thereafter is calculated by means of equations.

The instantaneous suspended sediment transport rate through a cross section is explained as a mass-flux, see equation A.1. Where Q is the water discharge in m^3/s , C is the depth averaged concentration kg/m^3 , ϵ is the dispersion coefficient m^2/s , b is the channel width (m), h is the water depth (m) and x is the stream wise coordinate. Thereafter the direction of the transport results from taken the average sediment transport over a tidal period, see equation A.2,

$$S(t) = QC - \epsilon bh \frac{\partial C}{\partial x} \quad (A.1)$$

$$S_{res} = \frac{1}{T} \int_T S(t) dt \quad (A.2)$$

The depth averaged concentration C is found by the advection-diffusion equation, which is in 1D displayed in equation A.3. In which the last part of the equation expresses the sediment exchange between the bed and the water column. As can be seen this is depended on the equilibrium value C_{eq} and the relaxation timescale T_a , this is the time it takes for the concentration to adapt towards the equilibrium value. The relaxation time scale is determined by equation A.4, and depended on the settling velocity, tidal period and the water depth. The horizontal diffusion coefficient depends on the timescale and is often neglected in studies considering semi-diurnal timescales.

$$b \frac{\partial(hC)}{\partial t} + \frac{\partial(QC)}{\partial x} - \frac{\partial}{\partial x} \epsilon bh \frac{\partial C}{\partial x} = bh \frac{C_{eq} - C}{T_a} \quad (A.3)$$

$$T_a = \frac{h}{w_s} T \quad (A.4)$$

The equilibrium concentration is often calculated by depth-averaging the Rouse profile, however, small errors in defining the reference height a can lead to large errors in the rouse profile Gatto et al. (2017). The equilibrium concentration can also be defined as is displayed in equation A.5. In which E and D are erosion and deposition fluxes, τ_{tot} is the total bed-shear stress, τ_{crit} is the critical bed-shear stress for erosion (this can be determined by Shields diagram (Bosboom and Stive, 2015)), M is an erosion constant in order of $10^{-5} kg/(m^2s)$, n is the erosion exponent which is 1 for silt and mud and 1.5 for sand fractions and α is equal to $C_a/C = 1/T$.

$$h \frac{C_{eq} - C}{T_a} = E - D = \max \left[M \frac{\tau_{tot} - \tau_e}{\tau_e} \right]^n, 0 \right] - \alpha w_s C \quad (A.5)$$

$$E - D = 0 \rightarrow C_{eq} = \frac{E}{\alpha w_s} \quad (A.6)$$

In order to use the equations stated above, there is one additional unknown that needs to be calculated, the settling velocity of the grains. The particle's falling velocity depends on its size, density and on the magnitude of the drag coefficient, which is depended on the grain Reynolds number (Bosboom and Stive, 2015), see equation A.7. In which w_s is the falling velocity, s is the relative density, g is the gravitational acceleration and C_D is the drag coefficient.

$$w_s = \sqrt{\frac{4(s-1)gD}{3C_D}} \quad (A.7)$$

The grain Reynolds number is defined as stated in equation A.8 and is depended on the settling velocity, the diameter of the grains and the kinematic viscosity coefficient which is $10^{-6} m^2/s$. By these two equations the settling velocity can be determined.

$$Re = \frac{w_s * D}{\nu} \quad (A.8)$$

A.2. Sediment transport mechanisms

The following sediment transport mechanisms are all taking place in sediment transport at tidal parks in the Rhine-Meuse estuary, and will be further elaborated in the following sections. Literature shows that lag-driven transport is dominant for finer sediment fractions such as silt and mud, and sand transport is dominated by the asymmetry of peak ebb/flood flow velocities (Gatto et al., 2017). However, due to the fact that tidal asymmetries and lag effects are classically regarded as drivers of sediment import from tidal channels to the flats the influence of wave forcing is often neglected (Gatto et al., 2017).

- Lag effects
- Tidal asymmetry
- Wave driven transport
- Spiral flow in river bends

A.2.1. Lag effects

When opting from a Lagrangian point of view, which assumes that one particle can represent a mean direction of the sediment transport and the frame of references moves with the sediment, an important feature is lag effects. This causes asymmetries of the sediment particle's trajectory under a periodically reversing flow, this type of asymmetries usually results in the landward displacement of sediment over the tidal cycle. There are four types of lag effects and these will be shortly elaborated below, and in addition are displayed in Figure A.3, in which a-b displays settling lags and e displays scour lag. In this figure the particle trajectories are displayed, with the black lines being the sediment particle, blue line being the flood water particle and the red line represents the ebb water particle. It is assumed that the threshold velocities are the same for erosion and deposition. from which the particle is picked up (erosion) is the same as for deposition.

Settling lag

The settling lag is based upon the coupling of non-vertical settling trajectories with a time lag between the time that the particle starts sinking and the moment it touches the bed (Gatto et al., 2017). The settling time scale can be estimated by $T_{\text{set}} = \frac{h}{w_s}$. During uniform conditions, with a sinusoidal velocity signal, this will not lead to a net sediment transport, as the ebb flow trajectory mirrors the flood trajectory and the sediment particle is not displaced over a whole tidal cycle.

However, when the conditions are not uniform, this type of settling lag results in a net sediment transport. In Figure A.3b, the situation is displayed with a dampened sinusoidal velocity profile. It can be seen that, when the particle moves inwards and thereafter settles, when the sediment particle is picked up again by the ebb flow, the velocity is smaller and thus the sediment particle settles quicker as the threshold velocity is reached earlier. The result is a net land inward transport. Besides that, bed level variation and water depth variation are factors influencing the sediment transport as a result from the settling lag.

The bed level variation can either be a very small slope, a shoal, or a very steep slope. For this mechanism the height up to which the sediment is transported in the water column is important, this is assumed to be 50 percent. If this is the case at a shoal, it indicates that the distance which the particle needs to travel is smaller during ebb than flow, and thus results in seaward transport (Gatto et al., 2017). If the bed level variation is steep enough, see Figure A.3c, the particle will not settle before the flood occurs and net landward sediment transport occurs (Gatto et al., 2017).

Threshold lag

The erosion threshold is based upon an assumption of a critical velocity, and thus a critical bed shear stress. If this erosion threshold is adopted, the settling lag is enhanced by threshold lag. As the flow is decreasing going inwards into a basin, the flow velocity near the end of the basin is too low to re-suspended the particle again and the sediment is not going to be picked up again by the ebb flow (Gatto et al., 2017).

Scour lag

Besides the erosion threshold, the deposition threshold is also an assumption based upon a critical velocity. If the erosion threshold > the deposition threshold, the settling lag is further enhanced by scour lag (Gatto et al., 2017), this mechanism is displayed in Figure A.3e. This mechanism results from the time delay in the re-entrainment of the sediment during flow reversal, as a result the sediment particle is moved further landwards.

Entrainment lag

The entrainment lag, is the time that it takes for the particle to cross the bed-load layer and be lifted up in the water column after it has been picked up from the bed. The time that it takes for the particles to be concentrated in the water column is estimated by the mixing time scale ($T_{mix} = \frac{10h}{u_*}$).

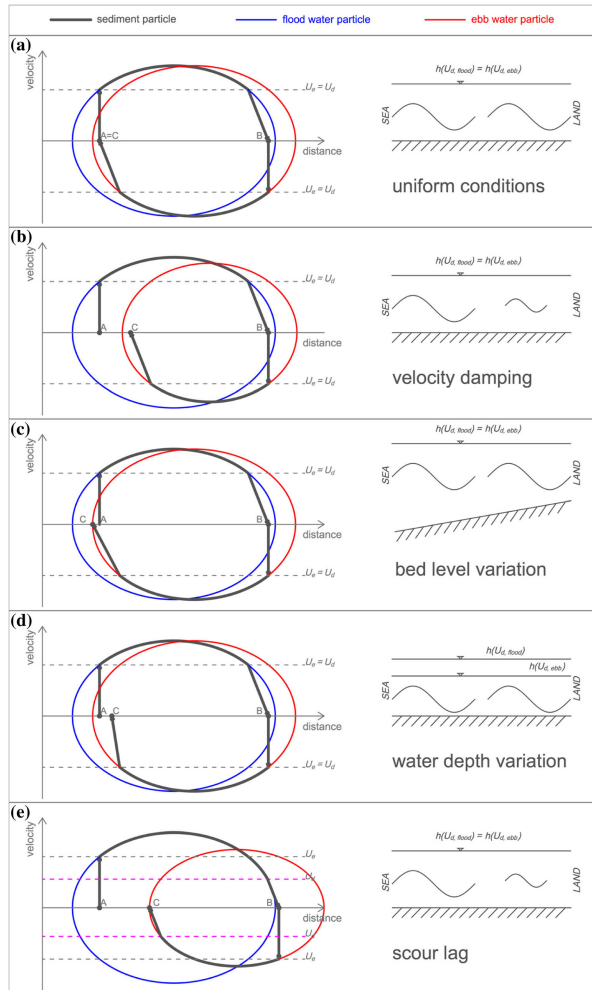


Figure A.3: Settling lag (a-d) and scour lag (e) mechanisms, the version of Gatto et al. (2017) which is the extended version of Pritchard and Hogg (2003)

A.2.2. Tidal asymmetry

By tidal asymmetry, the distortion between a perfect sinusoidal tide and the observed tide is meant, this can be well described by the inclusion of higher harmonics (Bosboom and Stive, 2015). These are integer fractions of the period of the basic astronomical constituents generated by attraction forces of earth, moon and sun and are called overtides or shallow-water tides. The source of the non linearity in tidal propagation are bottom friction and continuity (Bosboom and Stive, 2015). Two different asymmetries are considered, peak flow asymmetry and slack water asymmetry.

Peak flow asymmetry

The difference between the maximum ebb and flow velocities are called peak flow asymmetry, when the flood velocity is higher it is most likely that transport is in that direction since sediment responds non-linearly to the velocity (for bed load $S \propto u^5$ or $S \propto u^3$) (Bosboom and Stive, 2015). In the case of suspended sediment transport $S \propto u^3$ for cohesive sediment and $S \propto u^4$ for non-cohesive fractions.

Slack water asymmetry

Slack water is the name used for tidal flow reversal, and is defined as the period of time between the occurrence between maximum tidal elevation and zero velocity (Bosboom and Stive, 2015). High water slack is the flow reversal from flood to ebb and low water slack is the reversal from ebb to flow. When for instance the duration of high water slack is longer than low water slack, the sediment has more time to settle at the end of flood than at the end of ebb (Gatto et al., 2017).

Residual seaward velocity

A tidal wave travelling into an estuary is largely affected by friction, if this is the case, the velocity profile and the water level are out of phase, with the velocity profile leading the water level profile (Bosboom and Stive, 2015). If this phase difference is not exactly 90 degrees, and the tide thus propagates as a partly progressive wave, mass is transported landwards (Gatto et al., 2017). In terms of mass conservation, a tidal mean current is needed in seaward direction. This mechanism is similar as the well known undertow from short waves. This residual seaward velocity affects the peak-velocity asymmetry with a vertical shift of the velocity curve in which ebb flow is enhanced and flood flow is reduced (Prooijen, 2019).

A.2.3. Wave driven transport

Waves, as a result from wind or from passing vessels, result in re-suspension of the sediment. Besides that, it induces additional shear stresses on the bed in case of shallow channels and tidal flats (Gatto et al., 2017). According to Bosboom and Stive (2015) : 'In shallow water the contribution of the wave motion to the bed shear stress is often more important than the contribution by the mean current'.

B

Morphology of the river banks - additional data analysis

The bed-level data used in this research is obtained from measurement campaigns executed by Rijkswaterstaat. The available data on bed level consists of in total four years of measurements, measurements are executed in 2015, 2017, 2018, and two times in 2019. 2019-1 contains measurements from July and 2019-2 contains measurements from November in 2019. These bed level measurements are executed by multi-beam echo-sounders and are limited to the +0.5 m NAP line and all measured with respect to NAP.

Additional information on the amount of data per river bank, per year is displayed in table B.1. The last row of the table contains information on the total amount of measurements of all the river banks. This table contains information on the amount of measurement points, and this amount relative to the '100 %' data case, which is represented by data set 2019-1 as this contains the maximum amount of measurements. The values displayed in columns 7-10 represent the amount of data relative to data set 2019-1, this value can either be smaller or larger than one. If this value is larger than one, this indicates that the year displayed above the column contains more measurements than the '100 %' data set. If the value is smaller than one, the reverse is accounted for, this indicates that the year displayed above the column contains less measurements than the '100 %' data set.

This information shows that the data-set from 2019-2 relatively contains the least measurement points, although this is varying per river bank. When examining the total amount of measurements, it can be obtained that data-sets 2019-2 contains the least data points, followed by 2015 and 2017. The fact that the amount of measurements per yearly data-set differ, affects the interpretation of the results of the morphological evolution.

Taking into account the availability of data and the resulting hypsometric curves, conclusions can be drawn for each river bank. Both on the evolution of the total river bank, incorporating Figure 5.4 and the evolution of the intertidal area specifically, displayed in Figure B.1.

	Measurements per river bank					Percentage relative to 2019-1			
	2015	2017	2018	2019-1	2019-2	2015	2017	2018	2019-2
A	22720	21122	23064	23389	18902	0.97	0.90	0.99	0.81
B	26932	25521	26706	26992	23162	1.00	0.95	0.99	0.86
C	36790	35868	37043	37680	36406	0.98	0.95	0.98	0.97
D	38332	37264	37764	38999	34453	0.98	0.96	0.97	0.88
E	42778	42344	43977	45976	40583	0.93	0.92	0.96	0.88
F	48466	49643	50236	52363	48555	0.93	0.95	0.96	0.93
G	44549	38820	43408	43197	38158	1.03	0.90	1.00	0.88
H	66491	72202	73661	69534	68815	0.96	1.04	1.06	0.99
I	47620	48826	48349	46100	47241	1.03	1.06	1.05	1.02
J	22425	23590	22269	22788	22027	0.98	1.04	0.98	0.97
K	38268	39078	37969	38458	36113	1.00	1.02	0.99	0.94
L	71584	71590	71414	70603	68804	1.01	1.01	1.01	0.97
M	32884	36603	38507	37230	35742	0.88	0.98	1.03	0.96
N	35673	38313	39023	40139	36539	0.89	0.95	0.97	0.91
Total	575512	580784	593390	593448	555500	0.97	0.97	1.00	0.94

Table B.1: Amount of measurements per river bank, displayed for all five measurement campaigns. In the second part of the table the percentage of data relative to the '100 %' data (2019-1, maximum amount of data points) is displayed.

Figure B.1 displays the evolution of the tidal flats inside the river banks of the Nieuwe Waterweg. The grey shaded areas indicate the areas outside the tidal range. The growth of the intertidal flats indicated in this figure are affected by the data sets having unequal measurements. The growth obtained from the hypsometric curves in Figure B.1 is equal to the growth in total surface area from the total river bank displayed in Figure 5.4. As a result, it can be indicated that missing data points are at the location of the intertidal area. The shape of the curves inside the intertidal areas are either a linearly increasing or concave upward. Combining information on the amount of measurements inside the river bank, in combination with the resulting hypsometric curves, it can be concluded if the intertidal areas are growing. This is executed for each river bank below.

- River bank A: 2018 represents 99 % of 2019-1 data set, followed by, 97% in 2015, 90 %, 2017 and 81% 2019-2. An increase in bed elevation of the intertidal area is visible comparing the 2019-1 and 2018 case. This indicates that the intertidal area is growing in height and in addition probably in surface area. From 2015 to 2018 the height of the intertidal flat increased. From Figure 5.4 it can be obtained that there is no increase visible in bed level elevation below the lowest astronomical tide.
- River bank B: 2015 represents 100 % of the 2019-1 data set, followed by 99 % 2018, 95% 2017 and 86% 2019-2. An increase in bed level elevation is visible comparing the height of the intertidal flat in 2018 and 2019. This indicates that the intertidal area is growing in height and probably in surface area. From 2015 to 2018 the height of the intertidal flat did not increase. From Figure 5.4 it can be obtained that there is no increase visible in bed level elevation below the lowest astronomical tide.
- River bank C: 2018 represents 98 % of 2019-1 data set, followed by by 98 % 2015, 97% 2019-2 and 95 in % 2017. An increase in elevation of the tidal flat can be obtained from 2015 up to 2019-1. Incorporating the hypsometric curves of the total river bank, Figure 5.4, it can be obtained that in the period 2015 - 2018 - 2019, a shift is present in which the bed level elevation is increasing just below the lowest astronomical tide. This indicates that the sediment is deposited in the river bank close to the intertidal area.
- River bank D: 2015 represents 98 % of 2019-1 data set, followed by 97 % 2018, 96% 2017, and 88% 2019-2. An increase in elevation of the tidal flat can be obtained, this increase is present each year. Incorporating the hypsometric curves of the total river bank, Figure 5.4, it can be obtained that in the period 2015 - 2018 - 2019, a shift is present in which the bed level elevation is increasing just below the lowest astronomical tide. This indicates that the sediment is deposited in the river bank close to the intertidal area.

- River bank E: 2018 represents 96 % of 2019-1 data set, followed by, 93 % 2015, 92% 2017, and 88% 2019-2. The lack of data is relatively large, leading to a severe difference in intertidal area between 2019-1 and the other four measurement campaigns. An increase in elevation of the intertidal flat can be obtained from 2018 to 2019-1. From Figure 5.4 it can be obtained that there is no increase visible in bed level elevation below the lowest astronomical tide.
- River bank F: 2018 represents 96 % of 2019-1 data set, followed by, 95% 2017, 93 % 2015 and 93% 2019-2. The lack of data is relatively large, leading to a severe difference in intertidal area between 2019-1 and the other four measurement campaigns. From Figure 5.4, it can be obtained that the height at which the curve is constant decreased in elevation, this indicates that the average height of the river bank decreased. The curves close to the intertidal area do not show an increase over the years. Concluding, it can not be obtained if the intertidal area is growing.
- River bank G: 2015 represents 103 % of 2019-1 data set, followed by, 100 % 2018, 90% 2017 and 88% 2019-2. The data set of 2015 contains more measurements than 2019-1, however no intertidal area is present. A sand nourishment has been carried out after 2015, which is the cause for no intertidal area present in 2015 and for the large increase in bed level elevation in the whole river bank visible in Figure 5.4. This increase in bed level elevation of the river bank is gradually increasing in the years after the nourishment. The data sets 2019-1 and 2018 contain the same amount of measurements, from this a decline in elevation of intertidal area is observed. However, from 2015 a large increase of intertidal area is visible.
- River bank H: 2018 represents 106 % of 2019-1 data set, followed by, 104% 2017, 99 % 2019-2 and 96% 2015. From Figure 5.4 it can be obtained that the slope of the river bank became smaller over the year, although this can be the result of the differences in data points. There is not a clear increase or decrease of bed level elevation visible up to the intertidal area. The curves of 2017 and 2018 display the same shape inside the intertidal area, by which it can be concluded that the latter one was not increasing.
- River bank I: 2017 represents 106 % of 2019-1 data set, followed by, 105% 2018, 103% 2015 and 102 % 2019-2. All the data-sets contain more data than data set 2019-1. In 2015, the average height of the hypsometric curve was higher than the other curves, obtained from Figure 5.4. Besides, the intertidal area in 2015 was larger compared to the other years. From this it can be obtained that the intertidal area is decreasing in river bank I.
- River bank J: 2017 represents 104 % of 2019-1 data set, followed by, 98% 2015, 98 % 2018 and 97% 2019-2. Figure 5.4 shows an almost constant development of the river bank height up to the intertidal area over the years. Comparing the data-availability and the information from Figure B.1 no increase in intertidal area is obtained.
- River bank K: 2017 represents 102 % of 2019-1 data set, followed by, 100% 2015, 99 % 2018 and 94% 2019-2. In river bank K, from Figure 5.4 an increase in bed level elevation of the total river bank up to the intertidal area for all measurement campaigns. Especially, comparing 2015 with 2019 (containing an almost equal amount of data), clearly shows the increase in bed level elevation of the river bank. In terms of the intertidal area, a growth in elevation is obtained from 2018 to 2019. Data set 2017 contains more data and represents more intertidal area. Which again indicates that the lack of data probably coincides with the lack of data inside the intertidal area.
- River bank L: 2017 represents 101 % of 2019-1 data set, followed by, 101% 2018, 101 % 2015 and 97% 2019-2. In river bank L, the curves in Figure 5.4 display an increase in bed level elevation from -6 m NAP up to the intertidal area. In addition, it can be obtained that both the surface area and the height of the intertidal area increases.
- River bank M: 2018 represents 103 % of 2019-1 data set, followed by, 98% 2017, 96% 2019-2 and 88% 2015. In river bank M, the curves in Figure 5.4 shows a slight decrease in bed level elevation from -6 m NAP up to the intertidal area. The intertidal area did not increase significantly from 2017 to 2019 that show the same amount of data points. Concluding, the bed level outside the intertidal area is slightly decreasing and the intertidal area is slightly increasing.

- River bank N: 2018 represents 97 % of 2019-1 data set, followed by, 95% 2017, 91% 2019-2 and 89% 2015. In river bank M, the curves in Figure 5.4 display the same shape from -6 m NAP up to the intertidal area. The increase in tidal area is directly related to the increase in the amount of data. Therefore, it is assumed that the intertidal area did not increase at this location.

	River bank	Intertidal area
A	-	Increase
B	-	Increase
C	Increase	Increase
D	Increase	Increase
E	-	Increase
F	Decrease	-
G	Increase	Increase
H	-	-
I	-	Decrease
J	-	-
K	Increase	Increase
L	Increase	Increase
M	Decrease	Increase
N	-	-

Table B.2: Table containing the increase, decrease, or no difference (-) of bed level elevation inside the total river bank and the intertidal area obtained from the constructed hypsometric curves Figure 5.4 and B.1. The increase in the intertidal area can both indicate an increase in height or an increase in surface area. For more information, it is referred to the textual description of each river bank.

In table B.3, the average increase and decrease of the surface area in meters are displayed. From this it can be obtained that the bed level changes are small, in the order of a few centimeters. Although, table B.1 shows there is a significant difference in amount of measurement points over the years, this is not expected to affect the trend in bed level changes. This trend shows that, on average between 2015 and 2017 the bed levels were increasing, and between 2017 and 2019-1 the bed levels were decreasing. Aside from the average, river bank G, K and L show an increase in bed level elevation in both the period between 2017 and 2019, and 2015 and 2017. In particular, river bank G shows a large increase in bed level, in between these year a sand nourishment was executed in the river bank and therefore this value is relatively high. In front of river bank K and L a longitudinal wall is constructed in 2018, this effect is visible in the increase in bed level at location L. At this river bank, the increase in bed elevation is relatively larger during the period between 2017 and 2019 than the period 2015-2017. For river bank K this value is almost equal.

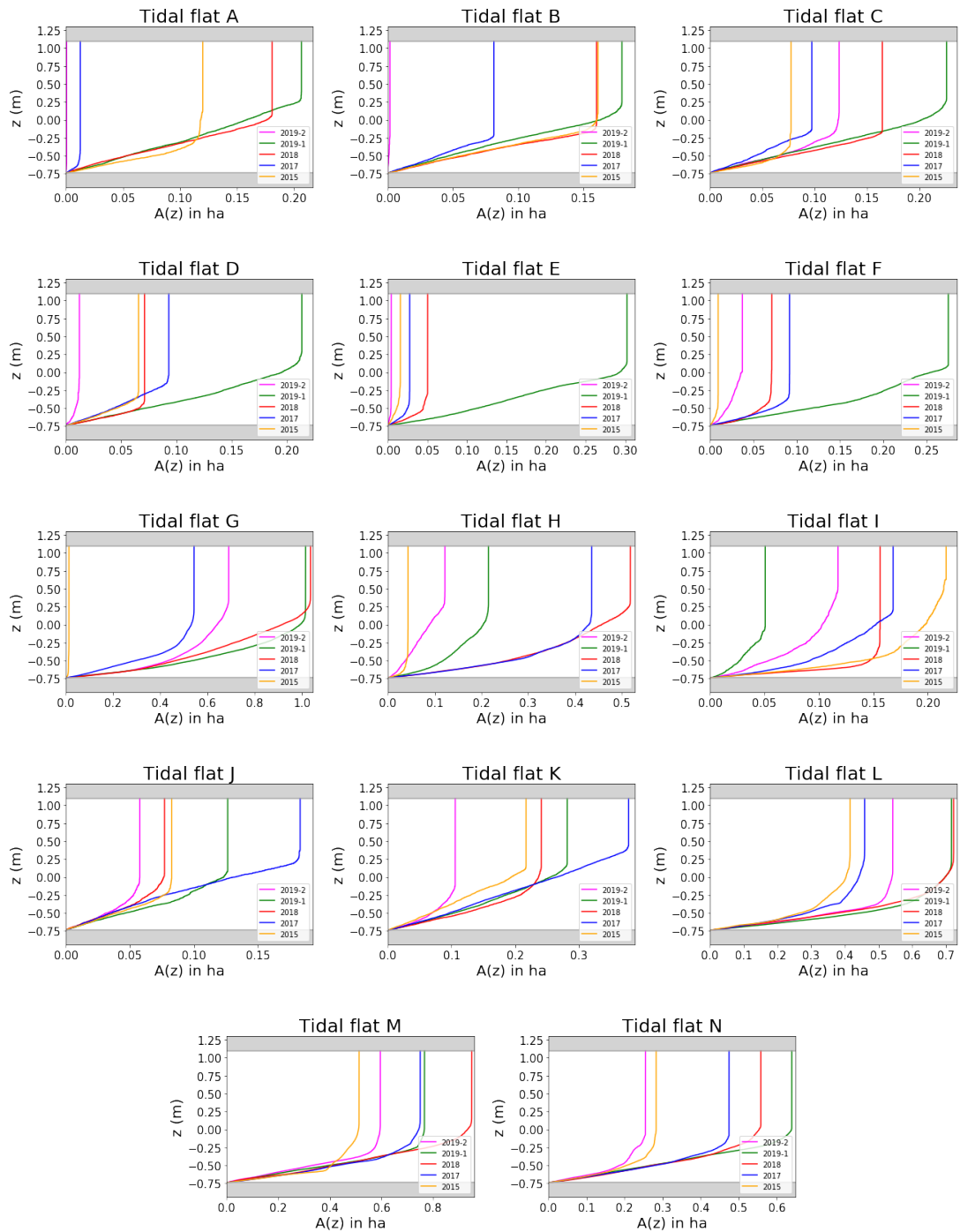


Figure B.1: Morphological evolution of the intertidal area of the river banks from -0.74 m NAP, obtained from 5 measurement campaigns. The lines indicate the years, orange : 2015, blue : 2017, red : 2018, green :2019-1 and pink 2019-2. The grey shaded indicate the area outside LAT and HW. For reference to location of letters, see Figure 5.2

	2015-2019			2017-2019			2015-2017		
	Positive	Negative	Total	Positive	Negative	Total	Positive	Negative	Total
A	0.035	-0.019	-0.002	0.052	-0.052	-0.026	0.049	-0.025	0.024
B	0.022	-0.039	-0.025	0.013	-0.061	-0.053	0.051	-0.017	0.028
C	0.034	-0.049	-0.022	0.011	-0.073	-0.064	0.065	-0.014	0.031
D	0.048	-0.065	-0.025	0.007	-0.077	-0.075	0.061	-0.029	0.037
E	0.073	-0.054	-0.023	0.029	-0.070	-0.058	0.067	-0.012	0.035
F	0.037	-0.090	-0.043	0.013	-0.080	-0.067	0.039	-0.029	0.024
G	0.820	-0.021	0.681	0.199	-0.040	0.091	0.659	-0.024	0.592
H	0.055	-0.148	-0.061	0.019	-0.101	-0.083	0.060	-0.104	0.022
I	0.067	-0.148	-0.122	0.034	-0.085	-0.076	0.028	-0.082	-0.046
J	0.046	-0.070	-0.024	0.008	-0.098	-0.091	0.075	-0.022	0.068
K	0.359	-0.005	0.391	0.090	-0.044	0.173	0.246	-0.001	0.217
L	0.282	-0.017	0.283	0.183	-0.019	0.189	0.104	-0.014	0.097
M	0.037	-0.063	-0.036	0.048	-0.057	-0.033	0.041	-0.049	-0.001
N	0.029	-0.024	-0.007	0.034	-0.043	-0.035	0.042	-0.007	0.034

Table B.3: Table displaying the average increase and decrease of total surface area of the river banks. In the first row the years are displayed from which the difference in elevation is calculated. The second row contains positive, negative and total. Positive indicates the average increase in elevation of bed levels that increased, and negative indicates the average decrease in elevation of bed level measurements that decreased. The values in the column total shows the averaged increase or decrease in elevation of all the measurements in the certain river bank



Calibration of the model and sensitivity analysis

C.1. Bed topography

In Chapter 6.2, the adaptation in bathymetry is described in order to include sediment transport in the hydrodynamic model. At the boundaries of the model, small disturbances were present, a so-called 'snowball effect' resulted in large erosion pits at the boundaries. This was prevented by changing the bed levels at the boundaries into a smooth variation of bed levels from the river bank to river bank. These bed levels are also constant for 6 grid cells in the direction of the main flow. Also, to solve the discontinuities at the boundaries a Thatcher-Harleman time-lag is implemented of 60 minutes. The Thatcher-Harleman time lag is used to avoid the discontinuity of differences in concentration at the reversal of the flow between the prescribed value and the computed value (Deltares, 2018).

C.2. Sensitivity analysis non-cohesive sediment

The sensitivity analysis regarding the transport of non-cohesive sediment consist of variations in hydrodynamic forcing and particle diameters.

In order to display the affect of both the diameters of the coarse sediment in combination with the effect of hydrodynamic boundary combinations of the latter one, all combinations are modelled. From this, the sensitivity of the model related to sediment transport can be estimated. The critical velocities for the different particles according to theory of Shields are determined in Chapter 4 and are equal to 0.44, 0.3 and 0.2 m/s for diameters of 300, 150 and 75 μm respectively. In order to compare the different simulations, the cumulative sedimentation and erosion in river bank L after six months of time are compared. Note that the scale on the y-axis changes.

Incorporating a sand diameter of 75 μm , it can be obtained that some sedimentation is present at the entrances. A diameter of 75 μ is relatively small for sand, and is almost comparable with the diameter of silt. The transport mechanisms of cohesive and non-cohesive sediment are somewhat different. Transport of 'coarse' sediment in areas under tidal forcing is mainly determined by the magnitudes of both ebb and flood flow.

Simulation A incorporates a morphological tide and thus corresponds with relatively small velocities present in the river bank. This effect is directly related to the transport of coarse sediment, and thus sediment is not transported further into the river bank as the velocities are too small. At the left entrance more sedimentation is present resulting from the geometry of the groynes in combination with the longitudinal wall. When comparing the effect of different simulations on the transport of sediment with a diameter of 75 μm , an increase of sedimentation is visible from A to C which is in accordance with the increase in velocity. For clarity, simulation B represents the implementation of a spring tide and simulation C represents a spring tide in combination with an additional surge of 1 meter. Comparing the resulting sediment transport of simulation B and C, it can be obtained that the additional surge leads to more sediment import. This is related to an increase in volume of water in the river bank, by which also more suspended sediment is imported in the river bank. No erosion of sediment is visible in the river bank incorporating a diameter of 75 μm . The input or export of sediment is as mentioned before related to the difference in magnitudes of velocities inside the river bank. The transport of sediment is a continuous process. The velocities present in the river bank do reach the critical velocities for re-suspension of sediment and so possible erosion. The resulting import or export is the difference between import and export of sediment. Incorporating a diameter of 75 μm shows that an import of very fine sediment is expected. This can be related to the velocities being flood dominant in the river

bank by which an import of sediment is visible. It should however be noted, that the results obtained with a sediment diameter of $75 \mu\text{m}$ display a lot more sedimentation present at the entrances than is obtained from data and is not in agreement with reality.

Incorporating a sand diameter of $150 \mu\text{m}$ in the model, the resulting import of sediment is much smaller. This is related to a higher critical velocity for larger sediment particles, therefore less sediment is brought into suspension and thus transported. When comparing the result of simulation A with these two different diameters, it can be obtained that the resulting sediment input is much smaller and almost negligible. Erosion is visible at the corner left corner of the longitudinal wall. The critical velocities for erosion are thus reached at this corner. This in combination with less sediment being brought into suspension, leads to erosion of sediment.

Comparing the different simulations with a diameter of $150 \mu\text{m}$ incorporated shows an increase in sedimentation at the left entrance of the river bank from A to C. Erosion pits are now visible at the right entrances resulting from simulation B and C. The increase in velocity thus results in an increase in sediment supply towards the river bank at the left entrance and erosion at the right entrance. The effect of the relatively small velocities present in the river bank is clearly visible, as the sediment imported at the entrances is not transported further into the river bank. The critical velocity of sediment with a diameter of $150 \mu\text{m}$ is around equal to 0.3 m/s , determined in Chapter 4. This velocity is thus clearly not reached further into the river bank.

Incorporating a sand diameter of $300 \mu\text{m}$ in the model in combination with a morphological tide (simulation A) results in no sedimentation at all and only erosion is visible. This indicates that the critical velocities (0.44 m/s) are hardly reached in the river bank are not often met in the river bank. In addition, the availability of suspended sediment is smaller. Coarse sand is therefore not likely to enter the river bank. The resulting erosion is only present at the left entrance.

Comparing the different simulations with a diameter of $300 \mu\text{m}$ incorporated shows an increase in both sedimentation and erosion at the left entrance of the river bank from A to C. An increase in erosion is also visible at the left entrance. Again the erosion pits at the corners of the longitudinal wall and the groynes are visible, this is in agreement with literature as the flow gets contracted at these locations.

When comparing the suspended sediment concentration of coarse sediment obtained from different simulations, the effect of higher velocities on the suspended sediment concentration in the navigation channel is clearly visible. In Figure C.2 both the velocities in the navigation channel in combination with the suspended sediment concentrations of sand with a diameter of $150 \mu\text{m}$ are displayed. The first velocity peak represent the ebb velocities and the second peak represent the flood velocities. From this it can be obtained that a relatively small change in velocity leads to a significant difference in suspended sediment concentration. In addition, the suspended sediment concentration is much larger resulting from the large ebb velocities in comparison with the flood velocities. This shows that the effect of an increase in velocity is significantly large, as is in agreement with literature. The transport of sediment is a function of both the velocity and the availability of sediment, and is also correlated. In addition, it is visible that coarse sediment directly responds to the flow. For instance, the velocity being zero coincides with the concentration being zero and maximum velocities coincide with maximum suspended sediment concentrations.

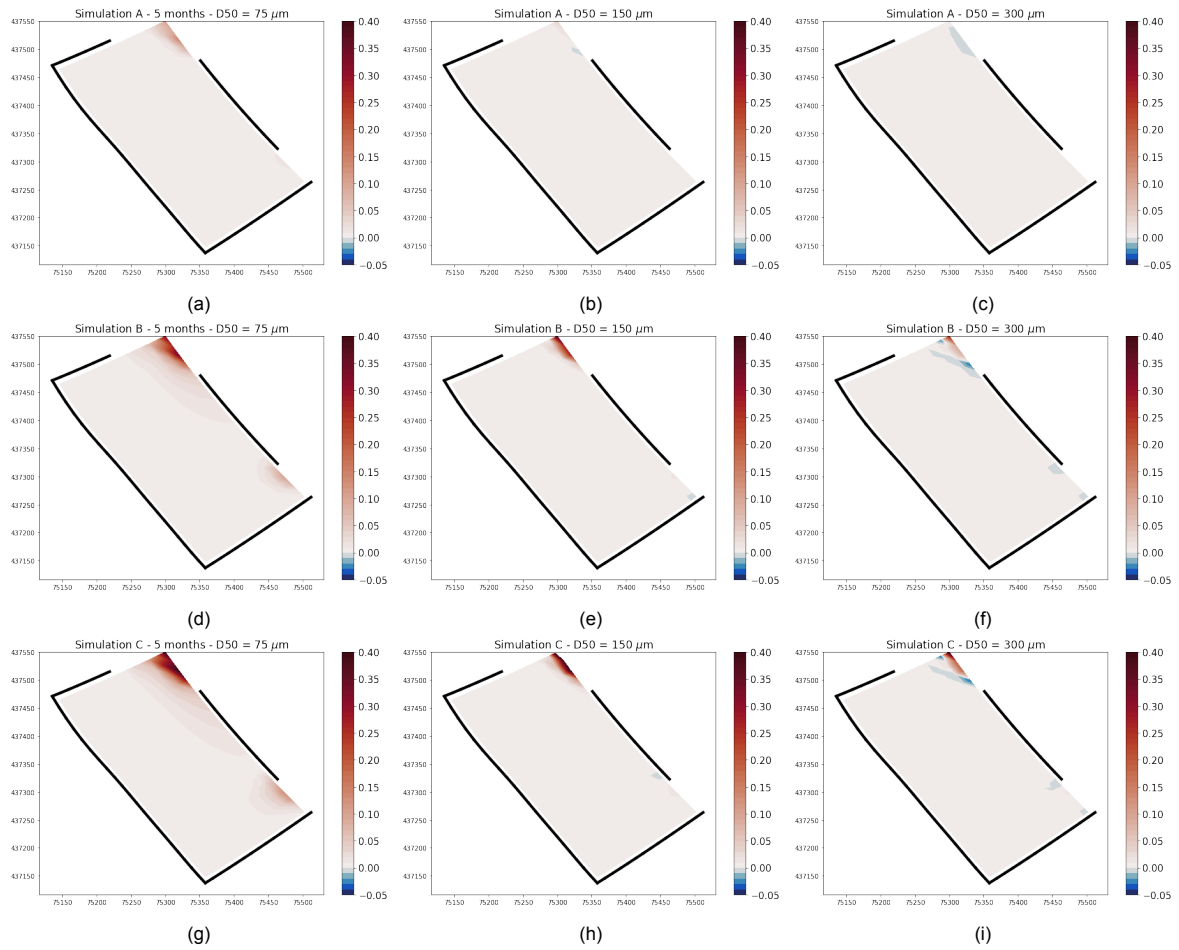


Figure C.1: Cumulative sedimentation / erosion obtained from simulations A,B and C in combination with three grading of sediment incorporated. The black lines in the figure indicate the locations of the longitudinal walls and groynes preset at the river bank. Incorporating a diameter of $75 \mu\text{m}$ the cumulative erosion/sedimentation is displayed after a time span of 5 months. In case of the other grading the results are obtained after 6 months. In all figures the scale displayed in the color bar is the same and displays erosion or sedimentation in meters.

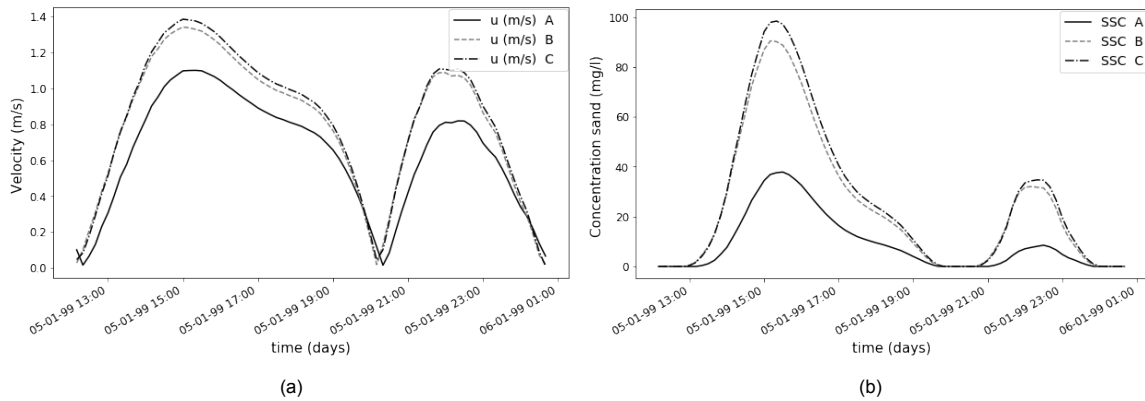


Figure C.2: Figure C.2a displays the depth averaged velocity profile in the middle of the navigation channel in front of river bank L for simulation A,B and C during one tidal cycle. The initial peak of velocities are ebb velocities and the second peak represent the flood velocities. In Figure C.2b the corresponding suspended sediment concentrations of sand are displayed for simulation A,B and C during the same tidal cycle. The sand diameter incorporated in the model is equal to $150 \mu\text{m}$.

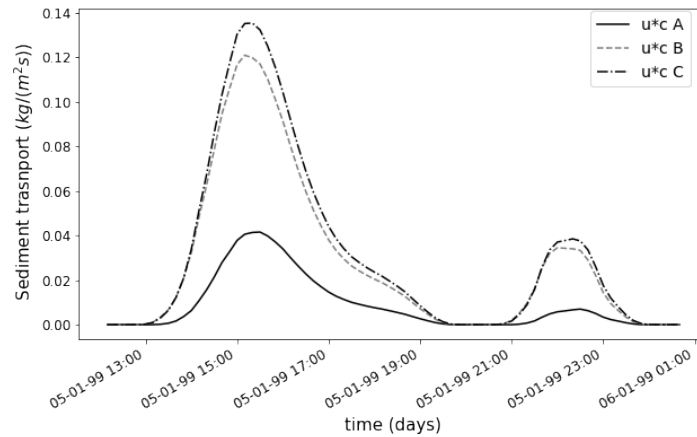


Figure C.3: Suspended sediment transport of sand with a diameter of $150 \mu\text{m}$ resulting from simulations A,B and C. A clear distinction can be visualised resulting from the transport of fine sediment during ebb and during flood. (first peak represents ebb and second peak represents flood).

Concluding, it can be obtained that coarser sediment is not likely to deposit in the river bank. This is mainly due to the velocities present in the river bank, as the velocities inside the navigation channel are large enough to bring the sediment into suspension. Besides the sediment not being likely to deposit in the river bank, coarse sediment present as base-layer is also likely to erode. This is in agreement with literature, from which it is obtained that at the tips of groynes erosion pits are likely to occur resulting from flow contractions in combination with large turbulence intensities (Schierneck and Verhagen, 2016). Medium coarse sediment is only likely to enter the river bank incorporating a spring tide, as the velocities present both in the river bank and the navigation channel increase. This increase in velocity results in further transport in the navigation channel and also higher suspended sediment concentrations. This sensitivity analysis is in agreement with literature, as spring tide results in higher sedimentation present in the river bank.

Taken into account that the additional effects of wind stresses and waves are not incorporated in the model, it is likely that the sediment is transported somewhat further into the river bank than is obtained from the model. From this analysis it can however be concluded that during a morphological tide, no large sedimentation of sand is expected in the river bank.

C.3. Sensitivity analysis cohesive sediment

The sensitivity of the model is tested regarding several parameters. The parameters considered in this research consist of the critical shear stress, the horizontal diffusivity, and the concentration of cohesive sediment.

C.3.1. Critical shear stress erosion silt

The model-set up for cohesive transport requires a critical stress for erosion and sedimentation for the computation of sediment transport. If the bed shear stress is larger than the critical stress for sedimentation, no sedimentation takes place. The reverse is accounted for with the critical stress for erosion, if the bed shear stresses are smaller no erosion takes place.

In the model simulations a high critical stress for sedimentation is incorporated, which indirectly implies that sedimentation occurs at all times (Winterwerp and Van Kesteren, 2004). The critical shear stress for erosion is a parameter which is determined by use of calibration, in Figure C.4 the resulting changes in bed level are displayed from different critical shear stresses for erosion. The adaptations are tested on a run with the hydrodynamic forcing being the morphological tide, and a silt concentration of 0.01 kg/m^3 . The critical stresses showed in the figures are 0.1 N/m^2 and 0.001 N/m^2 , these figures show the large impact of this parameter on the transport of silt into the groyne area. The implementation of critical shear stress for erosion of 0.001 N/m^2 shows hardly any sediment input in the area, except at

the left corners, which indicates the corresponding velocities at that location are very small. This could indicate that a combination of a low critical shear stress and a high concentration of sediment will lead to the same situation as an increase of diffusivity in combination with a high critical shear stress.

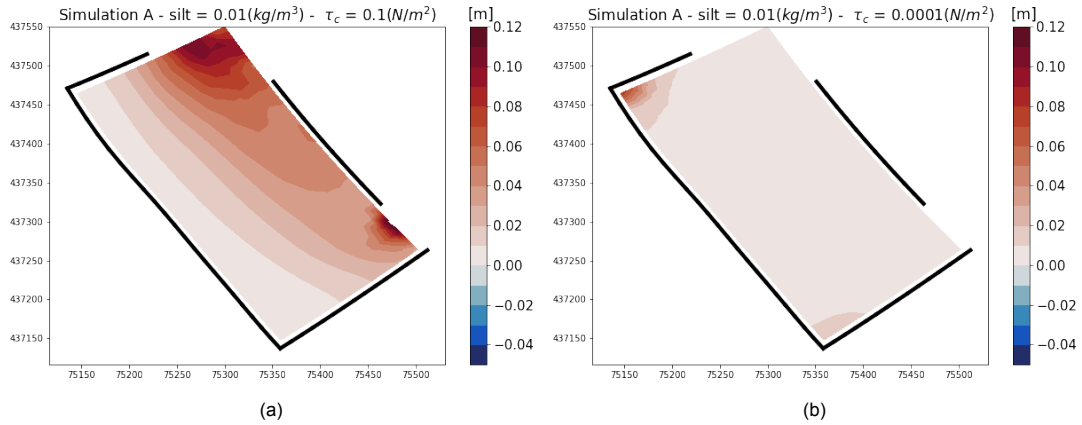


Figure C.4: Cumulative erosion/sedimentation after six months incorporating two different critical shear stresses. In Figure C.4a a critical shear stresses of erosion of 0.1 N/m^2 is incorporated. In Figure C.4b a critical shear stress for erosion of 0.0001 N/m^2 . The color bar indicates the erosion or sedimentation present in meters. Positive values display an increase in bed level, negative values indicate a decrease in bed level. The results are obtained incorporating a non-erodible bed layer.

C.3.2. Horizontal eddy diffusivity

The effect of diffusivity on the suspended sediment transport can be explained by use of the advection diffusion equation used in Delft3D, see equation C.3.2. In this equation, terms 2 and 3 represent the advection terms, and 4 and 5 represent the diffusive terms. The advection terms describe the motion of sediment in direction of the main flow, and the diffusive terms indicate the sediment being spread out.

$$\underbrace{\frac{\partial c^{(\ell)}}{\partial t}}_1 + \underbrace{\frac{\partial uc^{(\ell)}}{\partial x} + \frac{\partial vc^{(\ell)}}{\partial y}}_2 + \underbrace{\frac{\partial w - w_s^{(\ell)}}{\partial z} c^{(\ell)}}_3 + \underbrace{-\frac{\partial}{\partial x} \varepsilon_{s,x}^{(\ell)} \frac{\partial c^{(\ell)}}{\partial x} - \frac{\partial}{\partial y} \varepsilon_{s,y}^{(\ell)} \frac{\partial c^{(\ell)}}{\partial y}}_4 - \underbrace{\frac{\partial}{\partial z} \varepsilon_{s,z}^{(\ell)} \frac{\partial c^{(\ell)}}{\partial z}}_5 = 0 \quad (\text{C.1})$$

Three model simulations are executed on the effect of horizontal eddy diffusivity on sediment transport into the river bank in the model. The adaptations are tested on a hydrodynamic forcing being the morphological tide, and a silt concentration of 0.01 kg/m^3 . It can be obtained, that an increase in diffusivity, results in sediment being transported further inwards to the river bank. Also the magnitude of sedimentation increased.

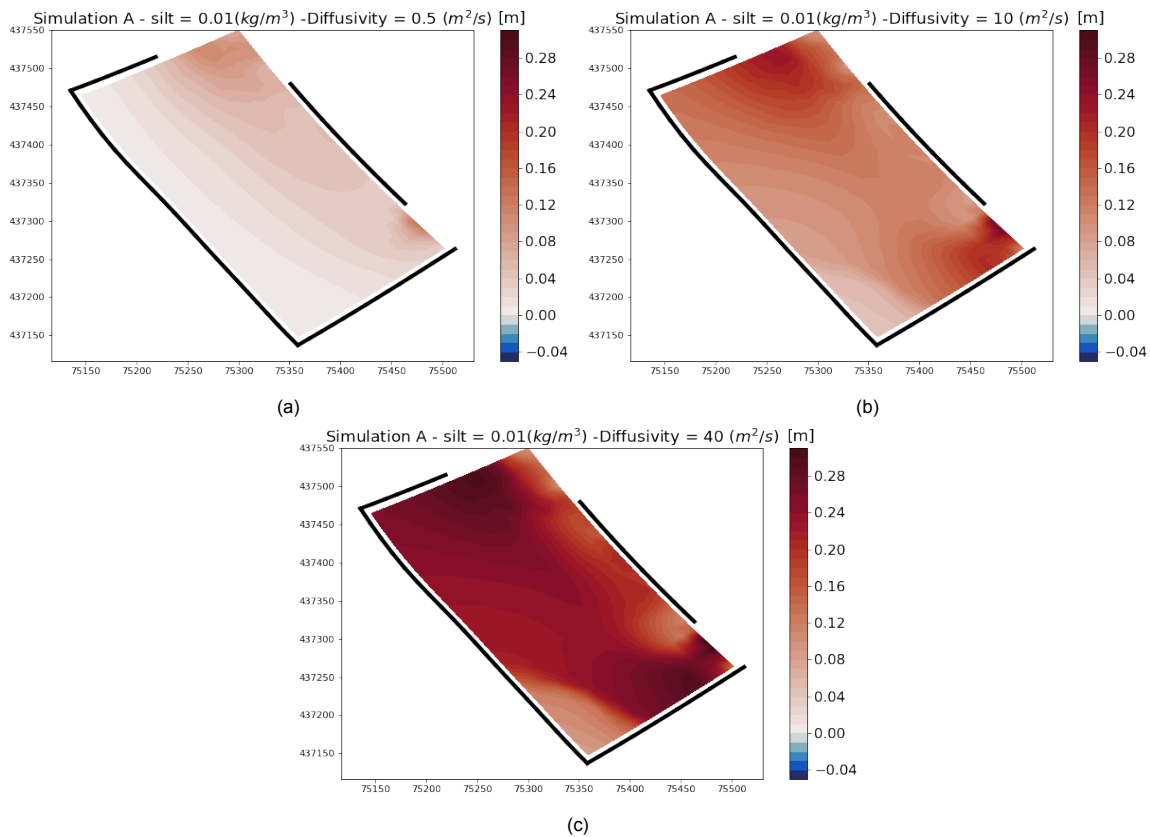


Figure C.5: The cumulative sedimentation erosion after six months is displayed in all figures incorporating a morphological tide. In addition, in all simulations a silt concentration of 0.01 kg/m^3 is incorporated. In Figure C.5a a horizontal eddy diffusivity of $0.5 \text{ (m}^2/\text{s)}$ is incorporated. In Figure C.5b a horizontal eddy diffusivity of $10 \text{ (m}^2/\text{s)}$ is incorporated. In Figure C.5c a horizontal eddy diffusivity of $40.0 \text{ (m}^2/\text{s)}$ is incorporated. The color bar indicates the erosion or sedimentation present in meters. Positive values display an increase in bed level, negative values indicate a decrease in bed level. The results are obtained incorporating a non-erodible bed layer.

C.3.3. Different concentrations of cohesive sediment

In order to calibrate the model, the results of the model should be verified with data. Data is available on the evolution of the bed level of the river bank, as is already discussed in Chapter 3. This data is averaged for a period of six months, in order to compare the results with the model in which the simulation time for sediment transport is six months. As is mentioned before, in this research sand and silt are modelled separately in order to get a clear vision on the sediment transport towards the river bank. For the cohesive sediment, silt, three different concentrations of the sediment are incorporated in the model separately, in order to display the effect of the concentration on the sediment transport. In addition, these concentrations are modelled in simulation A, B and C, i.e. incorporating a morphological tide, a spring tide and a spring tide in combination with a surge. The result of this sensitivity analysis is displayed in Figure C.6.

From this sensitivity analysis it can be obtained that a change in concentration of silt in the water column does not affect the pattern of relative sedimentation or erosion. For instance, when comparing Figure C.6a, C.6b and C.6c in which only the concentration is variable, the exact same pattern of sediment deposition is visible. The effect of hydrodynamic forcing on the transport of cohesive sediment is however clearly visible. The increase from morphological tidal forcing to a spring tide leads to sediment being further transported into the river bank. This is both related to the amount of suspended sediment available and the forcing mechanism being stronger incorporating an 'extremes' condition.

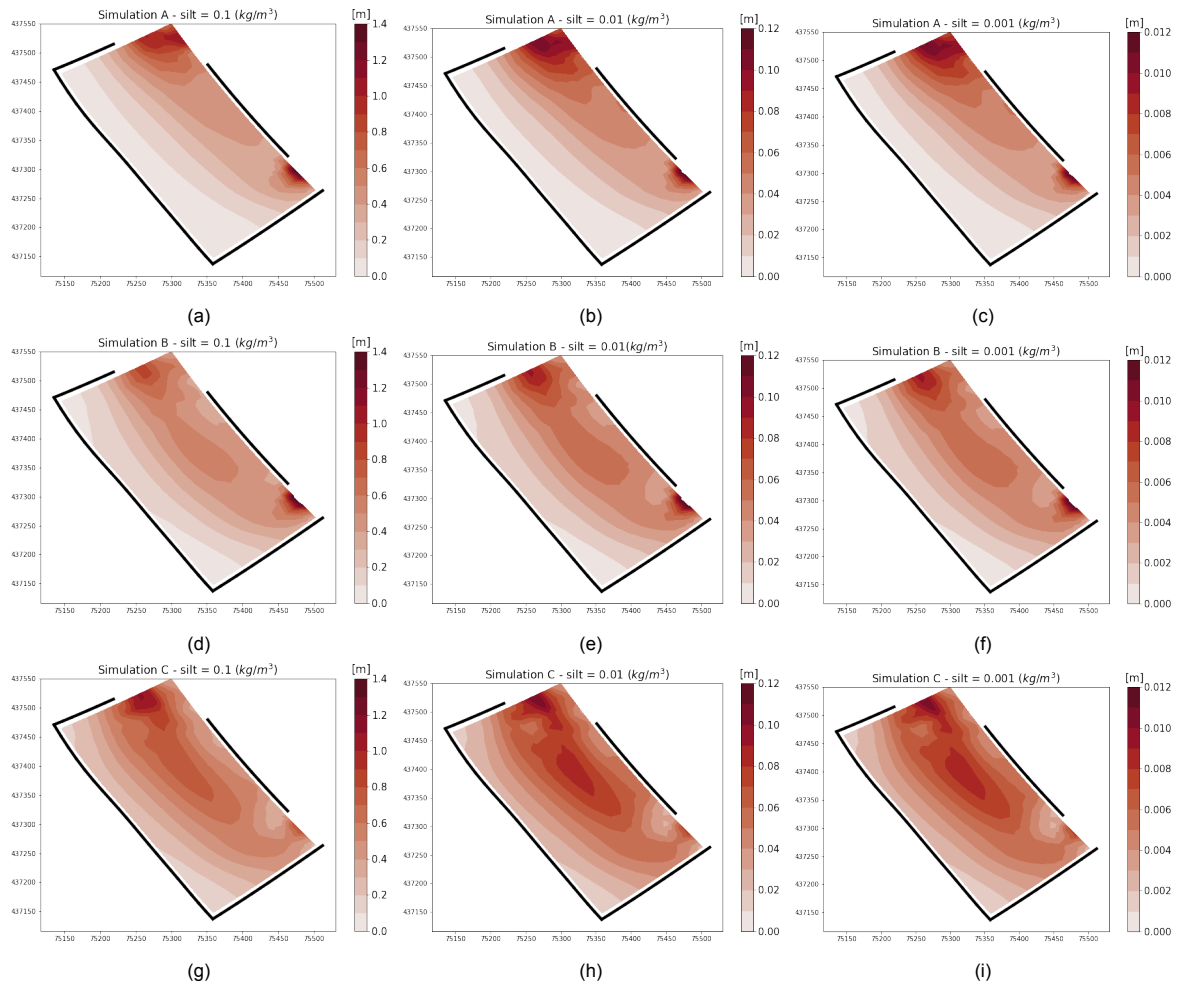


Figure C.6: Cumulative sedimentation / erosion obtained from simulations A,B and C in combination with three different concentrations of silt implemented in the model. The black lines in the figure indicate the locations of the longitudinal walls and groynes present at the river bank. In all figures the scale displayed in the color bar is the same and displays erosion or sedimentation in meters. Negative values indicate erosion and positive values indicate sedimentation of sediment. Note that the horizontal diffusivity incorporated in this sensitivity analysis is equal to $0.5 \text{ (m}^2/\text{s)}$ and thus varies from the final base-case model in which a diffusivity of $40 \text{ (m}^2/\text{s)}$ is incorporated in combination with a silt concentration of 0.001 kg/m^3

Supporting simulations

In this appendix additional simulation results are presented supporting the results presented in Chapter 7 and 8.

D.1. Flow patterns hydrodynamic forcing scenarios

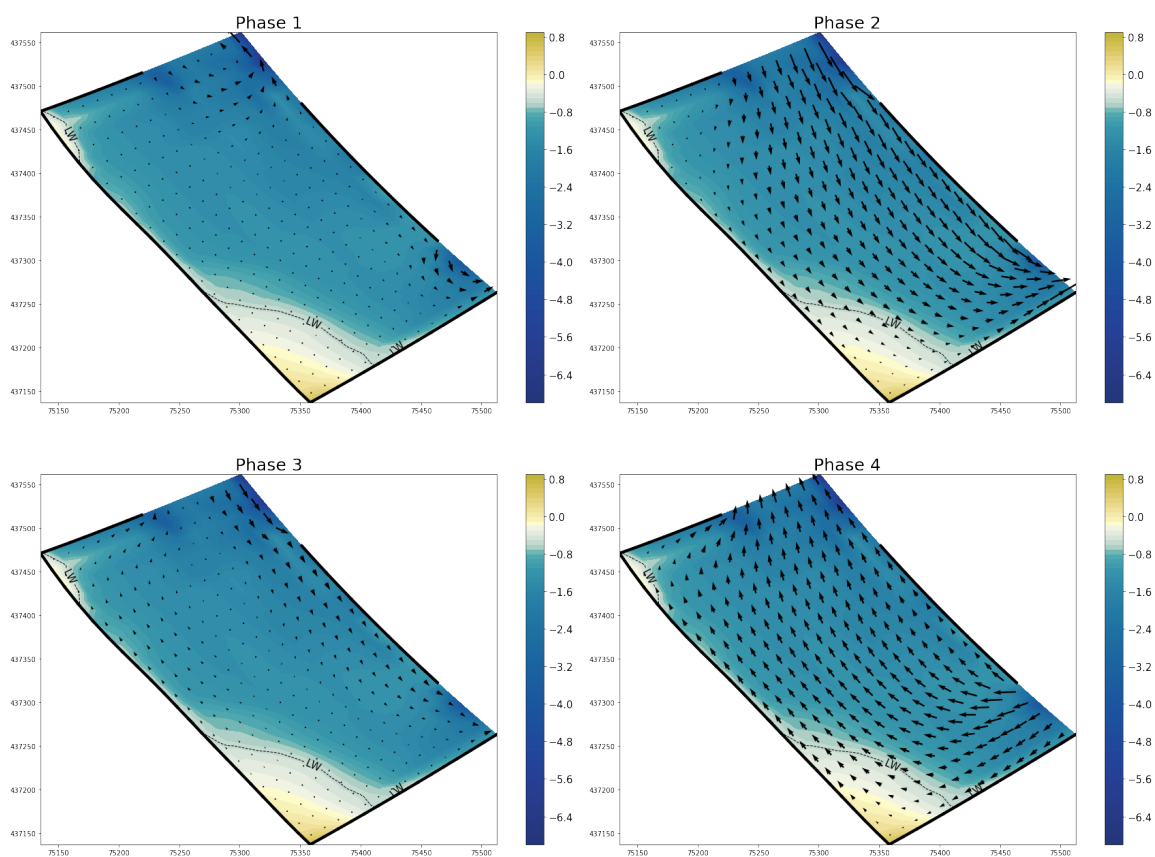


Figure D.1: Flow field in during different phases in the the river bank resulting from simulation A. The moments of time in which the figures are obtained are visualised in Figure 7.2. The color bar displays the bed level elevation relative to MSL in meters.

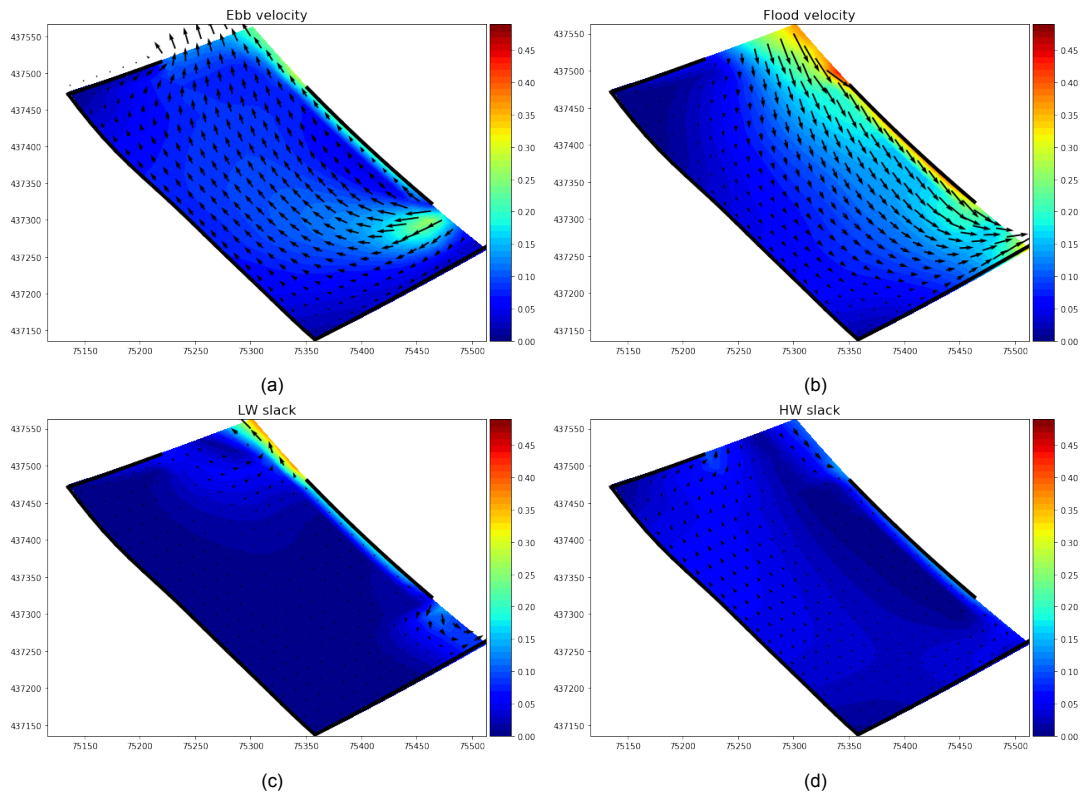


Figure D.2: Velocities magnitude and direction inside the river bank at different time frames resulting from simulation A.

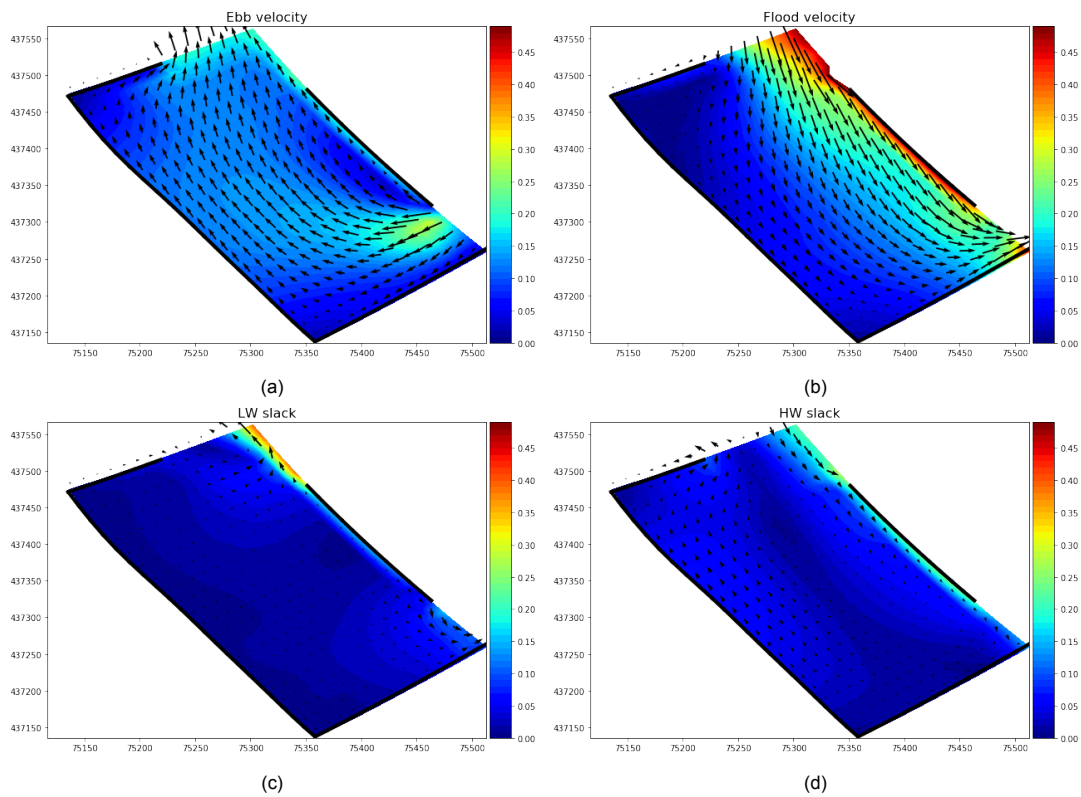


Figure D.3: Velocities magnitude and direction inside the river bank at different time frames resulting from simulation B

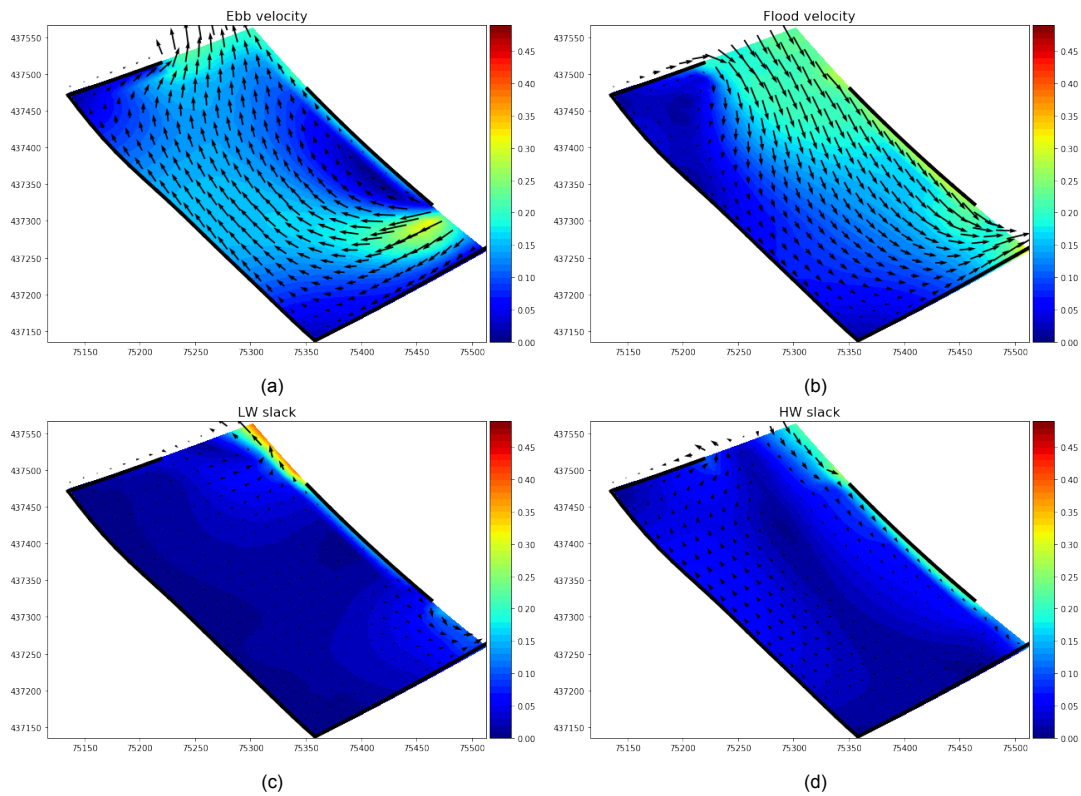


Figure D.4: Velocities magnitude in direction inside the river bank at different time frames resulting from simulation C.

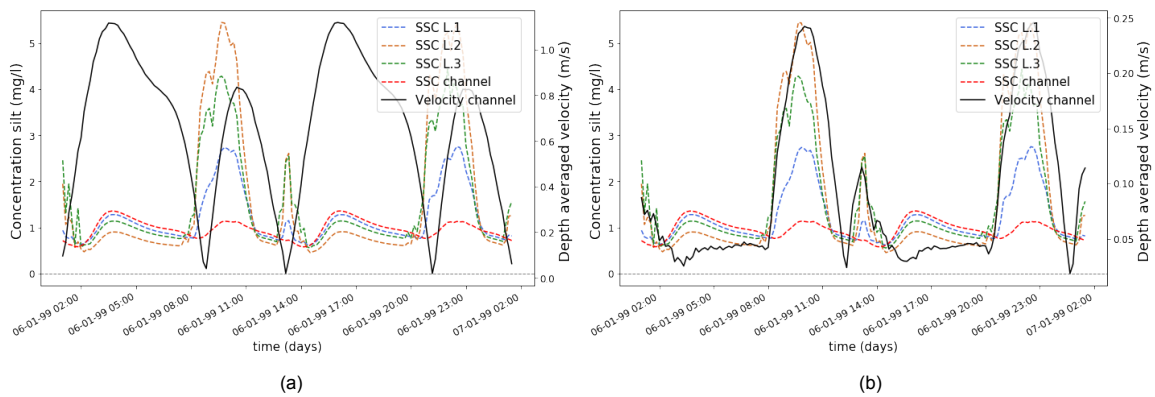


Figure D.5: In Figure D.5a the SSC at four locations in combination with the velocity profile inside the navigation channel are displayed in case of an erodible bottom in river bank L (simulation A). In Figure D.5b the SSC at four locations in combination with the velocity profile at observation point L.1 is displayed.

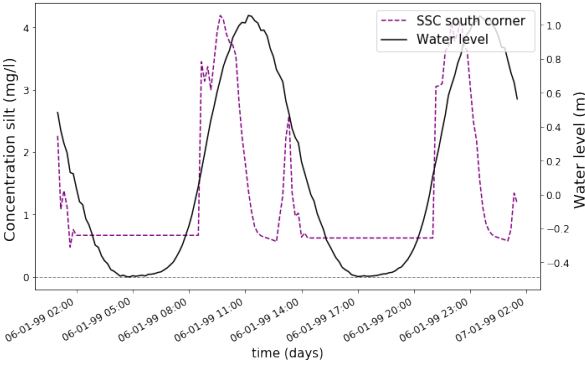


Figure D.6: SSC of silt in combination with the water level in the south located corner of river bank L (simulation A). The SSC is equal to the equilibrium concentration when no water is present at the inter tidal area.

D.2. Adaptations in bathymetry

D.2.1. Simulation D.1

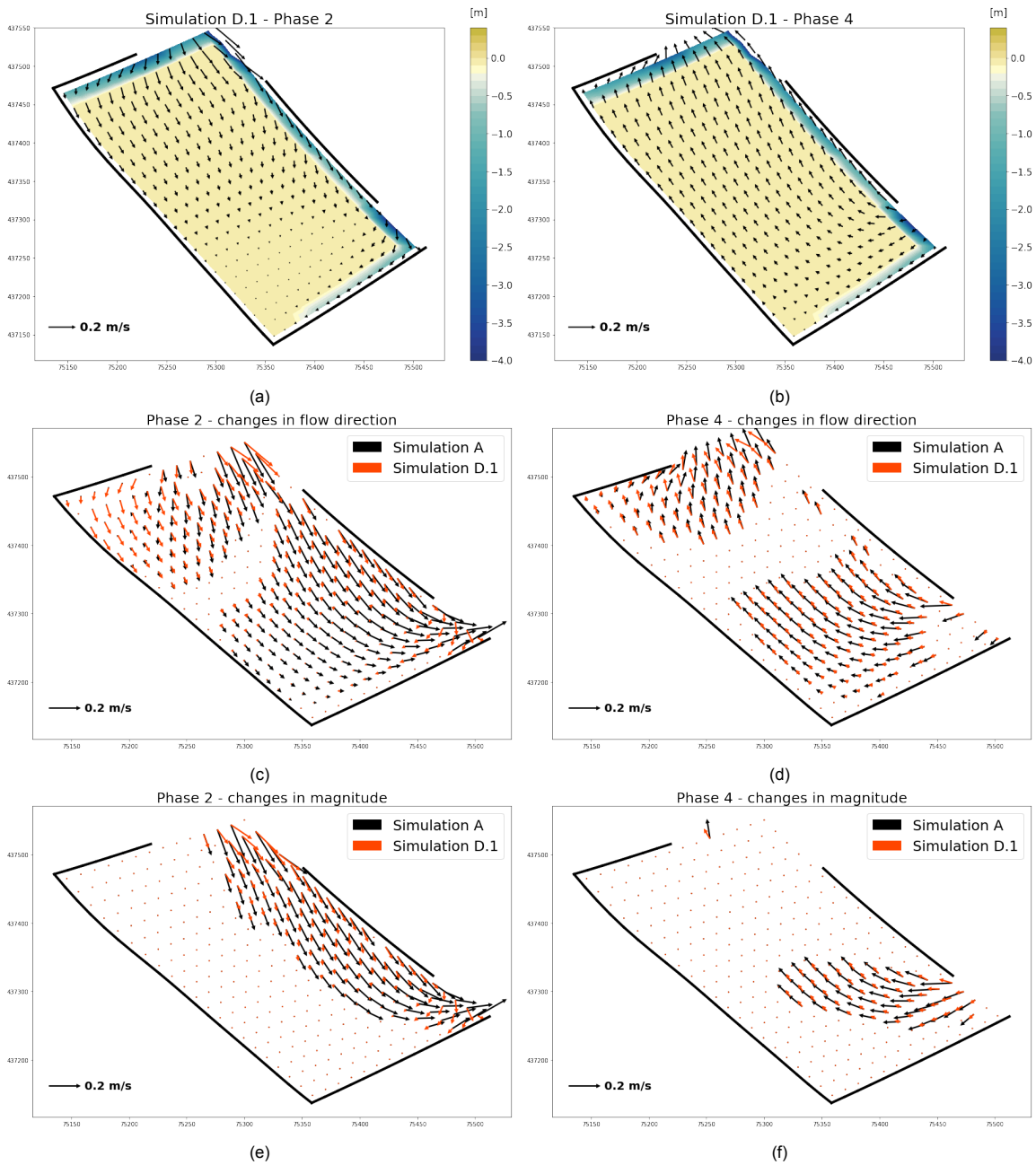


Figure D.7: Flow patterns observed during both flood and ebb in figures D.7a and D.7b respectively resulting from simulation D.1. The bathymetry displayed in this figure corresponds with the bathymetry used in the base-case. In Figure D.7c and D.7d the changes in flow direction obtained from both ebb and flood are displayed. The changes in flow direction are only displayed if the change of angle is larger than 6 degrees. In Figure D.7e and D.7f the changes in the magnitudes of the flow are displayed for both flood and ebb respectively. The changes in magnitude are only displayed if larger than 0.01 m/s, which is relatively small threshold. The time frames in which the flow patterns are observed are the same as in the base-case, see section 7.1.

D.2.2. Simulation D.2

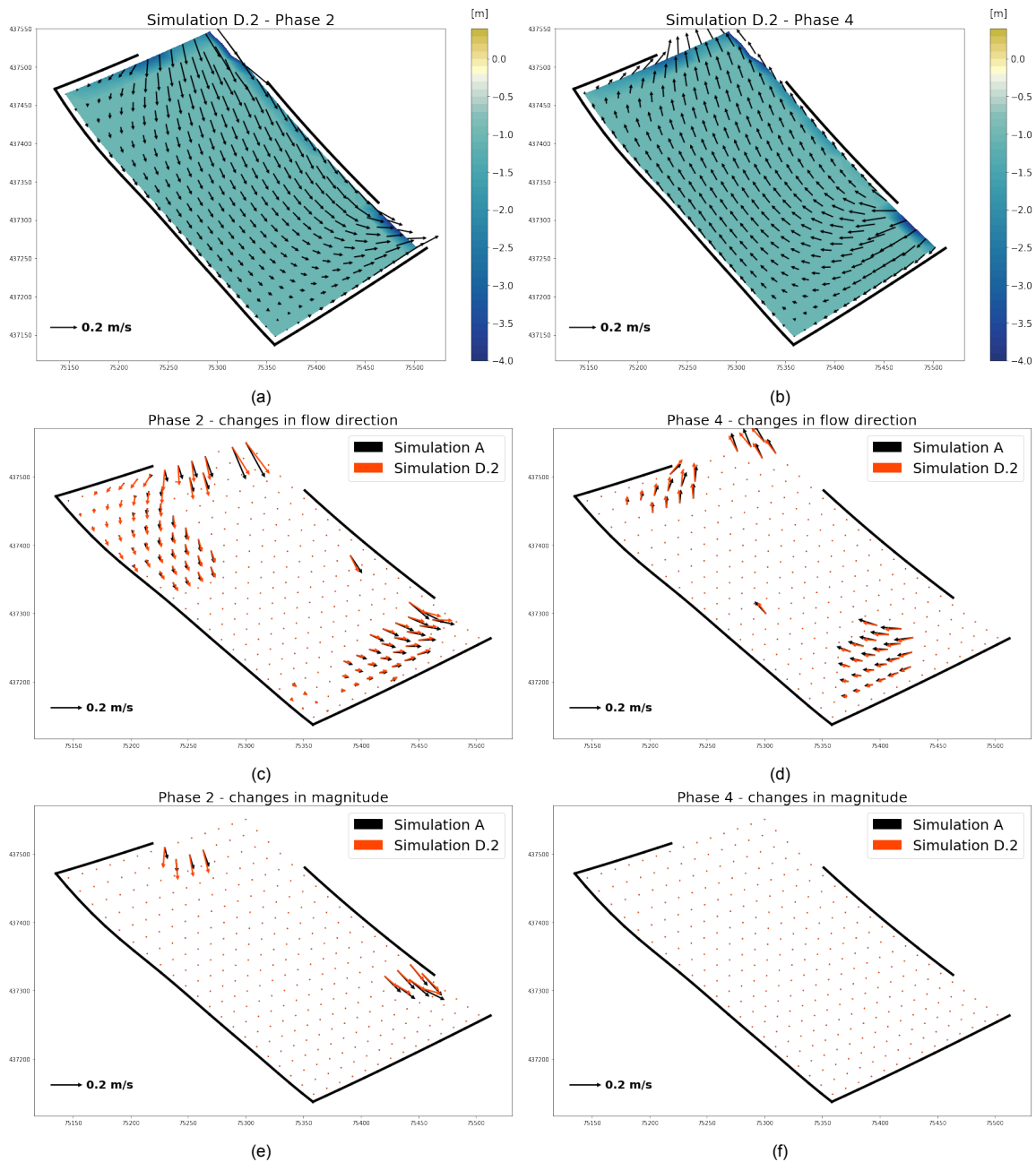


Figure D.8: Flow patterns observed during both flood and ebb in figures D.8a and D.8b respectively resulting from simulation D.2. In Figure D.8c and D.8d the changes in flow direction obtained from both ebb and flood are displayed. The changes in flow direction are only displayed if the change of angle is larger than 6 degrees. In Figure D.8e and D.8f the changes in the magnitudes of the flow are displayed for both flood and ebb respectively. The changes in magnitude are only displayed if larger than 0.01 m/s, which is relatively small threshold. The time frames in which the flow patterns are observed are the same as in the base-case, see section 7.1.

D.2.3. Simulation D.3

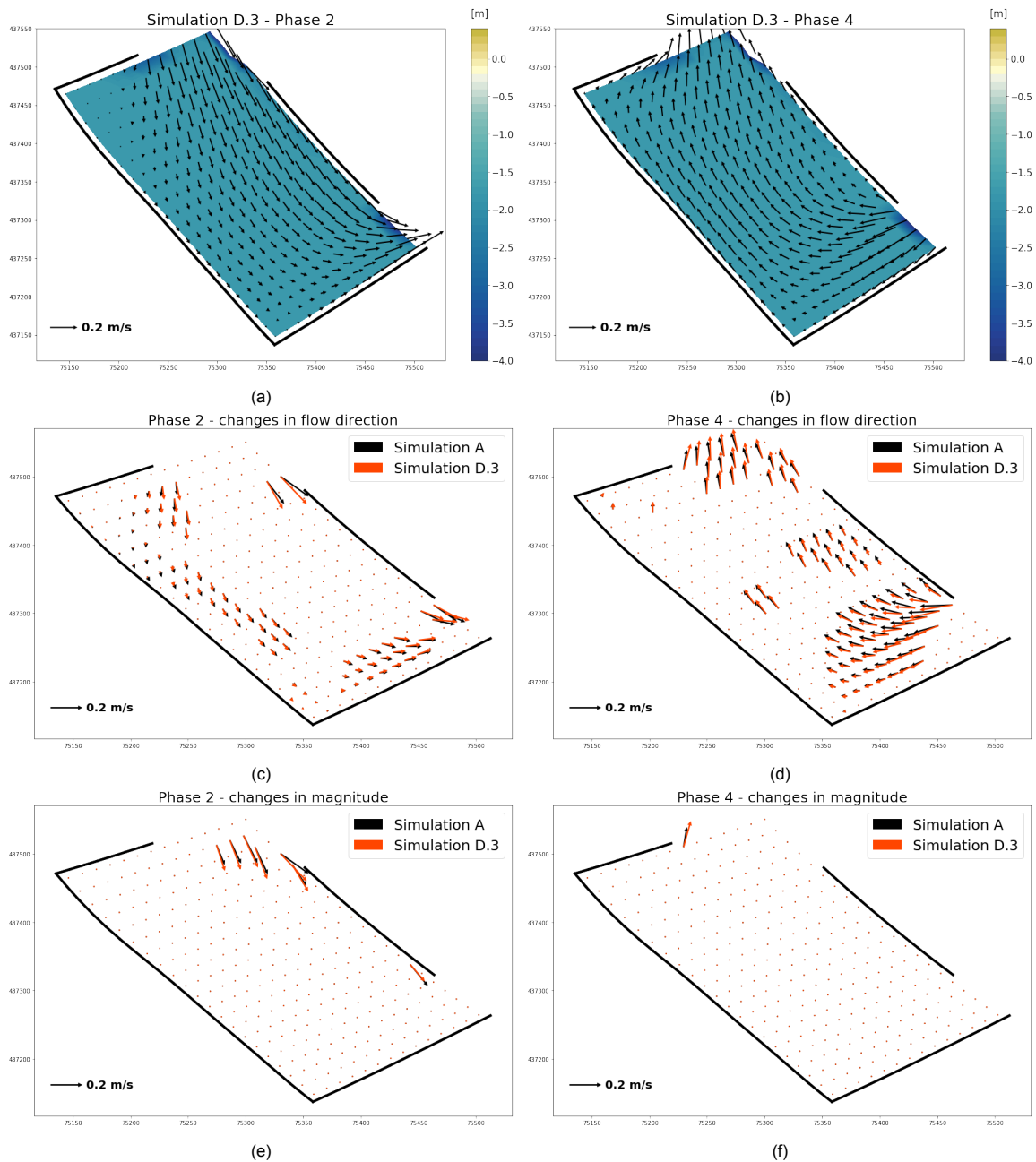


Figure D.9: Flow patterns observed during both flood and ebb in figures D.9a and D.9b respectively resulting from simulation D.2. In Figure D.9c and D.9d the changes in flow direction obtained from both ebb and flood are displayed. The changes in flow direction are only displayed if the change of angle is larger than 6 degrees. In Figure D.9e and D.9f the changes in the magnitudes of the flow are displayed for both flood and ebb respectively. The changes in magnitude are only displayed if larger than 0.01 m/s, which is relatively small threshold. The time frames in which the flow patterns are observed are the same as in the base-case, see section 7.1.

D.3. Adaptation longitudinal wall

D.3.1. Simulation E.1

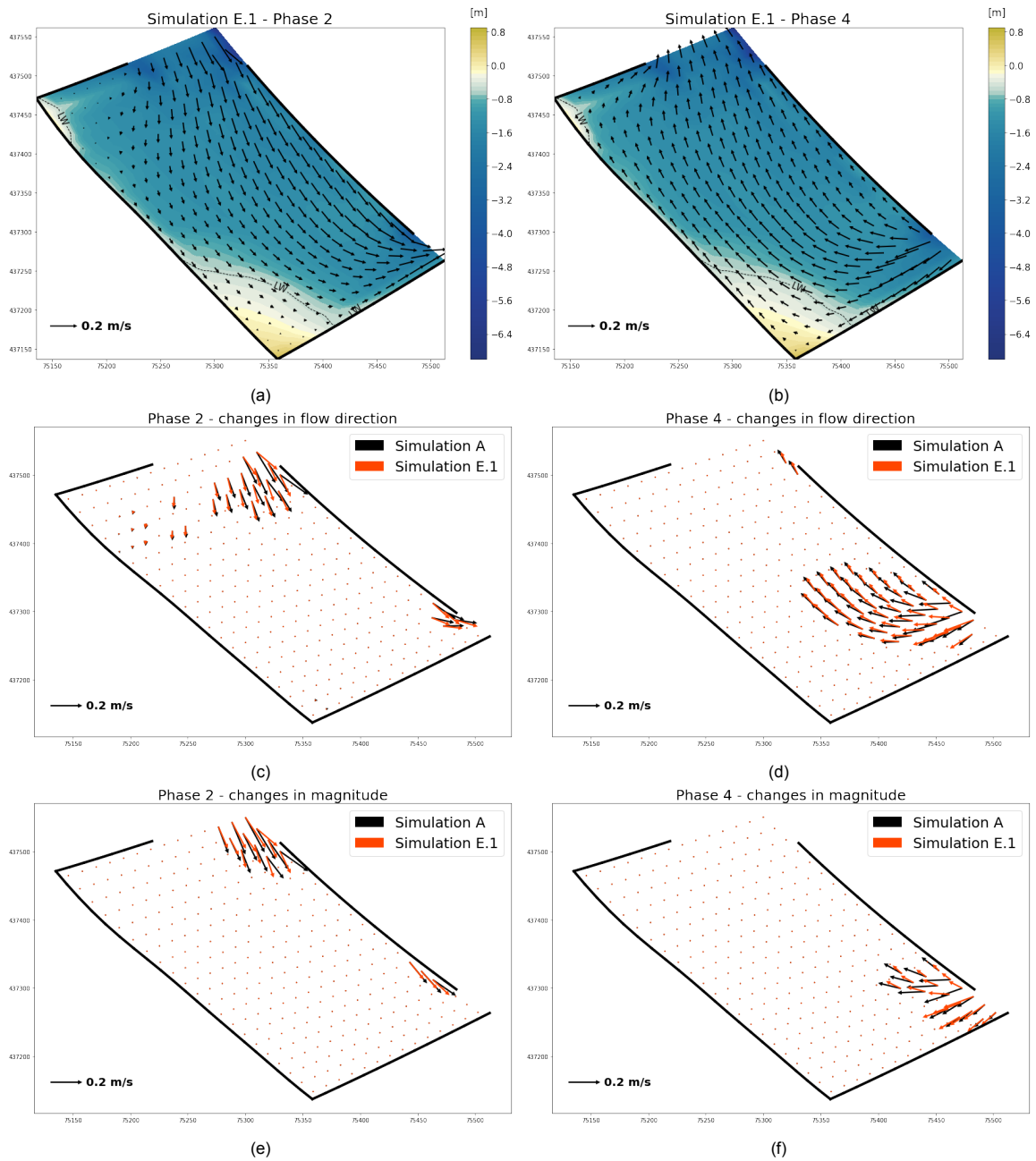


Figure D.10: Flow patterns observed during both flood and ebb in figures D.10a and D.10b respectively resulting from simulation E.1. In Figure D.10c and D.10d the changes in flow direction obtained from both ebb and flood are displayed. The changes in flow direction are only displayed if the change of angle is larger than 6 degrees. In Figure D.10e and D.10f the changes in the magnitudes of the flow are displayed for both flood and ebb respectively. The changes in magnitude are only displayed if larger than 0.01 m/s, which is relatively small threshold. The time frames in which the flow patterns are observed are the same as in the base-case, see section 7.1.

D.3.2. Simulation E.2

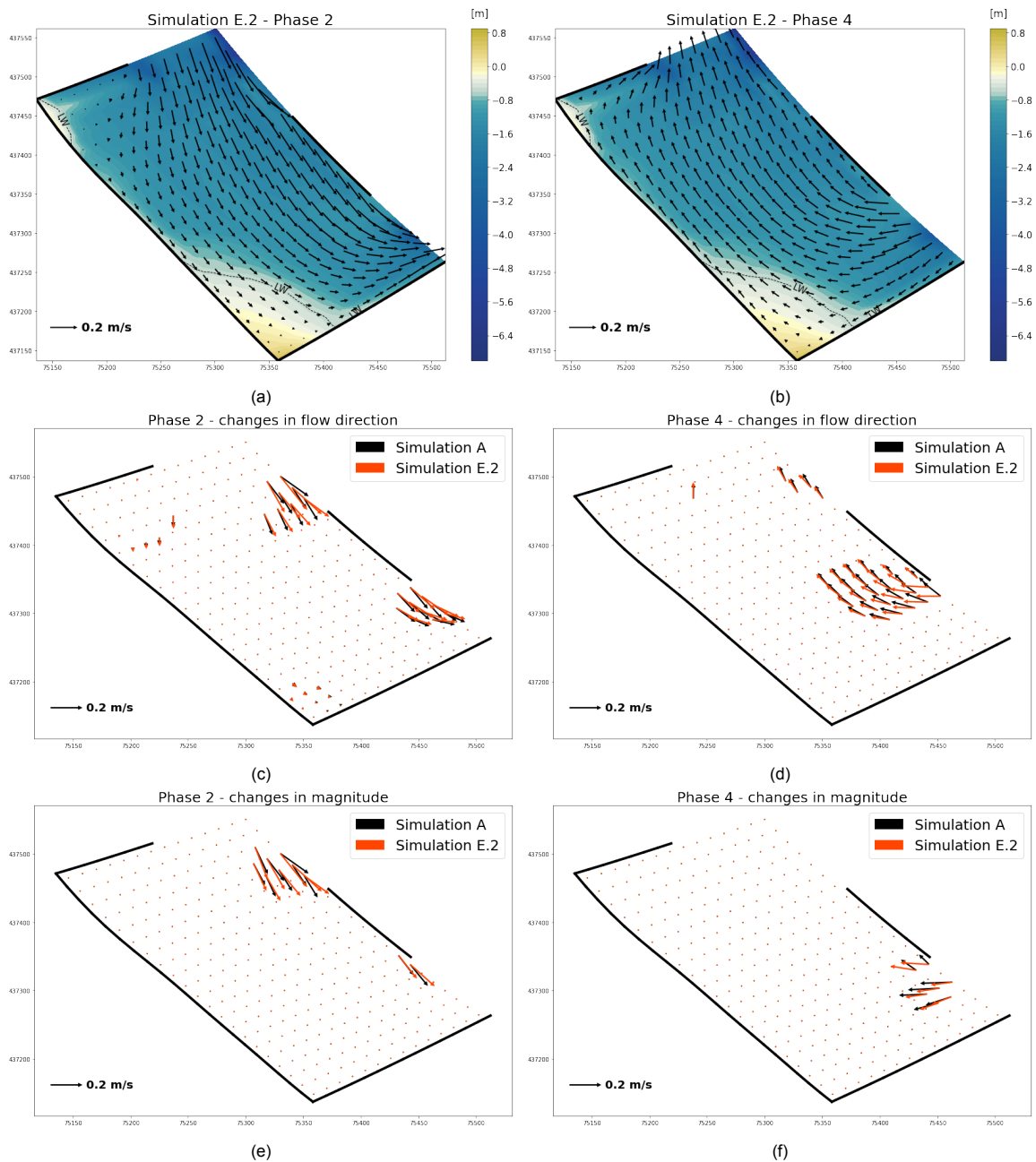


Figure D.11: Flow patterns observed during both flood and ebb in figures D.11a and D.11b respectively resulting from simulation E.2. In Figure D.11c and D.11d the changes in flow direction obtained from both ebb and flood are displayed. The changes in flow direction are only displayed if the change of angle is larger than 6 degrees. In Figure D.11e and D.11f the changes in the magnitudes of the flow are displayed for both flood and ebb respectively. The changes in magnitude are only displayed if larger than 0.01 m/s, which is relatively small threshold. The time frames in which the flow patterns are observed are the same as in the base-case, see section 7.1.

D.3.3. Simulation E.3

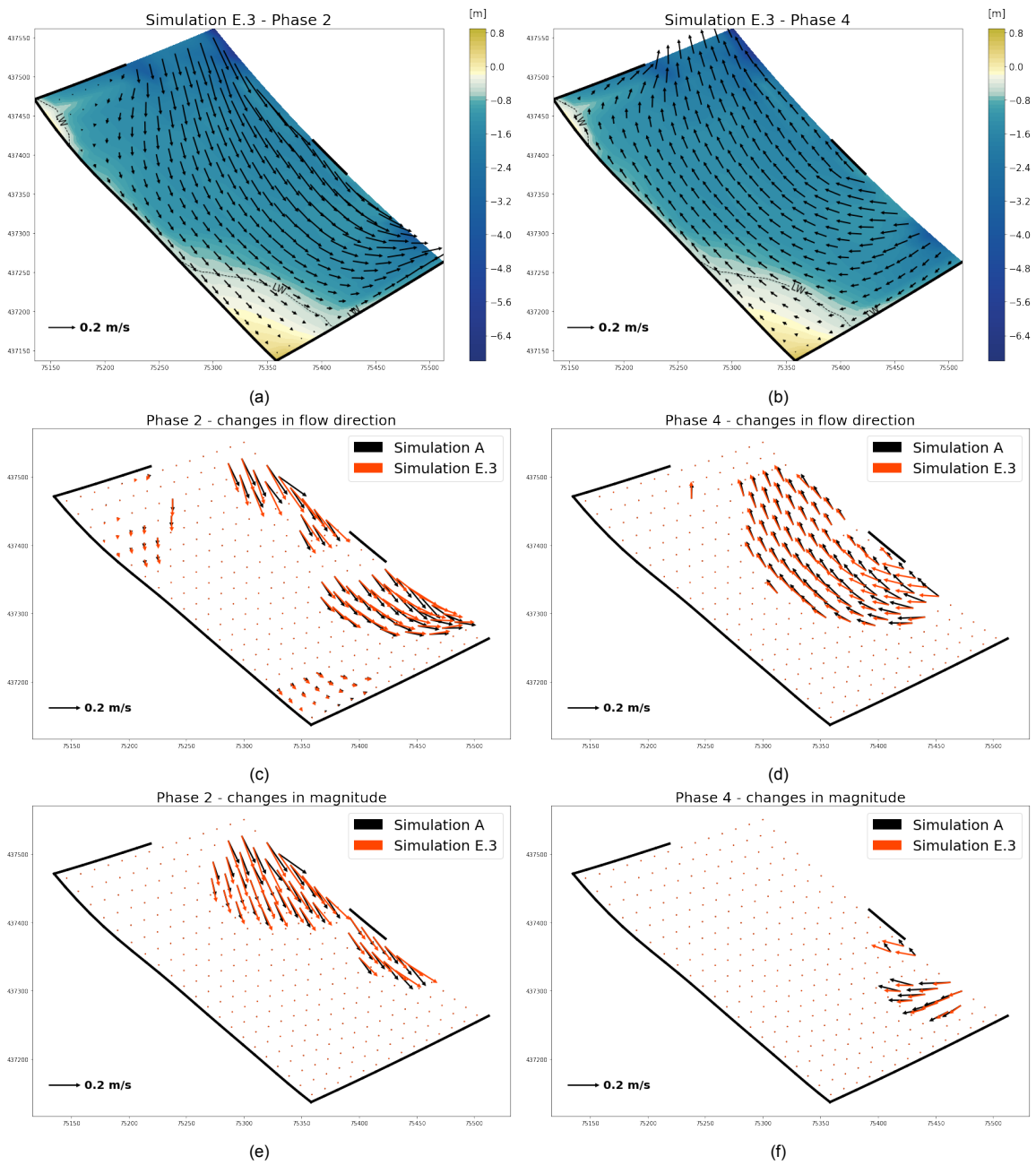


Figure D.12: Flow patterns observed during both flood and ebb in figures D.12a and D.12b respectively resulting from simulation E.3. In Figure D.12c and D.12d the changes in flow direction obtained from both ebb and flood are displayed. The changes in flow direction are only displayed if the change of angle is larger than 6 degrees. In Figure D.12e and D.12f the changes in the magnitudes of the flow are displayed for both flood and ebb respectively. The changes in magnitude are only displayed if larger than 0.01 m/s, which is relatively small threshold. The time frames in which the flow patterns are observed are the same as in the base-case, see section 7.1.

D.3.4. Simulation E.4

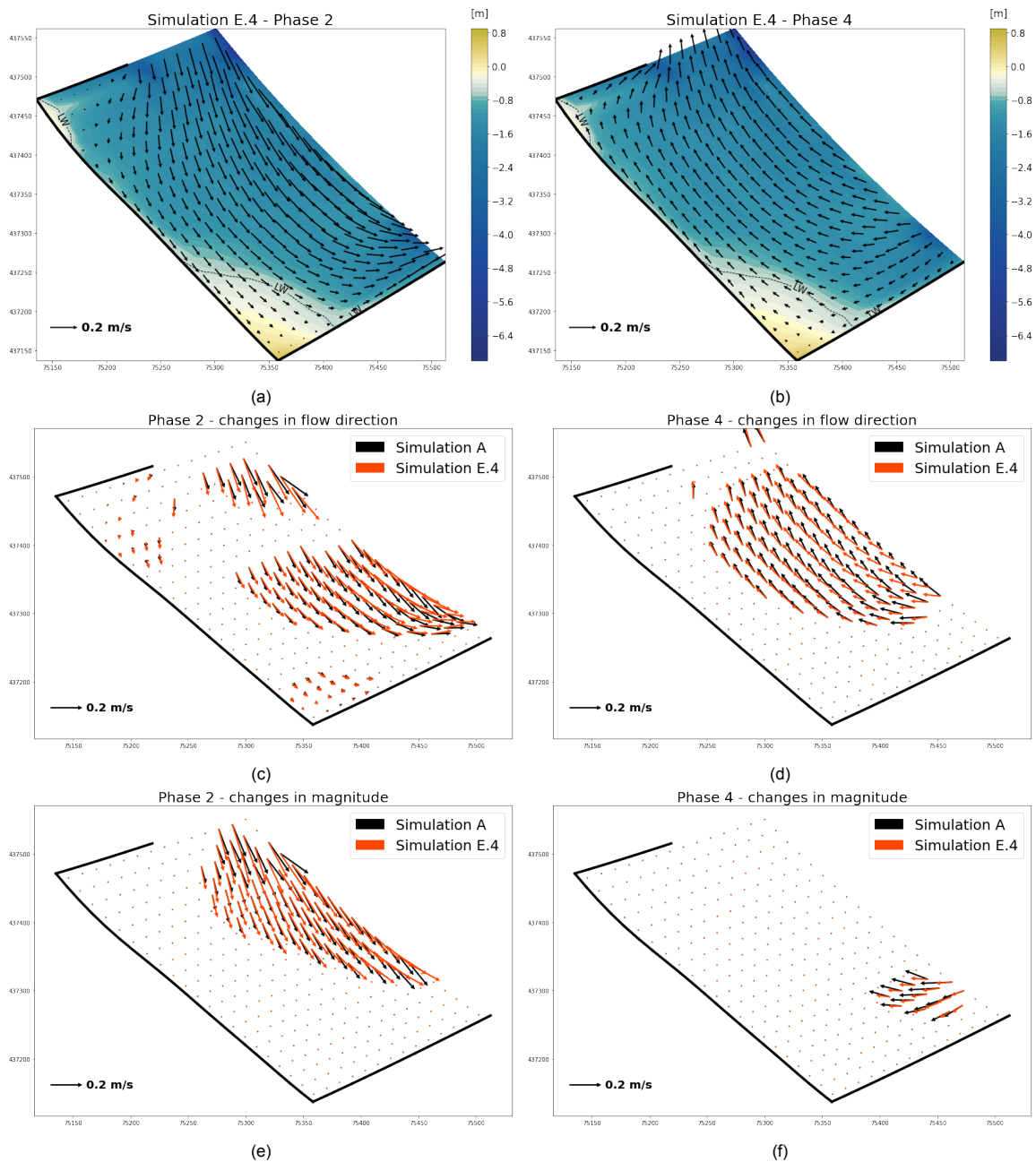


Figure D.13: Flow patterns observed during both flood and ebb in figures D.13a and D.13b respectively resulting from simulation E.4. In Figure D.13c and D.13d the changes in flow direction obtained from both ebb and flood are displayed. The changes in flow direction are only displayed if the change of angle is larger than 6 degrees. In Figure D.13e and D.13f the changes in the magnitudes of the flow are displayed for both flood and ebb respectively. The changes in magnitude are only displayed if larger than 0.01 m/s, which is relatively small threshold. The time frames in which the flow patterns are observed are the same as in the base-case, see section 7.1.

D.4. Adaptation groynes

D.4.1. Simulation F.1

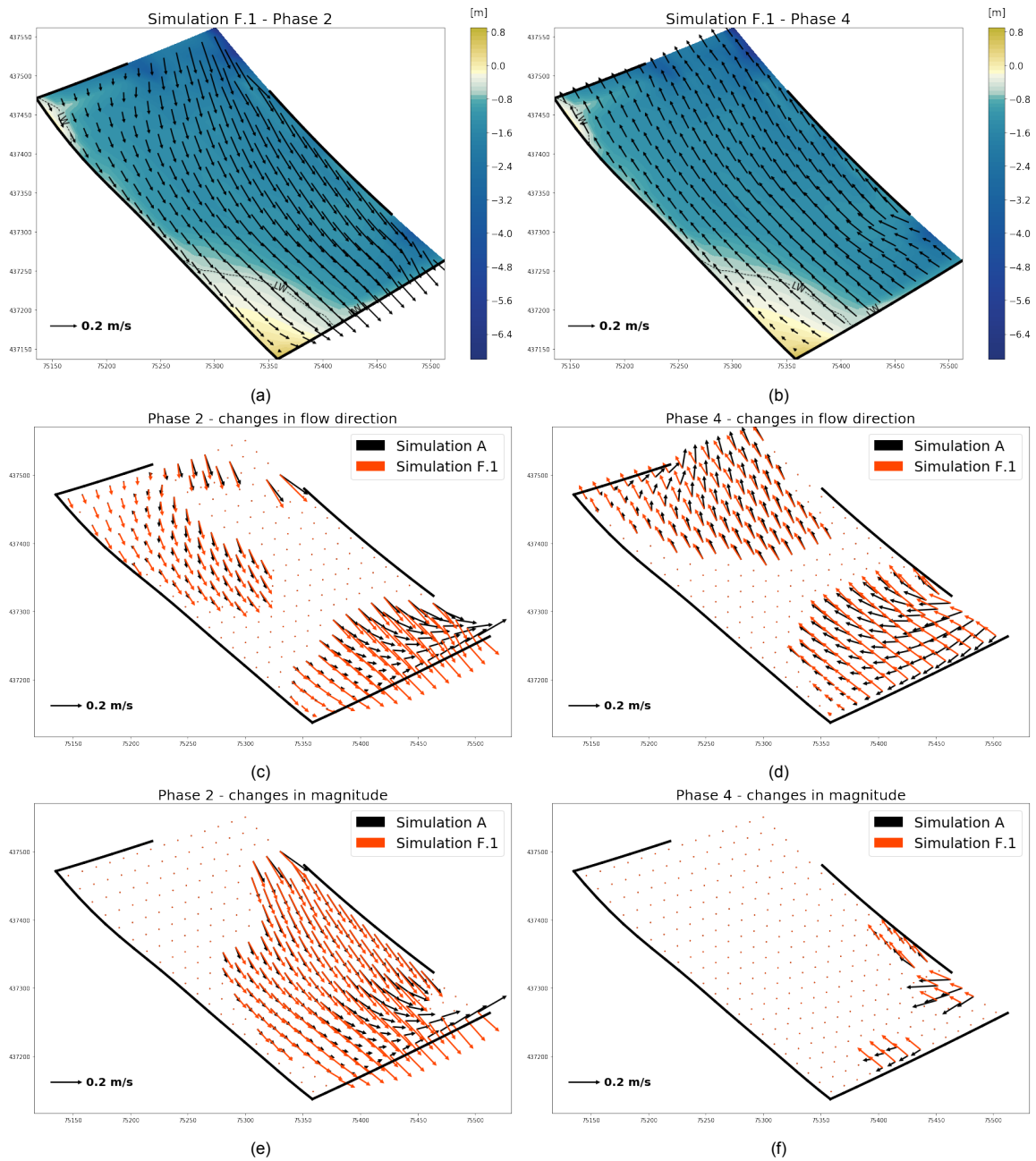


Figure D.14: Flow patterns observed during both flood and ebb in figures D.14a and D.14b respectively resulting from simulation F.1. In Figure D.14c and D.14d the changes in flow direction obtained from both ebb and flood are displayed. The changes in flow direction are only displayed if the change of angle is larger than 6 degrees. In Figure D.14e and D.14f the changes in the magnitudes of the flow are displayed for both flood and ebb respectively. The changes in magnitude are only displayed if larger than 0.01 m/s, which is relatively small threshold. The time frames in which the flow patterns are observed are the same as in the base-case, see section 7.1.

D.4.2. Simulation F.2

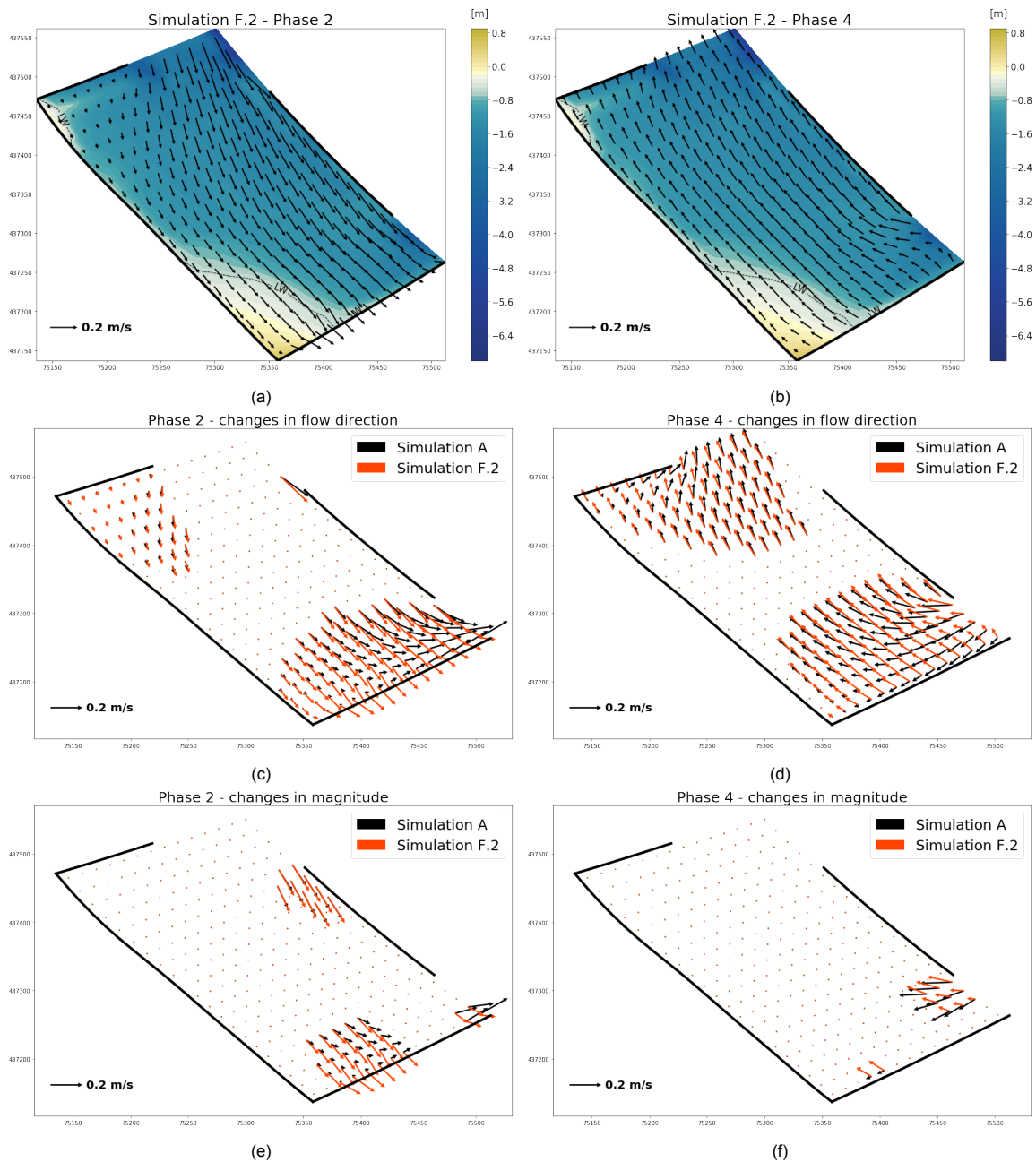


Figure D.15: Flow patterns observed during both flood and ebb in figures D.15a and D.15b respectively resulting from simulation F.2. In Figure D.15c and D.15d the changes in flow direction obtained from both ebb and flood are displayed. The changes in flow direction are only displayed if the change of angle is larger than 6 degrees. In Figure D.15e and D.15f the changes in the magnitudes of the flow are displayed for both flood and ebb respectively. The changes in magnitude are only displayed if larger than 0.01 m/s, which is relatively small threshold. The time frames in which the flow patterns are observed are the same as in the base-case, see section 7.1.

D.4.3. Simulation F.3

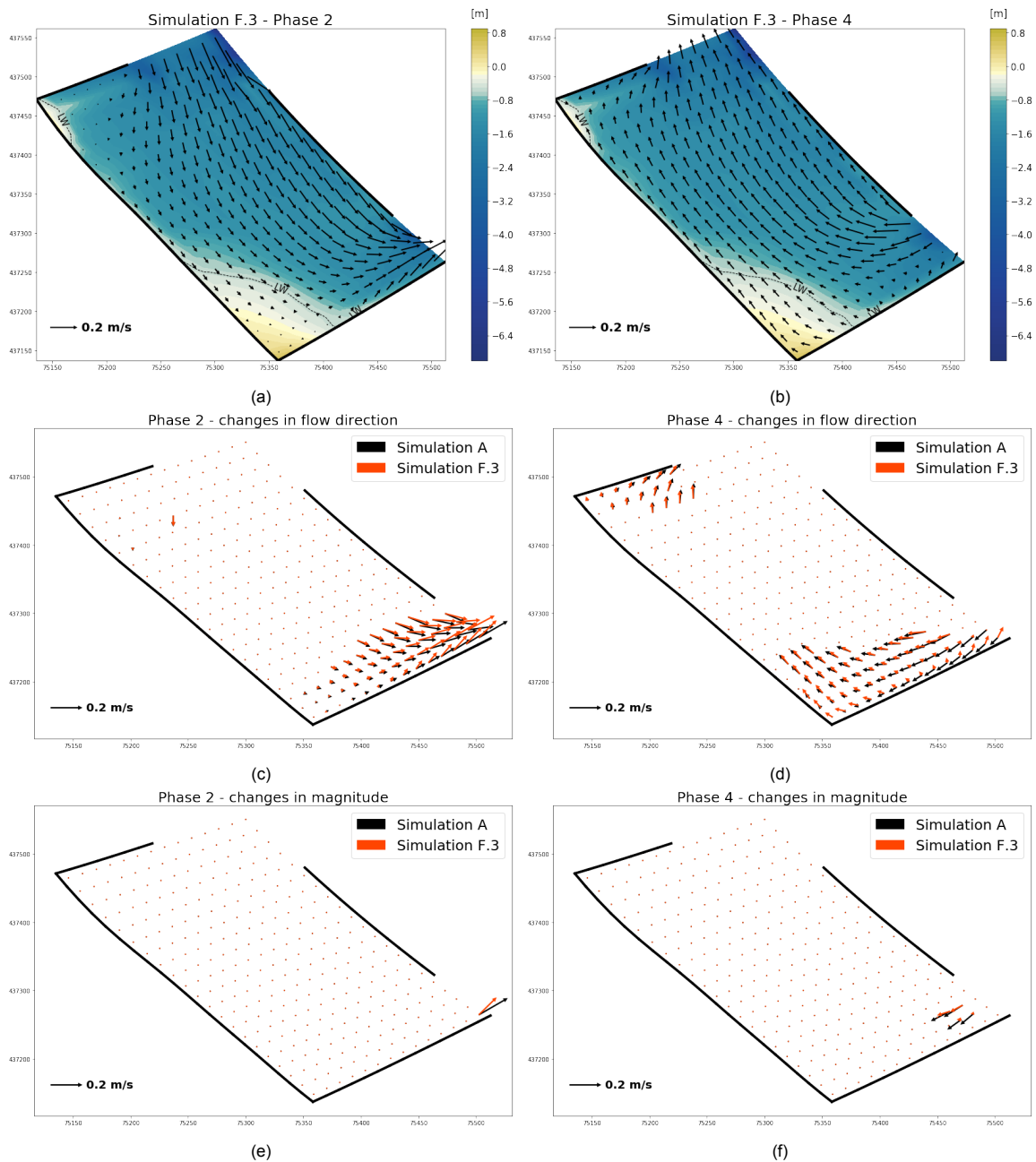


Figure D.16: Flow patterns observed during both flood and ebb in figures D.16a and D.16b respectively resulting from simulation F.3. In Figure D.16c and D.16d the changes in flow direction obtained from both ebb and flood are displayed. The changes in flow direction are only displayed if the change of angle is larger than 6 degrees. In Figure D.16e and D.16f the changes in the magnitudes of the flow are displayed for both flood and ebb respectively. The changes in magnitude are only displayed if larger than 0.01 m/s, which is a relatively small threshold. The time frames in which the flow patterns are observed are the same as in the base-case, see section 7.1.

D.4.4. Simulation F.4

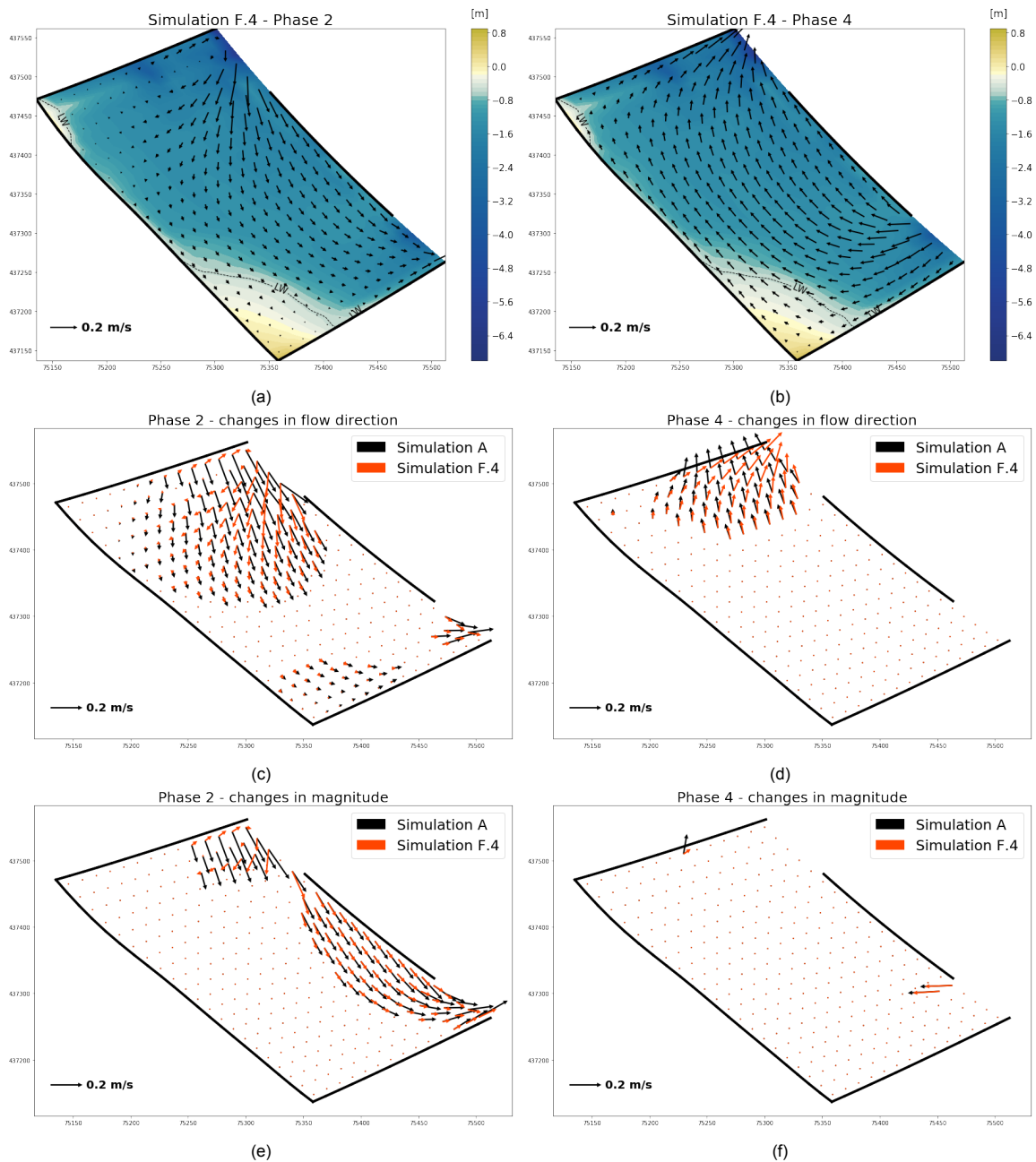


Figure D.17: Flow patterns observed during both flood and ebb in figures D.17a and D.17b respectively resulting from simulation F.4. In Figure D.17c and D.17d the changes in flow direction obtained from both ebb and flood are displayed. The changes in flow direction are only displayed if the change of angle is larger than 6 degrees. In Figure D.17e and D.17f the changes in the magnitudes of the flow are displayed for both flood and ebb respectively. The changes in magnitude are only displayed if larger than 0.01 m/s, which is relatively small threshold. The time frames in which the flow patterns are observed are the same as in the base-case, see section 7.1.

D.4.5. Simulation F.5

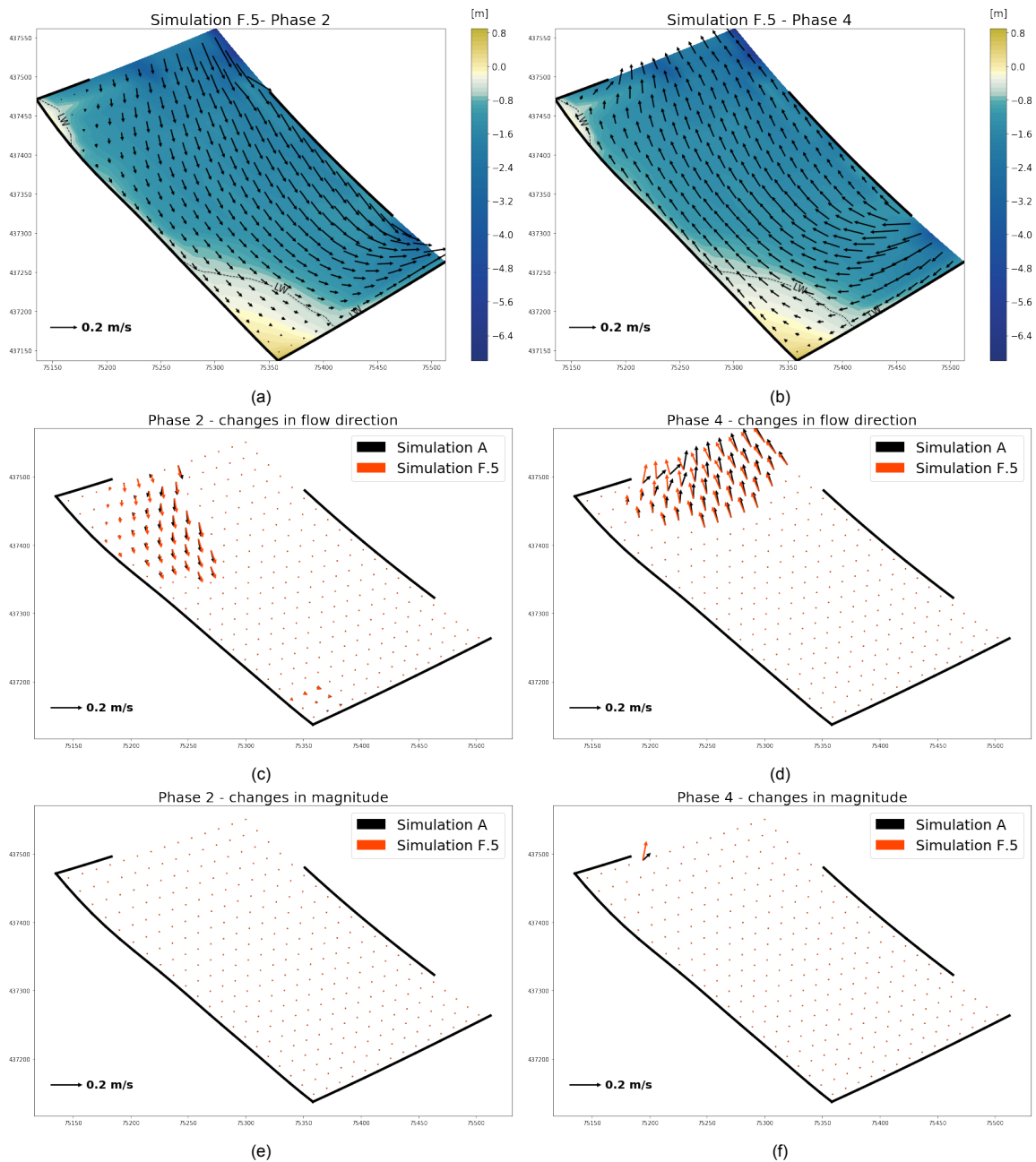


Figure D.18: Flow patterns observed during both flood and ebb in figures D.18a and D.18b respectively resulting from simulation F.5. In Figure D.18c and D.18d the changes in flow direction obtained from both ebb and flood are displayed. The changes in flow direction are only displayed if the change of angle is larger than 6 degrees. In Figure D.18e and D.18f the changes in the magnitudes of the flow are displayed for both flood and ebb respectively. The changes in magnitude are only displayed if larger than 0.01 m/s, which is relatively small threshold. The time frames in which the flow patterns are observed are the same as in the base-case, see section 7.1.

D.4.6. Simulation F.6

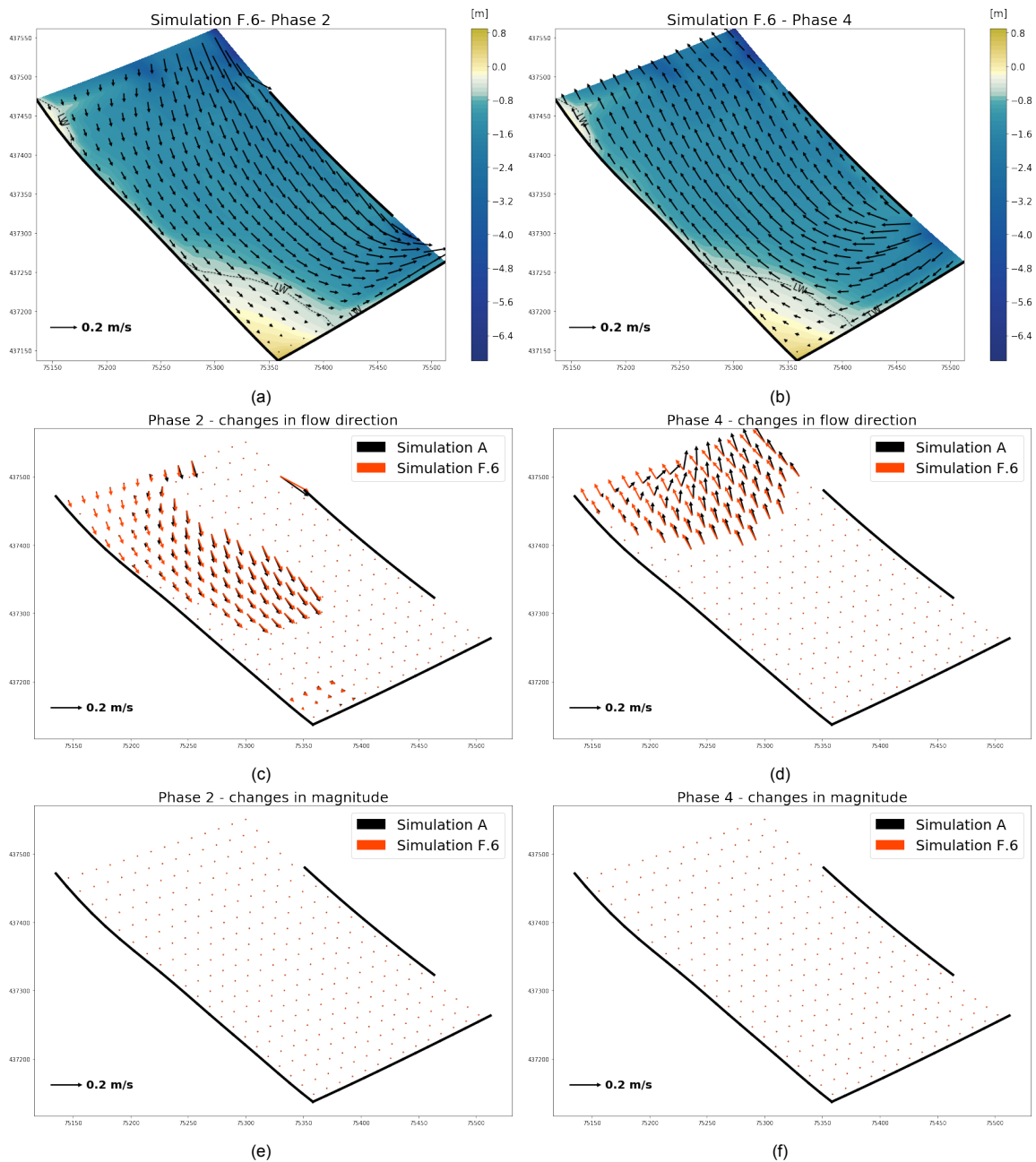


Figure D.19: Flow patterns observed during both flood and ebb in figures D.19a and D.19b respectively resulting from simulation F.6. In Figure D.19c and D.19d the changes in flow direction obtained from both ebb and flood are displayed. The changes in flow direction are only displayed if the change of angle is larger than 6 degrees. In Figure D.19e and D.19f the changes in the magnitudes of the flow are displayed for both flood and ebb respectively. The changes in magnitude are only displayed if larger than 0.01 m/s, which is relatively small threshold. The time frames in which the flow patterns are observed are the same as in the base-case, see section 7.1.

D.4.7. Simulation F.7

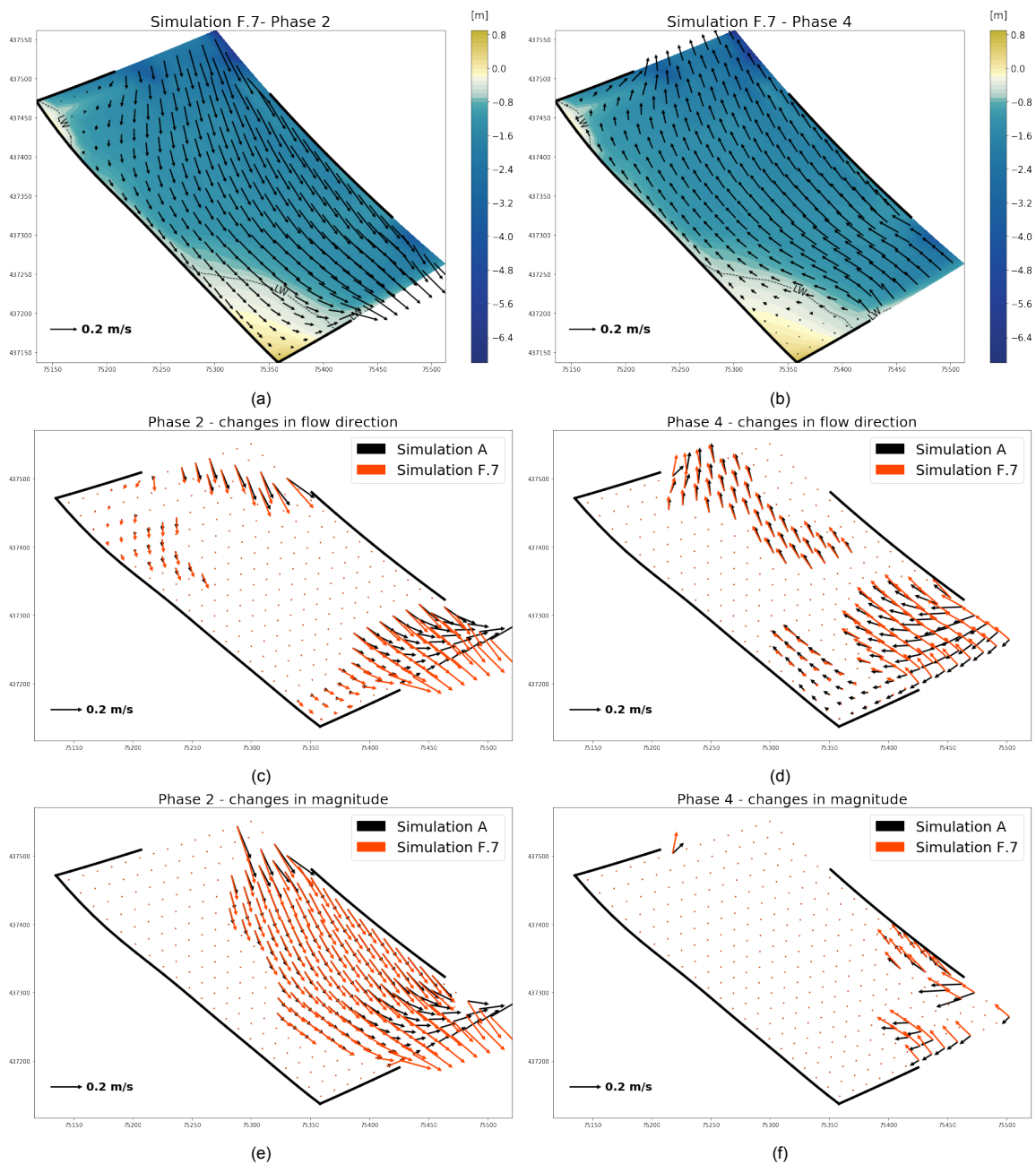


Figure D.20: Flow patterns observed during both flood and ebb in figures D.20a and D.20b respectively resulting from simulation F.7. In Figure D.20c and D.20d the changes in flow direction obtained from both ebb and flood are displayed. The changes in flow direction are only displayed if the change of angle is larger than 6 degrees. In Figure D.20e and D.20f the changes in the magnitudes of the flow are displayed for both flood and ebb respectively. The changes in magnitude are only displayed if larger than 0.01 m/s, which is relatively small threshold. The time frames in which the flow patterns are observed are the same as in the base-case, see section 7.1.

D.5. Adaptation inlet

D.5.1. Simulation G.1

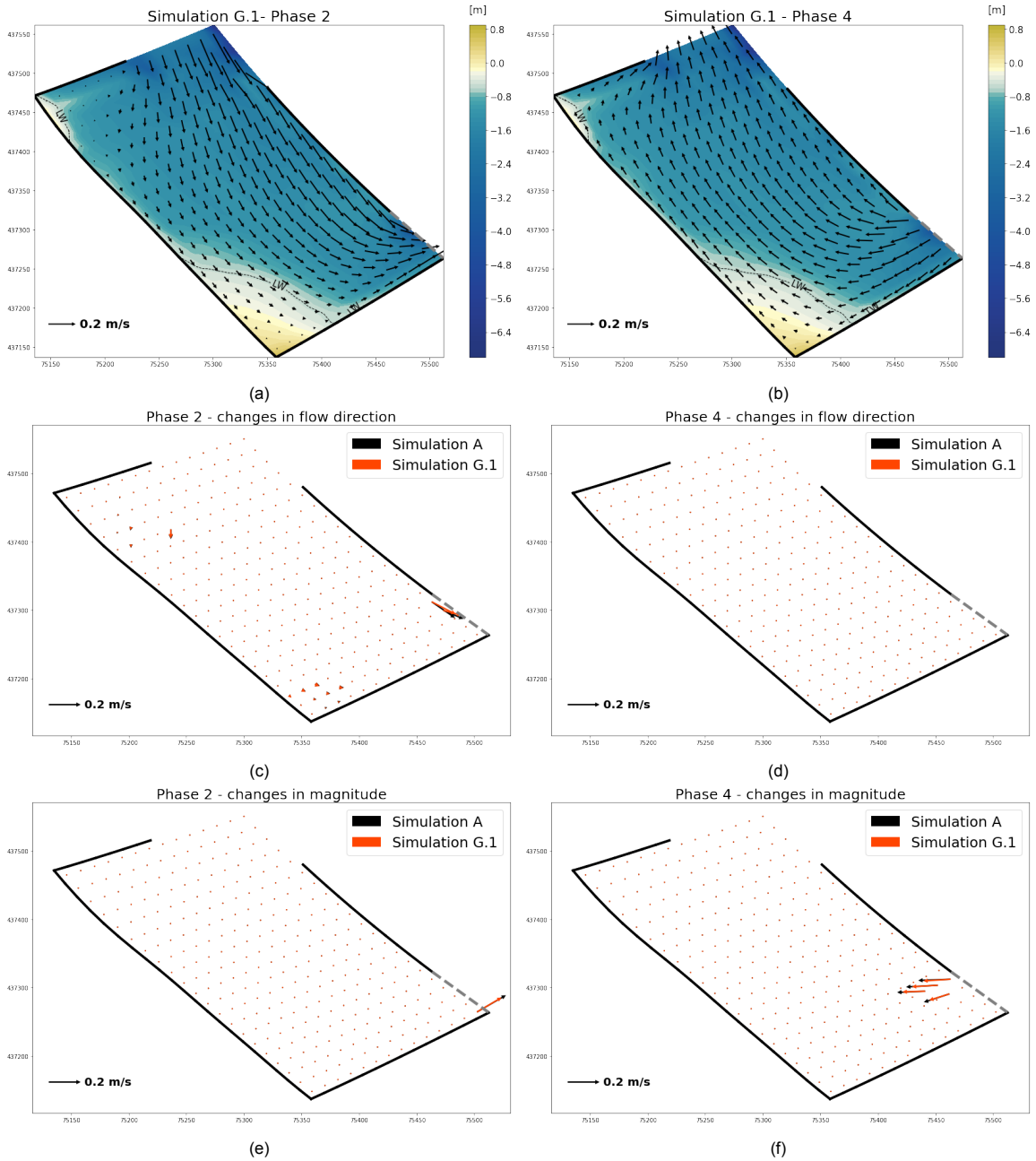


Figure D.21: Flow patterns observed during both flood and ebb in figures D.21a and D.21b respectively resulting from simulation G.1. In Figure D.21c and D.21d the changes in flow direction obtained from both ebb and flood are displayed. The changes in flow direction are only displayed if the change of angle is larger than 6 degrees. In Figure D.21e and D.21f the changes in the magnitudes of the flow are displayed for both flood and ebb respectively. The changes in magnitude are only displayed if larger than 0.01 m/s, which is relatively small threshold. The time frames in which the flow patterns are observed are the same as in the base-case, see section 7.1.

D.5.2. Simulation G.2

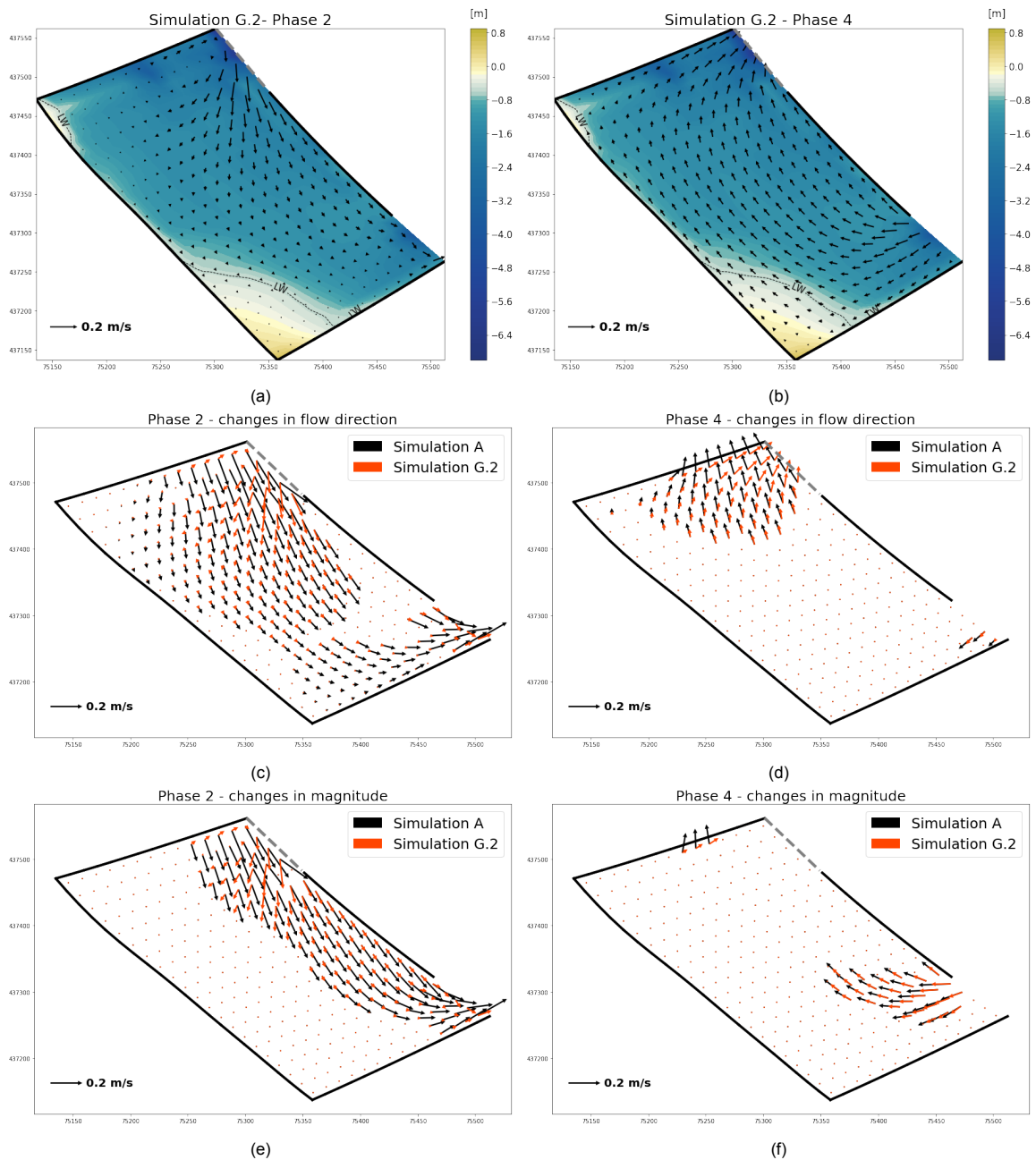


Figure D.22: Flow patterns observed during both flood and ebb in figures D.22a and D.22b respectively resulting from simulation G.2. In Figure D.22c and D.22d the changes in flow direction obtained from both ebb and flood are displayed. The changes in flow direction are only displayed if the change of angle is larger than 6 degrees. In Figure D.22e and D.22f the changes in the magnitudes of the flow are displayed for both flood and ebb respectively. The changes in magnitude are only displayed if larger than 0.01 m/s, which is relatively small threshold. The time frames in which the flow patterns are observed are the same as in the base-case, see section 7.1.

D.5.3. Simulation G.3

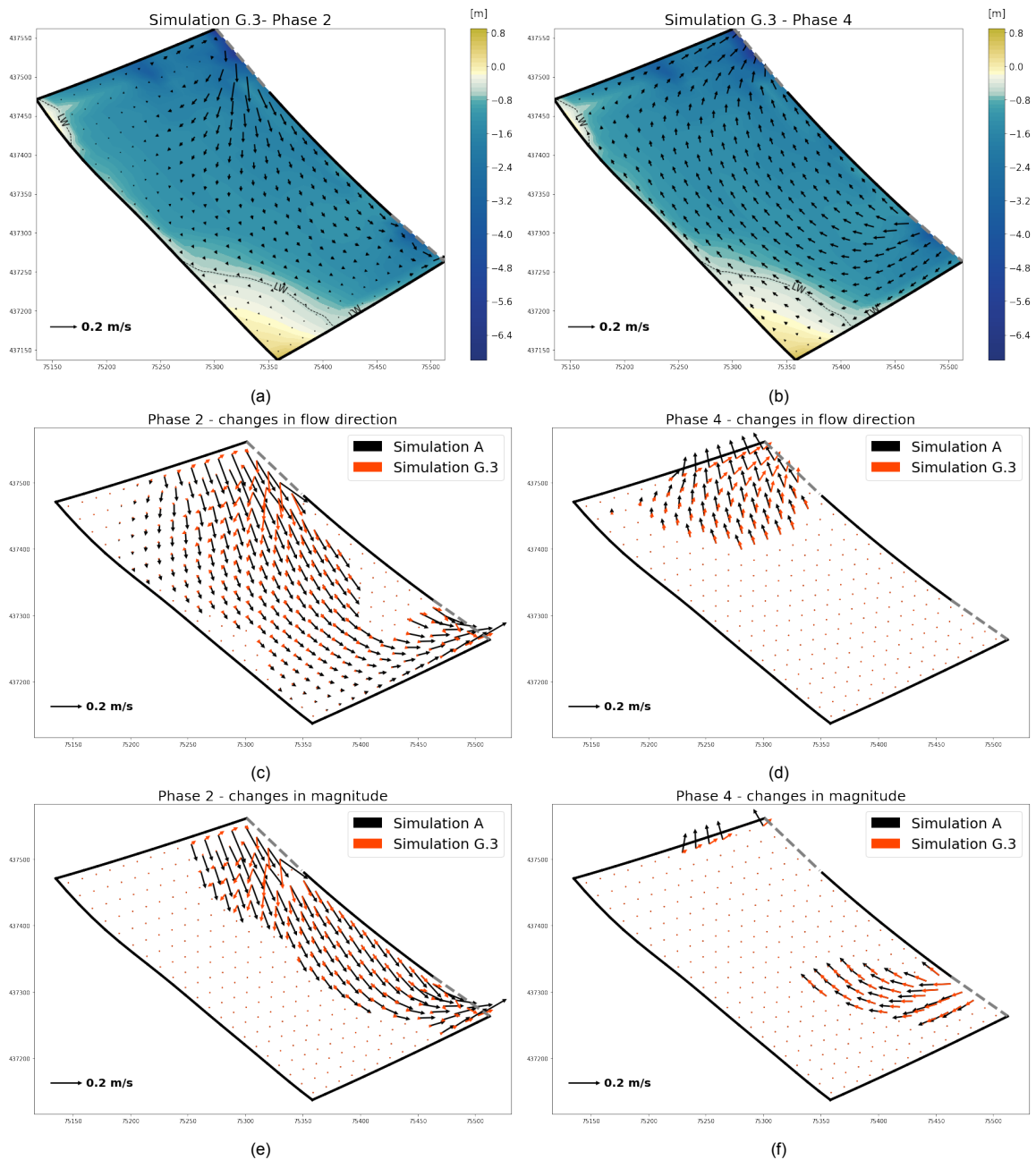


Figure D.23: Flow patterns observed during both flood and ebb in figures D.23a and D.23b respectively resulting from simulation G.3. In Figure D.23c and D.23d the changes in flow direction obtained from both ebb and flood are displayed. The changes in flow direction are only displayed if the change of angle is larger than 6 degrees. In Figure D.23e and D.23f the changes in the magnitudes of the flow are displayed for both flood and ebb respectively. The changes in magnitude are only displayed if larger than 0.01 m/s, which is relatively small threshold. The time frames in which the flow patterns are observed are the same as in the base-case, see section 7.1.

D.5.4. Simulation G.4

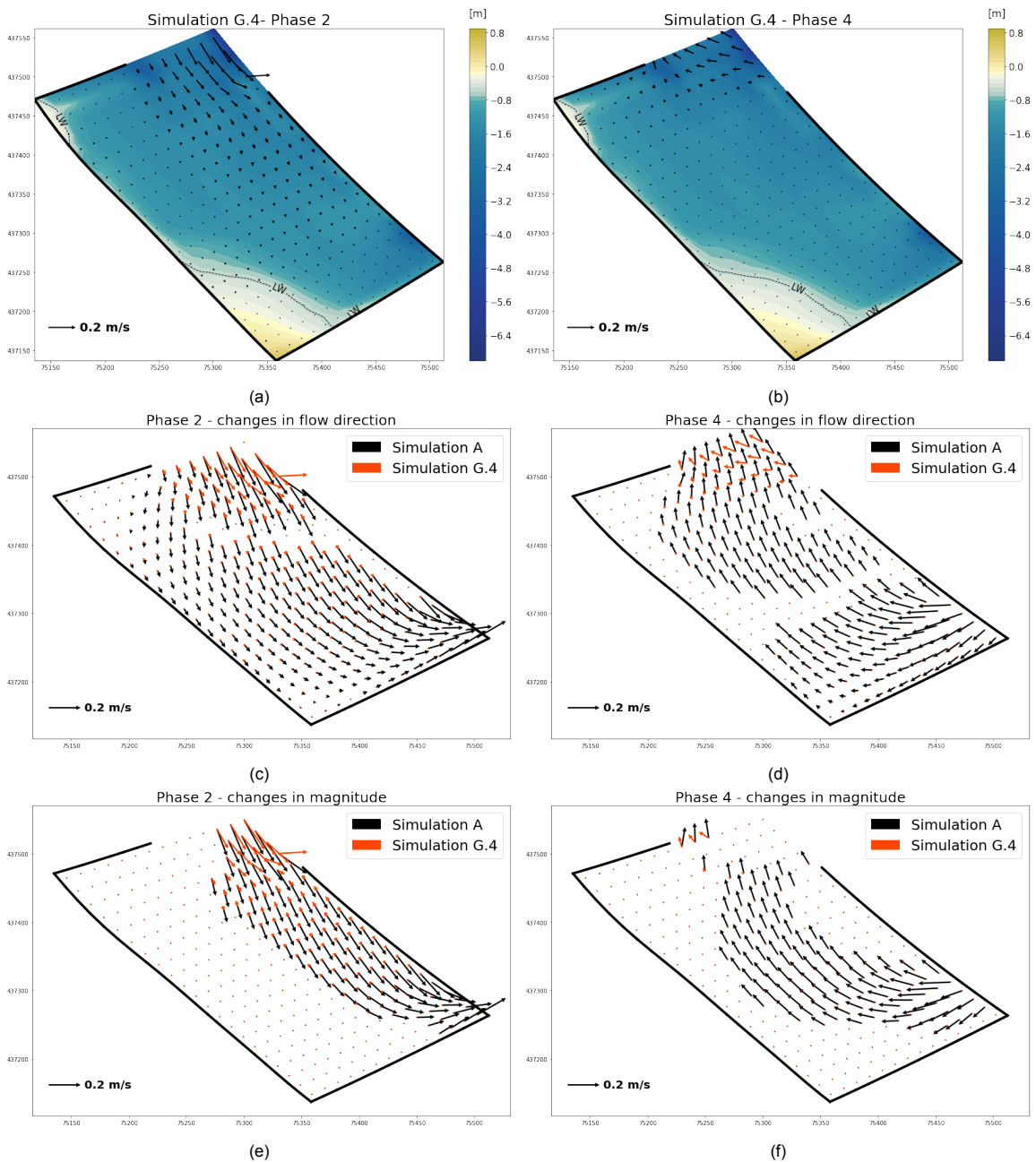


Figure D.24: Flow patterns observed during both flood and ebb in figures D.24a and D.24b respectively resulting from simulation G.4. In Figure D.24c and D.24d the changes in flow direction obtained from both ebb and flood are displayed. The changes in flow direction are only displayed if the change of angle is larger than 6 degrees. In Figure D.24e and D.24f the changes in the magnitudes of the flow are displayed for both flood and ebb respectively. The changes in magnitude are only displayed if larger than 0.01 m/s, which is relatively small threshold. The time frames in which the flow patterns are observed are the same as in the base-case, see section 7.1.

D.5.5. Simulation G.5

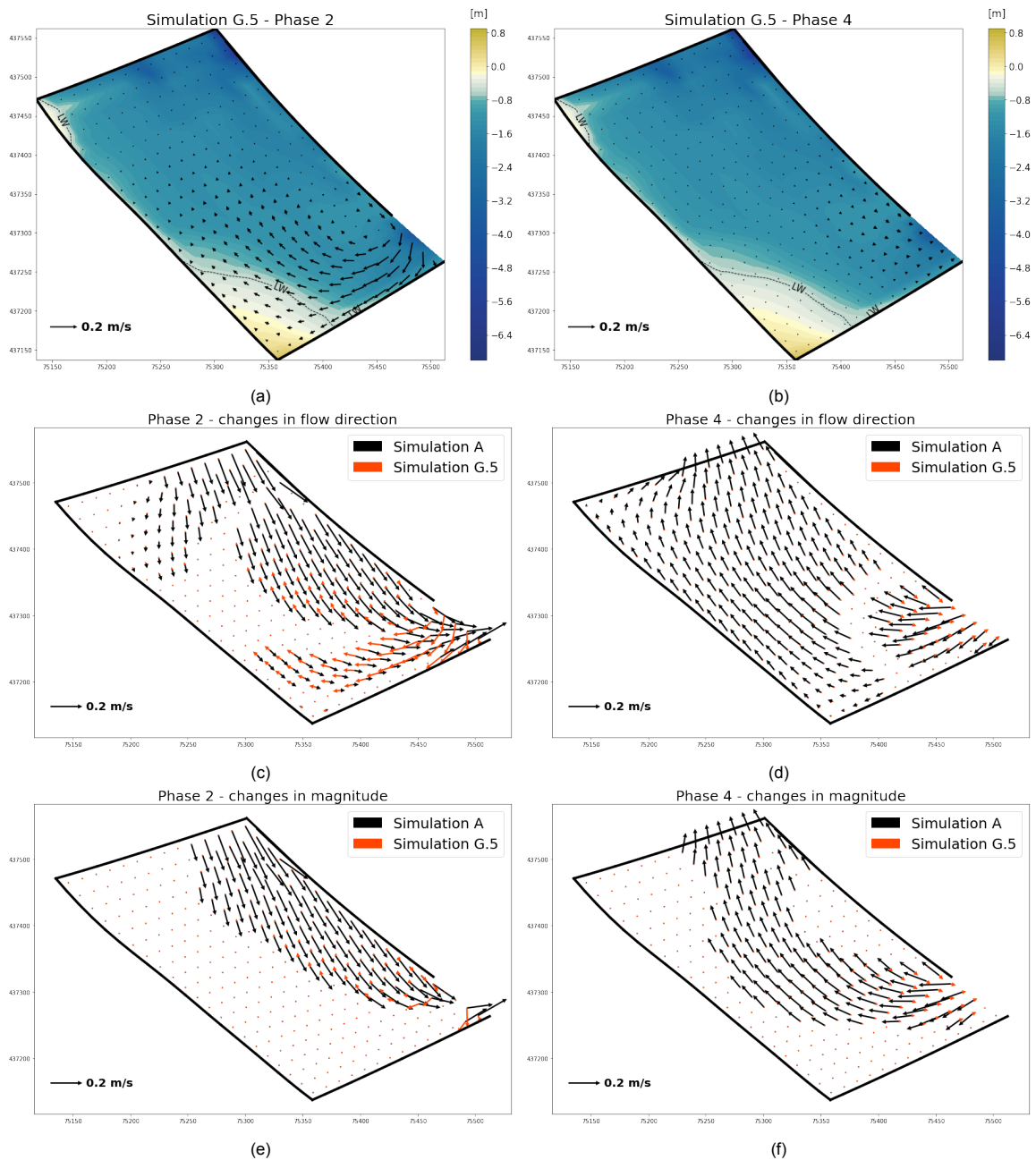


Figure D.25: Flow patterns observed during both flood and ebb in figures D.25a and D.25b respectively resulting from simulation G.5. In Figure D.25c and D.25d the changes in flow direction obtained from both ebb and flood are displayed. The changes in flow direction are only displayed if the change of angle is larger than 6 degrees. In Figure D.25e and D.25f the changes in the magnitudes of the flow are displayed for both flood and ebb respectively. The changes in magnitude are only displayed if larger than 0.01 m/s, which is relatively small threshold. The time frames in which the flow patterns are observed are the same as in the base-case, see section 7.1.

Morphodynamic results from variations in geometry

E.1. Bathymetry

E.1.1. Non-cohesive sediment

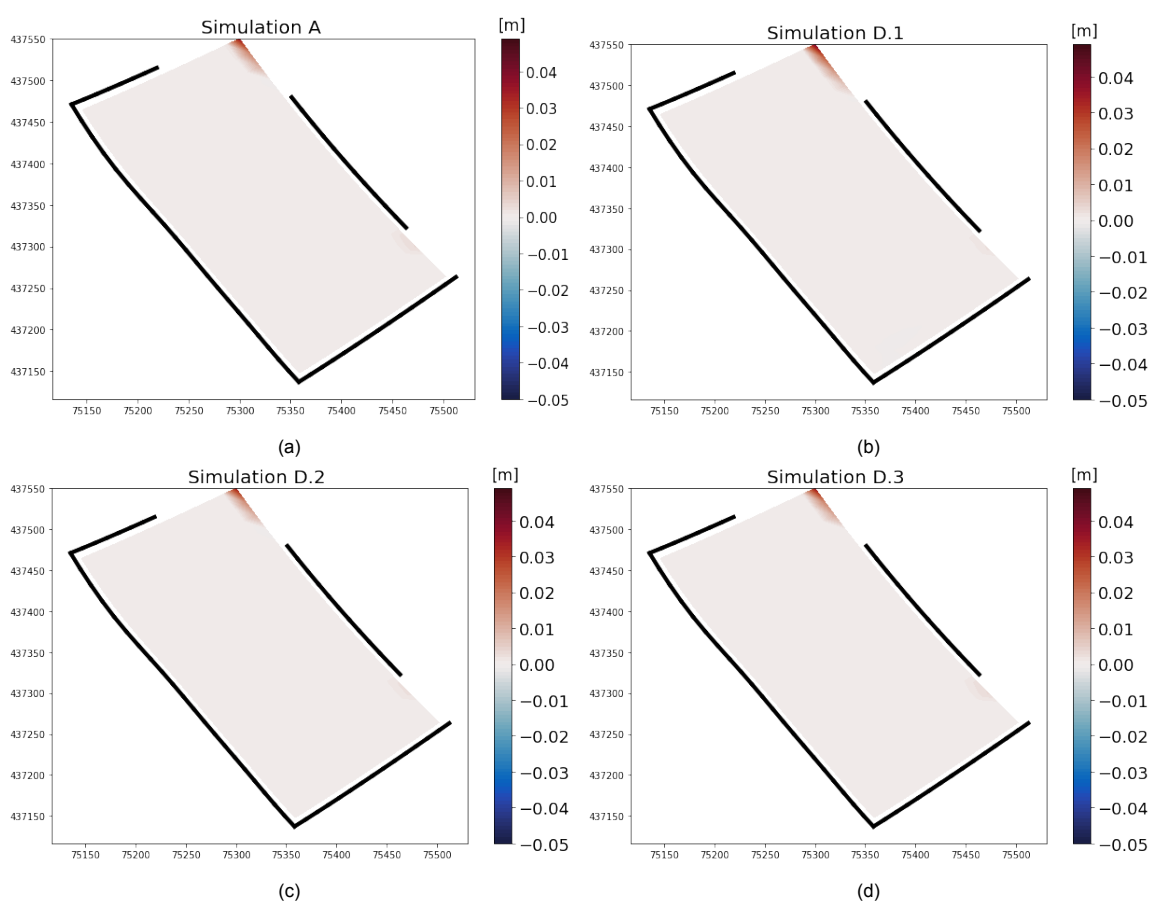


Figure E.1: The cumulative sedimentation / erosion resulting from simulations incorporating a different bathymetry. The bed layer consists of sand with a nominal diameter of $150 \mu\text{m}$.

E.1.2. Cohesive sediment
E.1.2.1. Non-erodible bed layer

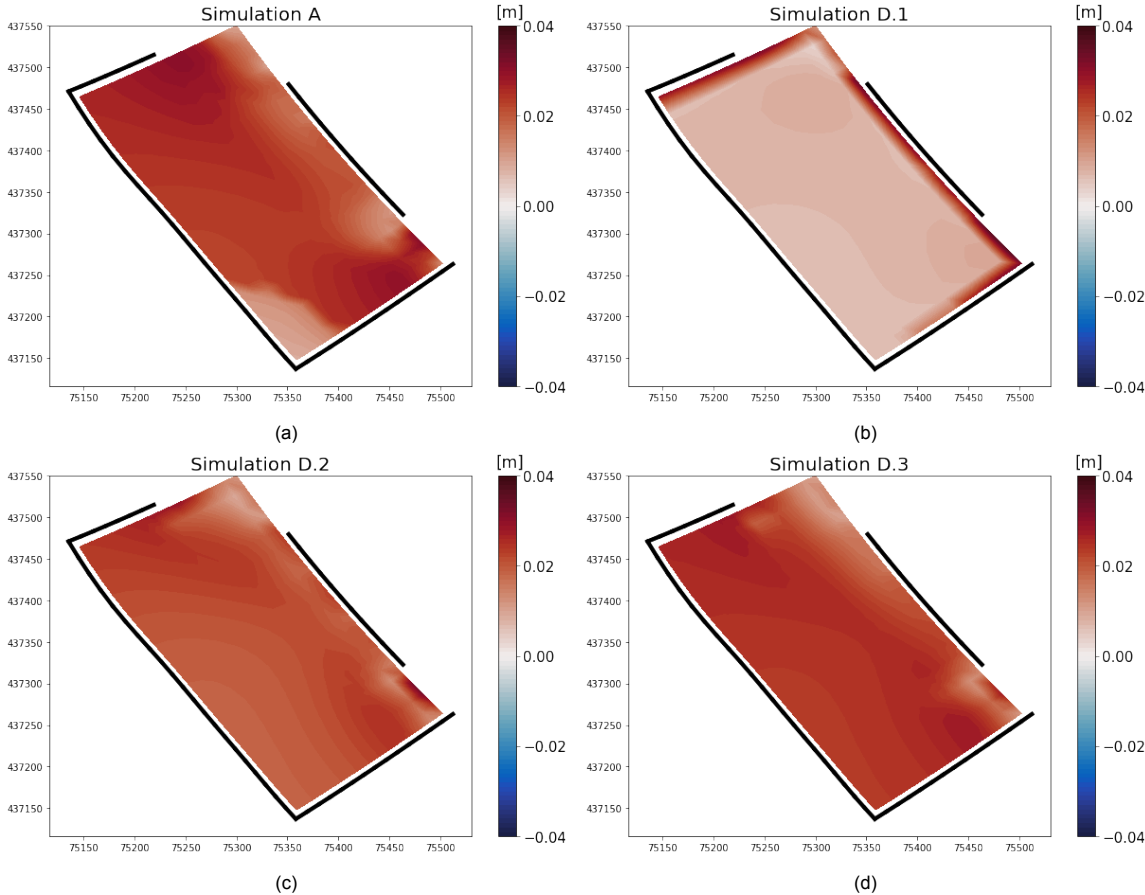


Figure E.2: The sedimentation pattern resulting from simulations incorporating a different bathymetry at the river bank. The bed layer is incorporated in the model as being non-erodible.

E.1.2.2. Erodeable bed layer

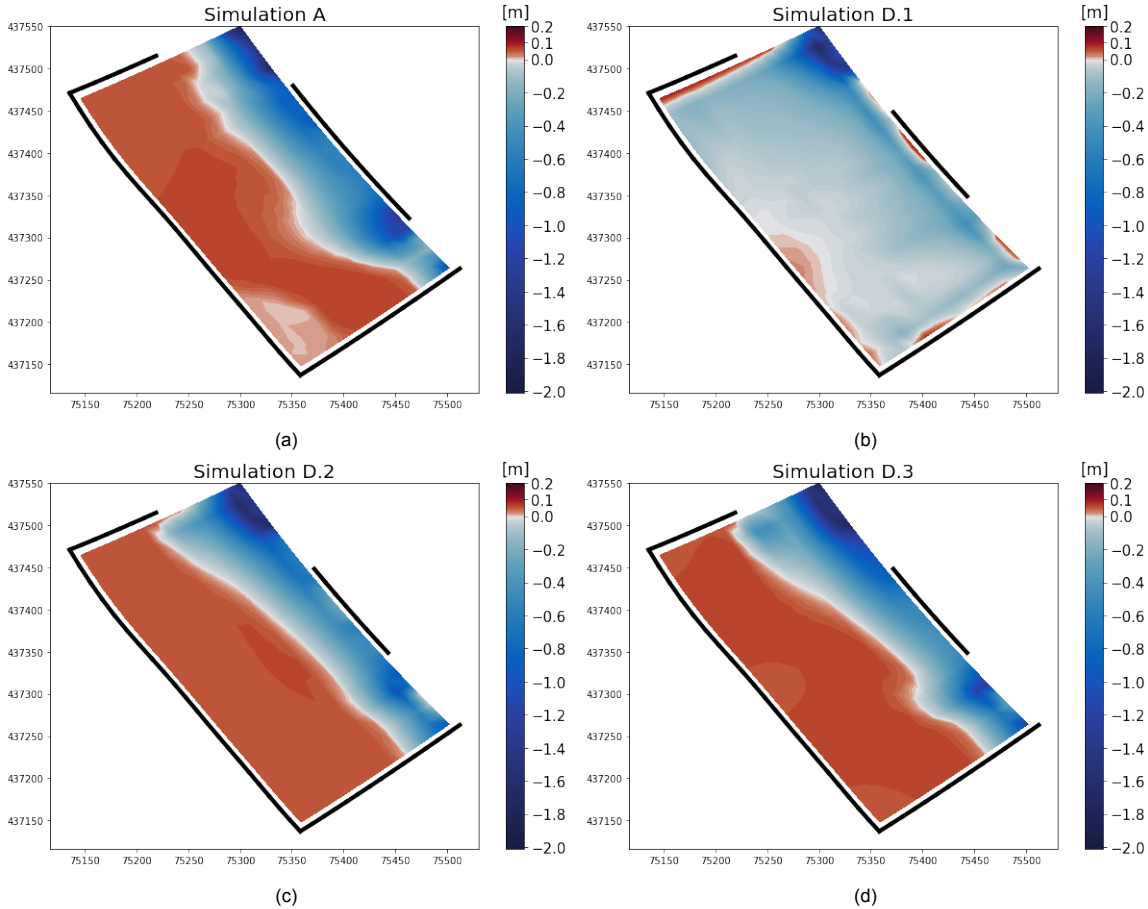


Figure E.3: The sedimentation pattern resulting from simulations incorporating a different bathymetry at the river bank. The bed layer is incorporated in the model as being erodible.

E.2. Longitudinal wall

E.2.1. Non-cohesive sediment

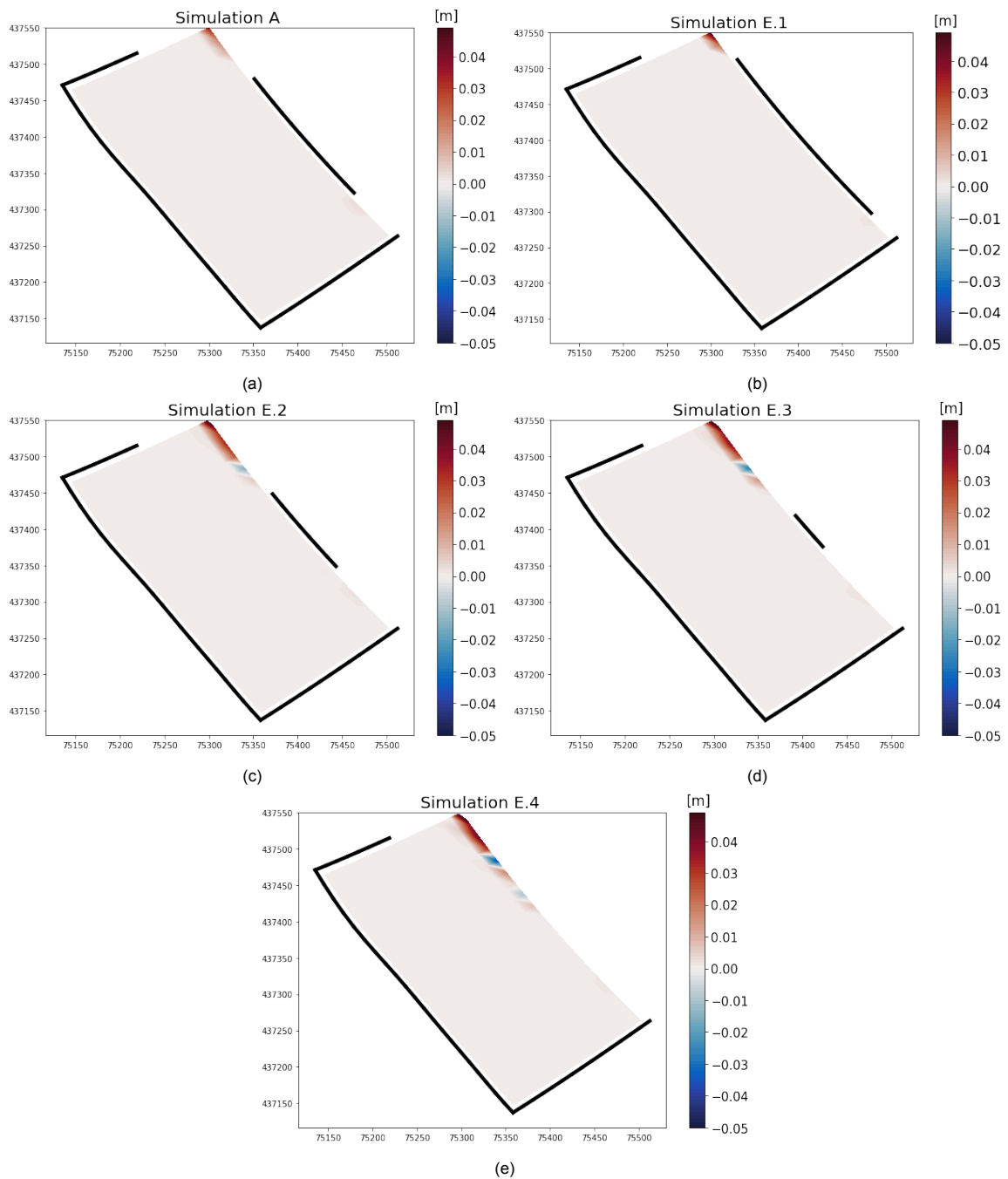


Figure E.4: The cumulative sedimentation / erosion resulting from simulations incorporating a different length in longitudinal wall. The bed layer consists of sand with a nominal diameter of $150 \mu\text{m}$.

E.2.2. Cohesive sediment

E.2.2.1. Non-erodible bed layer

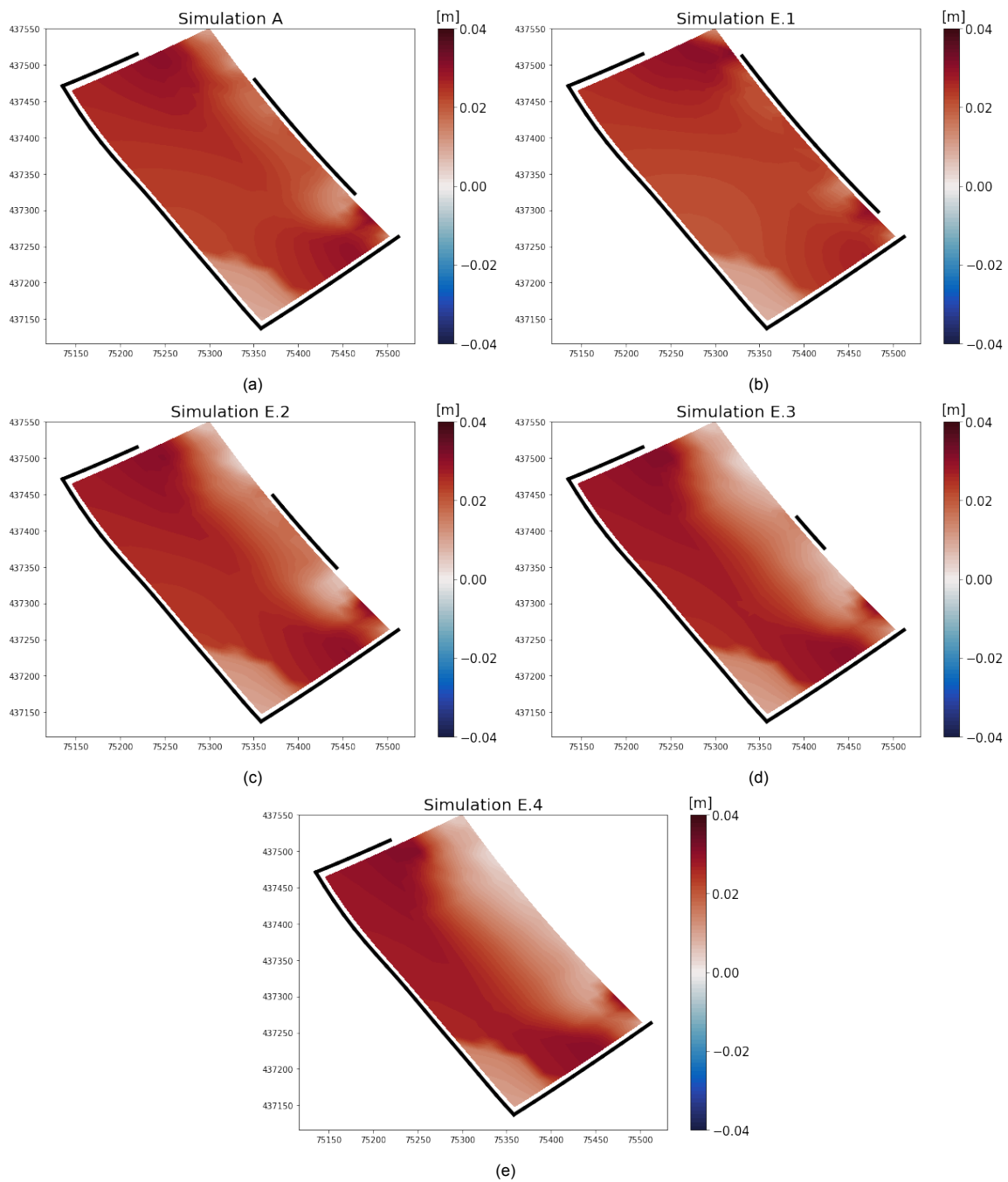


Figure E.5: The sedimentation pattern resulting from simulations incorporating a different bathymetry at the river bank. The bed layer is incorporated in the model as being non-erodible.

E.2.2.2. Erodeable bed layer

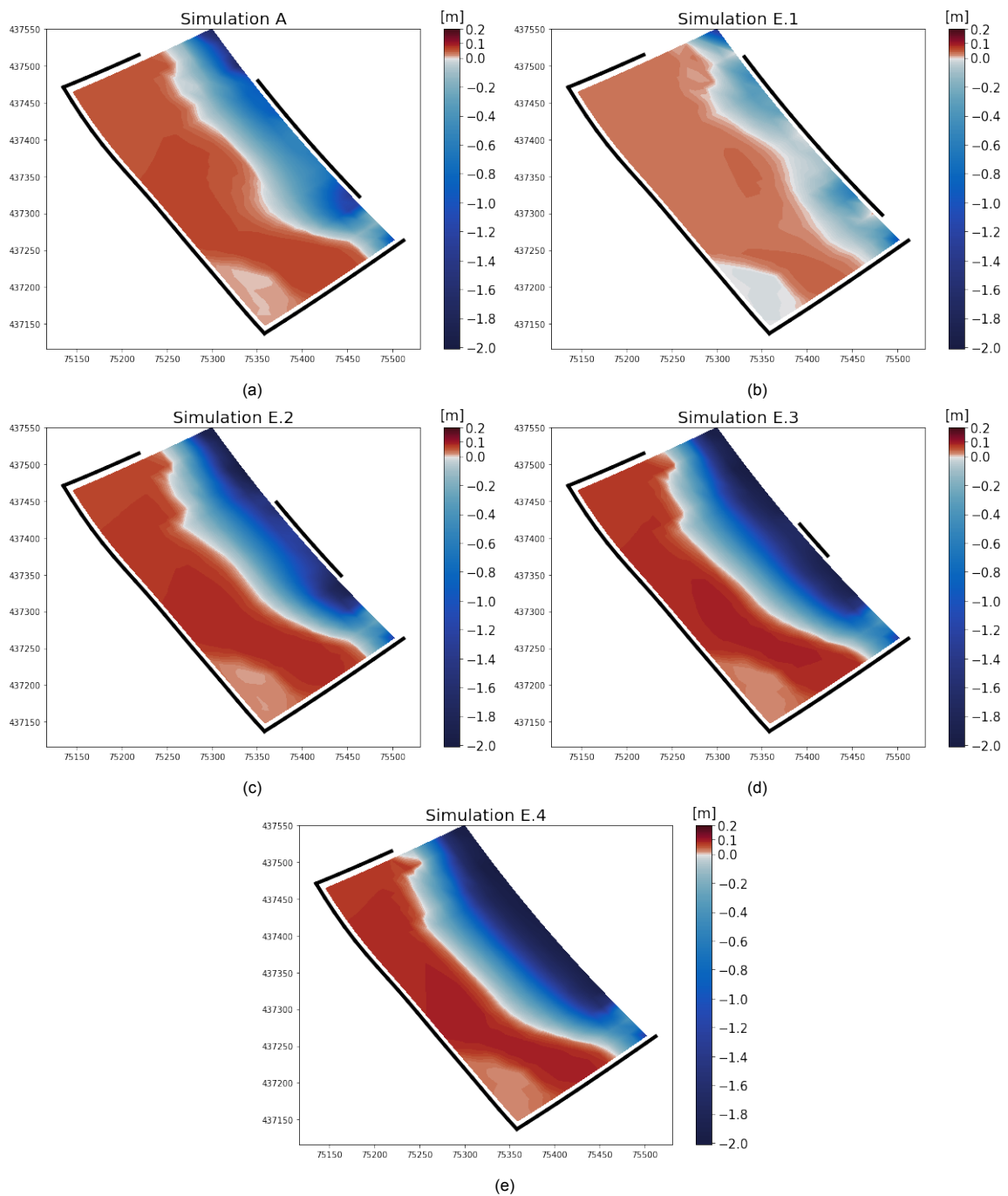


Figure E.6: The sedimentation pattern resulting from simulations incorporating a different length in longitudinal wall in front of the river bank. The bed layer is incorporated in the model as being erodible.

E.3. Groynes - submergence

E.3.1. Non-cohesive sediment

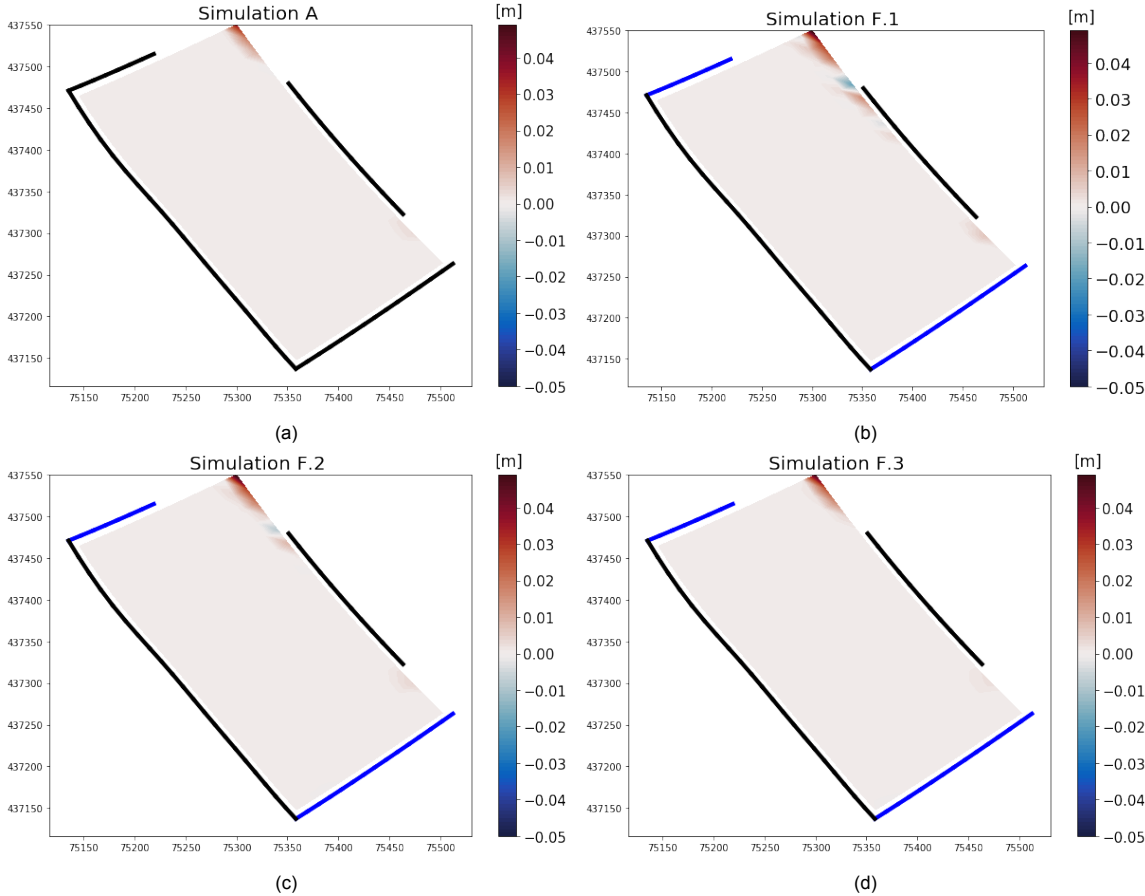


Figure E.7: The cumulative sedimentation / erosion resulting from simulations incorporating different heights of the groynes present at river bank L. The bed layer consists of sand with a nominal diameter of 150 μm .

E.3.2. Cohesive sediment

E.3.2.1. Non-erodible bed layer

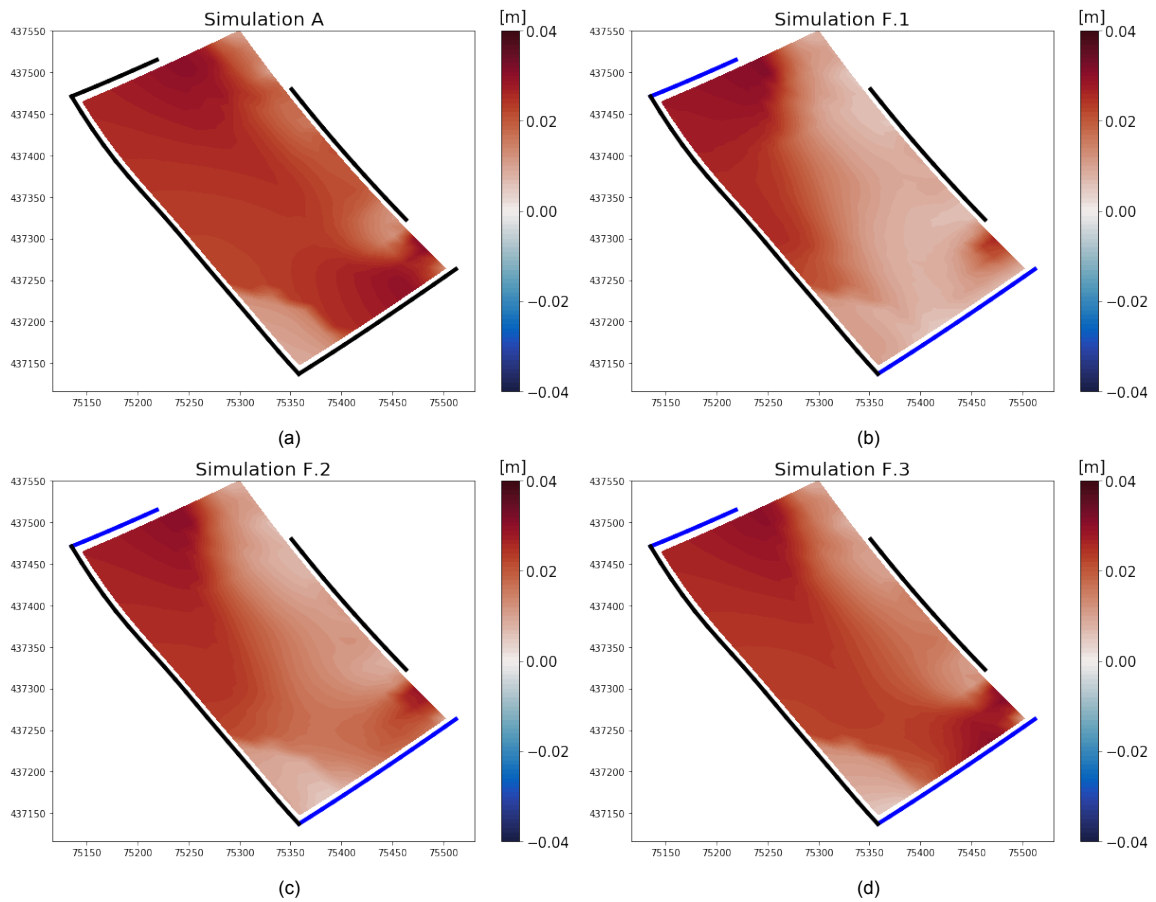


Figure E.8: The sedimentation pattern resulting from simulations incorporating a different height of the groynes. The bed layer is incorporated in the model as being non-erodible.

E.3.2.2. Erodeable bed layer

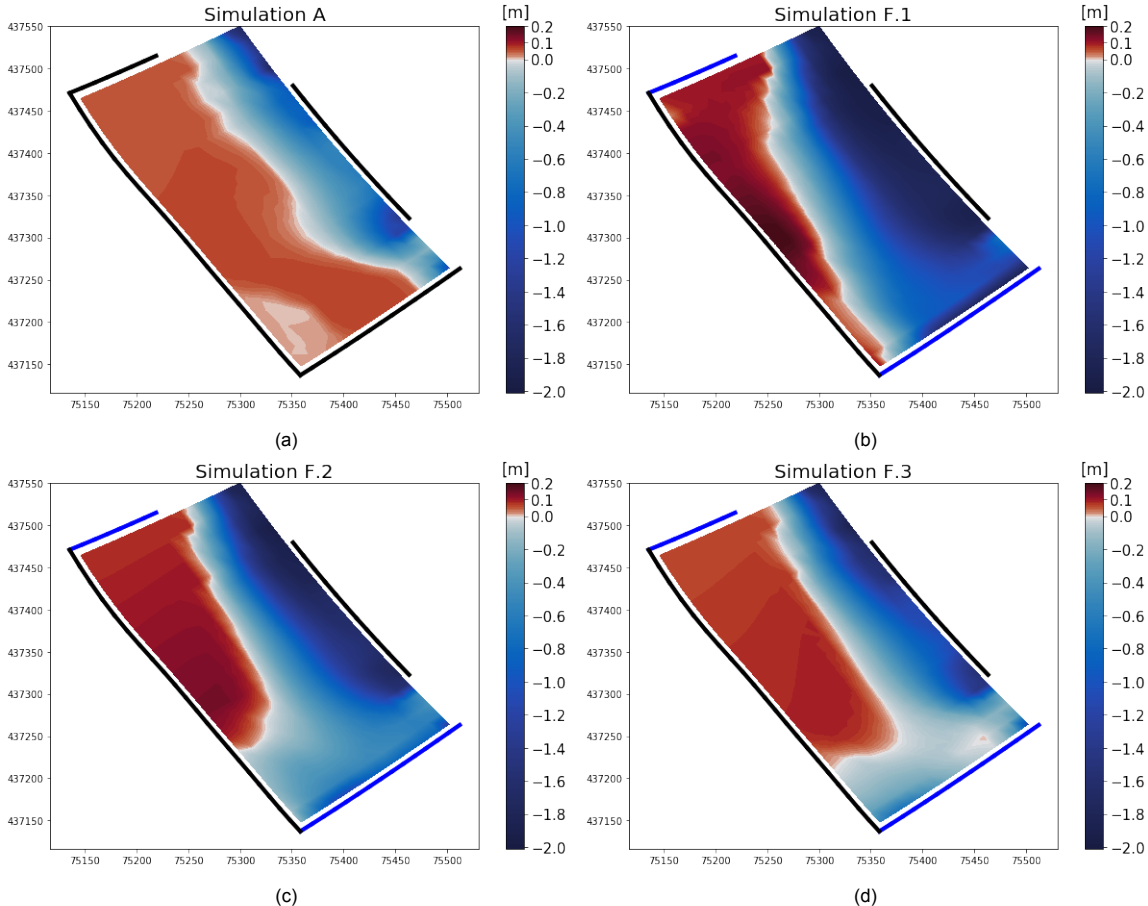


Figure E.9: The sedimentation pattern resulting from simulations incorporating a different height of the groynes. The bed layer is incorporated in the model as being erodible.

E.4. Groynes - length

E.4.1. Non-cohesive sediment

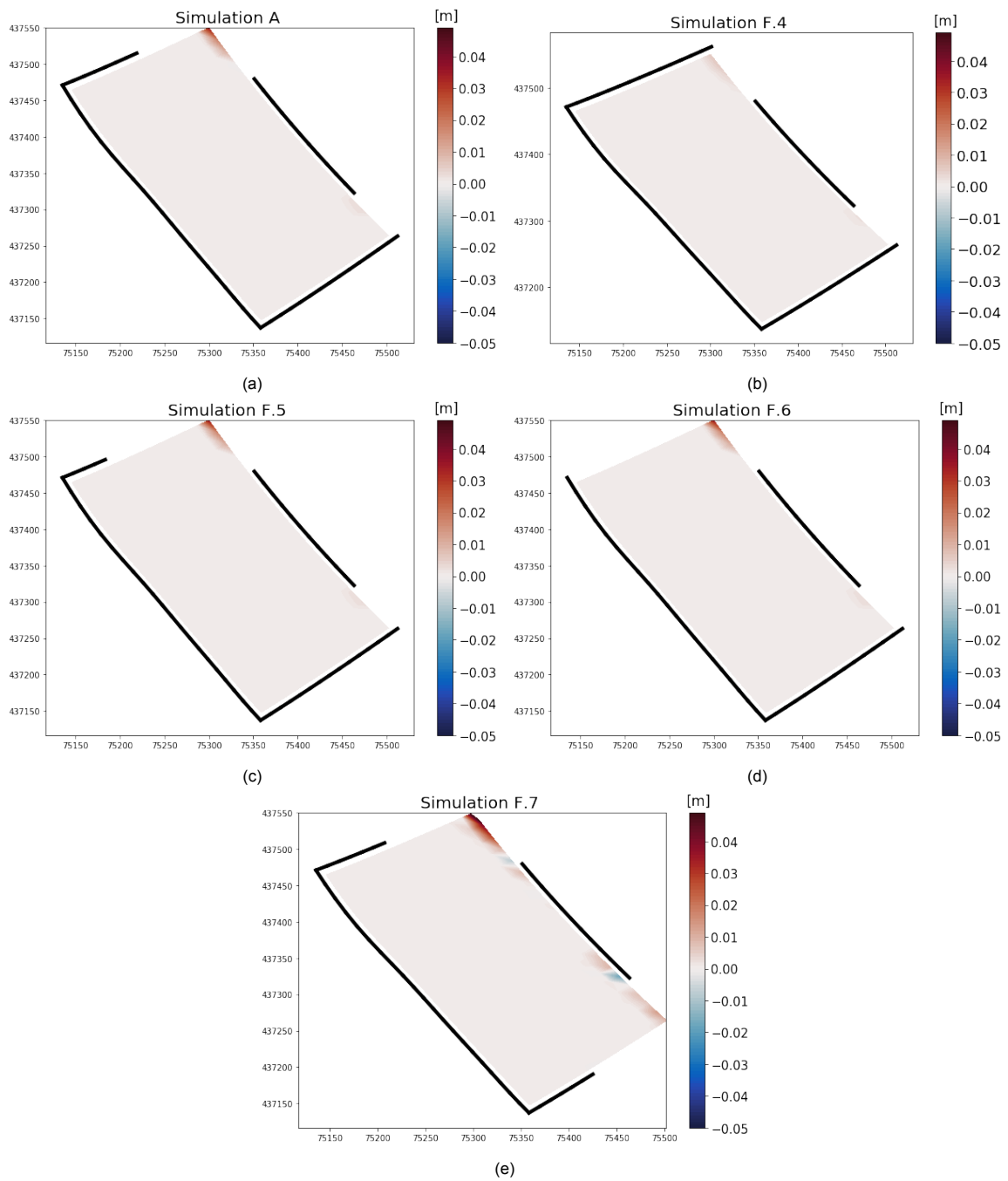


Figure E.10: The cumulative sedimentation / erosion resulting from simulations incorporating different length of groynes present at river bank L. The groynes which are adapted are visualised in blue. The bed layer consists of sand with a nominal diameter of $150 \mu\text{m}$.

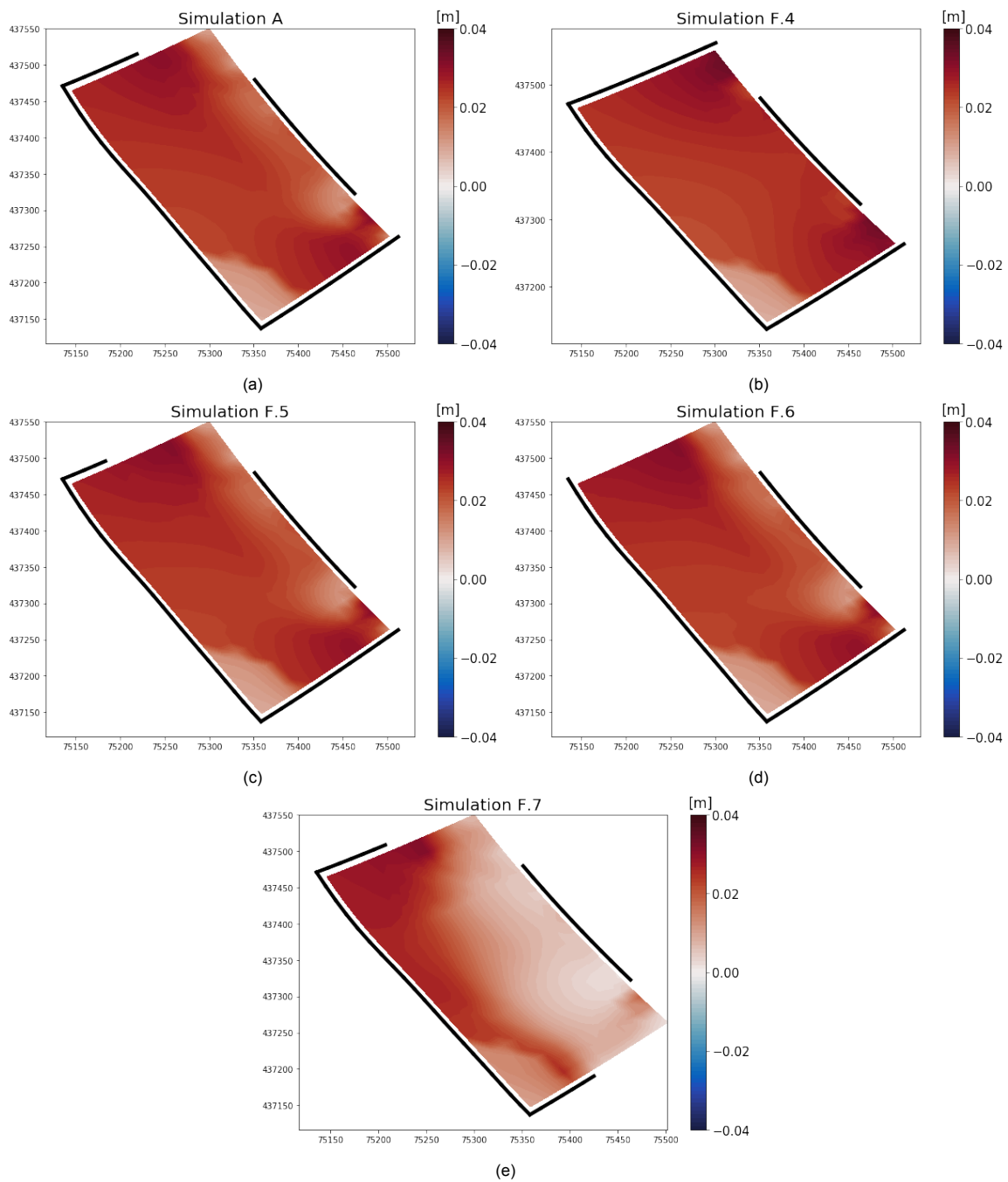
E.4.2. Cohesive sediment**E.4.2.1. Non-erodible bed layer**

Figure E.11: The sedimentation pattern resulting from simulations incorporating a different length of the groynes. The bed layer is incorporated in the model as being non-erodible.

E.4.2.2. Erodeable bed layer

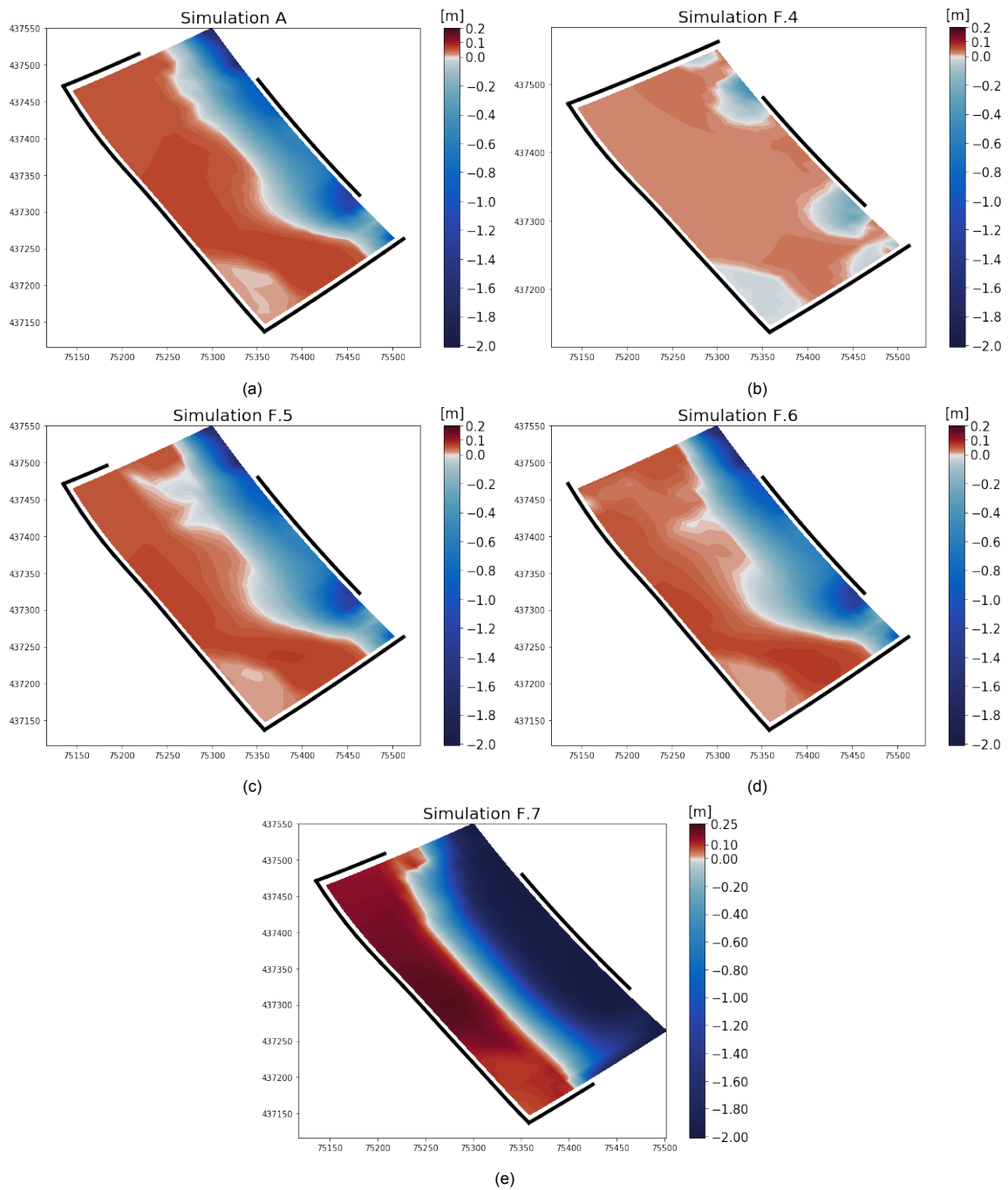


Figure E.12: The sedimentation pattern resulting from simulations incorporating a different length of the groynes. The bed layer is incorporated in the model as being erodible.

E.5. Inlet

E.5.1. Non-cohesive sediment

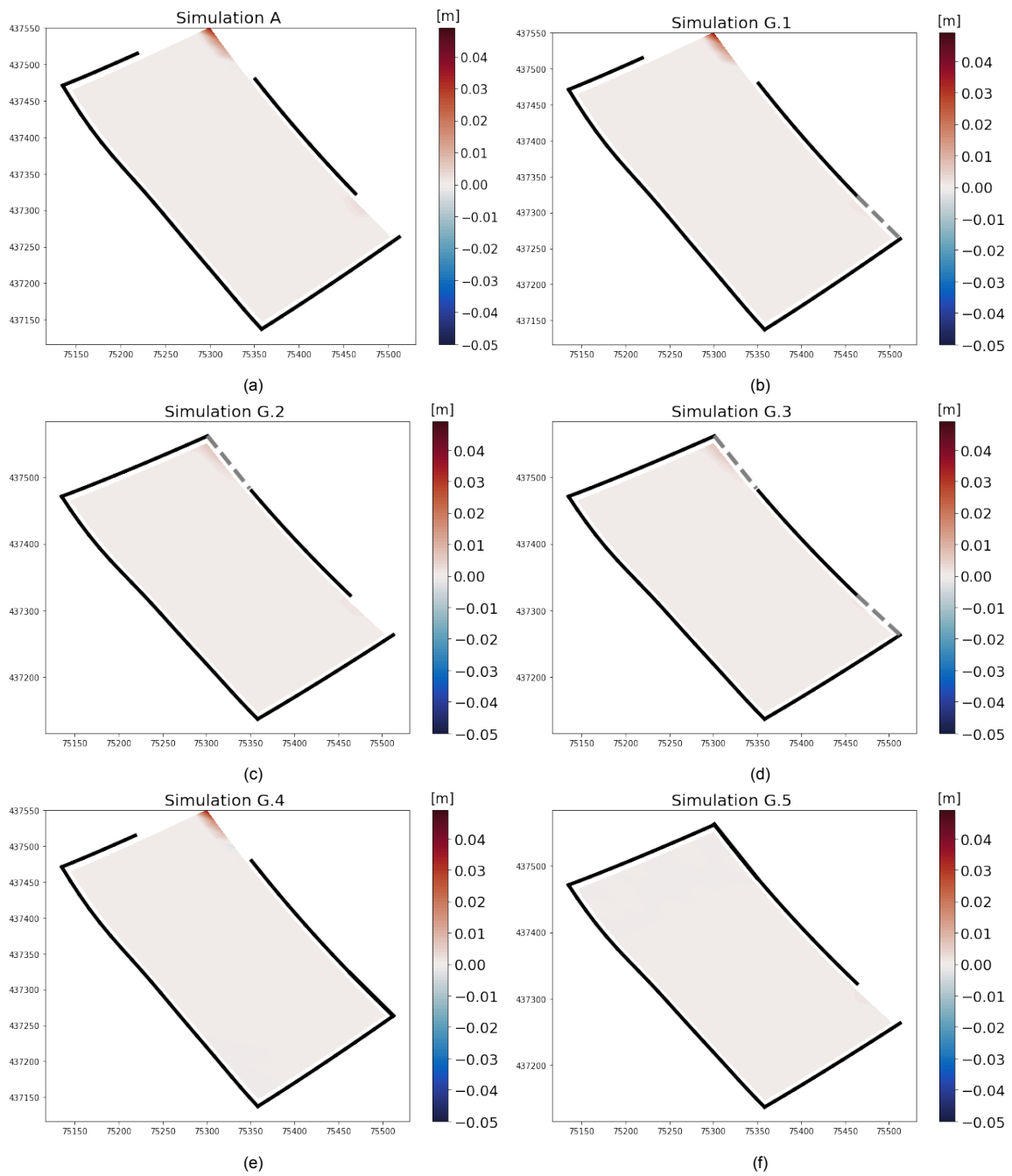


Figure E.13: The cumulative sedimentation / erosion resulting from simulations incorporating different surface areas of the entrances present at river bank L. The groynes which are adapted are visualised in blue. The bed layer consists of sand with a nominal diameter of $150 \mu\text{m}$.

E.5.2. Cohesive sediment

E.5.2.1. Non-erodible bed layer

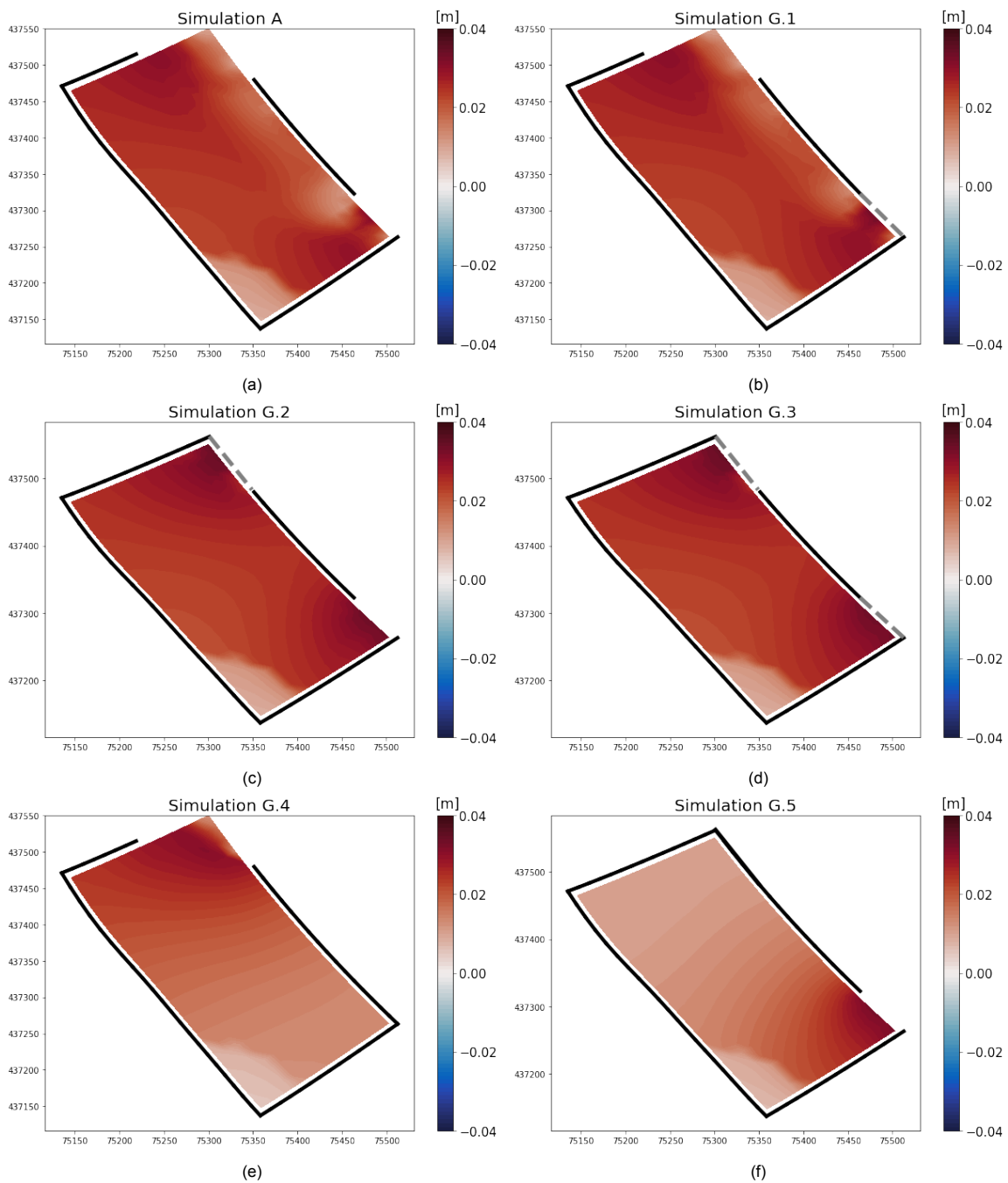


Figure E.14: The sedimentation pattern resulting from simulations incorporating a different surface area of the entrances of river bank L. The bed layer is incorporated in the model as being non-erodible.

E.5.2.2. Eroding bed layer

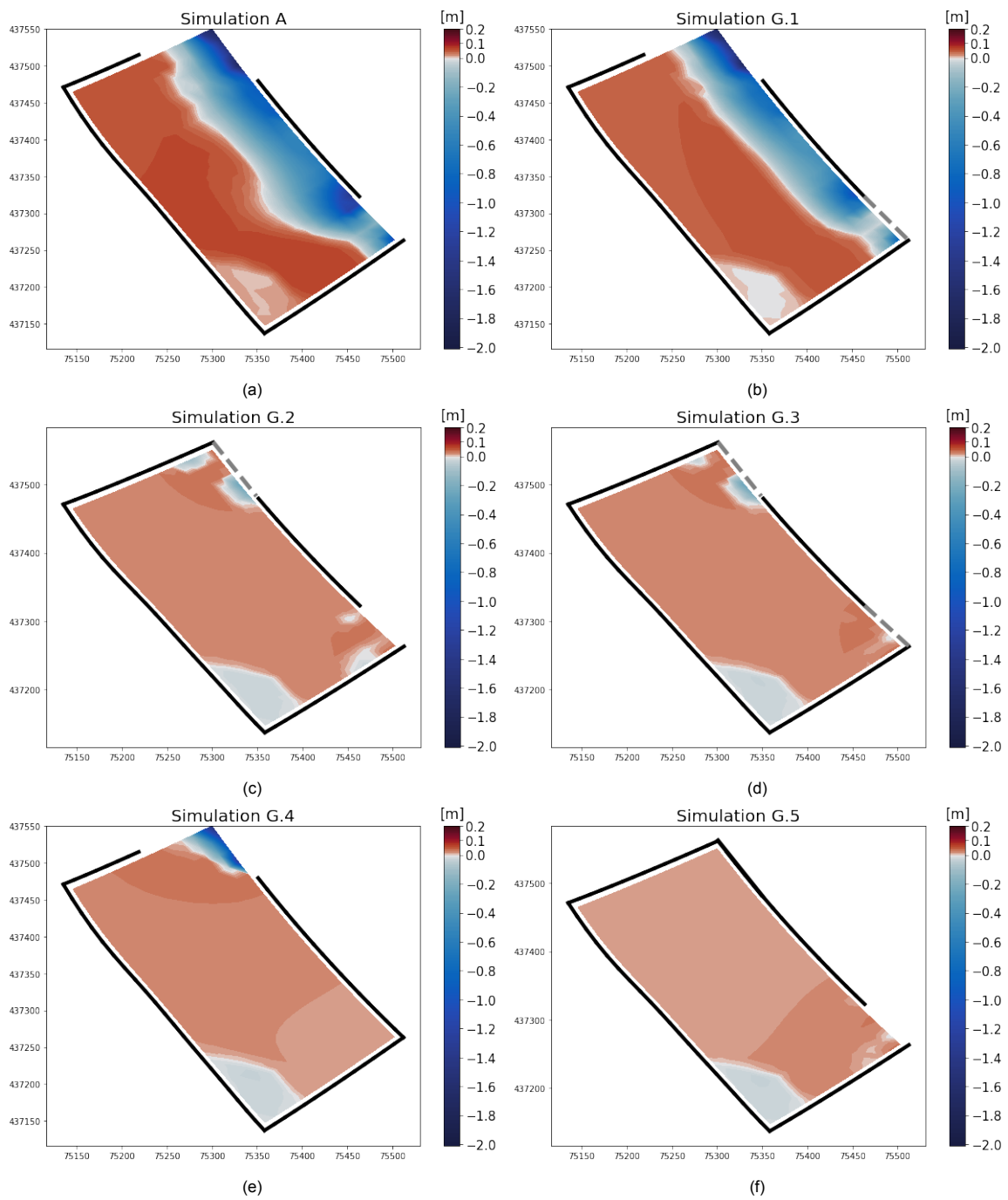


Figure E.15: The sedimentation pattern resulting from simulations incorporating a different surface surface area of the entrances of river bank L. The bed layer is incorporated in the model as being erodible.